BIOMECHANICAL STUDY OF SLEEPING SUPPORT AND SYSTEM OPTIMIZATION BASED ON SPINE ALIGNMENT

TUNG HO HONG

PhD

The Hong Kong Polytechnic University

2023

The Hong Kong Polytechnic University

Department of Biomedical Engineering

Biomechanical Study of Sleeping Support and System Optimization Based on Spine Alignment

Tung Ho HONG

A thesis submitted in partial fulfilment of the requirements for the degree of Doctor of Philosophy

Aug 2022

CERTIFICATE OF ORIGINALITY

I hereby declare that this thesis is my own work and that, to the best of my knowledge and belief, it reproduces no material previously published or written, nor material that has been accepted for the award of any other degree or diploma, except where due acknowledgement has been made in the text.

_______________________________ (Signed)

Tung Ho HONG (Name of student)

ABSTRACT

Sleep is a fundamental activity for maintaining health; people usually spend one-third of their time sleeping. The sleeping support system influences the spine alignment and impacts musculoskeletal health, sleep quality, and overall comfort. Previous studies suggest the sleeping support system should keep the spine in its neutral shape so that the intervertebral discs can be unloaded and rehydrated. However, limited studies have been conducted to measure spinal curvature in the position of lying supine because the back is in contact with the bed, making it challenging to observe. In addition, few studies have focused on disc loading in the supine position.

This study aims to understand the changes in spine alignment caused by sleeping support. The internal stress was revealed through computational simulation. The research results will help develop better sleeping support systems and improve sleep health.

A novel device was developed to measure the spine curvature in the supine position. This device contains a sensor tape and a tiny control box. The sensor tape was constructed based on a chain of inertial sensors, and it is thin and flexible with little influence on sleep posture. Sensors were assembled on self-developed flexible circuit boards using surface mount technology to achieve low thickness and high flexibility. Sensor data was read by the control box and sent to a computer by wireless connection. A special algorithm was developed to restore sensor inclinations to multiple arcs and connect them to curvature with high accuracy. The graphical user interface was programmed to display the shape of the sensor tape in real-time. The concept of axial tilt was introduced, the tilt angle can be displayed on the graphical user interface in real-time, and any abnormally twisted sensor will have a red cross

warning on the graphical user interface. When measuring a circle with a diameter of 200 mm, the device's measurement accuracy is about 99%.

Experiments were conducted; volunteers lay supine on three mattresses with different stiffness. They are named as hard, medium, and soft mattress; the indentation load deflection of mattresses was 120, 42, and 20 lbs, respectively. A cervical pillow was used to support the craniocervical region. The curvature measurement device was used for the measurement of the spinal curvature. Compared to the medium mattress, experimental results show that the head was raised by 30.5 ± 15.9 mm, and the neck was raised by 26.7 ± 14.9 mm if lying on the soft mattress. The lumbar lordosis fell by 10.6 ± 6.8 mm if lying on the hard mattress.

Finite element models were developed for biomechanical investigation. The result of the computational simulation showed a 49% increase in the peak cervical disc loading with the head-raised posture while lying on the soft mattress. High disc loading is not conducive to disc rehydration, and this problem should be considered when selecting a soft mattress. High peak contact pressures were observed if lying on the hard mattress; high contact pressures may cause discomfort and skin ulcers. Therefore, the hard mattress can be considered unsuitable for use. The computational simulation discovered insufficient upper back support when using the cervical pillow. This finding establishes a direction for product improvement.

In conclusion, novel devices were developed to address the gaps in existing research, including a curvature measurement tape that can measure the covered back in the supine position and a human finite element model to predict biomechanical information. This study found that the torso sank deeper in the soft mattress, but the head and neck sank less, resulting in a forward head position in the bed. The elevated head and neck caused a 49% increment in cervical disc peak loading, while the same pillow was used on the softer mattress. In that case, the head and neck support becomes stronger and may negatively impact musculoskeletal health, so it is necessary to consider using a softer or lower pillow.

PUBLICATIONS

Hong, T. T.-H., Wang, Y., Tan, Q., Zhang, G., Wong, D. W.-C., & Zhang, M. (2022). "Measurement of covered curvature based on a tape of integrated accelerometers." *Measurement*, 193, 110959. doi:10.1016/j.measurement.2022.110959

Hong, T. T.-H., Wang, Y., Wong, D. W.-C., Zhang, G., Tan, Q., Chen, T. L.-W., & Zhang, M. (2022). "The influence of mattress stiffness on spinal curvature and intervertebral disc stress—an experimental and computational study." *Biology*, 11(7). doi:10.3390/biology11071030

Zhang, G., Wong, D. W., Wong, I. K., Chen, T. L., **Hong, T. T.-H.**, Peng, Y., . . . Zhang, M. (2021). "plantar pressure variability and asymmetry in elderly performing 60-minute treadmill brisk-walking: paving the way towards fatigue-induced instability assessment using wearable in-shoe pressure sensors." *Sensors (Basel)*, 21(9). doi:10.3390/s21093217

Zhang, G., Wong, I. K., Chen, T. L., **Hong, T. T.-H.**, Wong, D. W., Peng, Y., . . . Zhang, M. (2020). "identifying fatigue indicators using gait variability measures: a longitudinal study on elderly brisk walking." *Sensors (Basel)*, 20(23). doi:10.3390/s20236983

Chen, T. L. W., Wang, Y., Peng, Y., Zhang, G., **Hong, T. T. H.**, & Zhang, M. (2023). "Dynamic finite element analyses to compare the influences of customised total talar replacement and total ankle arthroplasty on foot biomechanics during gait." *Journal of Orthopaedic Translation*, 38, 32-43. doi:10.1016/j.jot.2022.07.013

AWARDS

2022 Health Future Challenge - Co-innovation Award

ACKNOWLEDGEMENTS

I would say that my PhD career was an unforgettable precious experience in my life. I have gained a lot during the three years of struggle, and many people should be thanked.

First and foremost, I would like to express my sincere gratitude to Professor Ming Zhang, at the Department of Biomedical Engineering, The Hong Kong Polytechnic University. Many thanks to him for offering me the opportunity to pursue the PhD. As my chief supervisor, he has always been a source of suggestion, encouragement, support, and inspiration during my academic endeavors.

I would also like to extend a special thanks to Dr. Duo Wong and Dr. Annie Wang for their ideas, guidance, and help during my publications.

I thank Dr. Tony Chen, Ms. Ivy Wong, Dr. Fie Yan, Dr. Qitao Tan, Dr. Yinghu Peng, Mr. Guoxin Zhang, Mr. Fei Chen, and Ms. Fangbo Bing for their ideas, suggestions, and assistance throughout this study.

I thank all the teachers and non-teaching staff of the Department of Biomedical Engineering for their help and cooperation, especially Professor Mo Yang, for his suggestions and comments on my research project.

I thank the reviewers and journal editors, whether for the rejected manuscript or accepted articles. Their thoughtful advice and insights have allowed me to learn and improve while revising the manuscripts.

I would like to thank Mr. Robert Ko of Sambo Group Technology Ltd. Without his suggestion and encouragement, I probably would not have considered taking this PhD program.

Several organizations, including Sinomax Health & Household Products Limited, Infinitus (China) Co., Ltd., Li Ning Sports (China) Co., Ltd., Dr.Kong Footcare Limited, and Tech Hill Limited, are on my gratitude list for their help with technical advice and supply of experimental materials.

Finally, I would like to express my special thanks to my family and friends, whether from Hong Kong, mainland China, or overseas, for their consistent encouragement and support.

TABLE OF CONTENTS

LIST OF FIGURES

LIST OF TABLES

LIST OF ABBREVIATIONS

3D	Three-dimensional
ALL	Anterior Longitudinal Ligament
AVR	Advanced Virtual RISC
BI	Body Inclination
CAD	Computer-aided design
CLA	Cervical Lordosis Angle
CLD	Cervical Lordosis Distance
CMOS	Complementary Metal-Oxide-Semiconductor
CS	Chip Select
CT	Computed Tomography
DAT	Data Pin
E	Young's modulus
EDA	Electronic Design Automation
EEPROM	Erasable Programmable Read-Only Memory
FE	Finite Element
FPC	Flexible Printed Circuit
GND	Ground
GUI	Graphical User Interface
G_x, G_y, G_z	Gravity in three axial directions
HD	Head Distance
I2C	Inter-Integrated Circuit
IDE	Integrated Development Environment
ILD	indentation load deflection
LLA	Lumbar Lordosis Angle
LLD	Lumbar Lordosis Distance
MCU	Micro Control Unit

MEMS	Micro-Electro-Mechanical Systems
MISO	Master In Slave Out
MOSI	Master Out Slave In
MRI	Magnetic Resonance Imaging
OLED	Organic Light-Emitting Diodes
PCB	Printed Circuit Board
PLL	Posterior Longitudinal Ligament
r	Correlation coefficient
RGB	Red-Green-Blue
RST	Reset
SCK	Serial Clock
SCL	Serial Clock Line
SDA	Serial Data line
SMT	Surface Mount Technology
SPI	Serial Peripheral Interface
SRAM	Static Random Access Memory
STD	Standard Deviation
STL	stereolithography
TI	Torso Inclination
TKA	Thoracic Kyphosis Angle
TQFP	Thin Quad Flat Pack
U	Accelerometer Unit
v	Poisson's ratio
VCC	Voltage Common Collector

Chapter 1 Introduction

1.1 Background

Sleep is a fundamental activity for maintaining health; people usually spend one-third of their time sleeping. When waking up from well sleep, the body and mind are full of energy; on the contrary, poor sleep can lead to neck pain, back pain, listlessness, immune system disorders, and other health problems. Sleep quality can be affected by the environment, sleeping support system, lighting, temperature, humidity, and sound (Lan et al., 2017; Zhang et al., 2018). A proper sleeping support system is a critical element of good sleep. In the lying position, the sleeping support system carries the body weight and deforms both the body and the support. An ideal sleeping support system should be able to support the human body appropriately. Sleep therapists usually use spine alignment and pressure distribution as objective conditions for sleeping support evaluation (Fess et al., 2015; Wong et al., 2019). The human back is curved; a too-hard sleeping support system can not produce proper deformation to match the curve of the human back; the middle of the back cannot touch the mattress, resulting in abnormal spine kyphosis (Haex, 2004). Also, a hard surface results in concentrated and high pressure, subsequences induce discomfort, regional poor blood supply, and a higher risk of pressure ulcers in bed-borne patients (Stausberg et al., 2010).

On the other hand, sagging support results in discomfort and poor sleeping quality (Haex, 2004). Lateral and supine sleeping positions are the most common sleeping positions. The back is exposed in a lateral position and can be visually observed and measured by a camera or 3D scanner. Hence, the spine alignment in the lateral position has been widely studied (Leilnahari et al., 2011; Verhaert et al., 2012). While in a supine position, the back is contacted with the sleeping support system and is hard to measure. There is challenging to develop an effective tool for measuring spine curvature in the supine position (Wong et al., 2019).

Measurement of the spine curvature is necessary for various fields such as ergonomic design, rehabilitation, physical therapies, and orthopedics. The accessibility of the spine from the body back is not always practical. In the ergonomic design of the body support system for sleeping, maintaining normal spinal curvature is one of the most critical factors contributing to the design's reasonability. In the case of lying on the side, it is easy to measure the spine curvature (Wong et al., 2019); however, there have limited tools for direct curvature measurement in the case of lying on the back. X-ray, CT, and MRI could capture the spinal curvature in the back-covered situation and are commonly adopted in the medical treatment courses of spine disorders (Voinea et al., 2017), but with the shortcomings of patient radiation exposure. Photoelectronic, ultrasound, and other optical systems could accurately measure spine curvature, but they are commonly bulky systems involved and require total back exposure (Pivotto et al., 2021; Ran et al., 2020; Zhou et al., 2020). The customized indentation bars penetrated the mattress can obtain the approximated spine curvature (Zhong et al., 2014). But this method increased the experiment's difficulty and brought the experimental results' bias due to the thickness and hardness of the custom-made indentation bar.

Finite element methods were used for biomechanical analysis of sleep and spine injury. These studies provide useful biomechanical information on the deformation of the human body under different input conditions, especially the predictions inside the human body, which are challenging to obtain with traditional measurement methods. This study will refer to previous studies and integrate the human model and sleeping support system to reveal the interaction of the body and sleeping support systems in the lying position.

1.2 Project Significance

This study will understand the changes in spine alignment caused by sleeping support. The internal stress will be revealed through computer simulation. The research results will help develop better sleeping support systems and improve sleep health.

1.3 Research objective

Based on these premises, the current study aimed to apply new technologies in biomechanics study for investigation of the internal effect of the human body on sleep and neck pain prevention based on spine alignment, including:

1) To investigate the spine alignment in the supine position.

    i. Device development: A wearable curvature measurement tape to obtain the spine alignment in the supine position;

    ii. Experiment: Sleep on different stiffnesses of mattresses, using the spine alignment sensor to obtain the spine parameters in the supine position for further analysis;

    iii. Material test: Use a plastic tensile test machine to evaluate mattress and pillow materials' compressive properties for further analysis.

2) To understand the internal load transfer of the human body with different spine alignments using computational methods.

3) To provide guidelines for the optimal design of sleeping support systems.

1.4 Outline of this thesis

Chapter 1 includes a general overview of sleep, measurement of spinal alignment, finite element analysis of internal human loads, and biomechanical effects of sleep support systems on the human body. This chapter also summarizes the current state of research on related issues. The final part of the chapter develops a problem statement that presents the project's overall value.

Chapter 2 reviews the existing research and literature. This part reviewed the basics of the spine's anatomy and function, including the spine's basic mechanics formed by the connections of vertebrae and intervertebral discs, the ligaments and facet joints that stabilize the spine, and the muscles that can change the shape of the spine. The second part of this chapter covers understanding sleep function, sleep support systems, sleeping positions, spine deformation in lying positions, and spinal alignment measurements. The musculoskeletal health problems associated with sleep, including neck and low back pain, were reviewed in part three. Part 4 of this chapter reviews the application and methods of computer algorithms in musculoskeletal health. The last paragraphs of this chapter reveal research gaps to guide the initiative for upcoming work in the research.

Chapter 3 describes the methodology of this study. This study includes three main elements. First, a curvature measurement tape that integrates multiple inertial sensors was developed. This thin, flexible sensor tape can measure spinal curvature in the supine position. The design concept, hardware fabrication, software development, calibration, evaluation, and validation were described. The second part of this chapter describes the experimental design, including volunteer information, materials, equipment, experimental procedures, and acquisition parameters. The last part of this chapter stated the development procedures of the finite element model, including the construction of the human body model, creation of the sleep support system, meshing, boundary and loading conditions, and verification of the model.

Chapter 4 presents this study's results, including experimental results obtained by the curvature measurement tape and biomechanical information predicted by the finite element method.

Chapter 5 discusses the research results, including the device's performance and the reasons that caused the experimental and simulation results. Research limitations and future directions of work were presented in this chapter.

Chapter 6 concludes the study with the findings and conclusions of Chapters 3, 4, and 5.

Chapter 2 Literature review

2.1 Spine

The spine is the axial structural of the human body. It has weight-bearing, shock absorption, protection, and sports functions. The spine connects to the head to provide nutrition, nerve signals, and biomechanical support. The human spine mainly includes vertebrae and intervertebral discs; the spine structure is stabilized by ligaments and facet joints, supporting the trunk and protecting internal organs. The entire spine is divided into several segments, including seven pieces of cervical vertebrae, twelve pieces of thoracic vertebrae, five pieces of lumbar vertebrae, and the sacrum and coccyx. Humans' five sacrums and four coccyxes were fused, called "false vertebrae." The vertebrae have a spinous process protruding to the dorsal side, which can be felt subcutaneously on the midline of the back and is one of the critical signs of meridian positioning. A longitudinal spinal canal inside the spine contains the spinal cord and its membrane. An adult spine has a double S-shaped curve in the sagittal plane. If observed through the sagittal plane, the spine has four physiological curves: cervical lordosis, thoracic kyphosis, lumbar lordosis, and sacrum kyphosis. The curvature of the spine that protrudes forward from the neck and waist is called lordosis, while the opposite protruding chest and tail are called kyphosis. The spine is flexible, shock-absorbing, and provides strong support for humans who walk upright.

2.1.1 Anatomy

A spine is constructed by five regions: Cervical, Thoracic, Lumbar, Sacral, and Coccyx. The anatomical structure of the spine consists of several complex structures, including vertebrae, facet joints, intervertebral discs, spinal ligaments, muscles, spinal cord, and nerves (Vital & Cawley, 2020).

The accumulation of vertebral bodies forms the front of the spine, and its front is adjacent to the internal organs of the chest and abdomen. It not only protects the organs themselves but also protects the nerves and blood vessels leading to the organs. There is only a thin layer of loose tissue between them.

The back of the spine is composed of the arches, laminae, transverse, and spinous structures of each vertebra. They are connected to each other by ligaments, and the superficial surface only covers muscles, which are relatively close to the body surface and easy to touch.

2.1.1.1 Bones

The vertebral column is typically composed of 33 bony vertebrae (Figure 2.1). During evolution, the five sacrums and four tail bones were fused. The upper segment of the spine consists of 24 moveable vertebrae, including seven pieces of cervical, twelve pieces of thoracic, and five pieces of lumbar. The separated vertebrae are cushioned by intervertebral discs, except for the first and second vertebrae. The vertebral column forms an axial skeleton with a skull and ribs. Many ligaments, tendons, and muscles support the spine, giving it flexibility and a wide range of motion.

Except for C1 and C2, a vertebra consists of the vertebral arch and the vertebral body. The vertebral arches face the person's back. The vertebral body and the vertebral arch form the vertebral foramen that accommodates the spinal cord. Vertebrae can protect the fragile spinal cord.

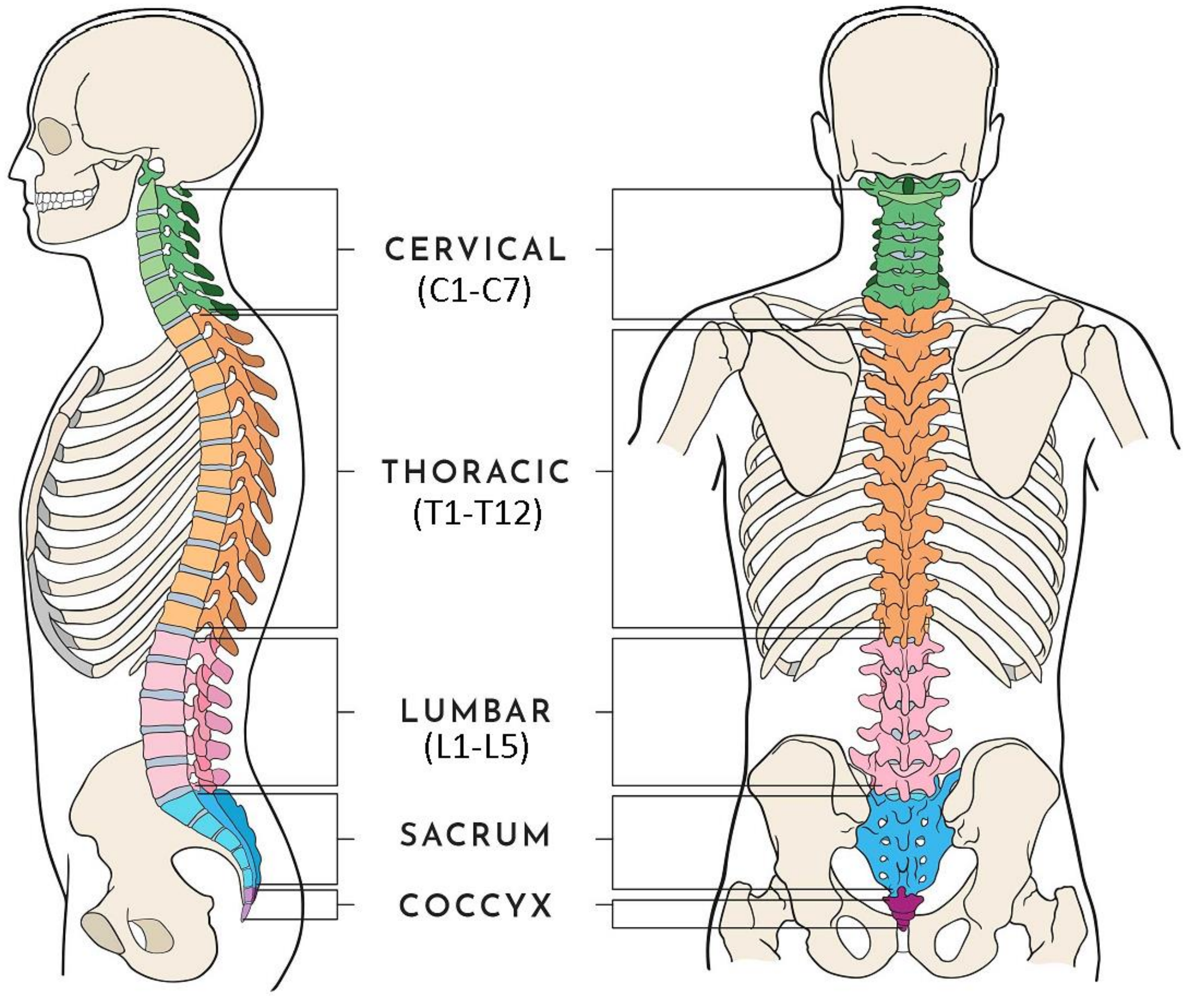

Figure 2.1. The spine (Mcgillion, 2022).

A human cervical spine consists of seven vertebrae (Figure 2.2). The dimensions of human cervical vertebrae are generally smaller than thoracic and lumbar vertebrae. The morphological characteristics of the first (C1) and second (C2) vertebrae closest to the skull differ from other typical vertebrae. The unique structure enables the head to rotate and swing flexibly. The remaining five cervical vertebrae have corpuscles that connect with the intervertebral discs, facet joints, and soft tissues.

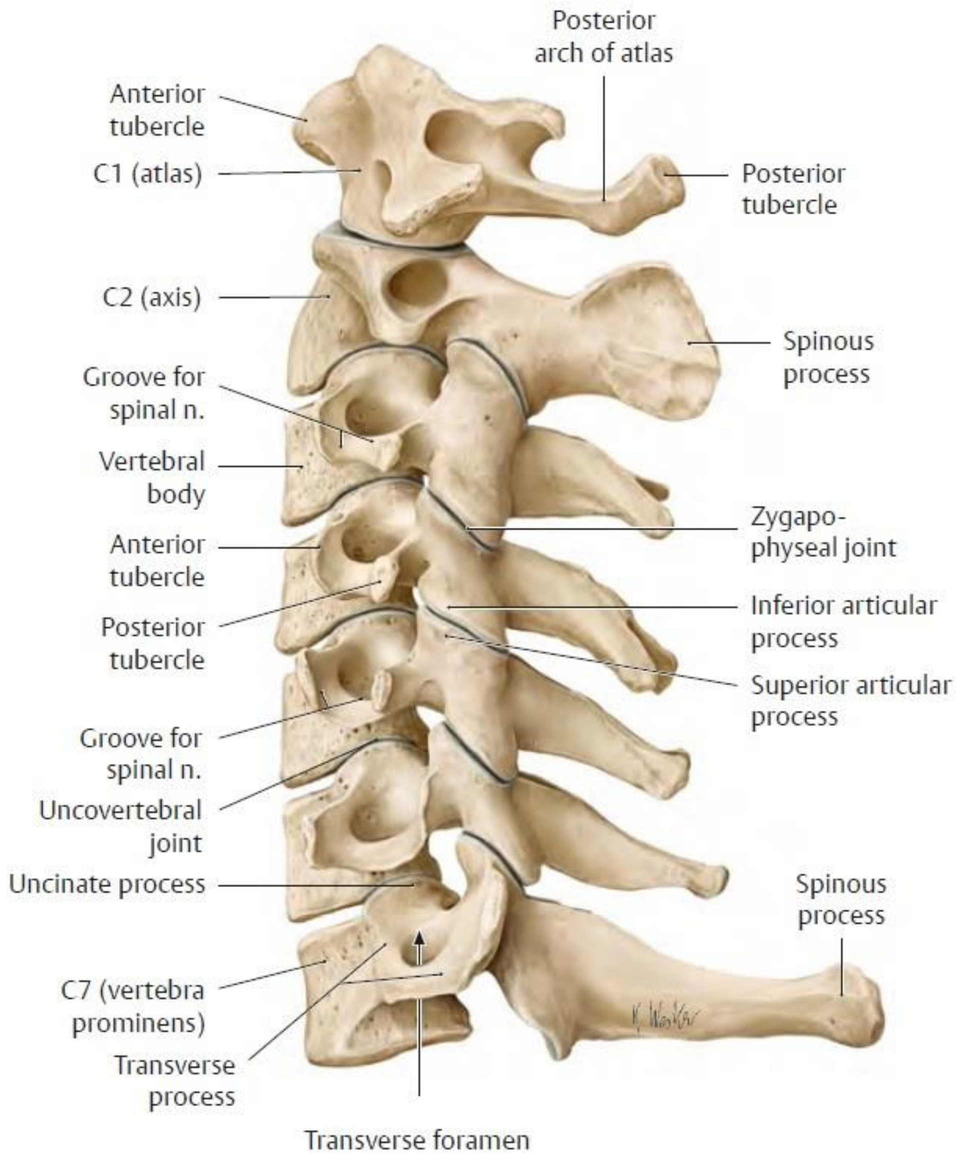

Figure 2.2. Left lateral view of cervical vertebrae (Gilroy et al., 2020).

The thoracic spine is in the middle part of the spine, located between the cervical and lumbar vertebrae (Figure 2.3). Humans have twelve thoracic vertebrae (T1-T12); the thoracic vertebrae have a larger size than the cervical vertebrae and smaller than the lumbar vertebrae. The one near the cervical spine is smaller, and that near the lumbar vertebrae is larger. The sides of the vertebral bodies are connected to the ribs. The mobility of the thoracic spine is usually less.

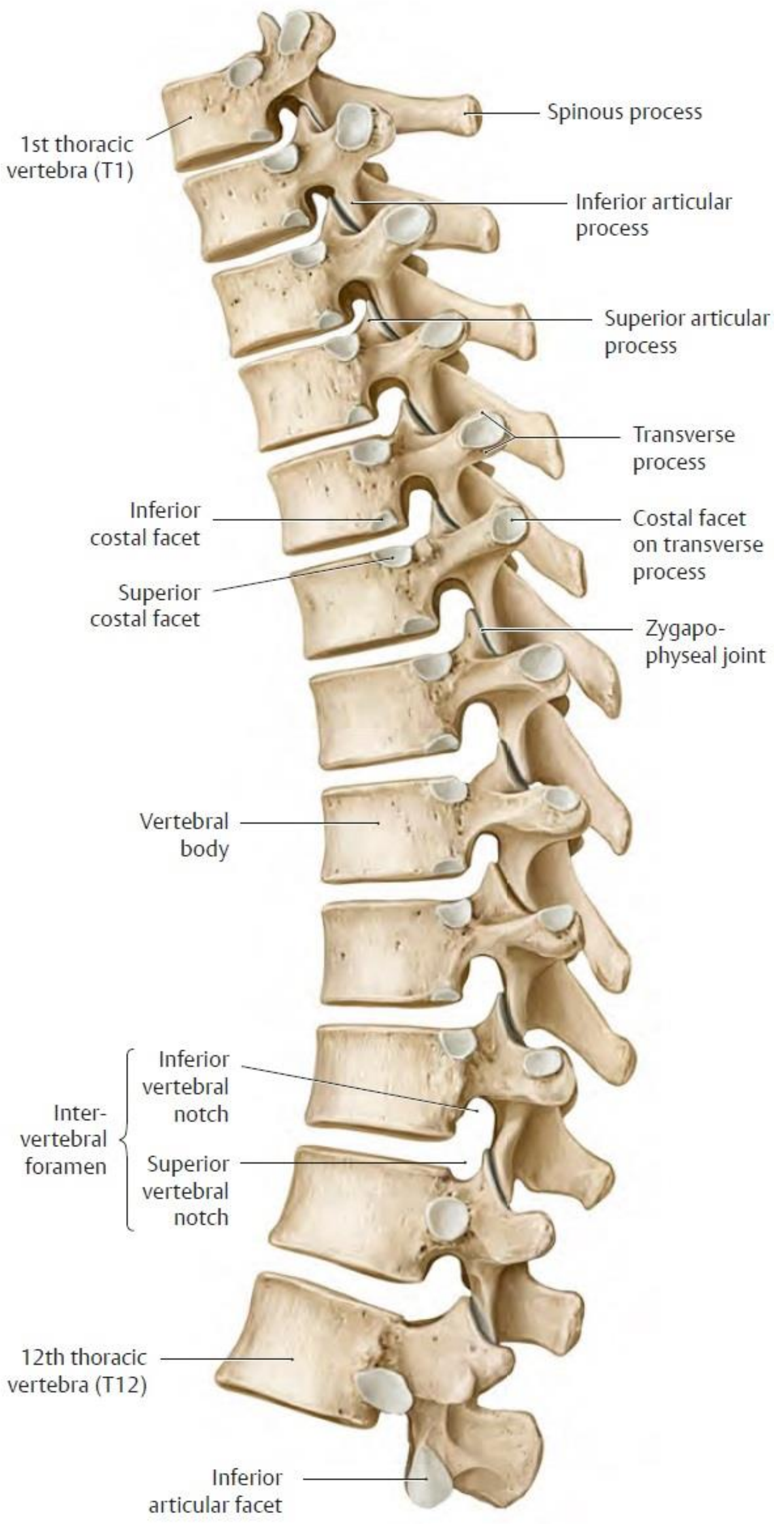

Figure 2.3. Left lateral view of thoracic vertebrae (Gilroy et al., 2020).

The ribcage is connected to the thoracic vertebrae. It forms a semi-rigid bone and cartilage structure from costal cartilage, sternum, etc., which has the primary ventilation function in the respiratory system and protects organs such as the heart, lungs, and large blood vessels. Because the thoracic cavity has significantly reduced intersegmental mobility, the magnitude of thoracic spine mobility is much lower (Vital & Cawley, 2020).

The lumbar spine is situated below the thoracic spine and above the sacrum (Figure 2.4). It consists of five large vertebrae (L1-L5). They have no transverse foramen within the transverse process and no facet joints on either side of the body. The robust lumbar vertebrae help support the body's weight and allow movement of the torso.

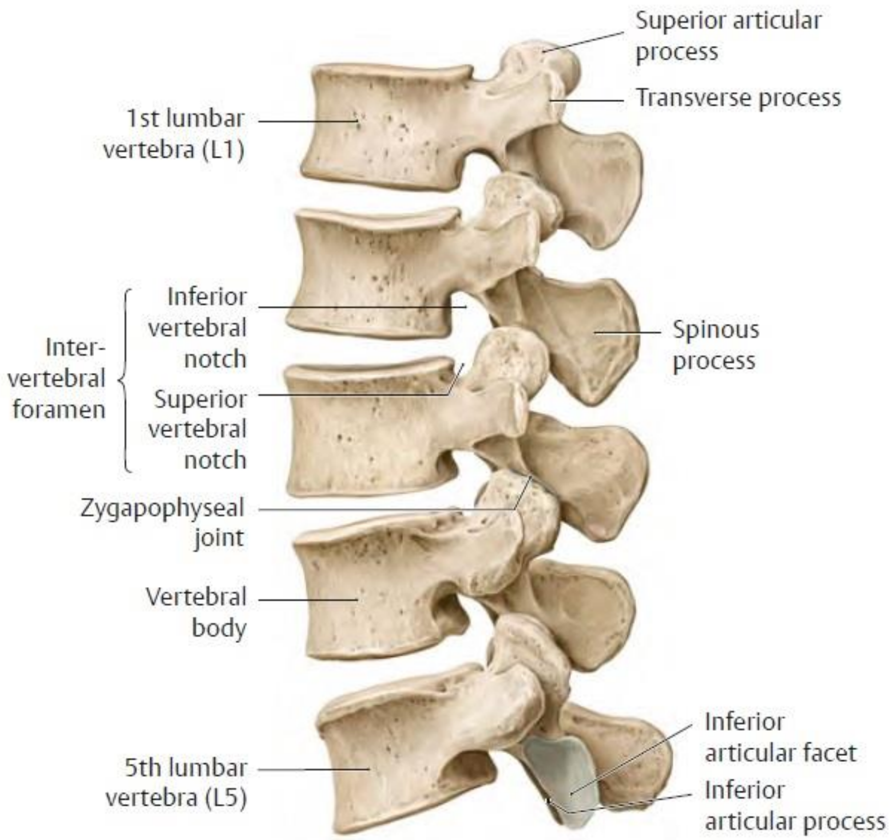

Figure 2.4. Left lateral view of lumbar vertebrae (Gilroy et al., 2020).

The sacrum is situated below the lumbar spine and is attached to the pelvis on both sides (Figure 2.5). The adult sacrum consists of five fused bones. The sacrum has a complex structure that supports the spine and accommodates the spinal nerves.

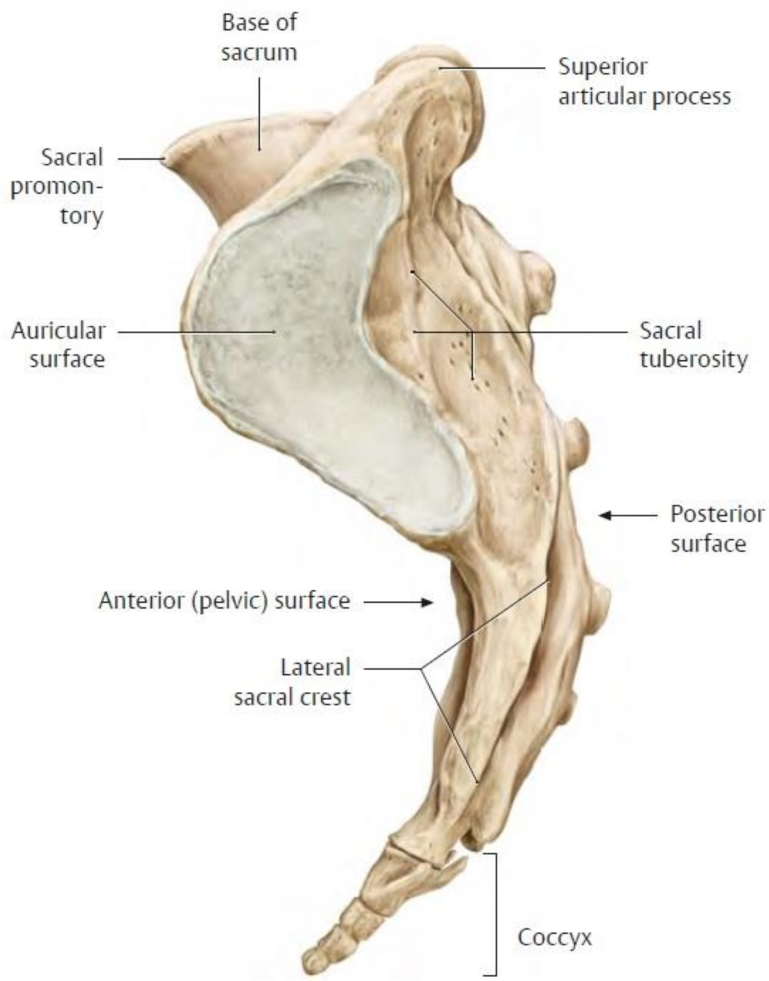

Figure 2.5. Left lateral view of the sacrum and coccyx (Gilroy et al., 2020).

The coccyx is the last segment of the spine and is the remnant of a degenerated tail (Figure 2.5); it consists of 4 coccygeal vertebrae fused. The coccyx is connected to the sacrum by fibrocartilaginous joints, allowing limited movement between the sacrum and the coccyx.

2.1.1.2 Intervertebral discs

The intervertebral disc is a fibrocartilage disc; intervertebral discs connect most vertebrae. The intervertebral disc can be compressed and deformed so the spine can move between certain angles. This tissue can absorb shocks and act as a biomechanical protector for the spine, brain, and other structures, such as nerves. There are 23 intervertebral discs in adults.

The intervertebral disc is generally constructed in two parts (Figure 2.6). The surrounding part is a dense tissue aligned in concentric circles by several layers of radial and annular collagen fibers and elastic fibers, namely annulus fibrosus. It is high toughness and connects each vertebrae's body. The annulus fibrosus has high flexibility, binds each vertebral body, protects the nucleus pulposus, and prevents it from protruding to the periphery.

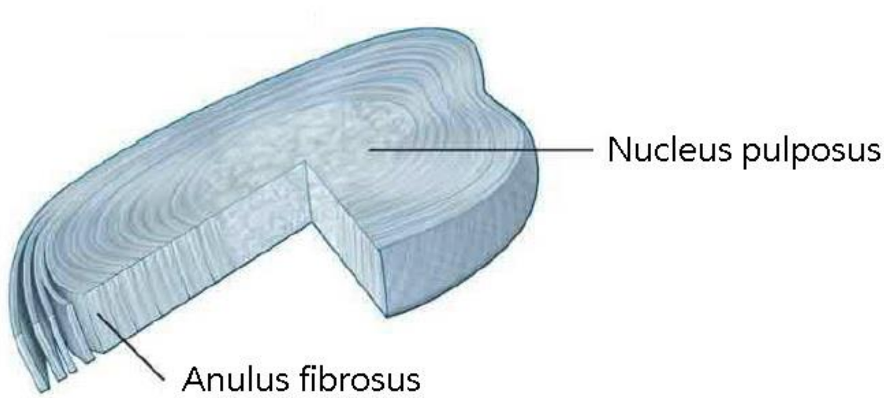

Figure 2.6. The sectional view of an intervertebral disc (Drake et al., 2020).

The central part of the intervertebral disc is the nucleus pulposus, which is the remains of the notochord during the embryo. The nucleus pulposus is somewhat soft, elastic, and resembles a semi-liquid gelatinous substance. Their ingredients are mainly polysaccharides and water. The nucleus pulposus is filled between the upper and lower cartilage plates and the annulus fibrosus, which can cushion the impact and stress of the spine.

Intervertebral discs do not have blood vessels, and the vertebral body provides nutrition through penetration. Intervertebral discs can rupture the annulus fibrosus due to aging, trauma, poor posture, overwork, muscle tension, tendon inflammation, and improper force. When the annulus ruptures, the nucleus pulposus easily protrudes posteriorly and protrudes into the spinal canal or intervertebral foramen, compressing the adjacent spinal cord or nerve roots, causing back pain, numbness, and pain in the hands and feet.

The central area of the disc is liquid, allowing the disc to absorb shock and change shape. (Adams et al., 2009). With age, the fluid area of the nucleus pulposus shrinks, and the pressure drops. The annulus fibrosus around the intervertebral disc is more prone to stress concentration with the change of spinal posture. Degeneration of the intervertebral disc is exacerbated by sustained loading or injury (Adams et al., 2009). Previous studies have found that the lumbar intervertebral discs lose and regain about one-fifth of their water per day (Botsford et al., 1994). Most of the water loss occurs due to the load on the intervertebral discs caused by daytime activities. Long-term dehydration causes loss of intervertebral disc height (Race et al., 2000). Therefore, it is critical to be unloaded at night to rehydrate intervertebral discs. The strength of the external load and how it is applied influence the growth and recovery of the intervertebral disc (Huysmans et al., 2006). Although limited to the measurement of lateral position, maintaining the spine in a neutral posture to minimize the load on the intervertebral disc is the goal of sleep research (Leilnahari et al., 2011). Therefore, this study aimed to minimize disc loading during sleep for systemic optimization.

2.1.1.3 Facet joints

The facet joints are a pair of synovial plane joints between the articular processes of two nearby vertebrae. An intervertebral disc and a couple of posterior facet joints connect the spinal segments. Hence, the vertebrae are linked by three supporting points. The three supporting points affect each other, and the degenerative changes of one joint will affect the entire complex biology (Perolat et al., 2018). The facet joints are wrapped by the facet capsule ligament (FCL) (Bermel et al., 2018).

2.1.1.4 Ligaments

Ligaments are a layered structure that mainly contains structural collagen fibers. Usually, they are surrounded by intercellular material of elastin, reticulin, and ground material (Fung, 1993). Inside the ligaments, collagen fibers are arranged in parallel bundles to support tensile loads (Figure 2.7).

Ligaments prevent extreme movements, stabilize the vertebrae and protect the underlying structures (Haex, 2004). There is three-axis mobility between the vertebral bodies. The ligament structure (including the intervertebral disc and bone restraint) is the structure that stabilizes the motion between the vertebrae and restricts the limit of the action between the vertebral bodies. In particular circumstances, such as minor trauma or significant trauma, the movement between the vertebral bodies can exceed the constraints of the ligament structure.

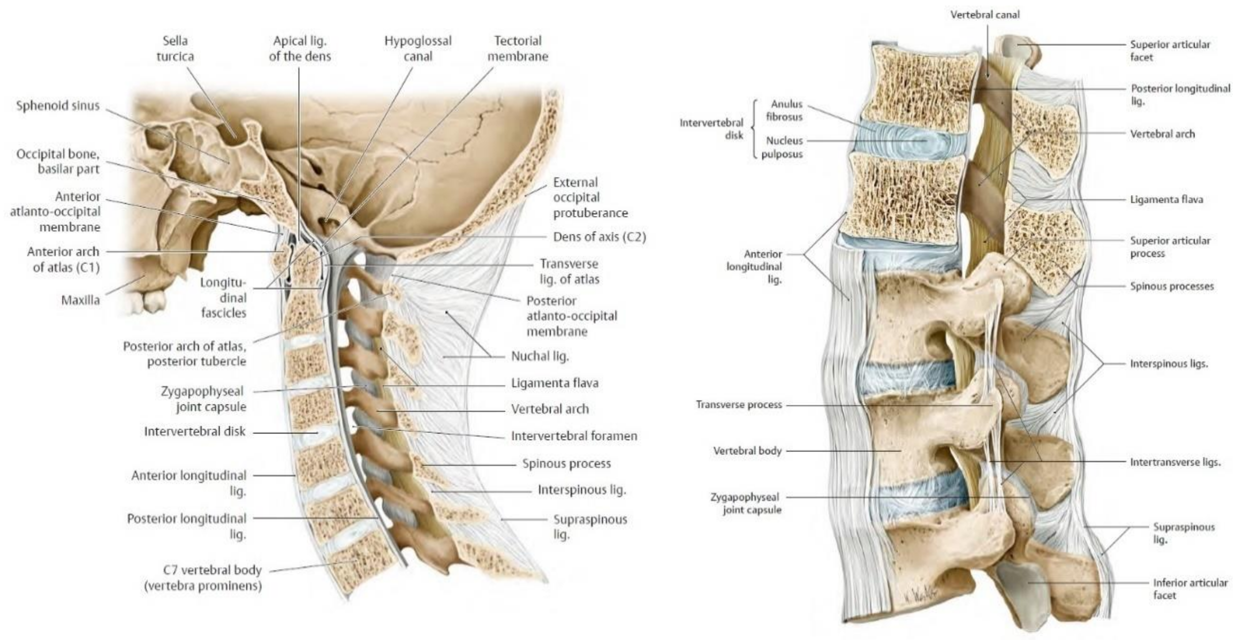

Figure 2.7. Spinal ligaments (Gilroy et al., 2020).

The anterior longitudinal ligaments (ALL) develop vertically along the length of the spine and are the primary structure supporting the intervertebral joints. The ALL firmly connects the anterior surfaces of each vertebral body. Its function is to limit extreme positions of spinal movement. It relaxes when bending over and is tensioned when bending backward. It also protects the intervertebral disc from being moved from its original location (Vital & Cawley, 2020).

Ligamenta flava (yellow ligaments) also acts to protect the spinal canal (Vital & Cawley, 2020). The yellow ligament connects the laminae of two adjacent vertebrae. The outer surface appears to be short and overlapped by the lamina. The yellow ligament is elastic, supports the spine in an upright position, and helps the spine recover after flexion.

Interspinous ligaments (intervertebral ligaments) are thin, membranous ligaments. This set of ligaments connects the spinous processes of nearby vertebrae in the spine and extends from the root to the tip of each spinous process. The function of the interspinous ligaments is to limit the curvature of the spine. (Vital & Cawley, 2020). This set of ligaments connected the yellow ligament in front and met with the supraspinous ligament behind.

The intertransverse ligaments lie behind the previous ligament and join two adjacent transverse processes after a vertical path (Vital & Cawley, 2020). The function of the intertransverse ligaments is to avoid an overbend of the spine in the coronal plane.

The posterior longitudinal ligaments (PLL) develop vertically along the spine's length and are the primary structure supporting the intervertebral joints. The PLL firmly connects the posterior surfaces of each vertebral body. Its function is to limit extreme positions of spinal movement. It relaxes when bending backward and is tensioned when bending over. It also protects the intervertebral disc from being moved from its original location (Vital & Cawley, 2020).

The facet capsular ligament wraps around the facet joint pairs at the posterior of the spine. It provides mechanical support for the facet joints and coupling and resisting the motion to help guide relative movement between the articular surfaces (Ban et al., 2017). Capsular ligament instability is thought to be one of the causes of neck pain (Steilen et al., 2014).

2.1.1.5 Muscles

Hundreds of muscles are connected between the spine and various body parts to realize the function of biomechanical support and movement of the human body. Different muscles connect complex physiological structures, including the head, upper limbs, lower limbs, abdomen, and pelvis. The deep plane muscle group consists of the interspinous and intertransverse muscles. The segmental muscles are located between the spinous and transverse processes, respectively. The midplane muscle group consists of the serratus posterior—upper and lower. The serratus posterior superior is located between the spinous processes of the posterior two cervical vertebrae and the spinous processes of the anterior two thoracic vertebrae and the first rib. The superficial muscle groups consist of the trapezius, rhomboids, and latissimus dorsi, which are the mobilizers of the spine and shoulder girdle (Vital & Cawley, 2020).

Major spinal muscles include:

Back muscles: The back muscles are anatomically divided into two layers (Figure 2.8). The back muscles close to the body surface are the superficial muscles, including the suboccipital muscle, latissimus dorsi, trapezius muscle, levator cap muscle, rhomboid muscle, and serratus. These muscles are located in the superficial back layer; their primary function is to exercise the shoulders and assist breathing. The role of deep muscles is to control and maintain the spine's shape.

Suboccipital muscles: They are four pairs of muscles located in the area below the triangle occiput. These muscles connect the jawline and provide the function of head extension and rotation.

Trapezius: The trapezius muscle is attached between the occiput, shoulder bone, vertebrae, and clavicle. This muscle group moves the shoulder bones and causes the head and neck to stretch, bend and rotate laterally.

Latissimus dorsi: The function of the latissimus dorsi is the internal rotation, adduction, and extension of the arm, and it also helps to breathe.

Scapularis muscle: The shoulder bone is lifted to rotate the shoulder joint and bend the neck on the same side.

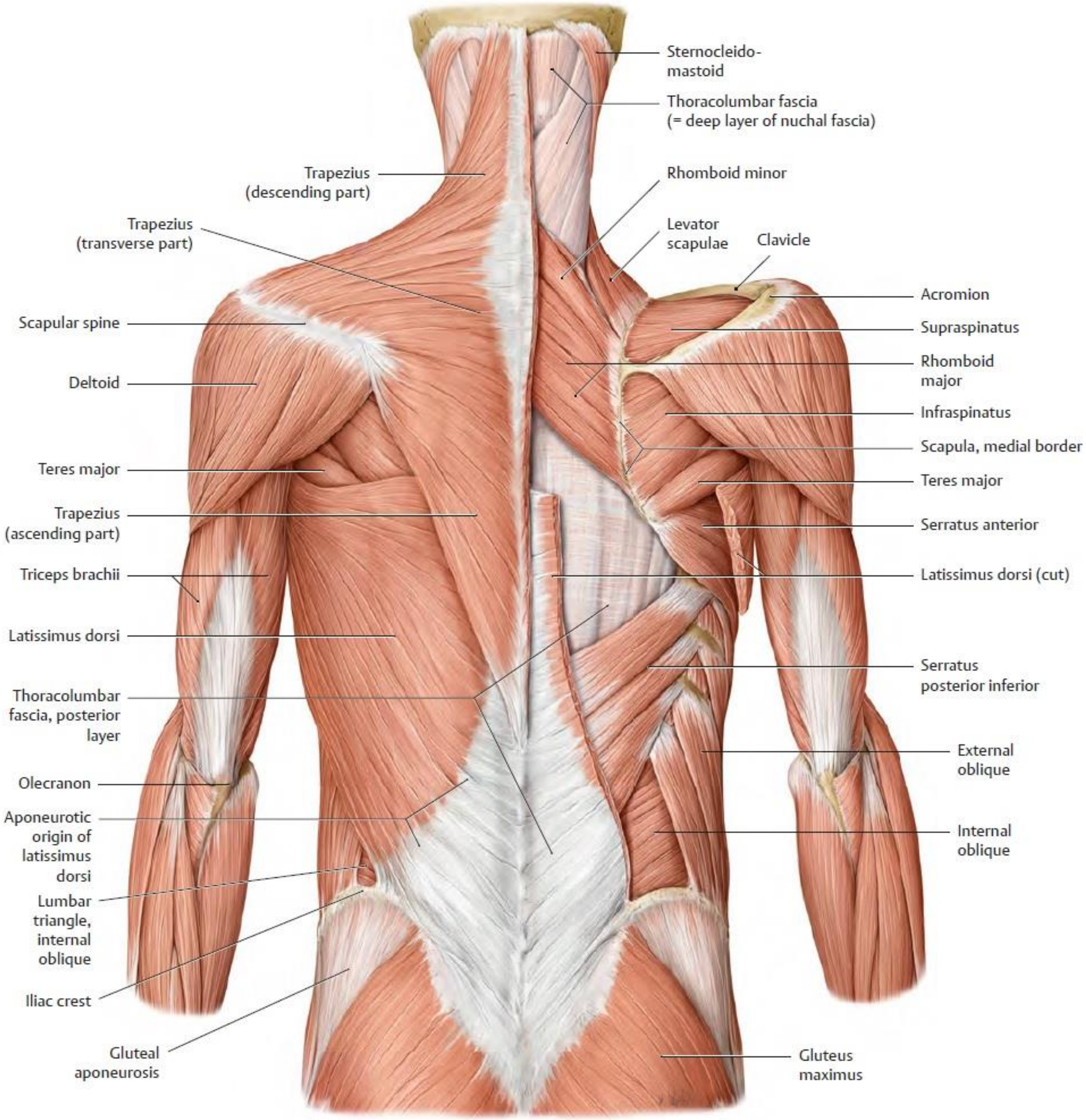

Figure 2.8. Back muscles anatomy (Gilroy et al., 2020).

2.1.2 Range of motion

Due to the deformability of the intervertebral disc, the spine can change shape in multiple axes and directions (Figure 2.9). Spinal movements include flexion, extension, lateral flexion, and rotation. Spinal motion can be measured in range or degree of motion. All movements begin in a neutral position as up straight standing with arms by the sides and eyes looking straight ahead.

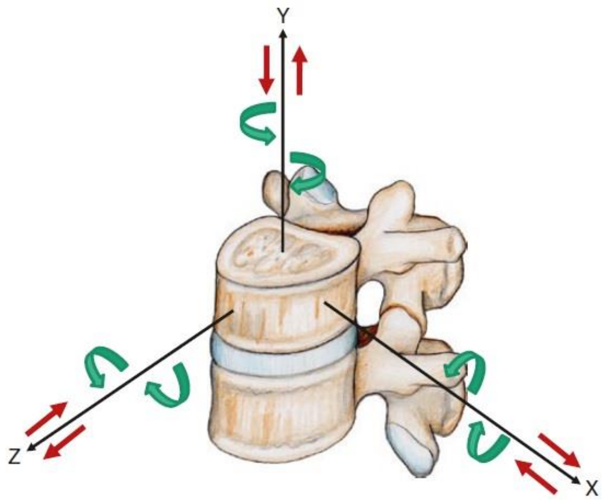

Figure 2.9. The three axes of vertebral movements (Vital & Cawley, 2020).

As structural differences, spinal motion is expressed in segmental magnitudes. Sometimes it is divided into several segments, including the upper cervical spine (Skull-C2), lower cervical, thoracic, and lumbar. Results vary from study to study. Figure 2.10 shows an example of spinal motion in the sagittal plane (Vital & Cawley, 2020). Overall, the cervical spine has the largest range of motion, followed by the lumbar spine, and the thoracic spine has the smallest range of motion since it is connected to the ribcage.

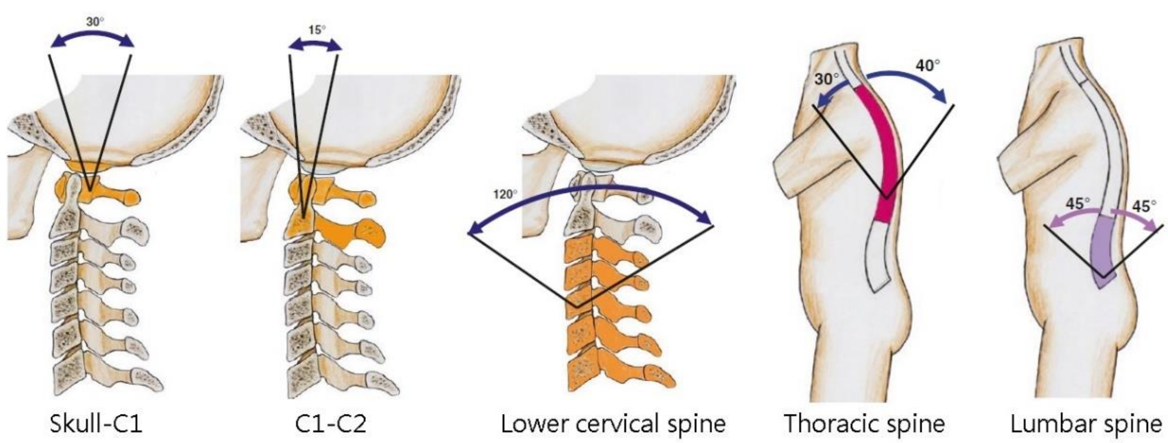

Figure 2.10. Range of motion in the sagittal plane (Vital & Cawley, 2020).

2.1.3 Spine alignment and measurement

The human spine presents an "S shape" in the sagittal plane (Figure 2.1), a masterpiece of biomechanics. The unique bone structure allows humans to stand and move on two feet. The function of waist bending enables a person to maintain the gravity center in the narrow area between the feet, enhance energy efficiency and reduce gravity's effect on ligaments, muscles, and joints (Diebo et al., 2015). Some parameters have been developed to evaluate and quantitively represent the "S-shaped" spine curvature.

Spinal curvature can be measured by internal measurement or external measurement. For example, internal assessment by medical imaging methods (Figure 2.11(a)), external measurement with flexible curved tape (Figure 2.11(b)), inclinometers (Figure 2.11(b)) & Figure 2.11(c)), or Microsoft Kinetic (Figure 2.11(d)). We consider spine parameters were defined in terms of ease of sampling, reliability, and the purpose of the study. In general, the exposed back is easy to observe and measure. Barrett et al. (Barrett et al., 2014; Yanagisawa et al., 2015) conducted a systematic review of fifteen measurements of thoracic kyphosis. There are several methods measurement methods developed for external measurement of spinal curvature, which include: spinal mouse, manual inclinometer (Barrett et al., 2018), digital inclinometer (Bucke et al., 2017), 3D ultrasound (Lee et al., 2019), photogrammetry (D'Amico et al., 2017; Furlanetto et al., 2016), and spinal wheel (Sheeran et al., 2010).

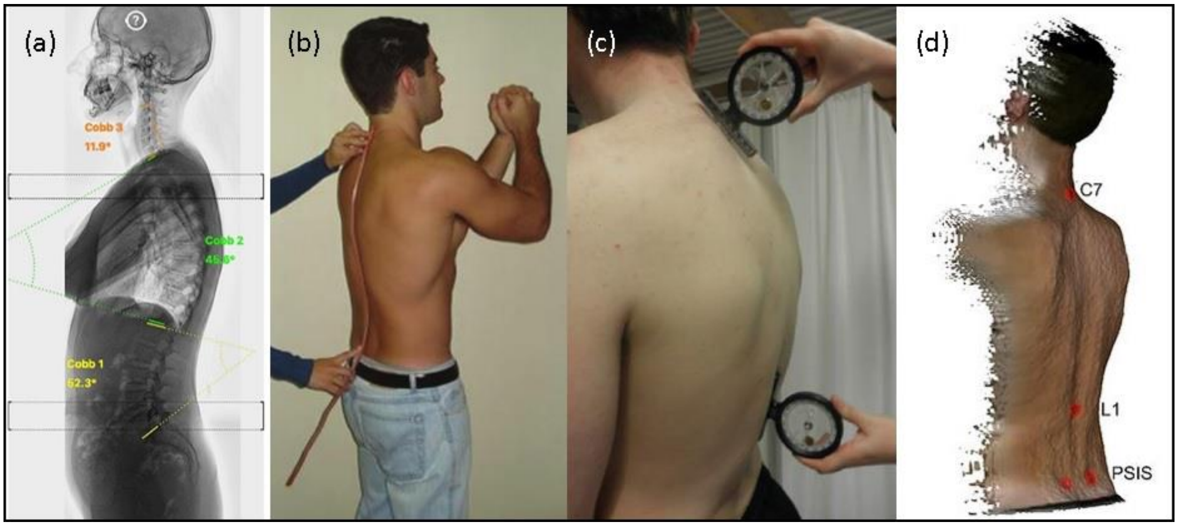

Figure 2.11. Measurement of spine curvature in the sagittal plane. (a) Internal measurement by X-ray (Totera et al., 2021); (b) External measurement by flexicurve tape (Hannink et al., 2020); (c) External measurement by inclinometer (Barrett et al., 2013); (d) External measurement by Microsoft Kinect V2 (Hannink et al., 2020).

There are three natural curvatures from cranial to caudal in the sagittal plane: cervical lordosis, thoracic kyphosis, and lumbar lordosis (Le Huec et al., 2019). In some cases, an angle value is being used to express the corresponding curvature (Yanagisawa et al., 2015); they are cervical lordosis angle (CLA), thoracic kyphosis angle (TKA), and lumbar lordosis angle (LLA). An example of spinal angles is shown in Figure 2.12(a). In addition to the measurement of angles, the curvature of the spine can be recorded and expressed in terms of the distance and depth of the curvature. Different studies defined spine parameters on their own. For example, Figure 2.12(b) shows the thoracic kyphosis height based on the vertebrae from C7 to L1, and the lumbar lordosis height based on the vertebrae from L1 to the posterior superior iliac spine; Figure 2.12(c) shows the thoracic kyphosis height based on the vertebrae from T2 to T12; Figure 2.12(d) shows the thoracic kyphosis width based on the vertebrae from C7 to an undefined endpoint, and the lumbar lordosis width based on the vertebrae from an undefined origin to S1 width; Figure 2.12(e) shows the thoracic kyphosis height based on vertebrae C7 to T12.

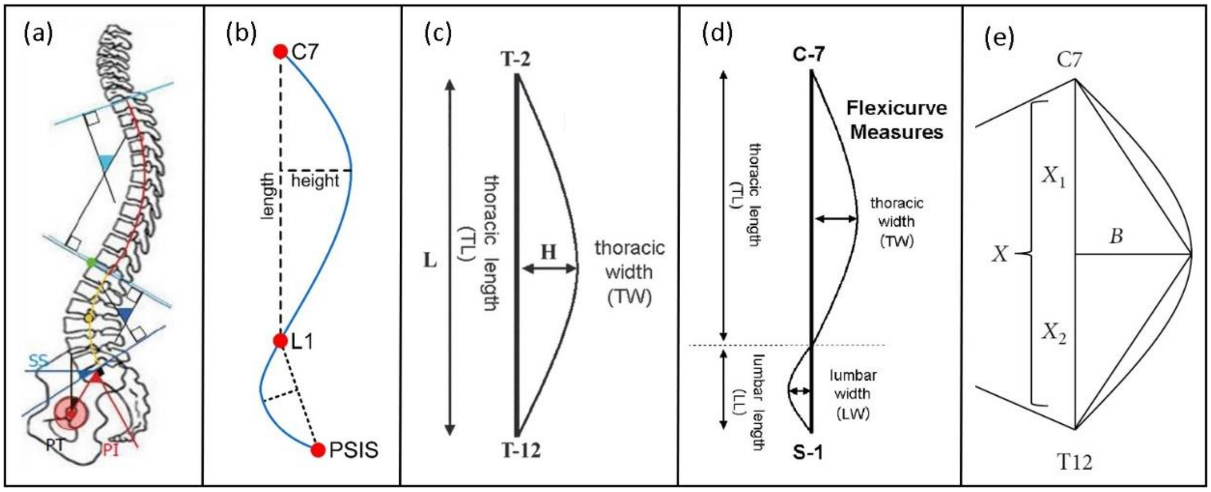

Figure 2.12. Spine parameters (a) Measurement of the thoracic kyphosis angle (TKA) from T1 to T11 and Measurement of the lumbar lordosis angle (LLA) from T12 to L5 (Barrey & Darnis, 2015); (b) Measurement of thoracic kyphosis height from C7 to L1 and measurement of lumbar height from L1 to PSIS (Hannink et al., 2020); (c) Measurement of thoracic width from T2 to T12 (Seidi et al., 2014); (d) Measurement of thoracic width from C7 to an unspecified ending point and measurement of lumbar width from an unspecified starting point to S1 (Hinman, 2004); (e) Measurement of thoracic width from C7 to T12 (Barrett et al., 2013).

2.1.3.2 Measurement of spine alignment by inertial units

In recent years, inertial measurement units have been used to measure the human body. With the back in an unexposed state, the inertial measurement unit can measure the curvature of the spine non-invasively and without radiation. A previous study (Wong & Wong, 2008) developed a method for monitoring changes in sitting posture with accelerometers. A three-axis accelerometer can be used to measure inclination, and multiple measurement units can be integrated to obtain a rough spine curve. Voinea et al. (Voinea et al., 2017) created the pose of the human spine with the tilt angles of five inertial sensors and a mathematical model, which can estimate and depict the spine's curve. Stollenwerk et al. proposed a system containing five inertia units to capture the spinal curvature. The dimensions of a single sensor are 3.3 cm × 1.6 cm × 1.0 cm. Five sensors were attached to the person's back and used to measure the curvature of the lumbar spine (Figure 2.13) (Stollenwerk et al., 2018).

Figure 2.13. Back view of sensors placement (Stollenwerk et al., 2018).

These studies demonstrate that inertial sensors are suitable for measuring human curves; however, these methods used a few sensor units and required complex algorithms or software (such as AutoCAD) to obtain the spinal curvature. These designs did not propose the ability to display curvature in real-time, and the algorithm could significantly affect the accuracy. The sensor units they used were relatively large and thick, which influenced the accuracy of the spine alignment curvature when the sensors were stuck to the human back for measurement in the supine position.

2.2 Sleep

Sleeping is a vital way for people to maintain health. People slept 7 to 9 hours daily (Chaudhry et al., 2020; Walsh et al., 2020). A proper body support system for sleeping is necessary for a night of high-quality sleep. Unreasonable body support will possibly decrease the quality of sleeping, potentially resulting in a high risk of diabetes, high blood pressure, memory cognition, and the immune system. The design and evaluation of the body support system, including the mattress and pillow, are highly related to the biomechanics of the musculoskeletal system.

2.2.1 Sleeping environment and support

The indoor environment, bed, bedding, lighting, temperature, humidity, sound, etc., will affect daily sleep (Lan et al., 2017; Zhang et al., 2018). The sleep support system undoubtedly plays a significant role in sleep quality.

The sleeping support system is considered the most crucial factor affecting the physical and mental quality of sleep (Haex, 2004). A typical sleeping support system is generally constructed of a mattress and one or several pillows for head support. The body and the sleep support system may be deformed when lying on the sleeping support system. A proper sleeping support system should distribute the body weight to avoid local high pressure, and the spine should be able to maintain a neutral shape to reduce musculoskeletal problems.

2.2.2 Mattress

The mattress is usually a rectangular pad to support the lying human body. It is used as a bed or placed on a bed frame as a part of the bed. The mattress may be used on the bed frame as part of the bed, or it may be designed to be used directly as a bed. Mattresses have a certain degree of elasticity. When a person lies on the mattress, both the human body and the mattress will deform to a certain extent, thereby supporting the body's weight. The often-used elastic materials for mattresses are foam materials, springs, or a combination of the two. The material properties can vary considerably; it can be a personal preference, whether in a uniform stiffness or uneven zonal support. Common mattress types identified by Sironi et al. are spring, gel, memory foam, latex, and hybrid (Sironi et al., 2019).

Foam materials commonly used in the production of mattresses include polyurethane, latex, memory foam, and gel foam. Materials vary in their bounce properties, heat dissipation capabilities, and breathability. When subjected to compression, the foam material exhibits a stress-strain curve with three regions; This is related to the resistance shown by the foam when a load or force is applied to it. The shape of the different curve areas will reflect some essential qualities of the foam related to the material's compressive or relaxation stress and strain behavior (Blackley, 2012).

Spring mattresses can also be built with different mechanical support properties in various regions, such as softer shoulder areas or harder pelvic areas. The spring array inside the mattress can be interconnected or individually bagged to allow independent deformation. The compressive stress-strain curve generally appears as a straight line of a metal spring compressed in the elastic region.

2.2.3 Pillow

Pillows are placed on the mattress for the head and neck biomechanical support to promote sleeping comfort. The primary function of a sleeping pillow is to support the cervical spine, and the ideal situation is to maintain the cervical spine in a neutral position (Frange & Coelho, 2022).

A proper sleeping pillow can promote the preferred spine alignment, improving sleep quality and duration. The position of the head and neck significantly impacts the overall quality of sleep. Past research has shown that poor sleeping posture can stress the structures of the cervical spine. Furthermore, in addition to disrupting sleep quality, poor cervical support may also be the source of pain symptoms, including tension headaches, neck pain, shoulder pain, muscle stiffness, etc. (Jeon et al., 2014; Radwan et al., 2015). Many studies have shown that promoting cervical lordosis in its neutral curvature is essential for maintaining healthy sleep (Fess et al., 2015; Persson, 2009; Ren et al., 2016).

Cotton, feather, polyurethane foam, and latex are commonly pillow-core materials. Various materials provide different levels of support and permeability. For example, pillows filled with down and feathers are looser and generally conform better to the head and neck contours; they are also more breathable than polyurethane pillows (Haex, 2004).

The shape of the pillow is a critical element in pillow design as it contributes to the amount of cervical support and the overall comfort of the user. Each user's most suitable pillow shape may depend on the sleeping position (Radwan et al., 2020). Bread-shaped pillows are the most common. The pillow core can be cotton, feather, foam, or a mix-up of materials. As technology advances, profiled pillows that claim enhanced performance are becoming more and more popular. The B-shaped cervical pillow is one of the representatives. This design supports the cervical lordosis with the thick edge and evenly distributes the contact pressure. Some contour pillows were designed with more complex three-dimensional shapes to achieve better cervical support; for example, the one in Kim et al.'s research (Kim et al., 2016).

The height of the pillow directly impacts the alignment of the spine. Many kinds of research on pillows have involved pillow height (Liu et al., 2011; Radwan et al., 2020; Ren et al., 2016).

Kim et al. (2015) used photography to measure the cervical spine alignment of 16 subjects when lying on their back. Comparing pillows with heights of 0, 10, and 20 cm showed that a pillow height of 10 cm is the most suitable for maintaining the best cervical spine alignment (Kim et al., 2015). However, the participant was lying on a rigid platform; the pillows with heights of 10 and 20 cm seemed stiff and could not be deformed during the skull weight (Figure 2.14). It likely significantly increased the body's contact pressure, which may not be suitable for use in real life. Similar results were presented by Sacco et al. (2015). They used three rectangular foam pillows that could not be deformed, with heights of 5 cm, 10 cm, and 14 cm. The experiment results were that 10 cm height was the most suitable. Ren et al. (2016) compared pillows with heights of 11, 13, 15, and 17 cm and tested the pressure distribution. The result was that a pillow height of 11 cm resulted in the lowest cervical and skull pressure. They also used the finite element modeling method to predict spine alignment. They found that as the height of the pillow increases, the spine results in an anterior shift (upshift) (Ren et al., 2016). However, from their experimental photos, it can be found that the pillow's height refers to the uncompressed elastic material (Figure 2.15). The compressed pillow height that actually supports the head was never described.

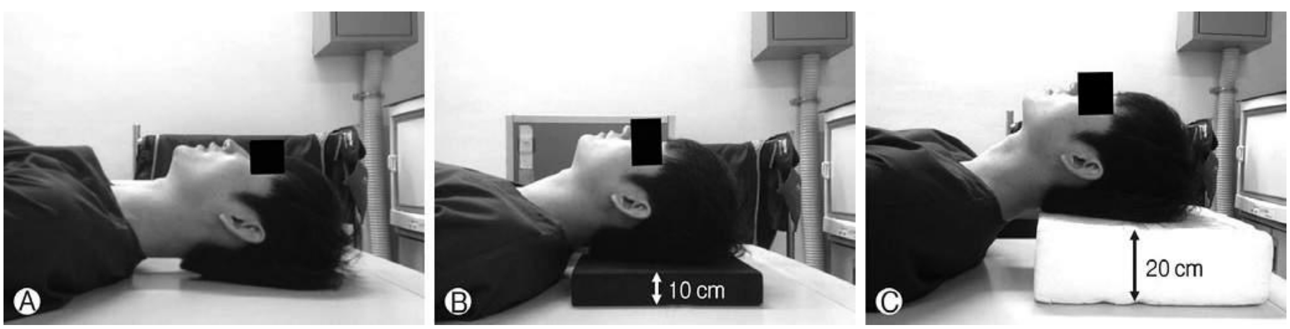

Figure 2.14. Photographs of Kim's experiment using pillows of various heights in a supine position (Kim et al., 2015).

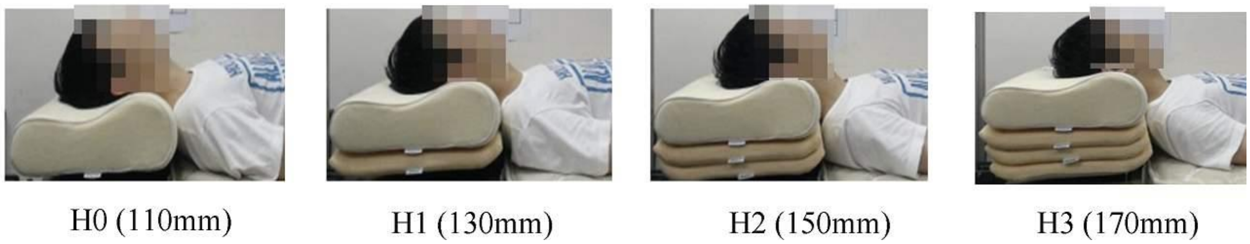

Figure 2.15. Craniocervical supports used in Ren's experiment (Ren et al., 2016).

Most existing research on pillow height did not consider the height change of the pillow after bearing the weight of the human body. The pillow and the mattress were deformed by the human body's weight (Figure 2.16). The compressed pillow height and mattress thickness are the height that exactly supports the body. Pillow height before and after compression and related effects are considered worthy of study (Radwan et al., 2020).

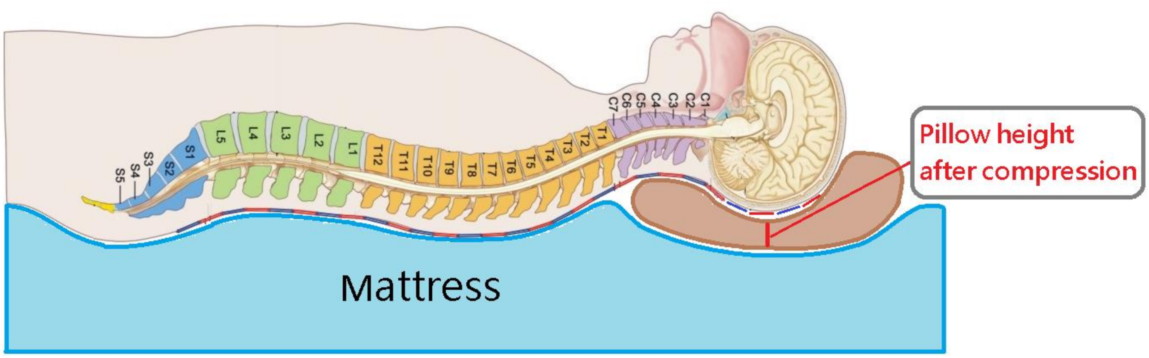

Figure 2.16. Illustration of a compressed pillow.

2.2.4 Spinal deformation in sleep

The spine shape may change from its original alignment in lying positions. In a supine or prone position, the spine is deformed in the sagittal plane, which appears in spinal extension and flexion (Figure 2.17). When lying on the side, the spine is bent in the coronal plane, which causes lateral inclinations. In some postures, disc rotation may occur. For example, a prone posture usually turns the head sideward to improve breathing and increase neck rotation (Haex, 2004). Due to the complex structure of intervertebral discs, the axial twist of discs is limited to about six degrees; the increase in twist raises the nucleus pressure (Adams & Dolan, 2005).

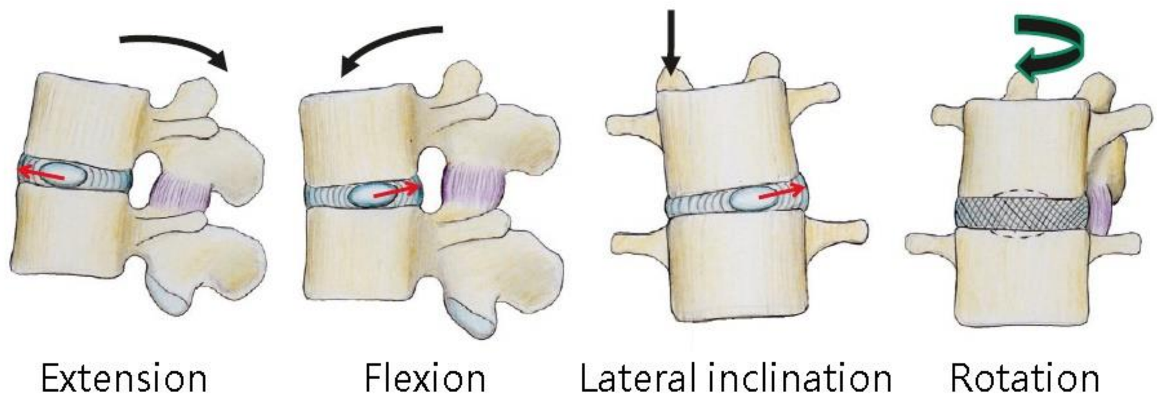

Figure 2.17. The motion of the nucleus and annulus in spine deformation (Vital & Cawley, 2020).

2.2.5 Sleep postures

Humans change their sleeping posture in both conscious and unconscious ways. People likely to change their sleeping posture about 25 times a night (Koninck et al., 1992). Changing the posture can prevent soft tissues under overloaded pressure and avoid muscle stiffness. The commonly adopted sleeping postures are supine, left lateral, and right lateral. Sometimes prone is also adopted.

2.2.5.1 Supine position

The supine position is the most common and comfortable sleeping position (Lee et al., 2020; Su & Xu, 2017). In a supine position, the body lies on its back and the face upward; A large surface distributes the body loading, and the contact pressure can be low. The sleeping support system is interactive with the body; In an ideal status, the lumbar spine should maintain a position between a smoothed lordosis and slightly flattered. However, while lying in too-hard support, the lumbar spine can't keep smoothening and has no contact between the lower back and the mattress (Haex, 2004). In contrast, when lying on a too-soft sleeping support system, the weight-concentrated region sinks deeply into the mattress, resulting in unnatural lumbar kyphosis (Haex, 2004). In the supine position, the back is contacted with the sleeping support system, that the covered back is challenging to observe.

2.2.5.2 Lateral position

Lateral position is another sleep posture humans usually adopt. This position can support the human spine in a proper way when the sleeping system and pillow are well-conceived (Haex, 2004). The human body may be deformed in the coronal plane. In contrast, the spinal curvatures in the sagittal plane, including cervical lordosis, thoracic kyphosis, and lumbar lordosis, can be maintained in their neutral shape. However, the spine faces lateral deformation under incorrect supports. When people lie on a hard mattress, only the vast areas of the body can be supported, such as the shoulder and pelvis. Suppose the shoulders and pelvis cannot sink into the mattress. In that case, the support of the cervical spine and back will be poor, and the shoulder joints and hips will undergo high pressure on the contact surface, resulting in pain and joint stiffness (Figure 2.18(a)) (Leilnahari et al., 2011).

In contrast, a mattress which too soft can lead to the pelvis area sinking deeper into the mattress and result in the cervical vertebrate C7 being higher than that of the pelvis (Figure 2.18(b)) (Leilnahari et al., 2011).

Comparing the soft and hard mattresses, the custom-made mattress with different stiffness elements trends supports the body better. It can maintain the spine in the neutral alignment (Figure 2.18(c)) (Leilnahari et al., 2011).

Figure 2.18. Images of a participant lateral lying on different mattresses mattress (Leilnahari et al., 2011). (a) Lateral lying on a firm mattress; (b) Lateral lying on a soft mattress; (c) Lateral lying on a custom-made.

2.2.5.3 Prone position

Prone sleep position has been defined as the most unfavorable posture concerning the back support (Haex, 2004). Gravity sinks the heaviest middle part of the body deep into the mattress. Still, the legs remain stretched, which causes a significant increase in lumbar lordosis significantly and leads to the rise of the facet joint pressure at the posterior side (Twomey & Taylor, 1983).

2.2.5.4 Detection of sleep positions

A night of healthy sleep requires several major posture changes throughout the night (Koninck et al., 1992; Verhaert et al., 2011). The literature on sleep posture, especially in the first half of this century, is mostly anecdotal or based on clinical speculation (Koninck et al., 1992). A camera was used to take a frame every 8 seconds, record the sleeping position, and score the four parts (head, torso, legs, and arms) to observe the development of human sleep posture and posture changes. Frequent sleeping position changes indicate poor sleep quality, such as keeping a sleep posture for less than 15 minutes (Koninck et al., 1992).

Liu et al. (2014) propose a design that uses bed sheets with pressure sensors and an algorithm framework for recognizing and monitoring sleep posture. The bed sheet system adopted textile sensors to generate high-resolution pressure distributions. This study proposes a framework for pressure graph analysis for monitoring sleep posture, including a set of geometric features for sleep position recognization and 3-sparse classifiers for posture characterization. Their method achieved an accuracy of 83.0% on average (Liu et al., 2014).

In recent years, some studies have mentioned the use of acceleration sensors for sleep posture measurement, which has high detection accuracy (Jeng & Wang, 2017; Jeng et al., 2021; Yoon et al., 2015). For example, Yoon et al. used an acceleration sensor attached to the chest (Figure 2.19) to achieve a detection accuracy of 99.16% (Yoon et al., 2015).

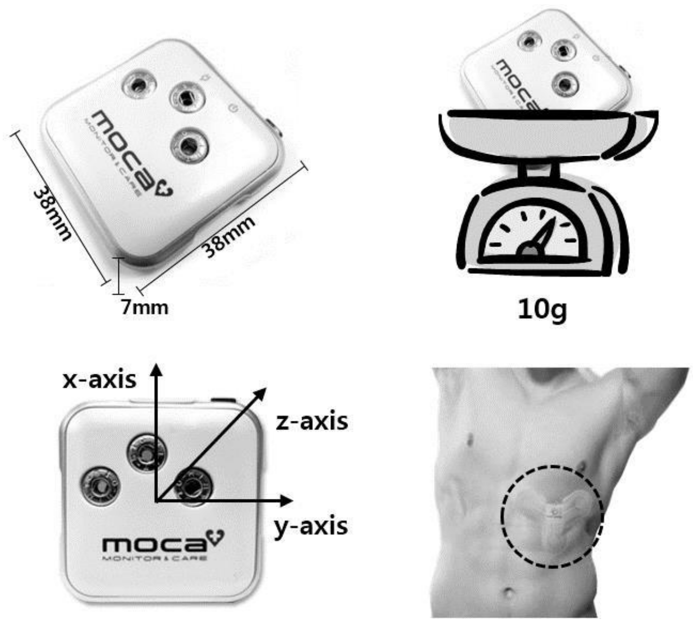

Figure 2.19. The device used and attached position of Yoon's research (Yoon et al., 2015).

2.2.6 Spine alignment in sleep

Keeping the spine in its neutral shape is considered the optimal spinal alignment during sleep (Radwan et al., 2015; Verhaert et al., 2011; Wong et al., 2019). The muscles can be relaxed, and intervertebral discs can be restored from daytime pressure. If the spine is unloaded at night and supported by its natural physiological shape, it should be able to recover from daily activities (Haex, 2004; Verhaert et al., 2011). For a side-sleep posture, when projected into the frontal plane, the optimal support makes the spine a straight line to achieve symmetrical spine loading (Gracovetsky & Farfan, 1986). Figure 2.20(a) shows an ideal spine alignment for lateral lying (up), possible malaligned spine while lateral lying on too-soft sleeping support (middle), and possible spine alignment while lateral lying on a firm sleeping support system (low).

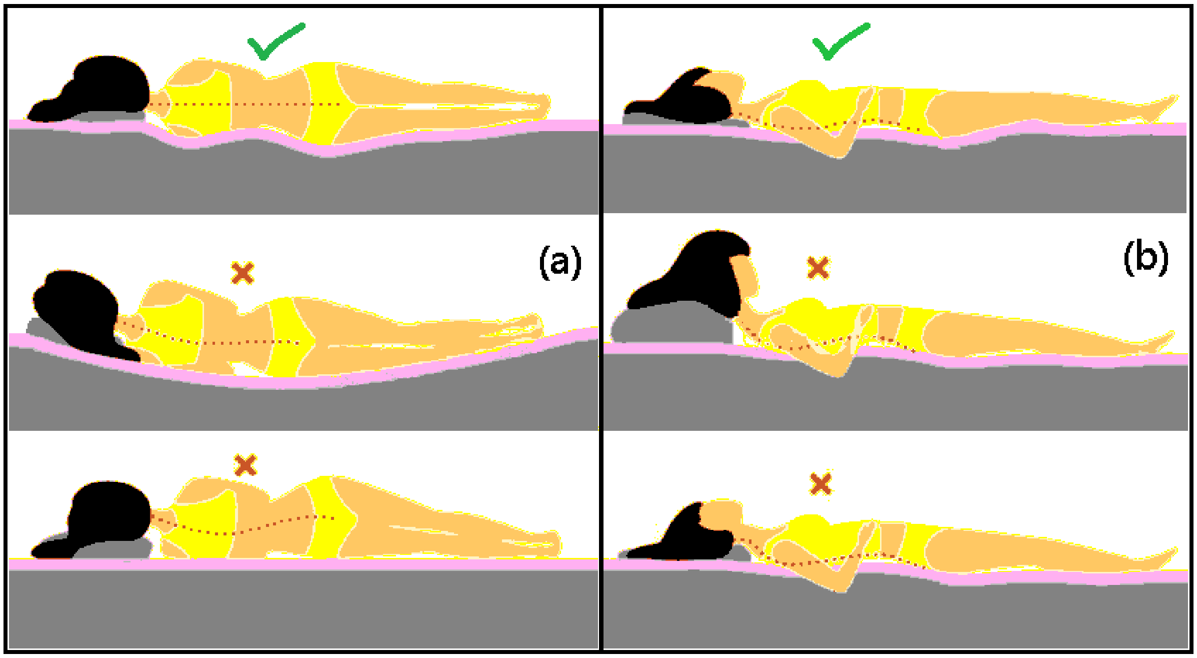

Figure 2.20. Preferred spine alignment in the lateral and supine positions (Theirl & Collentro, 2020). (a) Preferred spine alignment in lateral position (up), incorrect sleeping support (middle and low); (b) Preferred spine alignment in a supine position (up), incorrect sleeping support (middle and low).

The definition of the neutral spine alignment in the supine position is challenging. Some studies suggest the spine is slightly straighter than standing (Verhaert et al., 2011). Assuming that the gravity-induced compression in vertical standing is counteracted, the spine in the supine position is slightly flatter than in the standing position, which is considered ideal spine alignment. However, some studies consider the different forces on the spine when standing and lying (Wong et al., 2019). The author believes that the ideal spinal alignment for supine sleep can be referred to in free-floating conditions. Flotation therapy has also been shown to bring responses of relaxation, such as zero-gravity and reduced muscle tension (Dierendonck & Nijenhuis, 2007). However, based on the perspective of biomechanics, it can be considered that the neutral curvature of the spine (CLA, TKA, & LLA) in the lying posture should not be greater than in a standing position because it is considered to relieve the compression loading caused by gravity. Figure 2.20(b) illustrates the preferred spine alignment for the supine position (up), possible malaligned spine while lying on too soft sleeping support (middle), and possible spine alignment while supine lying on a firm sleeping support system (low).

2.2.6.1 Measurement of spine alignment in the supine position

Since the back is contacted with the sleeping support in the supine position, there are limited tools for measuring spine alignment in the supine position. MRI, CT, and X-ray could capture spine curvature in back-unexposed conditions and are commonly adopted in the medical treatment courses of spine disorders (Brink et al., 2017; Voinea et al., 2017), but with the shortcomings of patient radiation exposure. Optoelectronic, ultrasonic detectors, and optical measurement systems could accurately measure spine curvature, but they are commonly constrained to bulky devices and require total back exposure (Pivotto et al., 2021; Ran et al., 2020; Remondino, 2004).

The gold standard for quantifying the spine parameters is the use of lateral radiography(Fortin et al., 2011; Hasegawa et al., 2018). Medical imaging such as CT and MRI can clearly understand the spine in any lying position. However, the participants must be exposed to potentially harmful radiation environments, which involves high costs. Medical imaging methods are not convenient for clinical applications of spine assessment in sleeping due to the radiation damage, price, and size of the sleeping support system. Therefore, researchers have developed various non-radioactive methods to measure the angle of the spine in sleep positions (Barrett et al., 2014).

For spine curvature measurement in the supine position, a set of custom-made indentation bars was assembled into the mattress (Figure 2.21) (Zhong et al., 2014). However, this method increased the cost and difficulty of the experiment. The measurement resolution is low, and the experimental results can be biased due to the thickness and rigidity of the custom-made indentation bar.

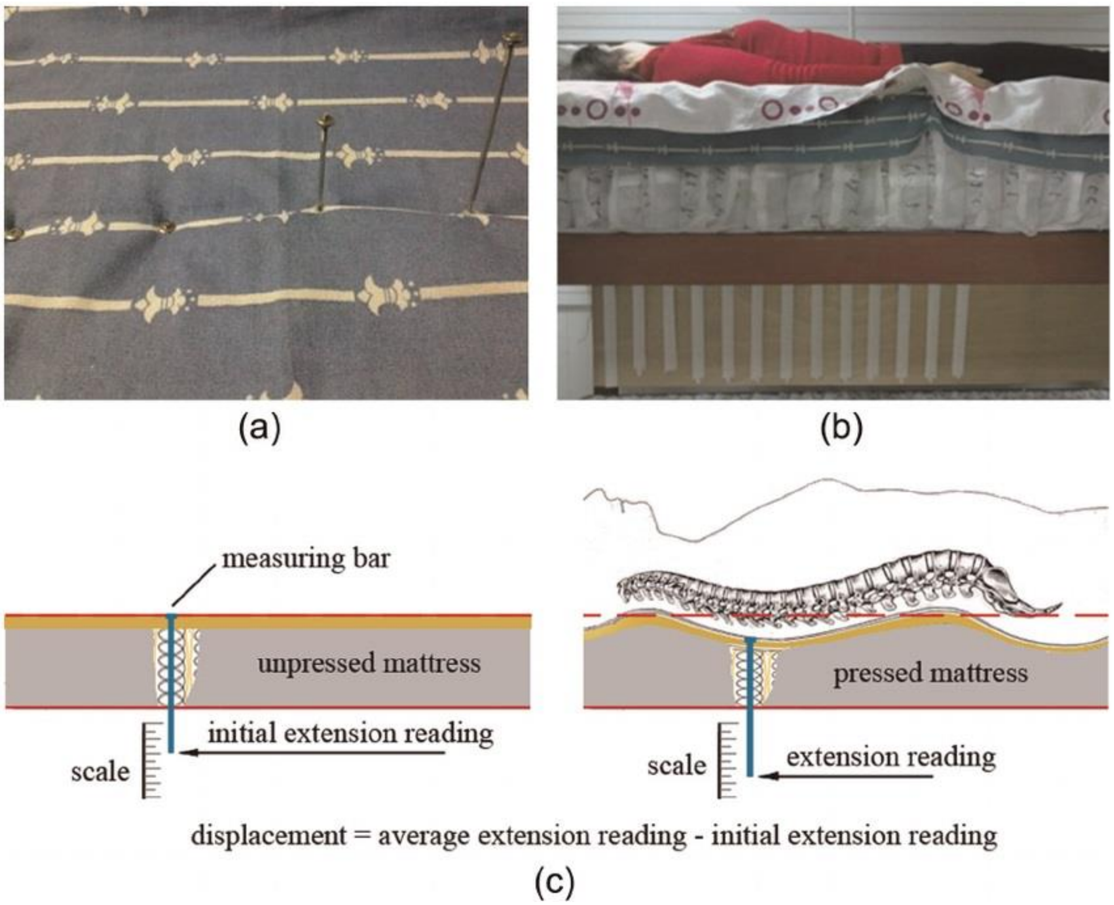

Figure 2.21. Indentation bar system for spinal curvature measurement (Zhong et al., 2014).

2.2.6.2 Measurement of spine alignment in the lateral position

Since the back is exposed while lying on the side, it greatly facilitates the measurement of morphology. Various optical tools can obtain spinal alignments, such as optical cameras (Figure 2.18), 3D scanners (Figure 2.22), or motion capture systems. Therefore, the spine alignment in the side sleeping position is widely observed and used to optimize the sleep support system (Leilnahari et al., 2011; Verhaert et al., 2012).

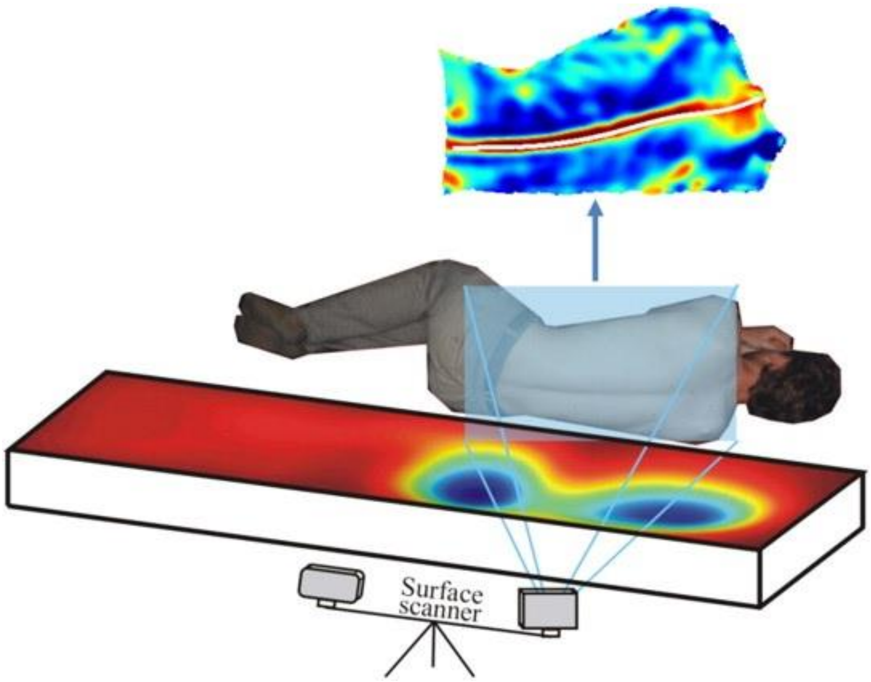

Figure 2.22. Illustration of back surface scanning (Verhaert et al., 2012).

2.2.7 Body pressure distribution

Contact pressure is a significant factor in evaluating sleep comfort. The pressure level can be translated into (dis)comfort and pain. Surface force or pressure causes skin deformation and triggers touch through mechanoreceptors. Excessive force triggers pain through nociceptive mechanisms (Buckle & Fernandes, 1998). Pressure-sensitive mats are commonly adopted to measure contact pressure between the sleeping support and the human body (Lee et al., 2015; Ren et al., 2016). The measurement system aims to be highly flexible, thin, and have high resolution. However, the sensor mat can spread the concentrated contact pressure and then underestimate the peak pressure (Wong et al., 2019). Figure 2.23 demonstrated a pressure distribution graph in a supine position measured by a pressure-sensitive mat (Bodi Trak-1526, Vista Medical Limited, Winnipeg, MB, Canada). The pressure-sensing mat consists of 1024 sensors (32 × 32 points)

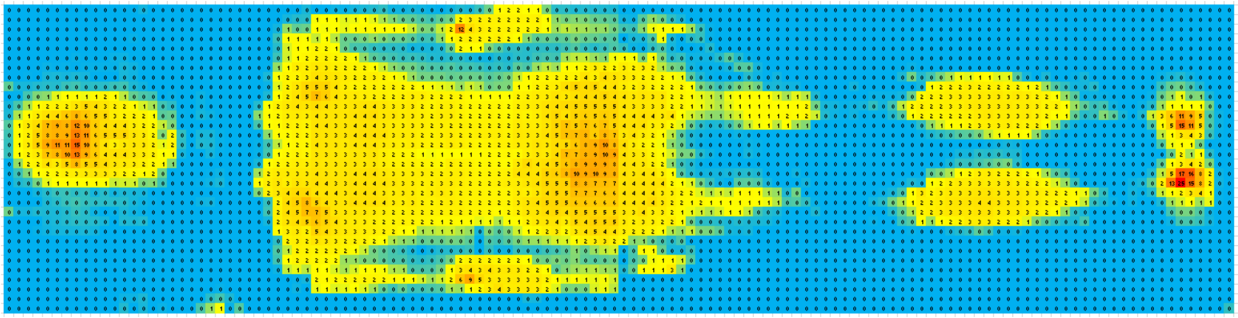

Figure 2.23. A graph of pressure distribution in a supine position.

2.3 Spinal musculoskeletal disorder

Spinal musculoskeletal disorders are more common in the neck and lumbar regions because these two parts are more involved in the spinal movement than the thoracic region.

2.3.1 Neck pain

Spinal musculoskeletal disorders are common health problems affecting many people around the world. The main syndromes of spinal musculoskeletal disorders include tissue stiffness, muscle weakness, pain, and limited range of motion. The most common problems are neck pain and lower back pain. It affects the spinal musculoskeletal system's health and causes dysfunction of the spine's muscles, ligaments, tendons, joints, and nerves. Often, these diseases bring different types of pain syndromes, limit the spine's range of motion, and even affect the function of the head and extremities.

Biomechanical "wear and tear" has long been considered the leading cause of intervertebral disc degeneration (Bakker et al., 2009; Battié et al., 2009; Vergroesen et al., 2015). High loading is linked to disc degeneration and low back pain (Coenen et al., 2014; Kingma et al., 2014; Seidler et al., 2009).

2.3.1.1 Prevalence of neck pain

Neck pain is a major health problem today. The annual prevalence rate exceeds 30% (Hurwitz et al., 2018; James et al., 2018). Regardless of treatment, most acute neck pain episodes can be relieved. Still, nearly half of individuals will continue to undergo some degree of pain or frequent episodes, leading to disability. Diseases also harm human health and quality of life and significantly impact individuals, families, health systems, and the social economy.

Neck pain is episodic pain, with varying degrees of recovery between attacks (Guzman et al., 2009), and is considered one of the most durable musculoskeletal pain syndromes. Neck pain may be related to serious conditions, such as neurological diseases, infections, obesity, tumors, cervical spine fractures, or idiopathic neck pain of unknown cause (Mahmoud et al., 2019).

Previous studies have found that poor craniocervical spine posture during sleep can put excessive loading on the cervical spine structure and affect sleep quality. Direct problems include tension headaches, neck pain, shoulder pain, and muscle stiffness (Jeon et al., 2014).

2.3.1.2 Ligament injury and neck pain

Cervical capsular ligaments (Figure 2.24) are the primary tissue to stabilize the cervical spine. They are located near the center of intervertebral rotation and provide essential stability in the cervical, especially in axial rotation (Rasoulinejad et al., 2012). In dynamic mechanical studies, it is found that the highest average peak force of the capsular ligament is as high as 220N (Ivancic et al., 2007). The cervical spine cannot be appropriately supported when the ligament is injured.

Based on research on human cadavers, it is found that the transaction or injury of the joint capsule ligament can significantly increase the rotation and lateral flexion of the neck (Nadeau et al., 2012). The laxity of the cystic ligament can occur immediately in a single macro trauma or from a microtrauma by repeated for the head’s bent or forward postures. In both cases, the cause of the damage occurs through a similar mechanism, resulting in the laxity of the capsular ligaments and excessive movement of the facet joints, which usually leads to instability of the spine in the cervical region and damage to the intervertebral discs and facet joints. (Steilen et al., 2014).

Most chronic neck pain is believed to be caused by degenerated intervertebral discs and facet joints (Cohen & Hooten, 2017). Therefore, the health of ligaments is associated with a considerable amount of neck pain.

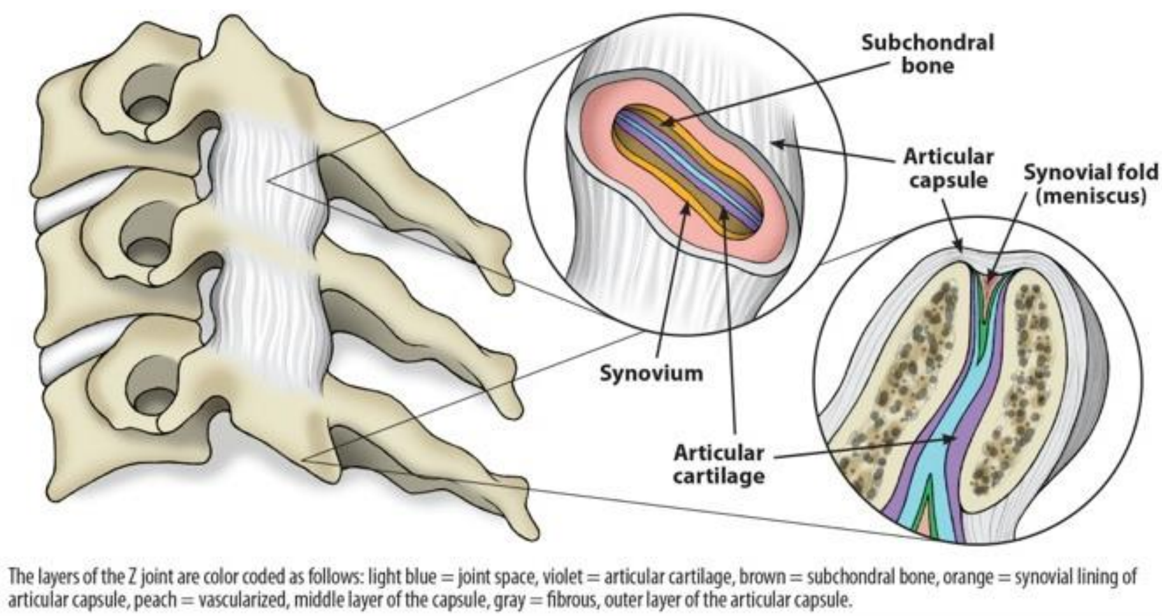

Figure 2.24. Anatomy of facet joints and capsular ligaments (Steilen et al., 2014).

Many works of the literature suggest that neck pain involves the degeneration of intervertebral discs and facet joints (Cohen & Hooten, 2017; Damasceno et al., 2018; Genebra et al., 2017; Kim, 2015; Peng et al., 2021). Some literature points out in-depth that the laxity of the capsular ligament is a major cause of cervical spine instability. The cervical ligament is very strong and is the primary stable tissue of the spine (Quinn et al., 2007). Laxation of the capsular ligament can happen immediately in a single trauma, such as a whiplash injury, or slowly develop in a cumulative microtrauma, such as repeated bent or forward head postures. The cause of the injury happens through a similar mechanism in both cases (Steilen et al., 2014). The injury leads to laxity of the capsular ligament and excessive movement of the facet joints, which often leads to the instability of the cervical spine. The long-term development of ligament laxity is defined as "creep" (Figure 2.25), which represents the elongation of the ligament under repeated or constant stress (Chen et al., 2009).

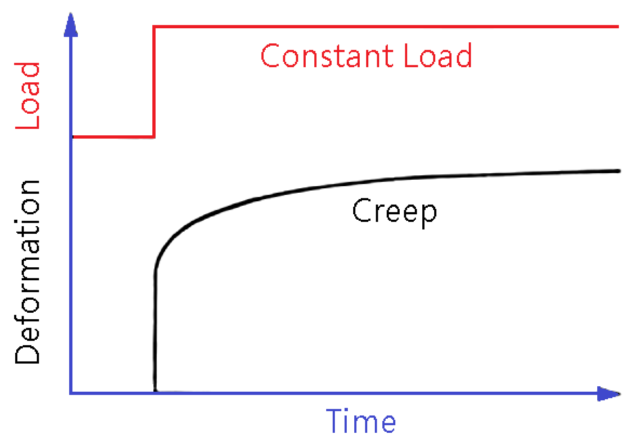

Figure 2.25. Ligament laxity and creep.

2.3.1.3 Treatment for neck pain

The treatment of chronic neck pain in a nonpharmacologic way generally includes exercise, physical therapy, laser therapy, massage, and acupuncture methods (Barreto & Svec, 2019). Physical exercise intervention is considered to have a particular therapeutic effect on non-specific neck pain (Price et al., 2020). However, the specific exercise mode, time, and intensity are inconclusive (De Zoete et al., 2021). Therefore, dealing with neck pain remains challenging.

Some studies suggest that ergonomic pillows can manage neck pain (Radwan et al., 2020). In a single-blind trial with a pre/post-test design, participants in the experimental group used ergonomic latex pillows. In contrast, participants in the control group slept on their commonly used pillows. After four weeks of the test period, participants in the experimental group had lower scores on the Numerical Pain Rating Scale and the Neck Disability Index, suggesting that an ergonomic latex pillow relieved neck pain (Fazli et al., 2018).

As a commercial practice, cervical pillows are advertised as helping to maintain a neutral cervical spine curve while lying on the back, allowing muscles and ligaments to relax and return to regular length. The cervical pillow may relieve neck pain by relieving and supporting tense muscles in the neck and shoulders. However, a survey of 134 participants (Shields et al., 2006) concluded that insufficient evidence could support the efficacy of cervical pillows for chronic neck pain.

2.3.2 Low back pain

Severe back pain is most common in the intervertebral discs, epiphyseal joints (also known as facet joints), and sacroiliac joints (Adams & Dolan, 2005). Physical disruption of these structures is strongly but distinctly linked to pain.

2.3.2.1 Prevalence of low back pain

Low back pain is a common health problem in adults, and its prevalence or incidence increases with age. In some Western countries, the prevalence of low back pain ranges from 1.4% to 20.0%; the incidence ranges from 0.024% to 7.0% (Fatoye et al., 2019). Risk factors include age, gender, high-intensity physical activity, and high loading on the spine.

2.3.2.2 Pathophysiology of low back pain

Low back pain typically comes from different causes. Common causes are myofascial pain, lumbar facet joint degeneration, intervertebral disc problems, neurological symptoms, and spinal stenosis (Urits et al., 2019).

Myofascial pain occurs more often after trauma or repetitive motion injury (Partanen et al., 2010). The pain was characterized by trigger points in the fascia, tendons, or myofascial muscles that, when stimulated, resulted in a pain response (Giamberardino et al., 2011).

Osteoarthritis of the lumbar facet joints or high pressure within the facet capsule may cause facet-mediated pain (Bogduk, 2008). Patients are described as having a unilateral or bilateral distribution of depth and pain.

39% of low back pain causes can be attributed to intervertebral disc-related pain (Comer & Conaghan, 2009). Typically, the pain is generated from the lower back's center and worsens during sitting, driving, lumbar flexion, bending, twisting, and coughing (Bogduk, 2012).

Spinal stenosis is a degenerative change in the lumbar spine. The nerves and blood vessels in the patient's lower back are compressed and cause pain.

2.3.2.3 Treatment for low back pain

Similar to neck pain, the causes of low back pain vary from person to person. Treatments also vary, and no single treatment was effective for all patients (Fatoye et al., 2019). Common treatments include physical therapy, rehabilitation therapy, supplements, medication, and even psychotherapy.

2.4 Computational simulations for biomechanical analysis

In addition to measuring data on the body's surface and the environment, understanding the changes in the internal structure of the human body can provide very valuable biomechanical parameters. However, the inside of the human body is almost impossible to measure directly. Computational methods such as finite element analysis can simulate the internal structure of the human body and are widely adopted. The computational approach can see insight into the human body to observe the contact pressure, internal stress distribution, and deformation of every part under loading. Based on input parameters, such as loading conditions, loading forces, material properties, and geometry, results can be presented in a way that simulates in vivo experiments. Compared with complicated, expensive, and invasive investigations, obtaining the required parameters using computational analysis has excellent advantages. However, model validation usually requires a limited number of measurements.

Furthermore, new concepts of sleeping support systems can be evaluated through the simulation platform without building any prototype, and even human bodies or components with extreme dimensions can be assessed.

Finite element models of the spine for biomechanical analysis have been widely adopted. Some are cervical ligament models (Barker & Cronin, 2020; John et al., 2019; Nikkhoo et al., 2019; Zafarparandeh et al., 2014), and some are lumbar spine models (Bojairami et al., 2020; Zhang et al., 2021). These models are mainly developed for quasi-static loading scenarios to investigate the changes in the internal structures when external loads are applied. Recently, finite element models integrating the sleeping support system and the human model have been developed and used in sleep analysis (Lee et al., 2017; Yoshida et al., 2010, 2012).

2.4.1 Two-dimensional finite element model

Since the human body and sleeping support system are three-dimensional structured, an ideal computational simulation must consider each component's deformation in three-dimensional space to obtain accurate computational results. However, constructing a 3D model is expensive and requires much time for computational simulation. Compared to three-dimensional FE models, a two-dimensional FE model has the advantage of model setup and modifications.

Two-dimensional FE models have been developed to explore sleep comfort. Yoshida et al. investigated the pressure distribution in the human body by two-dimensional finite element models to evaluate the sleeping comfort of mattresses. They constructed a male and a female finite element model using Japanese human body size statistics. The adoption of von Mises stress as an evaluation criterion for sleep comfort and iteratively performed finite element analysis while modifying Young's modulus of the mattress to investigate which mattress firmness creates the slightest pressure on the lumbar area (Yoshida et al., 2010).

This study constructed FE models of an adult Japanese male and an adult Japanese female. The computational simulation was performed in the supine lying position. The FE model was loaded into a FE analysis package (ANSYS Ver.10, CYBERNET SYSTEMS CO., LTD., Tokyo, Japan) for analysis (Figure 2.26). The study found that when lying supine on a mattress with a medium Young's modulus, the stress on the lumbar region was the lowest, and sleep comfort was considered the highest.

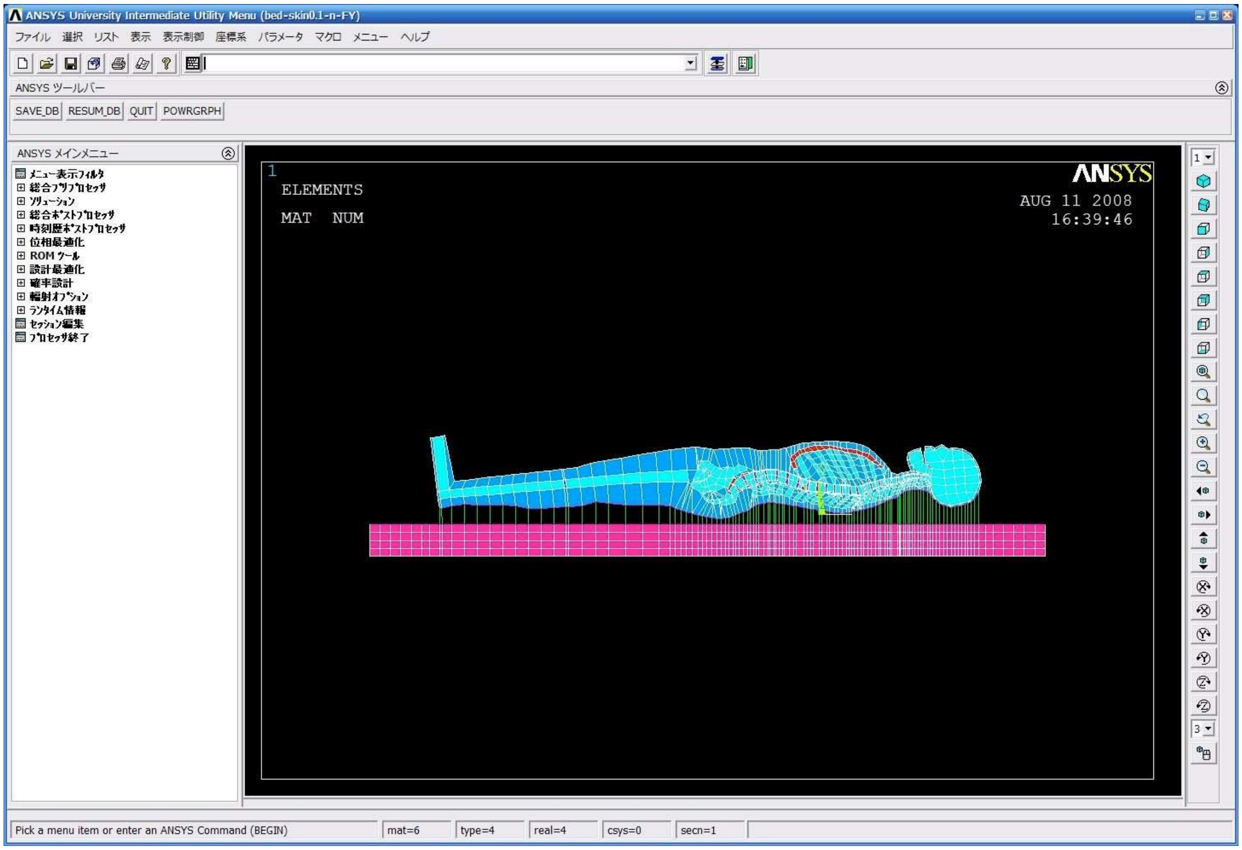

Figure 2.26. The ANSYS user interface and a two-dimensional male finite element model (Yoshida et al., 2010).

Considering that the distribution of stress in the human body may change due to differences in body shape, different body types have different preferences for mattresses. Therefore, they have another development of human finite element models of adult males in three postures and investigated the sleeping comfort of mattresses based on the relationship between the finite element analysis results and the sensory test results (Yoshida et al., 2012).

However, it is worth discussing whether the two-dimensional plane mold has sufficient ability to simulate three-dimensional objects. The model outputs limited parameters; for example, the contact pressure cannot be calculated. The validity of the model is not mentioned in the article.

2.4.2 Prediction of the contact pressure by finite element modeling

With the increasing life expectancy, so has the number of people in bed. The number of pressure ulcers caused by bed rest has also increased rapidly (Stausberg et al., 2010). Pressure ulcers usually result from local tissue necrosis due to a persistent decrease in blood flow. Lee et al. used Kinetic (Microsoft Corporation) to perform 3D scans of the body contours of three healthy 20-year-old men and reconstruct the images into computer models. A CAD software PTC Creo (PTC V.3.0, PTC Inc., Boston, USA) and medical imaging information processing software 3D-DOCTOR (3D-DOCTOR V4, Able Software Corporation, Boston, USA) were adopted to reconstruct the sliced image into a closed 3D model (Figure 2.27). The model consisted of a 2 mm thick skin covering the whole body and the solid bulk tissue of the entire body.

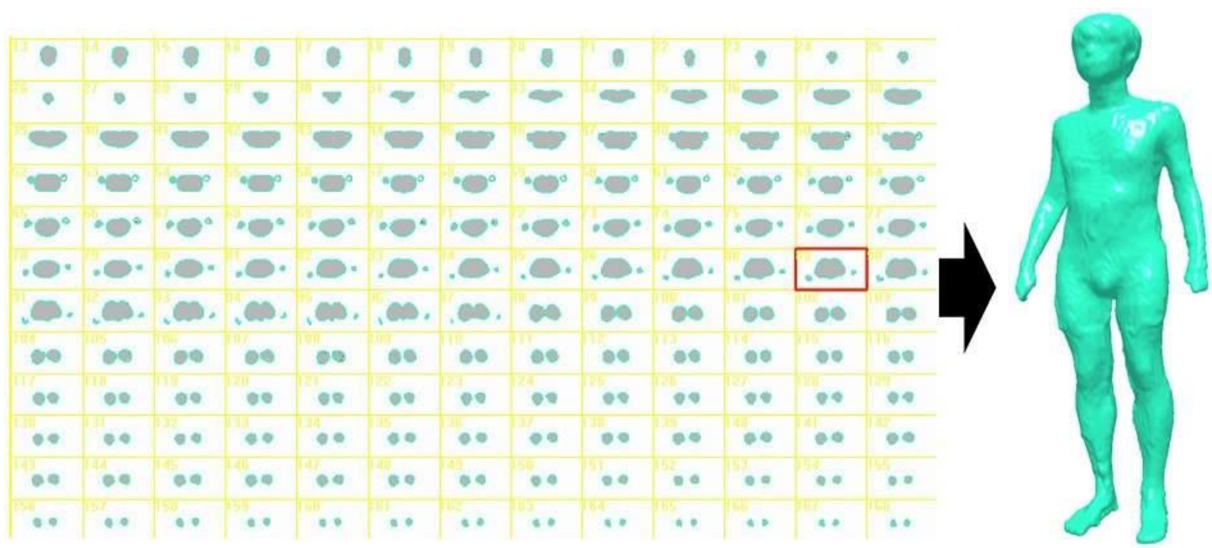

Figure 2.27. 3D reconstruction from the scanned images. (Lee et al., 2017).

The human models were meshed by mesh generation software (ICEM-CFD-V14, ANSYS Incorporated., Canonsburg, USA). The article mentioned that a mesh convergence test was carried out, and the mesh size was defined as 15 mm according to the test results (Lee et al., 2017). Participants lay supine on a rectangular and modified foam mattress, and the contact pressure between the human body and the mattress was measured using a pressure sensing pad (Pliance-FTX, Novel, Munich, Germany). The study compared the experimental pressure data and the pressure data predicted by the FE model; the FE prediction value of the scapula was significantly lower. After embedding a pair of simple scapula structures (Figure 2.28), the contact pressure in the scapula region was significantly increased, and these FE models were considered to be able to predict the supine posture.

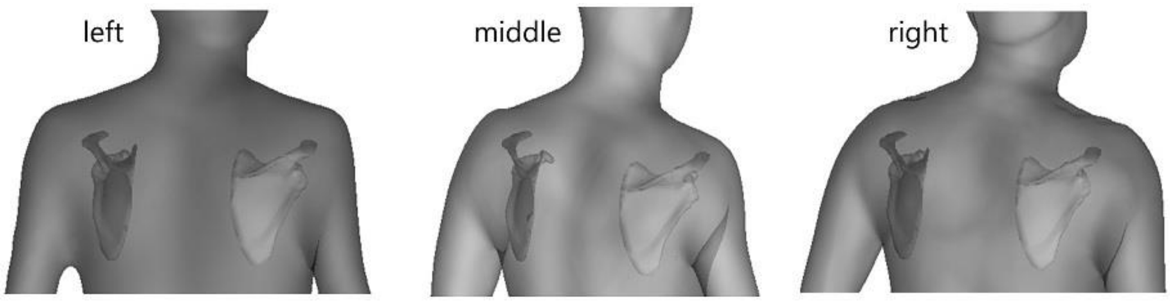

Figure 2.28. Illustration of the scapula pair inserted in the body (Lee et al., 2017).

This study demonstrates the ability to predict the contact pressure in the supine position using the finite element model. However, this 3D model was constructed without any bone or ligament except the simple scapula. The human body contains complex biomechanical structures, including bones, muscles, tendons, ligaments, facial and skin. These oversimplified models inevitably decreased prediction accuracy (Wong et al., 2019).

2.4.3 Development of a finite element model of the cervical spine

The cervical spine is a common site of spinal cord injury. Most injuries are soft tissue injuries, and traffic accidents are a significant contributor (Zafarparandeh et al., 2014). Biomechanical models are used to understand the causes of injuries and mechanisms of dysfunction. Finite element modeling can provide researchers with different perspectives on spine biomechanics. The output data includes stress and load distribution under various conditions and be used as a design reference (Yoganandan et al., 1996; Zafarparandeh & Lazoglu, 2012).

Cervical FE modeling procedures typically include geometry reconstruction, assignment of material properties, meshing, loading conditions, boundary conditions, and validation through different in vitro studies. Zafarparandeh et al. reviewed recent advances in finite element modeling of the cervical spine and reviewed the FE modeling procedures for the cervical spine.

2.4.3.1 Model geometry acquisition

The first step in FE modeling is obtaining all parts' geometry. The geometry of a neck ligament model generally includes three distinct groups: vertebrae, intervertebral discs, and ligaments. This combination provides the essential functions of the cervical spine. Various methods are described in the literature to construct the geometry of each part. Vertebrae geometry can be obtained from CT or MRI scans, while intervertebral discs are usually created by filling the gap in the space between two vertebrae. Ligaments are modeled according to their origin and insertion.

2.4.3.2 Mesh generation

Geometry construction and mesh generation are two interdependent steps. Spine components are sometimes modeled directly from meshes (Figure 2.29(a)) rather than based on medical image geometry (Figure 2.29(b)). Vertebrae have the most complex geometry in model building, including many freeform surfaces. Common mesh types for solid models include tetrahedral and hexahedral elements. Tetrahedral elements are easily generated on the curved surfaces of vertebrae (Zafarparandeh et al., 2014).

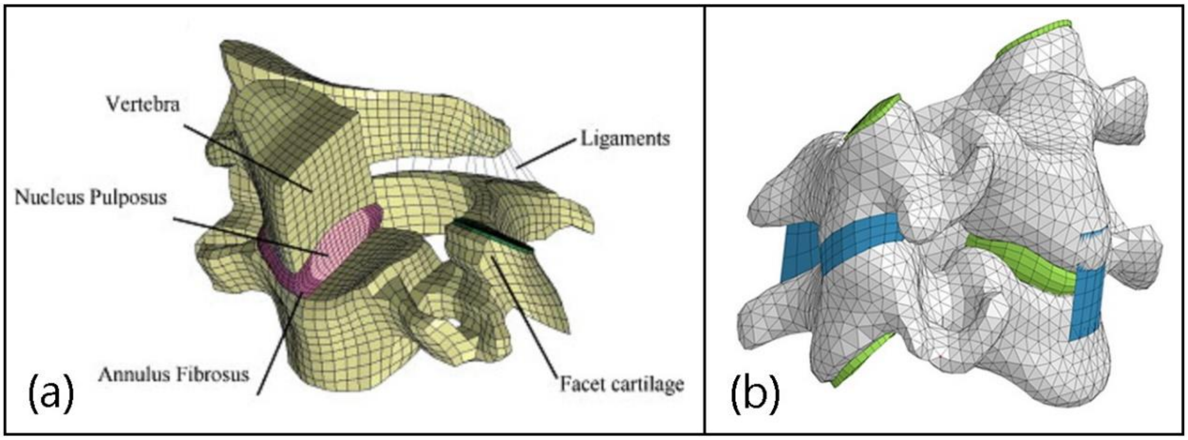

Figure 2.29. Mesh generation of vertebrae (a) Vertebrae models constructed based on mesh (Panzer et al., 2011); (b) Vertebrae models constructed based on medical image (Östh et al., 2017).

2.4.3.3 Material properties and segmentations

The intervertebral disc has a complex geometry, including the annulus fibrosus and nucleus pulposus. Some studies represent the intervertebral disc with a simple isotropic elastic model. In comparison, some others focus on detailed modeling of the intervertebral disc structure (Zafarparandeh et al., 2014). The methods include: modeling the annular space with the strain energy function of two fiber families, modeling the nucleus pulposus with a hyperelastic incompressible Neo-Hookean model, building the nucleus pulposus with fluid elements, and modeling the intervertebral disc as a three-layer structure, including upper and lower end plates.

The role of ligaments is to resist tension or traction to limit the displacement of body parts. As uniaxial structures, ligaments are often modeled as simple elastic beams. Standard beam formulations for these elements impose non- physiologic loads during compression, and cable elements in tension only are preferred.

2.4.3.4 Boundary and loading conditions

The setting of boundary conditions is usually done after building the model geometry, setting up the mesh, and assigning material properties to each component. The boundary conditions are established at the end of the model. In a cervical FE model, all nodes on the lower surface of the lowermost vertebra are constrained to zero displacements. In a quasi-static study, a force representing the weight of the skull is applied vertically to the upper part of the model (Zhang et al., 2006). Other types of loading can be applied above the uppermost vertebra, such as neck flexion, extension, lateral flexion, and rotation. Loads can be applied to the vertebra to simulate body weight (Yoganandan et al., 1996).

2.4.3.5 Model validation

The validation process is the last step in constructing the FE model. The purpose of validation is to evaluate the ability of the model's predictions to respond to real scenarios. Evaluation can be done by comparing the model's predictions with experimental measurements. The experimental data needed to validate the cervical spine finite element model can be obtained from in vitro measurements or cadaveric studies.

2.5 Research gaps

Maintaining proper spine alignment is critical to sleep health. However, most studies are limited to observing spine alignment in the lateral position, although supine is considered the most common and comfortable position (Lee et al., 2020; Su & Xu, 2017).

Studies suggest keeping the spine in its neutral shape to minimize internal stress, but the internal stress is still unknown.

There are studies on pillows or mattresses, but rare ones considered both.

Chapter 3 Methods

The aims and objectives of the study are to develop a curvature measurement tape that can acquire the spine parameters in the supine position. The measured parameters will be used to evaluate the biomechanical effects of sleeping support systems for individuals during experiments. Finite element simulations will be performed to observe intervertebral disc loading on different sleeping supports.

This study consisted of 3 parts:

Part 1: Development of a curvature measurement tape which able to measure the covered curvature. This device will be placed between the sleeping support system and the volunteer's back. It should be flexible and thin enough to limit the inference of sleep posture during measurement. The measured curvature should be displayed in real-time, and the twist of the sensor tape should be monitored.

Part 2: Experiments of volunteers lying supine on different stiffness of mattresses. The spine alignment should be measured and analyzed.

Part 3: Development of a computational model for finite element analysis. The simulation results will include intervertebral disc loading and other musculoskeletal parameters.

3.1 Development of a curvature measurement device

A thin, flexible sensor tape will be developed to measure the spine alignment in the supine position. The development procedure generally includes hardware development, algorithm design, programming, calibration, graphical user interface development, and device validation.

3.1.1 Design

The spine is located at the midline of the back of the trunk. The average spine length in males is approximately 710 mm; the length of the sacral and coccyx is 125 mm (Gray, 1973). The curvature measurement tape needs to be long enough to cover the midline from the head to the buttocks when placed on the person's back to measure the entire spinal curvature in the supine position. It considers various heights and spine lengths. As reviewed in Section 2.1, a spinal curvature involves several natural curves of the spine, such as cervical lordosis, thoracic kyphosis, and lumbar lordosis. The curvature measurement tape consists of 30 accelerometer units in a 30 mm pitch to measure these curvatures with relatively reasonable resolution and high accuracy. This sensor tape has a sufficient length to cover the human back from the cervical C1 to the sacral S1 (Figure 3.1).

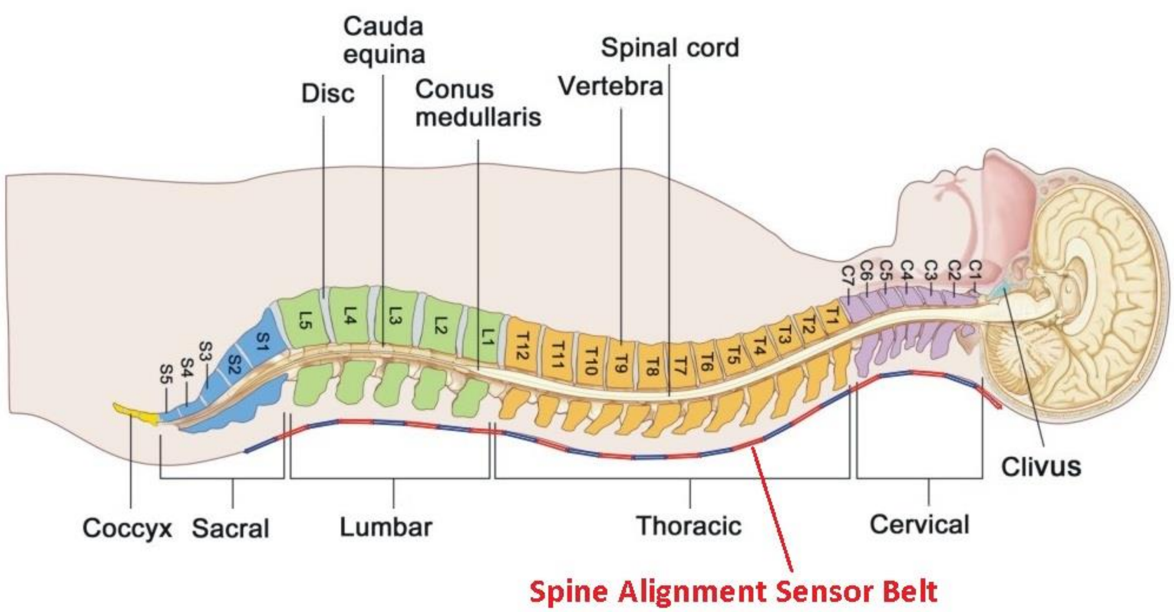

Figure 3.1. Illustration of the curvature measurement tape attached to a human back.

The device should be thin and flexible to avoid interfering with the sleep posture. In the preliminary design, existing sensor modules were adopted and connected by thin wires. Based on the size of the existing accelerometer board, the size of a single sensor unit was set to 30 × 30 mm, with a 6 mm thickness. Each sensor unit detects its inclination, and the signal is collected by a micro control unit (MCU). A self-developed algorithm can convert the inclination data to coordinates or a curvature (Figure 3.2). The MCU collects the signal from each sensor unit, conducts data processing, and sends the spine alignment parameters to a computer or mobile device by wireless connection. The spine alignment parameters can be displayed by the computer or mobile device in real-time and saved for further analysis.

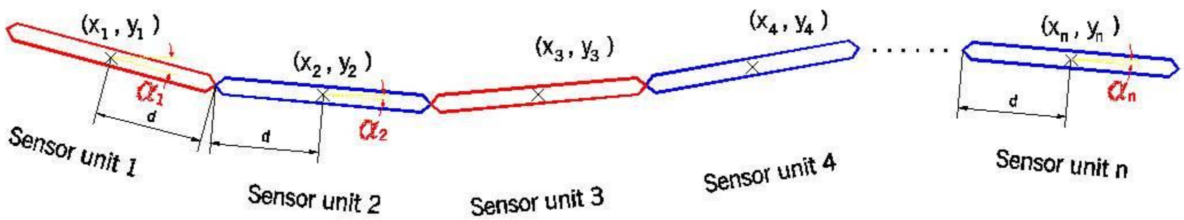

Figure 3.2. Calculation of coordinates.

3.1.2 Electronic components

3.1.2.1 Sensors

Each sensor tape integrates 30 accelerometers, and choosing a suitable model of the sensor chip is critical. The selection criteria include part price, accuracy, resolution, unit size, formate of data output, and type of connection interface. After referring to some literature (Busching et al., 2012; Stollenwerk et al., 2018; Yoon et al., 2015), we consider that ADXL345 (Analog Equipment, Wilmington, USA) is a suitable model.

ADXL345 is a three-axis MEMS accelerometer with a compact size, low power consumption, and high resolution (13-bit) that can measure accelerations in a range of ±16 g. Furthermore, the chip has a built-in Inter-Integrated Circuit (I^2C) signal interface. Using an I^2C connection requires only two signal wires, and each I2C interface can connect multiple devices, facilitating the development of concise circuits. Each ADXL345 has two selectable I2C addresses, and they are 0x1d and 0x53. Two sensors can be wired in parallel and transmit data individually. The supply voltage of the ADXL345 is 2.0 – 3.5 VDC; the wide range of input voltages makes circuit development easier. The current consumption in measurement mode is as low as 23 uA, which is especially beneficial for power control of such a device with dozens of sensors connected. The thickness of the ADXL345 is only 1.0 mm; this is critical for the thickness control of the whole sensor tape.

3.1.2.2 Microcontroller

The functions of the MCU are to collect the inclination data from each sensor unit, conduct data processing, send the measured curvature to a computer, and store the data in a storage device. A low-cost, popular, low-power, easy-to-program chip is most suitable for static capture applications that only require low sample rates. A Thin Quad Flat Pack (TQFP) microchip (ATmega328P, Atmel Corporation, San Jose, USA) has been adopted. ATmega328P is a type of Advanced Virtual RISC (AVR) microcontroller. This microcontroller processes the data up to 8 bits with 2048 bytes of internal built-in static random access memory (SRAM) and 1024 bytes of electrically erasable programmable read-only memory (EEPROM), which can store system settings (Figure 3.3).

This RISC-based 8-bit AVR microcontroller incorporates 32 KB of in-system programming flash memory, conveniently enabling program updates.

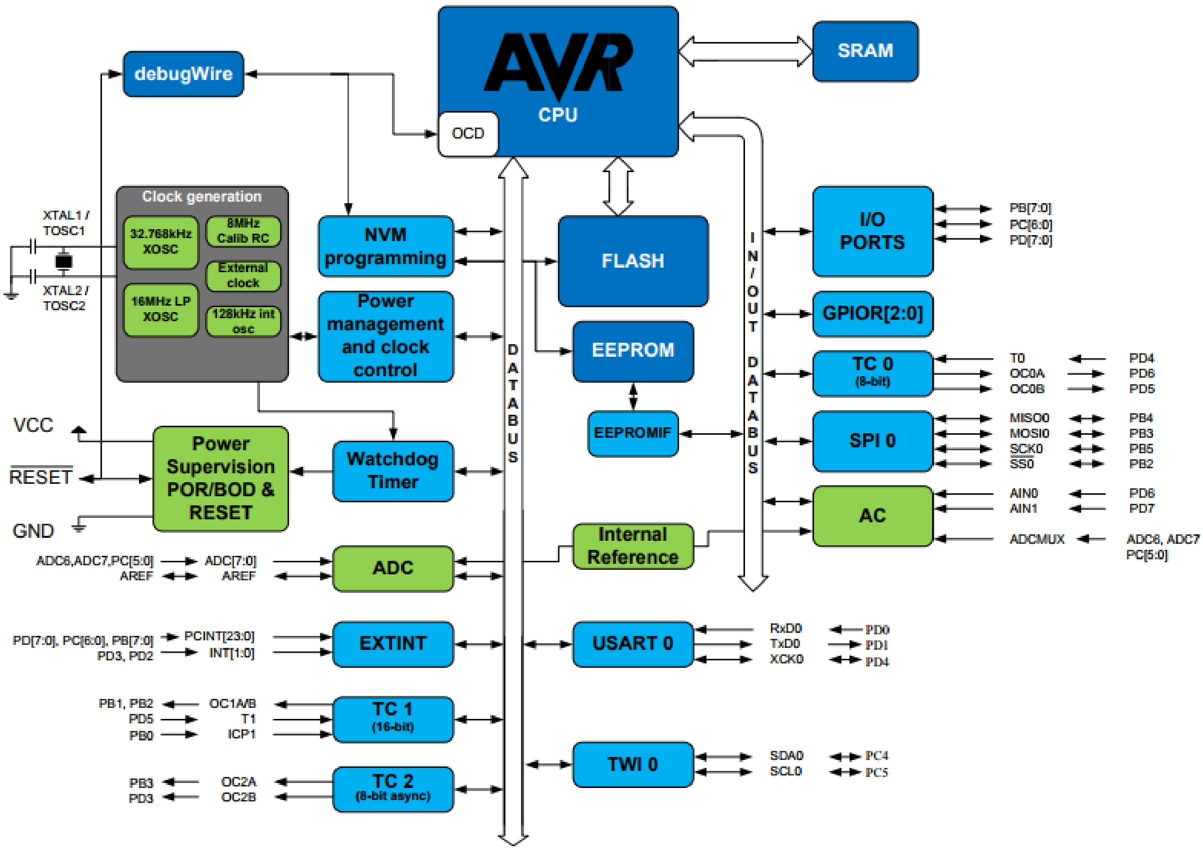

Figure 3.3. International configuration of an ATMEGA328p MCU (Watson, 2017).

3.1.2.3 Peripherals

Several peripheral components need to be connected to keep the device working. The most challenging part of developing the sensor tape was connecting 30 individual accelerometers. The connection between sensors needs to be simple and convenient, using as few connecting wires as possible to facilitate manufacturing and maintenance. Since each ADXL345 has two I2C addresses to join 30 sensor units, several I^2C switches (TCA9548A, Texas Instruments Inc., Texas, USA) should be connected to expand the capability of the number of I^2C peripherals. There are eight bi-directional I^2C ports constructed inside a TCA9548A chip; the channels can be accessed via the I^2C bus. The SDA/SCL upstream pairs are fanned out to downstream pairs of eight channels. An individual SCL/SDA channel or combination of multiple channels can be connected, depending on the set-up of the programmable control register. Multiple downstream channels can be connected to resolve the conflict of limited I^2C slave addresses. Each I^2C switch can control up to eight sensor units in this design. However, to limit the segment length and reduce the number of internal segment wires, six sensor units are inside a segment, and five I^2C switches would be connected to form the sensor tape.

For convenience in operation, the device should be able to send the measured data to the computer in real-time through a wireless connection. Both Wi-Fi and Bluetooth are technologies that achieve short-range wireless communication by using radio frequencies to transmit signals. Although both are forms of wireless communication, they differ in functionality, purpose, and other factors. The Bluetooth protocol supports data transmission between devices in a short range. For example, mobile phone connected to headsets by Bluetooth is often used to enable hands-free use. Wi-Fi allows devices to connect to the Internet. Since Bluetooth only requires an adapter on every connected device, it is easier to use and has low power consumption than Wi-Fi. Therefore, a Bluetooth connection was adopted for this project. The MCU was connected to a generic Bluetooth 2.0 module (HC-05, Bluetooth Maker Factory Limited, Shanghai, China) to create a wireless data connection with a laptop computer. HC-05 is an easy-to-use, small-sized, low-cost Bluetooth module for wireless connection. This module constructs CSR Bluecore 04 outer single-chip Bluetooth system using Complementary Metal-Oxide-Semiconductor (CMOS) technology to achieve low power consumption. This module is compatible with the Bluetooth V2.0+ EDR protocol, which can easily connect to a Windows computer or an Android mobile device.

Creating a data storage function in the control box can avoid data loss. The Micro-SD card is a proprietary non-volatile memory card format for portable devices; it is the smallest memory card on the market, with a dimension of 11 × 15 × 1 mm. An SDHC (High Capacity) memory card can store a large amount of spine alignment data, which is ideal for local data storage integration into the control box. A generic Micro-SD card adaptor was connected to the MCU. The measured spinal curvature data can be stored in a Micro-SD card through the Micro-SD card adaptor.

The control box has included a real-time clock module (DS-1302, Maxim Integrated Limited, San Jose, USA). This chip is a battery-backed general-purpose clock that can count year, month, date of the mouth, date of the week, hours, minutes, and seconds with leap-year compensation valid until 2100. It can provide a timestamp, which can be saved in the Micro-SD memory card with the measured spine alignment data.

The system status and measured spine alignment data can be displayed on a 0.96-inch graphical organic light-emitting diodes (OLED) display (128 × 64 pixels, Vishay Intertechnology Inc, Malvern, USA). This display module has a built-in SSD1306BZ controller, which can be easily connected through the I^2C interface. It is small in size, low in operating voltage, and low in power consumption.

The control box is powered by a 300mAH lithium battery (282850, Generic, Taobao, China). Due to the low-power consumption design, this battery can support up to 5 hours of working time.

3.1.3 Design of electronic circuits

3.1.3.1 Circuit design of the sensor tape

Customized electronic circuits are required to connect all the sensors for data assessment by the MCU. The sensor tape consists of five identical segments, each connecting six sensor units.

Five sections linked thirty sensor units, and each section connected six sensor units through an I2C switch (Figure 3.4). A concise electronic circuit was designed for this study, requiring only four wires to connect between segments and the control box. The four wires include two for power transfer: the voltage common collector (VCC) as 3.3v and the ground (GND), and a couple of wires for data transmission; they are serial clock (SCL) and serial data (SDA). The lithium battery inside the control box provided the power supply, connected in parallel to every sensor unit and I^2C switch. The signal output of the IMU was connected to the I^2C switch through two signal wires (SCL and SDA). The five sections were connected in parallel by four wires, VCC and GND were used for power supply, and SCL and SDA were used for signal transmission (Figure 3.4). One end of the sensor tape was connected to a four-pins connector, which can connect to the control box.

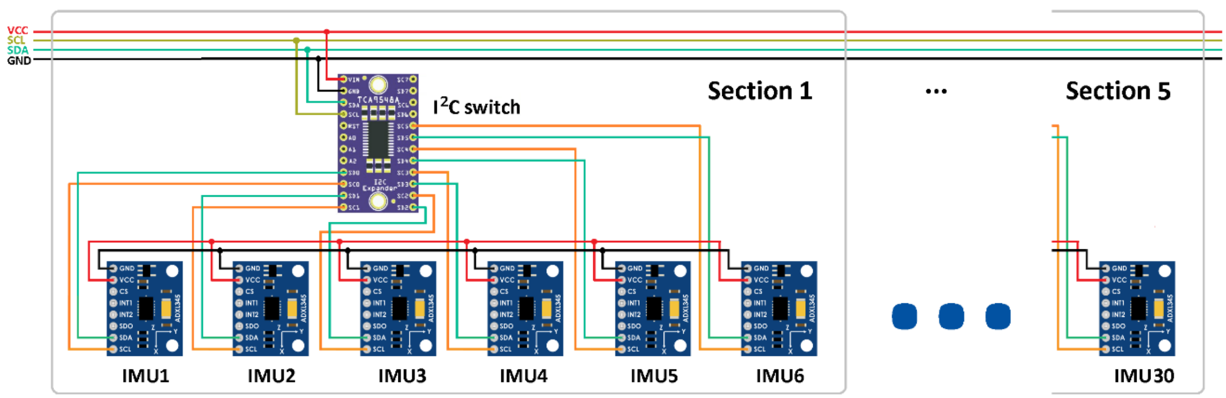

Figure 3.4. Block diagram of a sensor segment.

3.1.3.2 Circuit design of the control box

The control box contains an MCU, a battery, and peripheral components. The built-in lithium battery of the control box supplies power to the system for the operation of the device. This lithium battery powered the electronic components inside the control box and the sensor tape connected to the control box. A block diagram is shown in Figure 3.5 to display the connected electronic modules inside the control box. The modules of OLED display, Bluetooth, Micro-SD storage, and real-time clock were connected to the ATMEGA328P MCU. The OLED display was connected to the MCU through the I^2C interface, which was wired to the default I^2C ports A4 and A5.

The Bluetooth module was connected to the MCU through a soft serial protocol. The RX port of the Bluetooth module was connected to D2 of the MCU, and the TX port was connected to D3.

The real-time clock DS1302 has a built-in simple serial interface for signal transmission. There are three wires connections as the serial clock (SCK) connected to D6 for data synchronization movement, the bidirectional data pin (DAT) connected to D7 or input and push-pull output, and the reset (RST) pin connected to D8 for chip enable.

The Micro-SD adaptor was connected to the MCU by a serial peripheral interface (SPI) connection. There are four wires connected; they are the chip select (CS) pin was connected to D10, the master out slave in (MOSI) pin was connected to D11, the master in slave out (MISO) pin was connected to D12, and the serial clock (SCK) pin was connected to D13. For functional control, there is a control button connected to A3.

The device also includes a power management system. If the device is idle or the battery voltage is too low, the system will power off to avoid damage to the battery. The charging circuit for the Lithium battery enables the device to be charged through the Micro-USB port.

The sensor tape was connected to the control box through a four-core thin wire for data transmission. These four wires include two for the power supply and another two for the I^2C signal transmission. This design simplifies the connection between devices as much as possible.

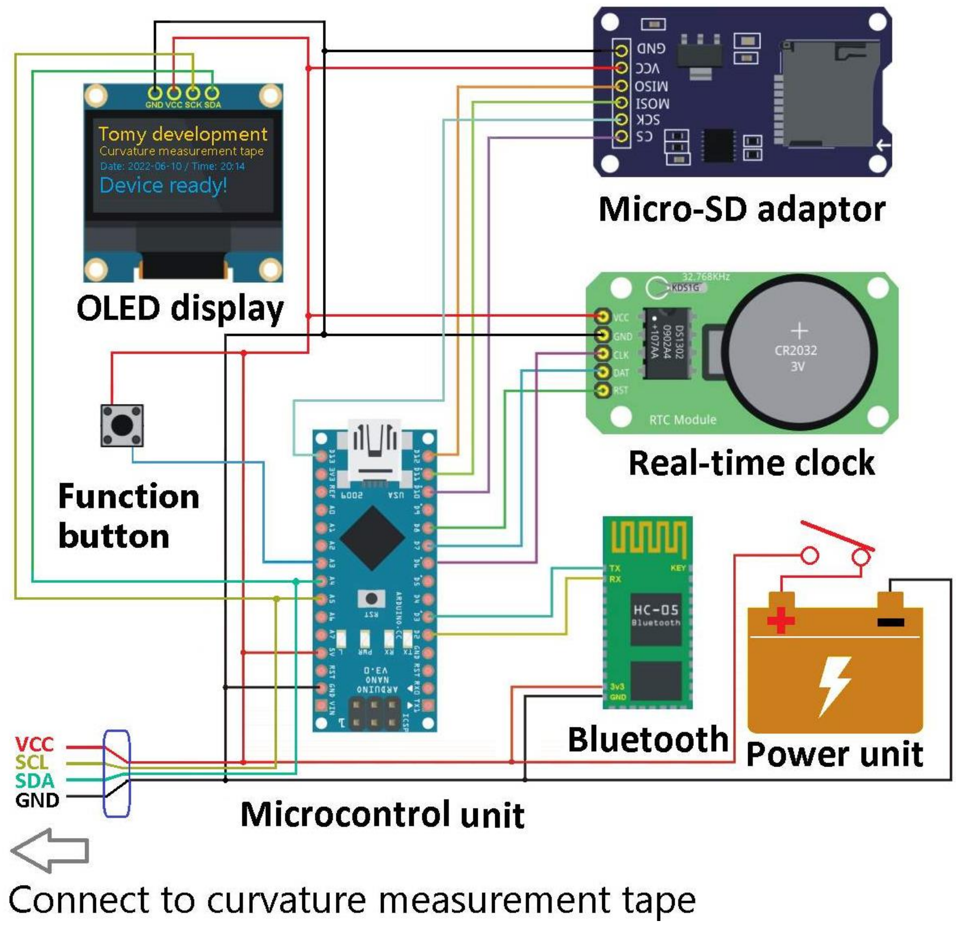

Figure 3.5. Block diagram of the control box.

3.1.4 Programming

The MCU operated based on an Arduino system (Arduino 1.85, Arduino LLC, Boston, USA). Arduino is an open-source electronics platform. The integrated development environment (IDE) is an application with cross-platform support. It was written in the Java language with a simple and easy-to-use interface. The program flowchart is shown in Figure 3.6. An initialization procedure was conducted while the system started up; on the connection of power, the OLED display, Micro-SD adapter, and the sensor tape reset. After the system initialization, the system runs in a loop. The MCU collects sensor data one by one. Then, sensor calibration proceeded for every individual accelerometer, based on the calibration database early created and stored inside the EEPROM of the MCU. The time chop from the real-time clock was also sent to the microcontroller. The MCU combined the measured sensor data and a time chop to a sentence and sent it to the display unit. The system also detects the stats of the function button; while it is pressed, the measured spinal data can be stored in the Micro-SD adaptor. Sensor data is sent via Bluetooth if the Bluetooth module is paired with a computer or mobile device.

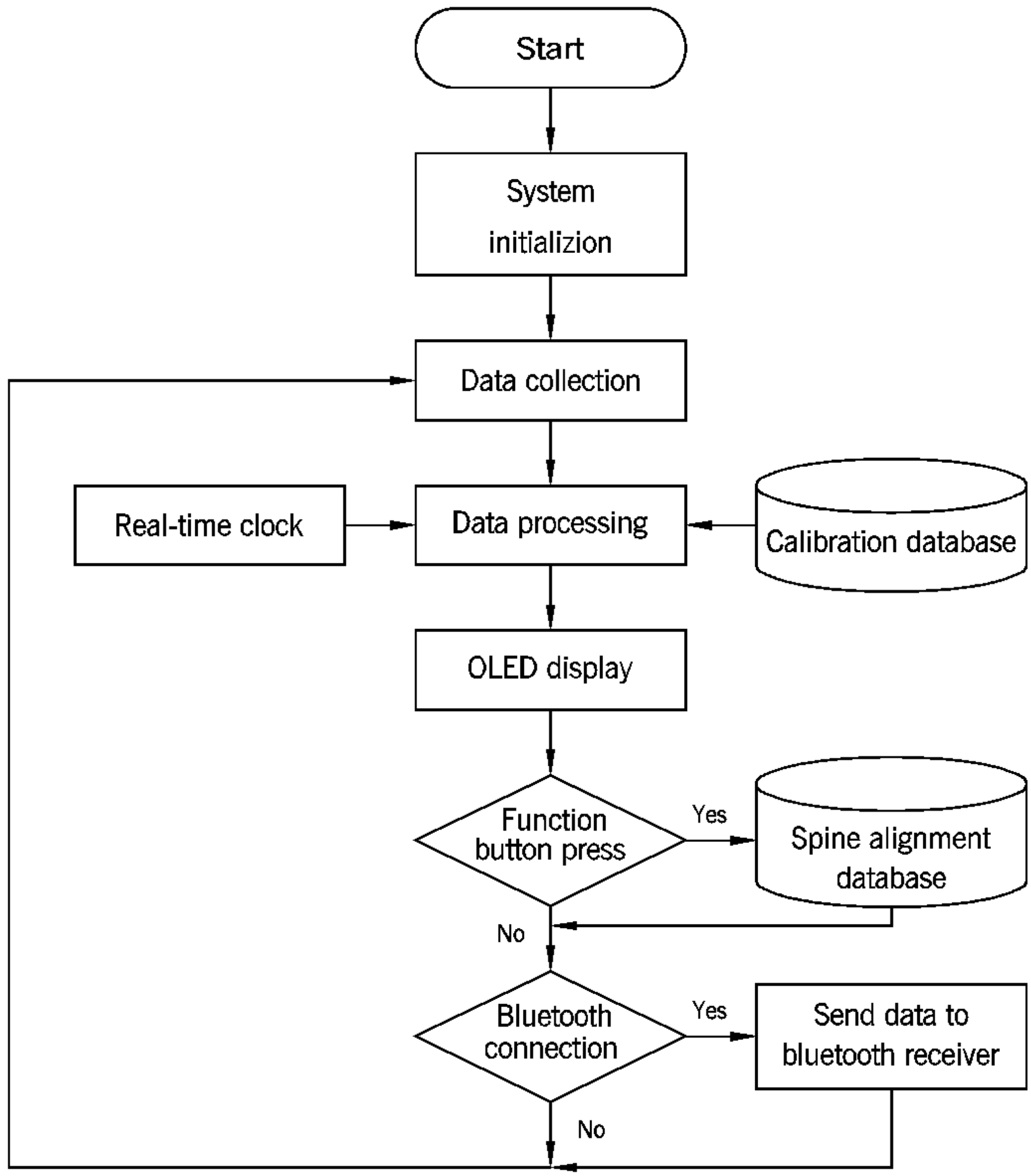

Figure 3.6. Flowchart of the microcontroller unit.

3.1.5 Preliminary version

A preliminary version of the curvature measurement device was designed and developed for functional evaluation.

3.1.5.1 Sensor tape

The preliminary design of the sensor tape was based on existing functional circuit blocks. As the circuit design described in Section 2.3.3.1, the whole sensor tape was constructed by the connection of five segments. Each segment contains six sensor units and an I^2C switch (Figure 3.7). Based on the circuit design, the I^2C switch was embedded in the 3rd sensor unit and overlapped the accelerometer. Each sensor board was installed on a plastic base using 3D printing. The units were connected by a hinge, which allowed units to rotate freely. There were thin and soft wires connecting the sensors and the I^2C switch; only four wires were needed to connect the segments.

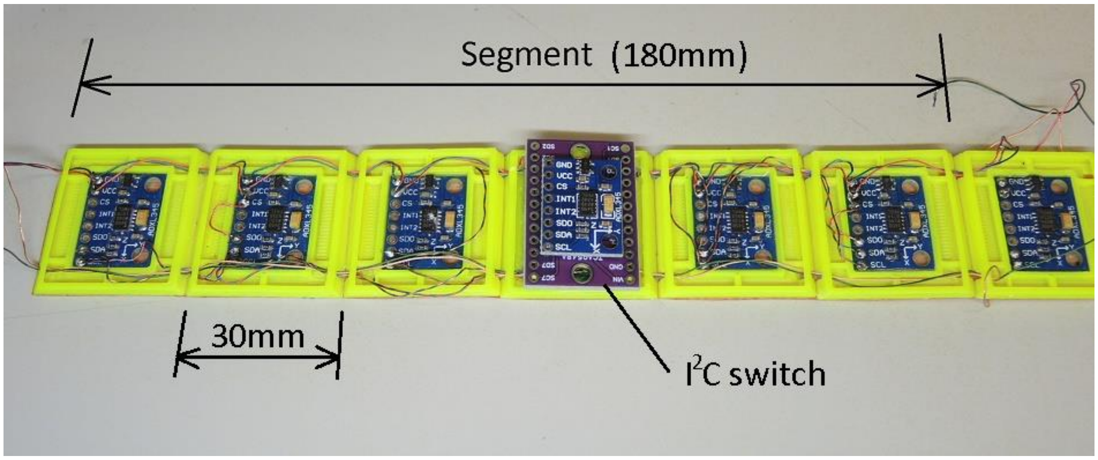

Figure 3.7. Preliminary design of the sensor tape.

Five sensor segments were connected to form the whole sensor tape. The length of the sensor tape is 900 mm, which is long enough to cover the human spine. Figure 3.8 shows the side view of the sensor tape containing 30 sensor units. Sensor units were connected by plastic tape that can function as a hinge to allow the rotation between sensor units. A buckle was installed on the starting side of the sensor tape, which can be buckled on a swimming cap with a buckle holder (Figure 3.9) so that the starting position of the sensor tape can be fixed through the worn of the swimming cap.

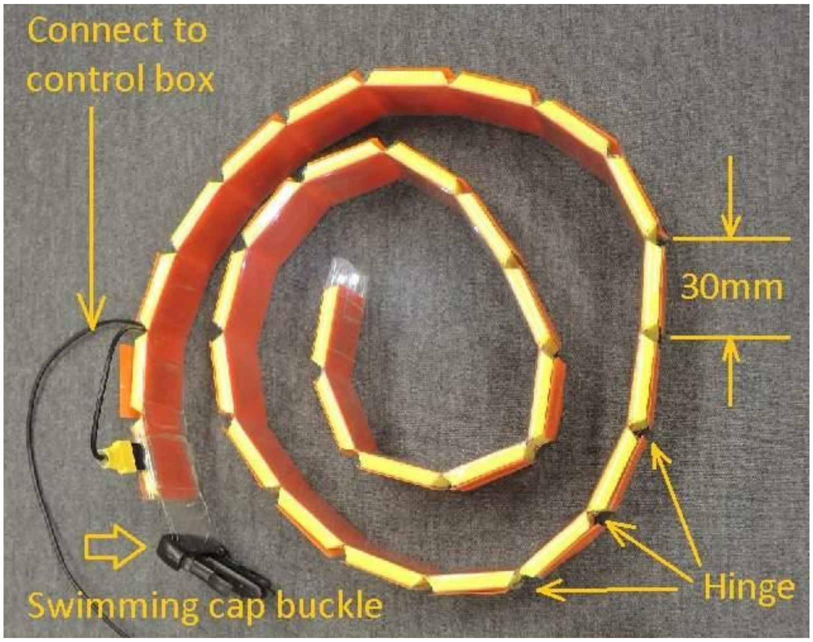

Figure 3.8. Side view of the preliminary version of sensor tape.

Figure 3.9. A buckle holder installed on the swimming cap.

3.1.5.2 Control box

Since this project involved connecting multiple modules and the development of new algorithms, a system was constructed with existing functional circuit blocks to test the design feasibility. For evaluation, several existing modules were assembled on a protoboard (Figure 3.10). Wires were used to link up the electronic modules. Since the solderless prototype board does not require soldering and reusability, it can be easily used to create temporary prototypes and conduct circuit design experiments. The sensor tape was connected to this protoboard by a four-core wire, and the signal was processed through the MCU and sent to the Bluetooth module, OLED display, and the Micro-SD adaptor with a time-stamped signal. A rechargeable lithium-polymer battery powers this system.

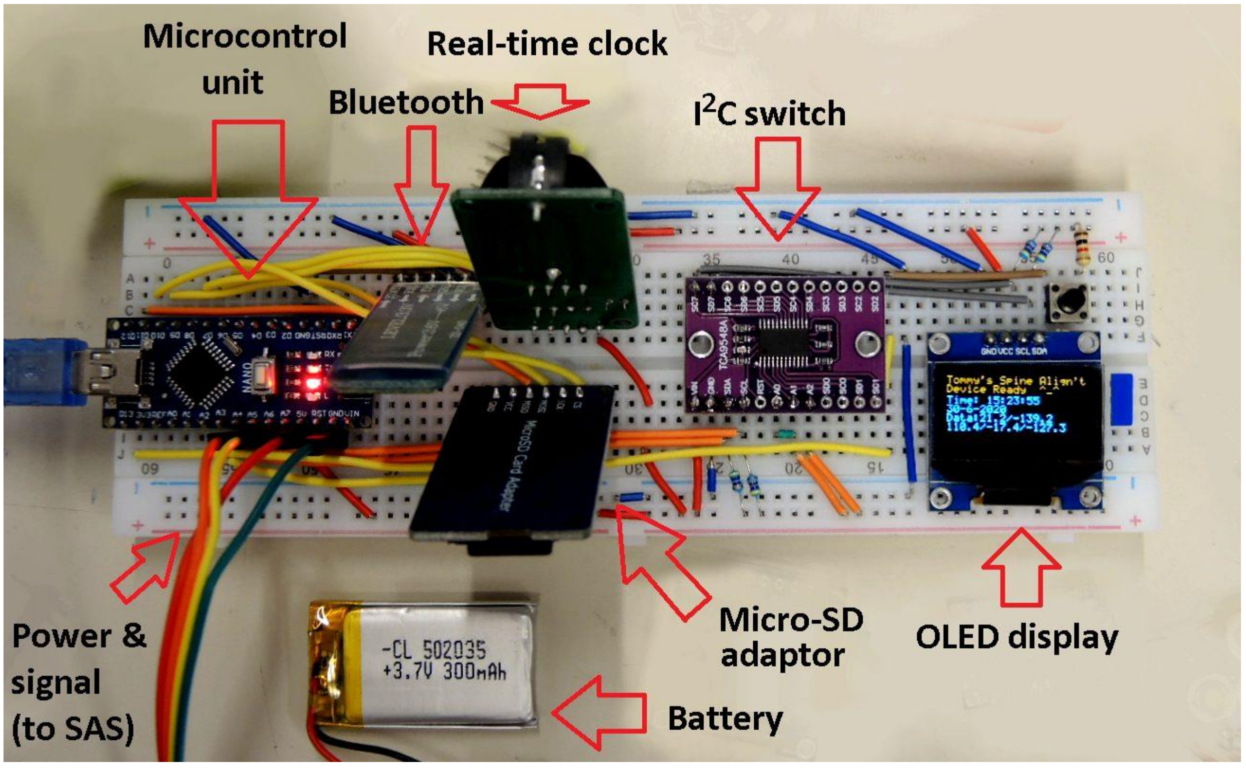

Figure 3.10. A protoboard with electronic modules for functional evaluation.

The program was developed and tested with the protoboard. However, carrying the protoboard for experiments is inconvenient, and the circuit blocks may become loose from the protoboard and cause failure. Therefore, a compact control box was developed. Circuit blocks were connected and assembled into a much smaller package. Figure 3.11 shows the hand-make control box with all components presented and displayed in Figure 3.10. This control box was made by 3D printing, and the size is approximately 25 × 25 × 40 mm, which significantly improved usability and stability.

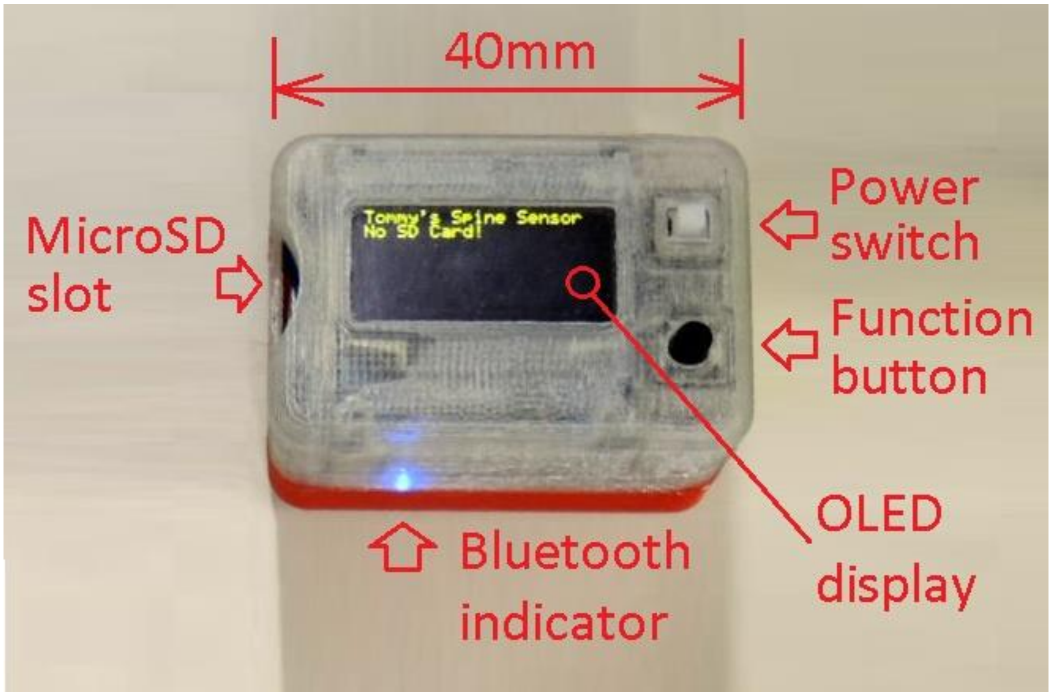

Figure 3.11. The control box.

The MCU was programmed to convert the inclination of sensors into coordinates based on equations (1) and (2). The parameters are shown in Figure 3.12.

$$X_n = d \times \mathrm{Cos}(\alpha_n) + d \times \mathrm{Cos}(\alpha_{(n-1)}) + X_{(n-1)} \quad (1)$$

$$Y_n = d \times \mathrm{Sin}(\alpha_n) + d \times \mathrm{Sin}(\alpha_{(n-1)}) + Y_{(n-1)} \quad (2)$$

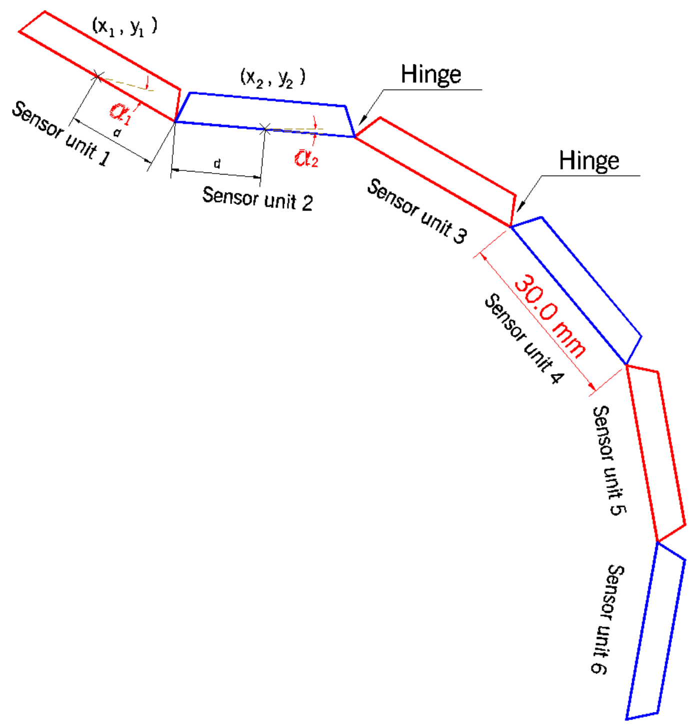

Figure 3.12. Parameters of equations for coordinates calculation.

3.1.5.3 Graphical user interface

A software package was developed using the processing programming platform (Processing 3.1, Casey-Reas and Ben-Fry, USA). The application processes and displays the spinal curvature in real-time on the graphical user interface from the data collected via the Bluetooth interface. As shown in Figure 3.13, the integrated data was depicted as a curve on the graphical user interface representing the arrangement of the sensor tape. Each sensor unit can measure its inclination, representing the slope of a line of 30 mm in length. Thirty sensors measured 30 lines, which were connected end-to-end to restore the shape of the sensor tape. The user interface was programmed with data input dialogs of experimental information. The recording information includes the volunteer's name, the lying position, the type of body support, and the time of the experiment (Figure 3.13). The data could be saved in text format from the software package for further analysis by other software. The experimental information can be read during post data processing stage, which facilitates data analysis.

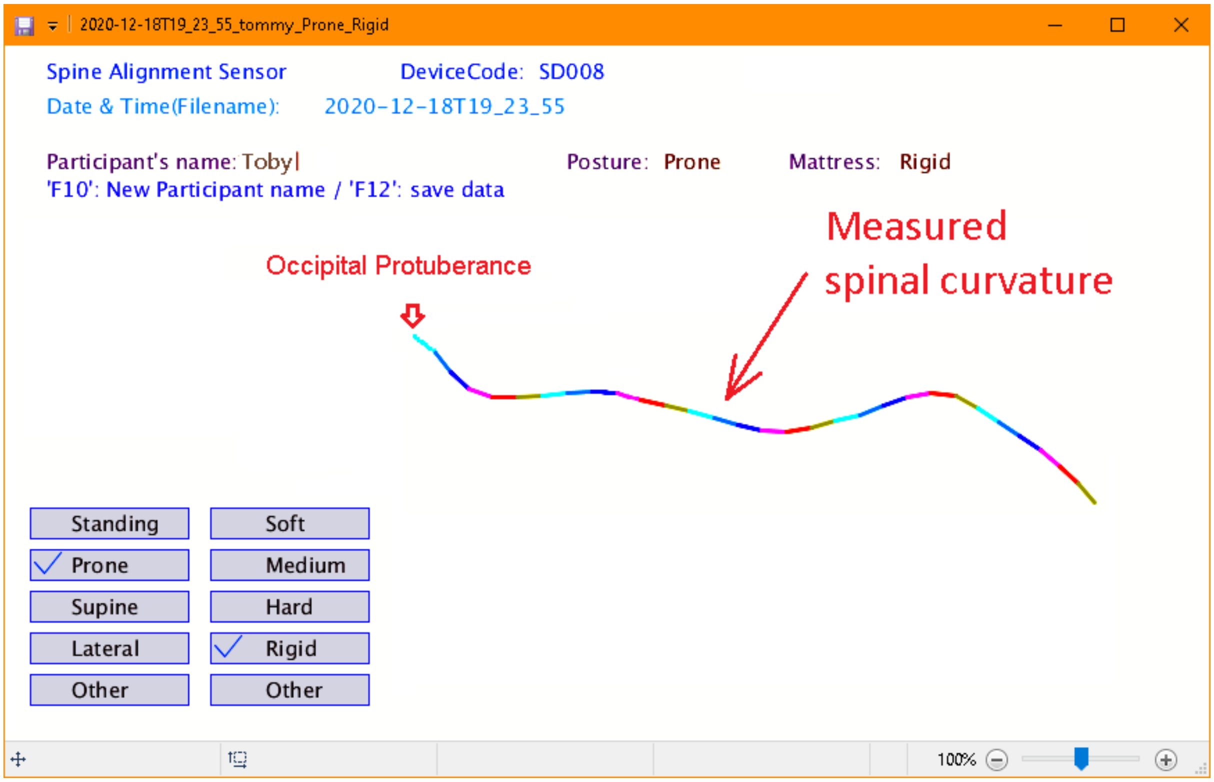

Figure 3.13. Design of graphical user interface of the curvature measurement tape.

3.1.5.4 Device evaluation

The preliminary version of the curvature measurement tape was evaluated due to a simple experiment. An ethylene-vinyl acetate foam mat of 5 mm thickness was placed on the ground, which can be considered a rigid plate. The volunteer was lying in a prone position, and the head and neck were supported by a prone pillow (PP8320000073, ZhenZhiBao, Nanchang, China). The volunteer wore a swimming cap with a buckle holder so that the starting of the sensor tape could be fixed. The curvature tape was placed on the volunteer's back (Figure 3.14) to capture the spinal curvature in a prone position.

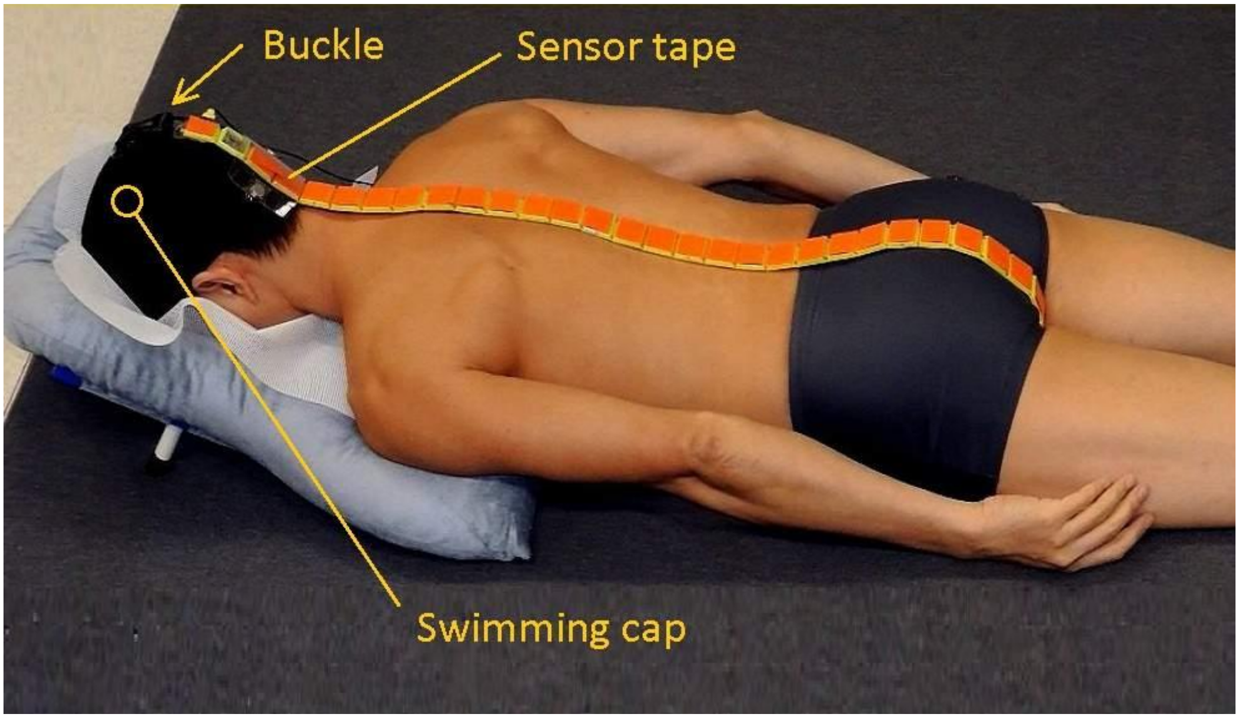

Figure 3.14. The design of data collection in a prone position.

The preliminary version of the curvature measurement tape was tested and evaluated. There are limitations found:

(1) The sensor tape is considered somewhat thick, which may influence the sleep posture. The thickness of a sensor unit is 6 mm; it may have similar accuracy to the literature (Haex, 2004), which is barely acceptable. There is no doubt that thinner sensor tape would reduce interference with the sleeping position.

(2) The sensor unit was 3D printed, with a solid circuit board inside. Therefore, the sensor unit is rigid as a whole, and the sensor tape can be deformed only by the rotation of the hinges between the sensor units. However, the rigid sensor units limited the sensor tape's ability to fit the measuring surface. It is more or less uncomfortable for the volunteer while lying supine on this sensor tape constructed by rigid sensor units.

(3) This algorithm depicted the shape of the curvature measurement tape in a plane perpendicular to the gravity direction. Since each sensor unit is rigid, a 30 mm straight line was used to represent a sensor unit (Figure 3.15). A straight line was used to express a part of the curvature. When measuring a circle of ø200 mm, a gap of 1.12 mm was found between the line's end and the ring. It yields a measurement error of 2.2%, and the error increases when measuring smaller arcs. This study aims to develop a flexible curvature measurement tape. Therefore, the algorithm should be improved, and the new algorithm should be able to depict a curvature by the connection of arcs but not straight lines.

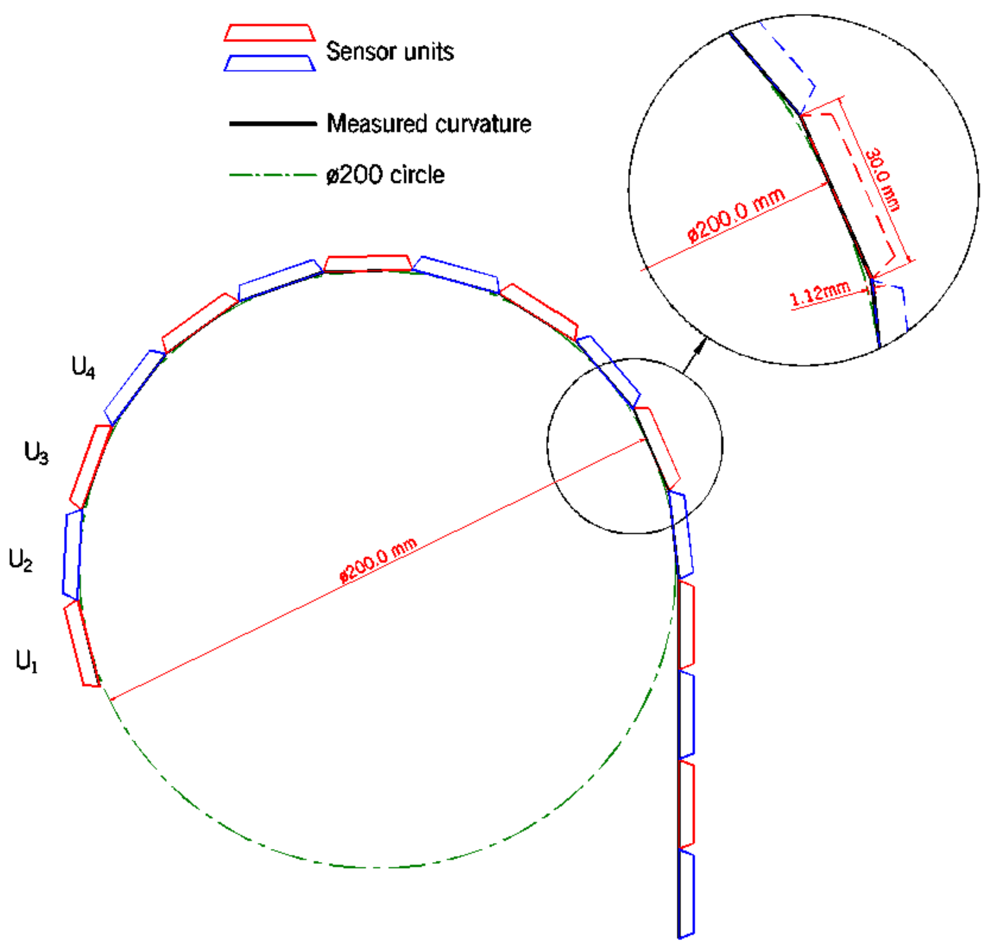

Figure 3.15. The measured curvature by the preliminary version curvature measurement tape.

(4) This sensor tape is designed to measure the curvature of the spine in the supine position. Since the sensor tape was placed between the sleeping support system and the volunteer's back, it cannot be observed visually while using it. Therefore, in some extreme cases, the sensor tape may be twisted. The system should be able to monitor the twisting of sensor tape and remind the operator when the twist occurs.

(5) Since the ADXL345 accelerometer is a low-price low-end inertial sensor, the sensors were shipped uncalibrated and should be bias-corrected to achieve high-accuracy measurement. For example, place the sensor tape horizontally (Figure 3.16(a)); the measurement result of an uncalibrated device exhibit apparent deviations, with curvature fluctuations, as shown in Figure 3.16(b). The ideal measurement result should be a flat, straight line, as shown in Figure 3.16(c). Hence, the accelerometer's inherent deviation and the assembly's bias should be corrected.

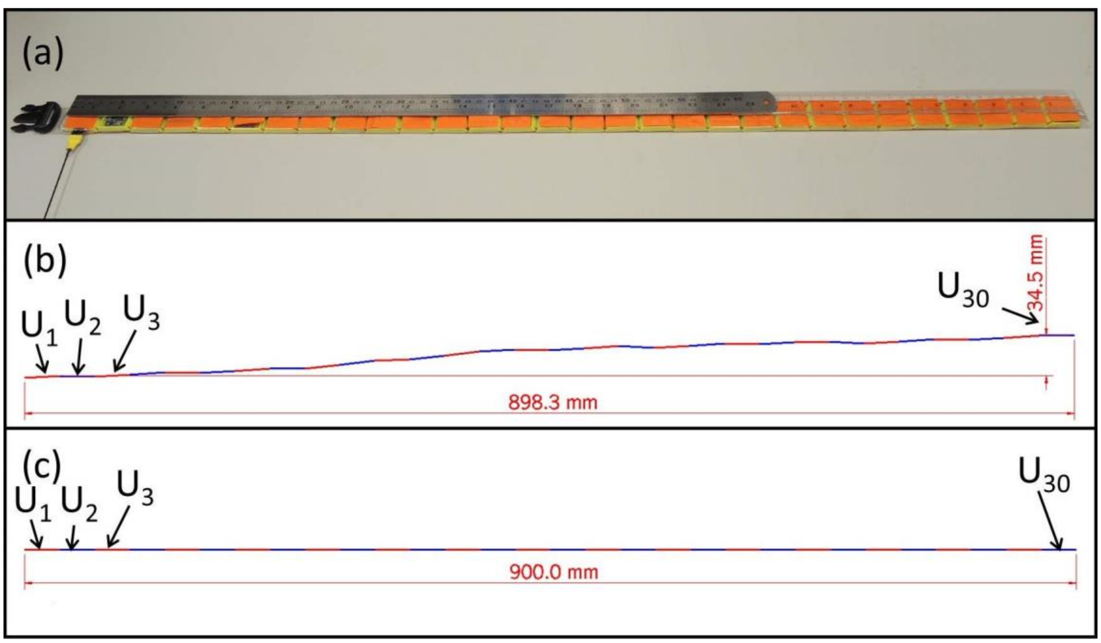

Figure 3.16. The preliminary version of the curvature measurement tape and its measured curvature. (a) The sensor tape placed horizontally flat; (b) The measured curvature without calibration; (c) An illustration of ideal measured curvature.

In summary, a sensor tape made of surface mount technology (SMT) will improve measurement accuracy. At the same time, new algorithms should be developed to improve the measurement accuracy and monitor the axial tilt of sensor units.

3.1.6 Improved version

Due to the lack of studies that reported the connectivity of dozens of inertial sensors, the preliminary version of the curvature measurement tape was constructed for functional evaluation. As described in Section 3.1.3, the concise circuit is able to connect 30 accelerometers via the I^2C interface. After extensive program modifications and circuit tweaks, the curvature measurement tape's preliminary version works correctly. The sampling rate is about 5 Hz, sufficient for static captures such as the spine measurements in the supine position.

Through the pilot experiments, we consider that the preliminary version of the curvature measurement tape is feasible to measure spine alignment in the supine position. However, it is still a bit thick and lacks flexibility. Therefore, custom-made flexible printed circuits will be adopted as the substrate of the sensor tape. Regarding the improvement of the algorithm, multiple arcs will be used to represent the measured curvature. Device calibration will be conducted to correct the chip's inherent deviation and sensor assembly bias. Finally, consider adding an axial tilt detection function to the graphical user interface, which can remind the operator when the sensor tape is twisted.

3.1.6.1 Sensor tape made of flexible printed circuits

A flexible printed circuit (FPC) board is sometimes considered a printed circuit board (PCB) that can bend. It consists of layers of an insulating polymer film with conductive circuit patterns affixed to it, usually coated with a thin polymer coating to protect the conductor circuit. The thickness of an FPC can be as low as 0.1 mm. The thinner sensor tape can lower the posture interference while placing it between the sleeping support system and the human back for spinal curvature measurement. The flexible circuit board was designed using an electronic design automation (EDA) application (Eagle, Autodesk Inc., California, USA). The design drawing is shown in Figure 3.17. There are six sensor units inside a segment. The I^2C switch was placed near sensor unit 3 (U_3) to reduce the wire quantity of an internal segment. All sensors were connected to the I^2C switch through the I^2C interface.

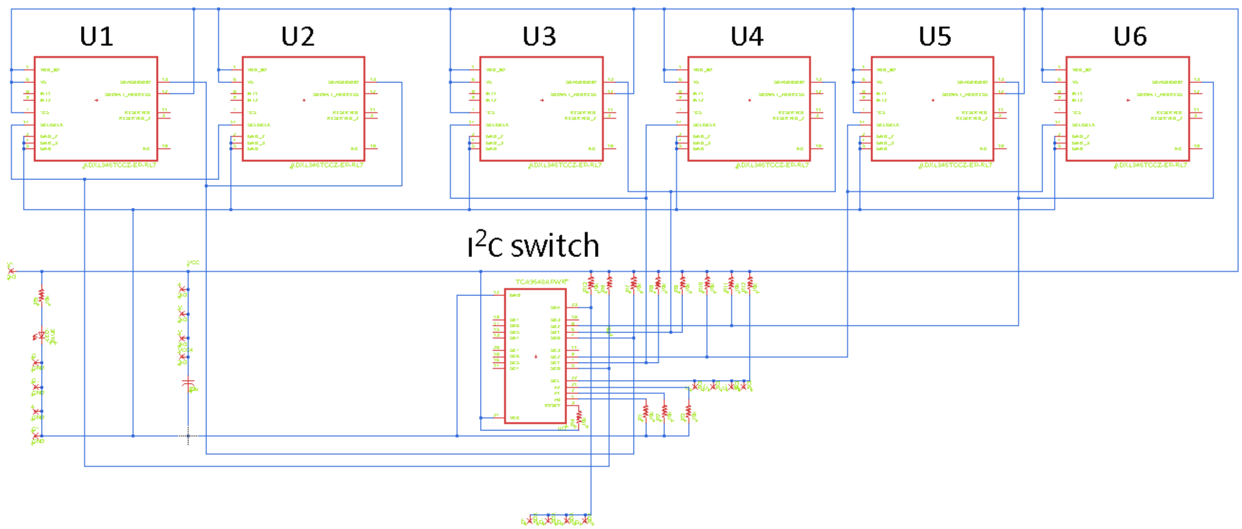

Figure 3.17. The circuit design of the sensor tape.

The dimension of the FPC is 210 × 25 × 0.1 mm, which includes six sensor units and a connection tail that can be connected to another segment. The distance between two adjacent sensors is 30 mm. A narrow circuit bridge connects the sensor units on the FPC, and this design can ensure the flexibility of the sensor tape. Every sensor segment has the same length of 180 mm and extends a small tail that can be linked to the starting area of the conjunction segment to create a long sensor tape. Using short and repeating segmented connections to create a long sensor tape ensures that short sensor segments are easy to manufacture and maintain. Five sensor segments formed the sensor tape with a total of 870 mm length. Based on this concept, the total length of the sensor tape can be modified by the change in segment quantity. Figure 3.18 shows a single sensor segment in the upper part of the figure. The connected sensor tape, which contains five segments, is shown in the lower part of the figure.

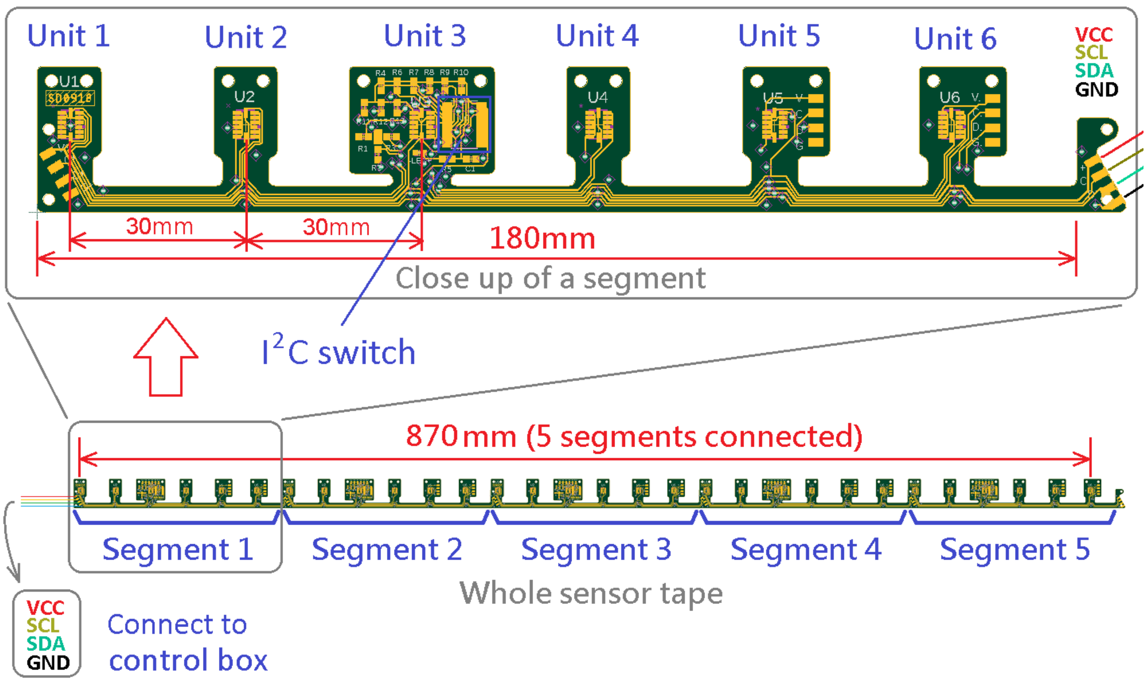

Figure 3.18. Design drawing of the sensor segment and the whole sensor tape.

An FPC factory fabricated the FPC, and the sensor chips and the I^2C switch were assembled using surface mounting technology (SMT). The installation process should ensure the sensors are located in the correct position of the FPC to ensure the curvature measurement tape can be used for high-accuracy measurement.

The sensor tape must be as thin and flexible as possible to accommodate the curvature of a human back without disturbing the sleeping position. FPCs based on flexible plastic substrates bring high flexibility to the sensor tape. The typical thickness of an FPC is 0.1 mm. The ADXL345 sensor in a land grid array package is 1.0 mm thick, and the TCA9548A I^2C switch in a thin, smaller outline package is also 1.0 mm in thickness. The total thickness of the assembled electronic parts is about 1.1 mm. The FPC with assembled electronic components was wrapped with a 0.2 mm thick flexible thermoplastic polyurethane film for mechanical protection and waterproofing. The polyurethane film outer layer ensures that the sensor tape can be used in environments that contact wet and liquid. In addition, the waterproof function is conducive to sterilization. Figure 3.19 shows the sectional side view of the sensor tape with the indicated part thickness and overall thickness.

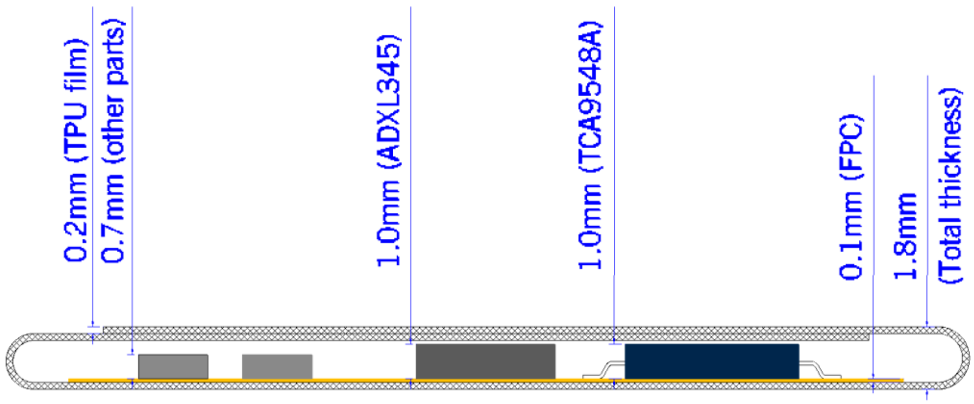

Figure 3.19. The sectional view of the sensor tape with dimensions.

Figure 3.20(a) shows the assembled sensor tape. Five sensor segments were connected to form the whole sensor tape with 870 mm in length. Figure 3.20(b) shows a close-up of the sensor tape. It can be seen from the picture that the sensor tape is very soft and has bent under gravity. Hence, the flexible sensor tape can be closely adapted to the measurement object's surface. However, the length of the sensor tape is fixed and cannot be stretched. Figure 3.20(c) shows the measured thickness of the sensor tape. The thickest point is where the accelerometer was mounted; however, it is only 1.8 mm. The bridge between the two adjacent sensor units is less than 1.0 mm in thickness. The sensor tape's flexible and low-thickness properties can reduce distraction and discomfort for participants.

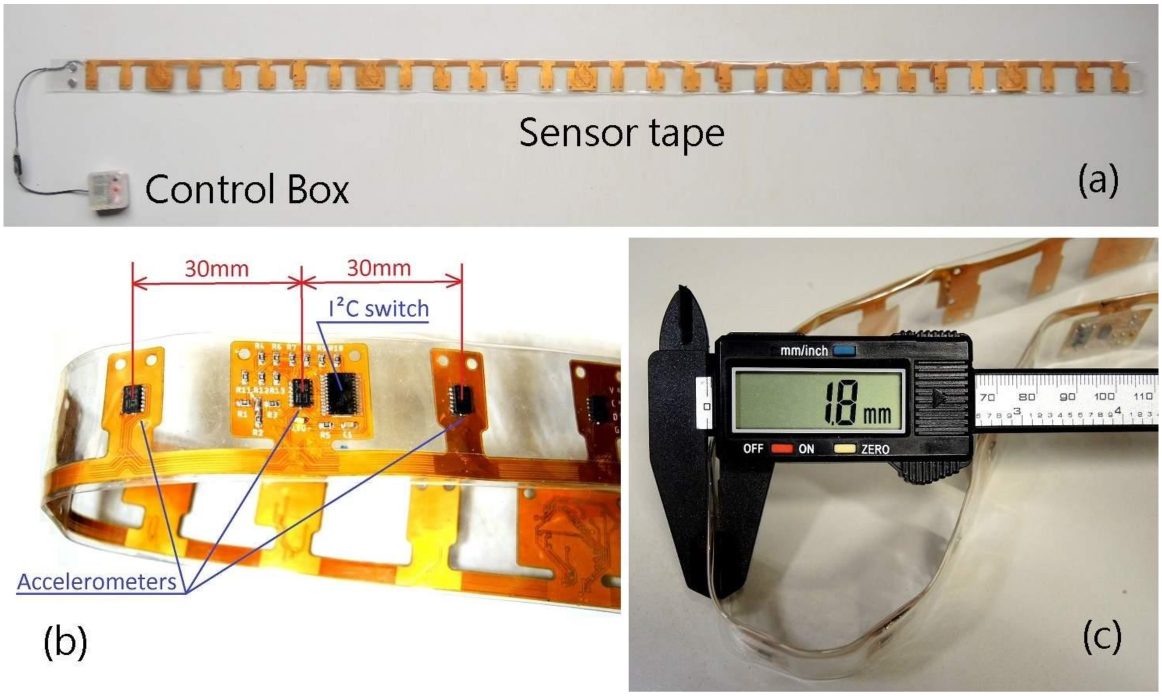

Figure 3.20. The assembled sensor tape (Hong et al., 2022). (a) The sensor tape was placed flat; (b) A part of the sensor tape; (c) Thickness of the sensor tape.

3.1.6.2 Customized circuit board for the control box

Considering the control box has integrated several modules with complex wiring, another printed circuit board was developed to reduce the control box size. The circuit diagram is shown in Figure 3.21; this is a multi-function circuit board based on the description in Section 3.1.3.2. The electronic circuit contains an ATMEGA328P MCU and peripheral chips and elements such as the real-time clock, Micro-SD adaptor, WS2812b RGB-color LED indicator, voltage regulator, and a lithium battery charging controller. The OLED display unit and the Bluetooth module can be connected to the MCU's digital input/output ports.

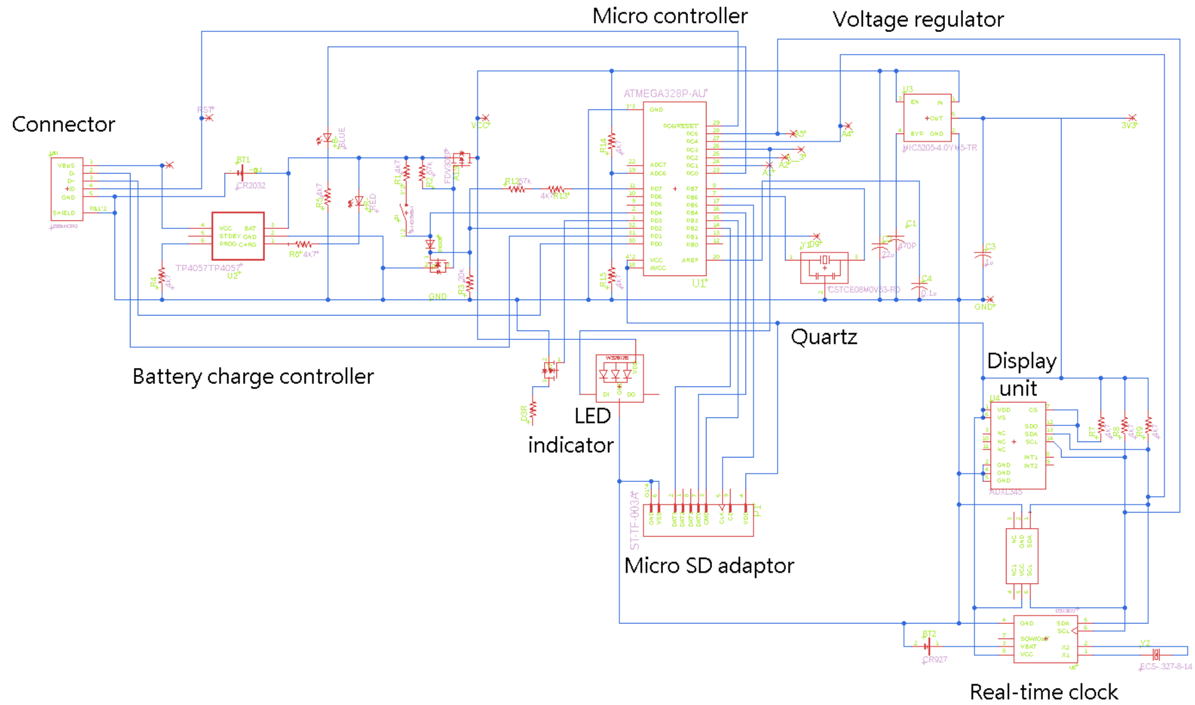

Figure 3.21. Circuit diagram of the improved control box.

The printed circuit boards were produced by JLCPCB (Jlcpcb, Shenzhen, China). The PCB was made to 28 × 28 mm, with a 0.8 mm thickness (Figure 3.22) that can be installed in a 3D printed control box.

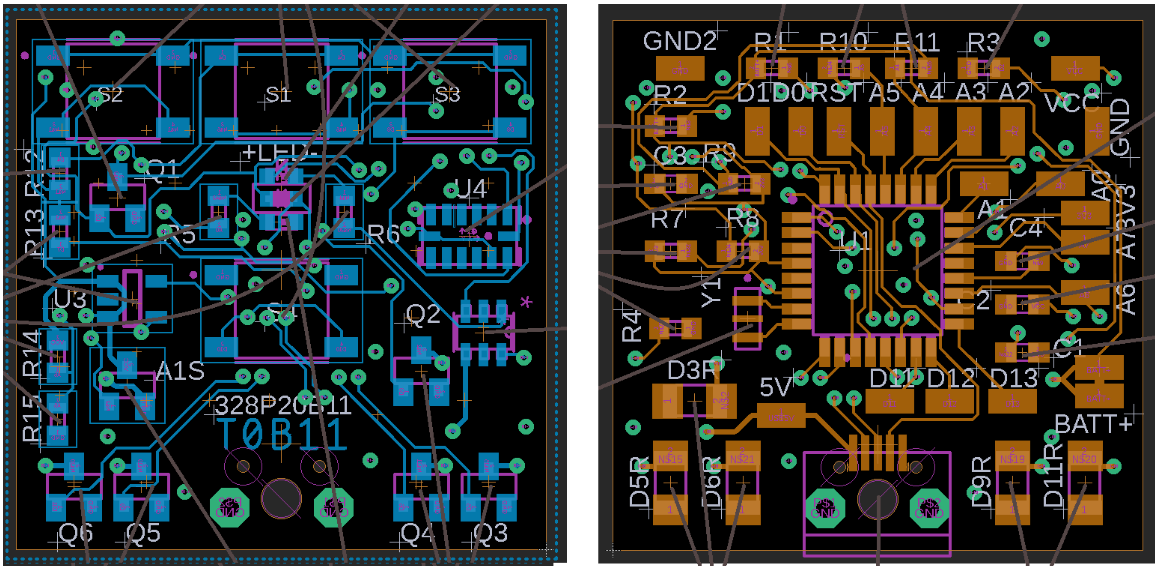

Figure 3.22. Design of the printed circuit board for the control box.

3.1.6.3 Improved algorithm

The preliminary version of curvature tape used 30 mm length rigid sensor units. The algorithm restored the measured curvature by the connection of thirty lines. However, as discussed in Section 3.1.5.4, the rigid sensor units cannot fit well on curved surfaces. Hence, the base of the sensor tape was changed to FPCs.

The new sensor tape conforms well to the surface being measured. A new algorithm was developed for the unique design of sensor tape. As shown in Figure 3.23, the measuring curvature was divided into multiple arcs based on the nodes of sensor units, and two adjacent sensor units sensed an arc.

Multiple sensor units (U_1-U_n) were located on the sensor tape; the distance between two adjacent sensor units was fixed. The measuring curvature was split into numerous arcs, with the sensor units situated at the ends of the arcs. A pair of accelerometer units measure the tangent of endpoints of the conjunction arcs, and the arc length can be calculated; based on the measured starting and ending points and the arc length, the geometry of the arc can be reconstructed.

Figure 3.23 shows a curvature constructed of arcs. The accelerometer units detect the tangent angles as the output value of the pitches. Accelerometer units U_1 and U_2 sensed their inclinations in $pitch_1$ and $pitch_2$, which measures the geometry of arc_1. The coordinates represent by the starting point of arc_1 (x_1, y_1), the midpoint of arc1 (x_{1m}, y_{1m}), and the ending point of arc1. The ending point of arc1 is also the starting point of arc_2, defined as (x_2, y_2). This algorithm quantifies the measured curvature using a series of coordinates.

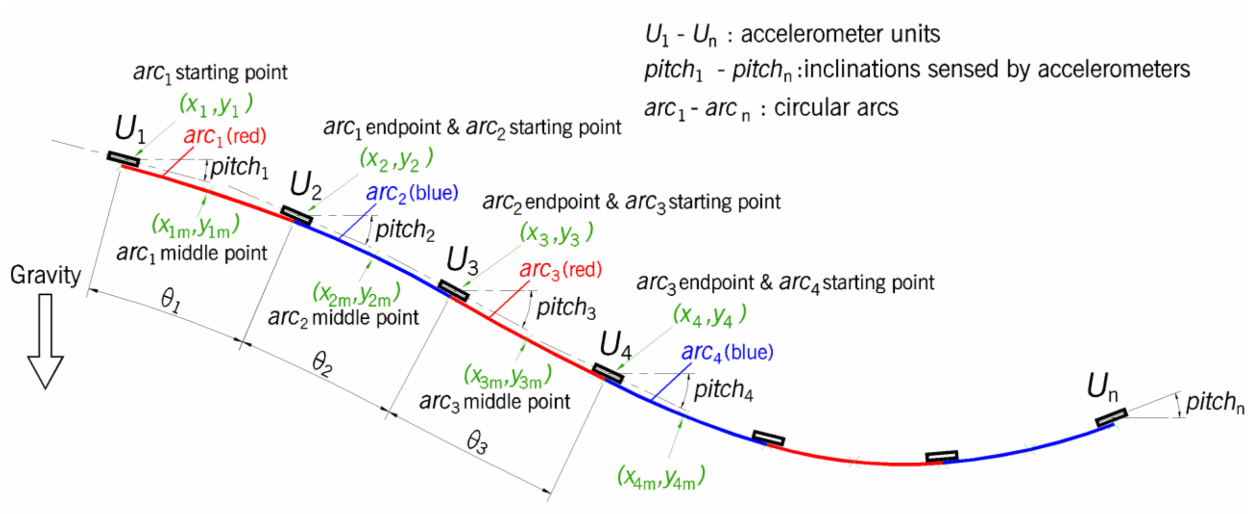

Figure 3.23. The design concept of the curvature measurement tape (Hong et al., 2022).

The Arduino language was used to program the microcontroller. The sensor tape has an integration of 30 sensor units; the sensor's output signal was collected by the microcontroller through the I^2C switch and conducted deviation correction of each sensor by sequence. The output signal was converted to Euler's angle, and inclinations were sent to the computer via Bluetooth. The accelerometer outputs static gravitational accelerations in three axes: G_x, G_y, and G_z. The program uses Euler's equations to convert the three-axis data into pitch and roll angles. In this design, pitch value was adopted to calculate the tangent of the arc. The calculation of pitch was based on equations (3):

$$\boldsymbol{pitch} = \mathbf{arctan}\left(\frac{G_y}{\sqrt{G_x^2 + G_z^2}}\right) \tag{3}$$

With the Processing software platform (Processing 3.1, Casey Reas and Ben Fry, USA), a software package was developed to process the data from the curve measurement tape. The software package processed the data collection process via the Bluetooth interface, and the graphical user interface was used to display the curvature of the sensor tape in real-time. The angle (θ) between the two accelerometers can be calculated using equation (4):

$$\boldsymbol{\theta = pitch_n - pitch_{n+1}} \qquad (4)$$

The adjacent sensor units has a fixed distance as 30 mm. When measuring an arc, the 30 mm distance becomes the chord length of the arc, as shown in Figure 3.24. Therefore, the distance between two nearby accelerometers was defined as the length of the chord (Lc). It can be calculated using equation (5):

$$\boldsymbol{L_c = \frac{sin\frac{\theta}{2} \times Arc \times 360}{\theta \times \pi}} \qquad (5)$$

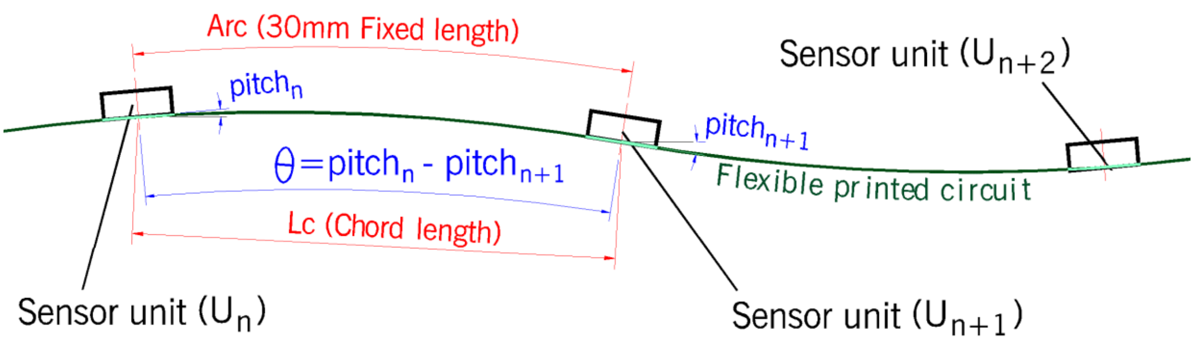

Figure 3.24. Illustration of chord length calculation (Hong et al., 2022).

The coordinates were used to draw a curve on the graphical user interface (GUI) to represent the sensor tape's shape. For further analysis, data were recorded in the format of AutoCAD script. The unit of output data presents a straight line or an arc with three points (X_{start}, Y_{start}, X_{mid}, Y_{mid}, X_{end}, and Y_{end}), and the entire curve is represented by the connection of 29 circular arcs or straight lines (Hong et al., 2022).

3.1.6.4 Management of axial tilt

This study defined the axial tilt as the inclination of the sensor tape along its length axis, as shown in Figure 3.25. Since the accelerometer cannot measure yaw, a sizeable axial tilt may affect the device's measurement accuracy, so it should be monitored. The longitudinal direction of this device is the x-axis of the sensor unit, which is the roll inclination angle. It can be calculated with the following equation:

$$\boldsymbol{roll} = \mathbf{arctan}\left(\frac{-G_y}{G_z}\right) \qquad (6)$$

The sensor tape was located between the sleeping support system and the volunteer's back and used in a covered environment so that the sensor twist could not be visually observed. When the sensor tape is twisted, the sensor unit in the relevant part will be detected with a significant axial tilt value. The axial tilt value will be displayed in the GUI in real-time to monitor the status of the sensor tape.

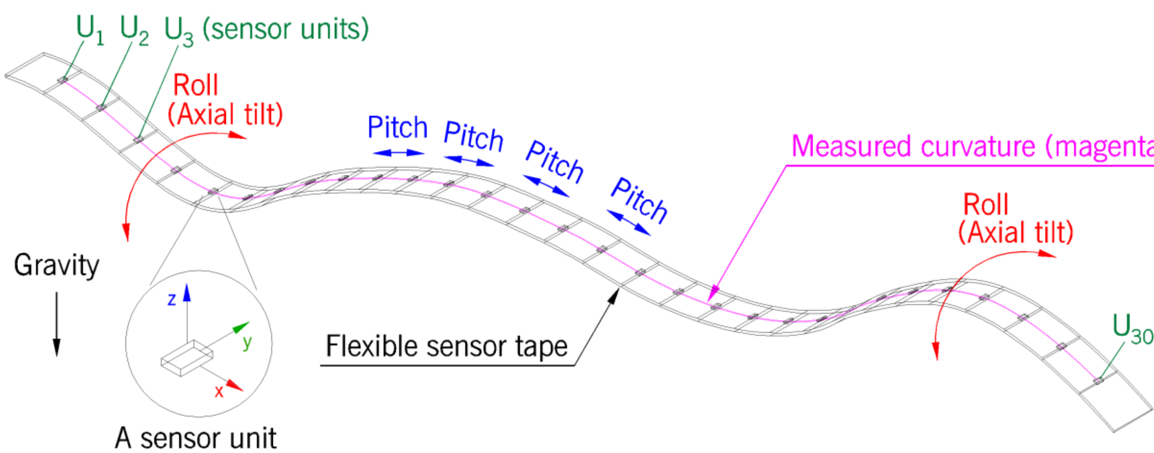

Figure 3.25. Illustration of the axial tilt (Hong et al., 2022).

3.1.6.5 User interface development

The new GUI was improved from the preliminary version. Due to the updated algorithm, the system depicted 29 straight lines or arcs based on the data obtained from 30 sensors (Figure 3.26(a)). The GUI displays a simplified curvature, in which an arc is instead by two connected lines to save computer power. Another noticeable modification of the improved GUI is the addition of axial tilt management.

The participant name or job name can be entered at the upper part of the GUI, which can facilitate future data tracking; The participant's posture and the mattress used in the experiment can be picked and recorded at the bottom left of the GUI. A combination of arrows at the bottom right of the GUI provides the zoom and pan function to scale or move the depicted curvature to facilitate direct observation.

The sensors sensed the three-axis gravity value, calculated the roll, and displayed it on the GUI. In the case of abnormal axial tilt detected, the system will alter the operator. Figure 3.26(b) shows the four manually tilted sensors. The corresponding sensors (U_7, U_8, U_9, and U_{10}) with abnormal axial tilts were marked on the GUI (Figure 3.26(a)).

A cross in red color was drawn at the corresponding sensor position of the curvature, and a red square was displayed at the bottom of the GUI to remind the operator of the abnormal axial tilt. The acceptable range of tilt angle was estimated through a tilt test, and the results are shown in Section 3.1.7.1.

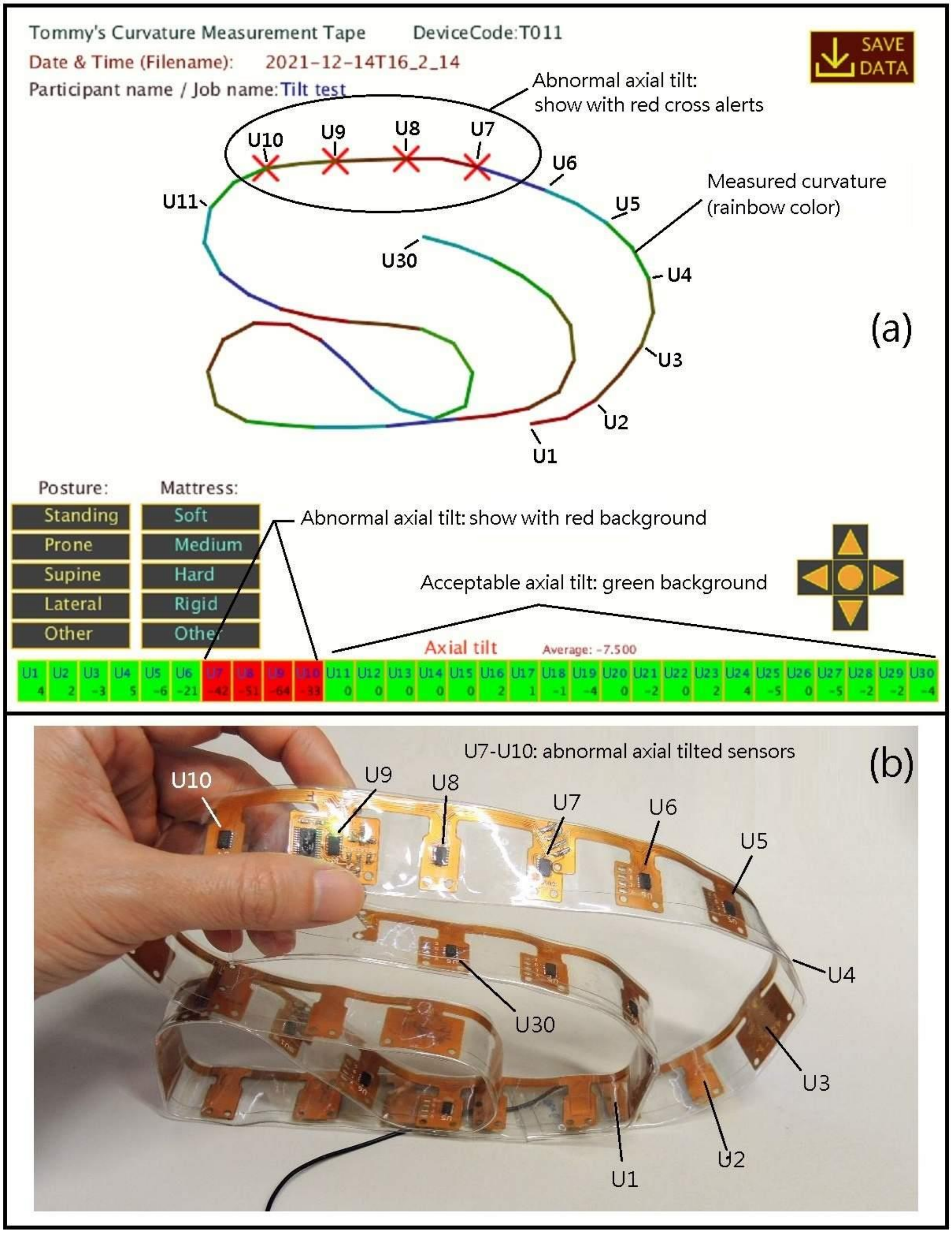

Figure 3.26. The improved graphical user interface and the sensor tape (Hong et al., 2022). (a) The measured curvature, which the placement of the sensor tape is shown in (b), with four sensors (U_7, U_8, U_9, and U_{10}) under excessive axial tilt; (b) The sensor tape with four sensors undergoes excessive axial tilt (U_7, U_8, U_9, and U_{10})).

3.1.6.6 System calibration

Since the ADXL345 accelerometer is a low-price low-end inertial sensor shipped uncalibrated, calibrations should be performed to enhance the measurement accuracy. From the introduction of the official datasheet and the sensor test results, it can be found that the accelerometers' inherent error mainly comes from the zero-gravity offset and the sensitivity deviation, as shown in Figure 3.27.

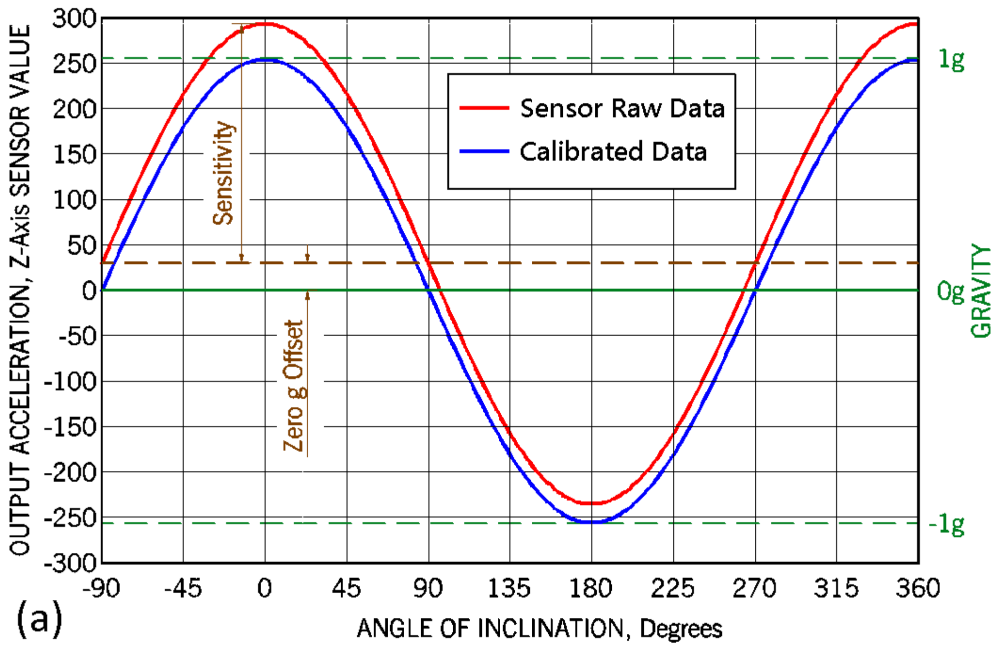

Figure 3.27. A sample graph of sensor inherent bias (red) and calibrated data (blue).

The zero-gravity offset represents the sensor reading in no gravity condition; its theoretical value is zero, but a shift may appear in the measured value. The sensitivity offset is the instrument error of the measurement range; when measuring ± 1g gravity, the output value of the unit's built-in analog-to-digital converter should be ± 255, but the measurement value may be scaled. The bias of all axes should be compensated separately by the program using the following formula.

$$\boldsymbol{G_{out} = G_{raw} \times S_c + O_c} \quad (7)$$

The zero-gravity offset was compensated using the parameter ***Oc***. With proper compensation, the sensor outputs zero in no gravity situation. The sensitivity error was calibrated using the parameter ***Sc*** to enable the sensor output at 255 under 1 g gravity and -255 under -1 g gravity.

When assembling the sensor to the FPC, the bottom of the chip may not be ideally parallel to the plane of the bottom of the FPC, and the part may rotate slightly. The SMT mounting of the accelerometers may lead to some angular misalignment. The assembled sensor tape should be calibrated to correct assembly errors and enhance measurement accuracy. A simple correction tool was developed, as shown in Figure 3.28; the whole sensor tape was installed on a rigid bar, with all sensor units in the same alignment. When the correction device was placed horizontally, the program was used to correct the output angle value to 0°; When the correction device was placed vertically, the system output angle value was converted to 90°.

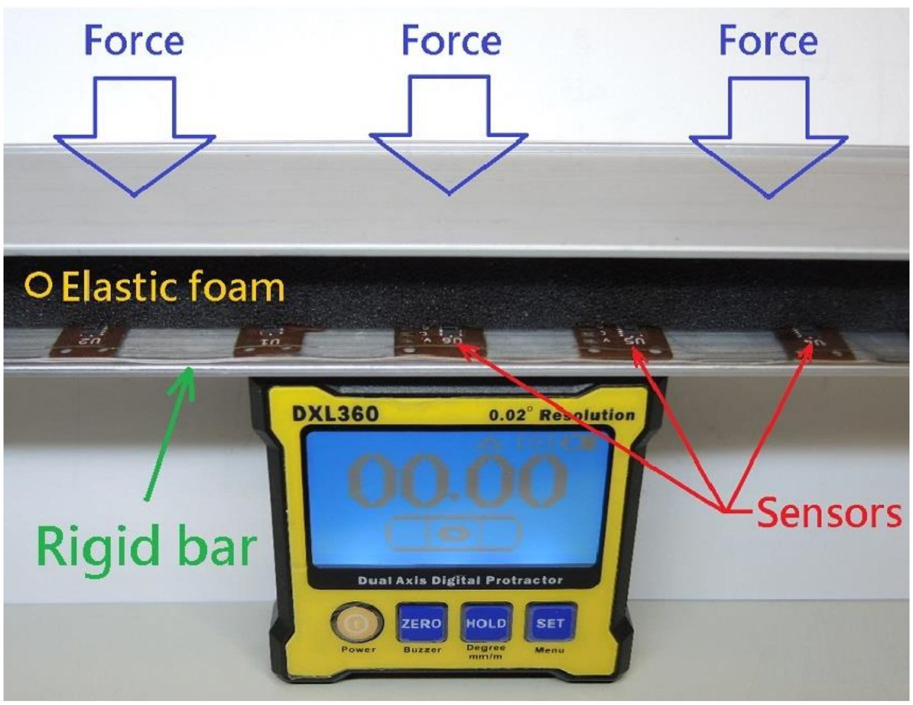

Figure 3.28. Design of the sensor tape calibration.

3.1.7 Device verification and validation

The device was validated and validated before it was put into use. The purpose of validation and validation was to understand the curvature measurement tape's ability to measure spinal curvature. Tests were performed to understand the device's accuracy, reliability under an axial tilt, and acceptance of axial tile value. Experiments were conducted to evaluate the device's reliability and repeatability.

3.1.7.1 Management of axial tilt

A MEMS accelerometer can detect its inclination, including pitch and roll, but cannot detect yaw. Therefore, if the sensor tape's measurement plane is perpendicular to gravity's direction, the system will not work. In this study, while the measurement plane is parallel to gravity's direction, the axial tile is defined as 0°; if the measurement plane is perpendicular to the direction of gravity, the axial tilt is 90°.

This study developed a circular mount based on 3D printing. The circular base was adopted to understand the measurement capabilities of the sensor tape under various axial tilt angles. The outer diameter of the circular mount is 200 mm, and the sensor tape can be wrapped around it (Figure 3.29(a)). The bottom of the circular base was mounted on a three-axis digital protractor (DXL-360, Jinyan Company, Shenzhen, China) to create a controlled axial tilt environment (Figure 3.29(b)). The circular mount can be rotated along its vertical plane for different axial tilt angles under control (Figure 3.29(c)). The sensor tape was axially tilted from the angle of 0° to 80° at 10° intervals with an accuracy of ± 1° to understand the measurement ability of the system under different axial tilt angles.

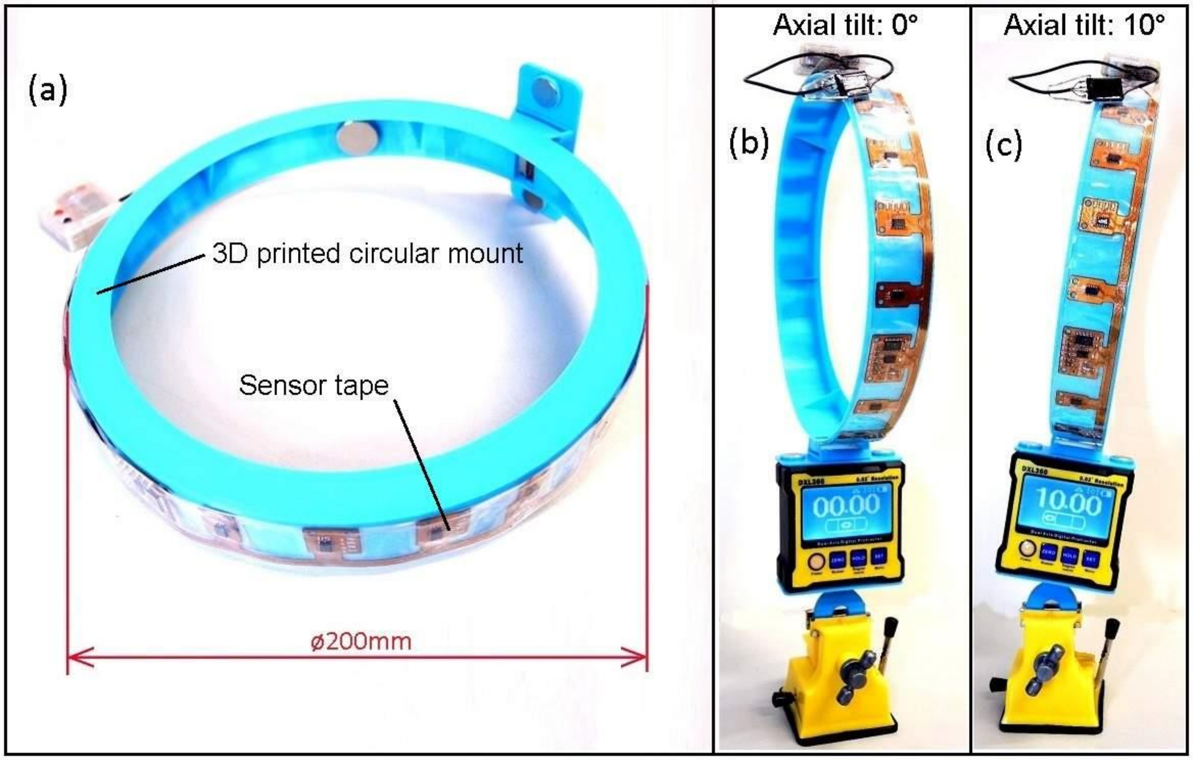

Figure 3.29. The design of circular mount and demonstration of axial tilt test (Hong et al., 2022). (a) Design of the circular mount and the curvature measurement tape; (b) The circular mount and the curvature measurement tape mounted on a digital protractor with 0° axial tilted; (c) The set with a 0° axial tilted placement.

This test aims to understand the device's ability to measure at different axial tilt angles. The circular mount was placed at different angles of axial tilt, the curvature installed on the circular mount was tilted axially, ranged from 0° - 80° at an interval of 10° with ± 1° accuracy, and ten measurements were taken at each value of axial tilt. The sensor tape was randomly attached to the circular base for a measure, removed after the measurement, and reinstallation is required for another test. The acquired sensor data was sent to the computer and restored to a curve with CAD software (AutoCAD-R13, Autodesk Incorporated, California, USA). Under ideal circumstances, the measured curvature is the same as a ø200 mm circle. Figure 3.30 shows one curve for each tilt angle tested from 0° to 80° of axial tilt. Under a slight inclination, the measured curve almost overlaps the ø200 mm reference circle. While the increase of tilt angle, the curve deforms. As presented in Table 3.1, the mean value and the standard deviation (STD) of the curvature width were calculated and compared to define the acceptable axial tilt angle of the device.

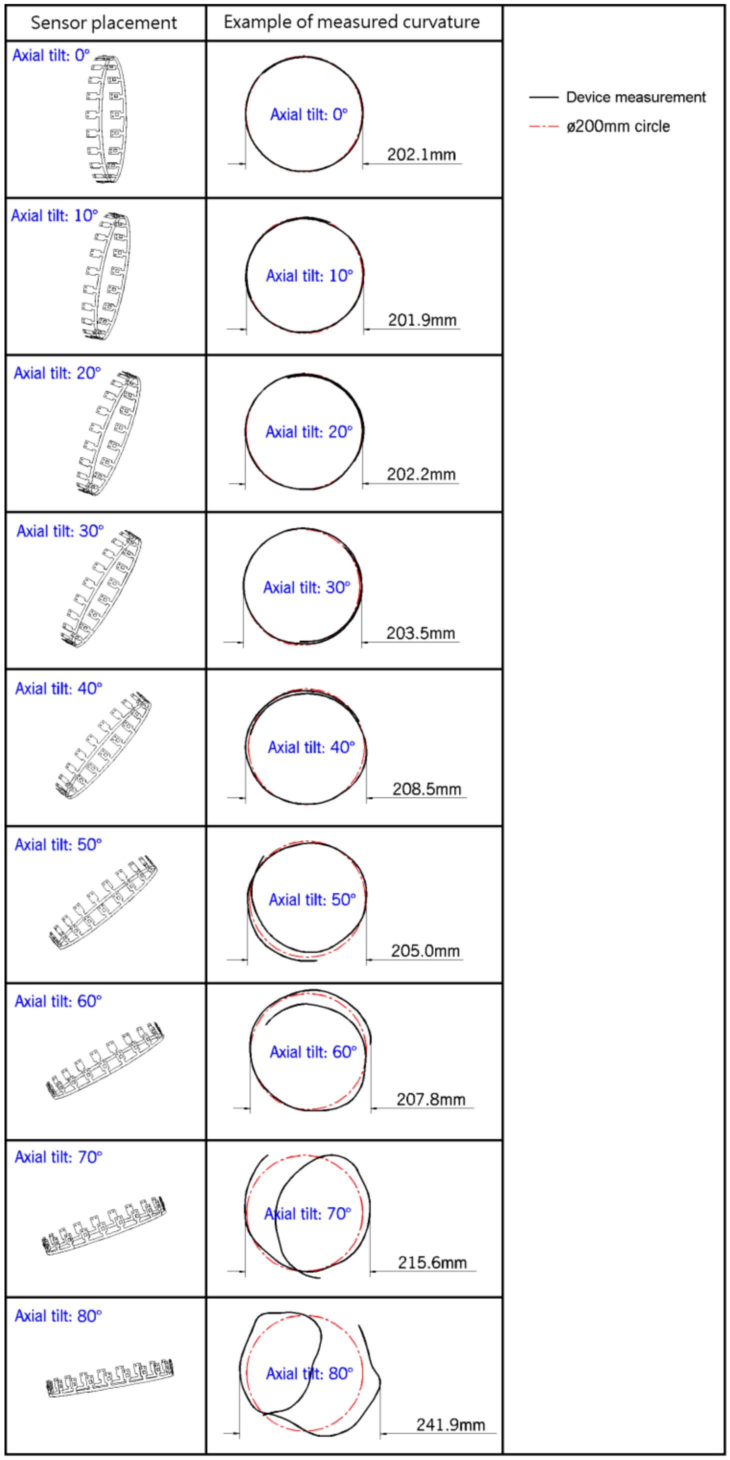

Figure 3.30. Example of a measured curvature while measuring the ø200 mm circular mount at various axial tilts.

Table 3.1. Mean value and standard deviation of the width of the circular mount at different axial tilts with ten measurements per angle (Hong et al., 2022).

Tilt value	Mean (mm)	STD (mm)	Determination
0°	201.58	0.86	Acceptable
10°	201.74	0.91	
20°	201.79	1.03	
30°	201.87	1.39	
40°	202.19	2.85	Unacceptable
50°	203.05	4.09	
60°	203.67	5.06	
70°	205.87	9.69	
80°	227.77	28.45	

The accuracy of the curvature measurement device is relatively high at axial tilts of less than 40°. The mean value of the width of the measured curves varies in the range of 201.58 mm - 201.87 mm, which is about 99% accurate compared to the diameter of the circular base. The standard deviation is between 0.85 mm - 1.39 mm, which exhibits high accuracy. A small standard deviation indicates that the data has low dispersion, and the value is usually closer to the mean. However, as the axial tilt angle increases, the device accuracy decreases. When the axial tilt angle reached 40°, the measured curve width was 202.19 mm, and the standard deviation was 2.85 mm; the standard deviation has a 105% increase compared with the 30° axial tilt. The larger standard deviation indicates a higher degree of data dispersion, which decreases the measurement accuracy. Therefore, ± 30° was set as the acceptable axial tilt range, allowing the system to work with high measurement accuracy. The occurrence of axial tilt exceeding 30° will be displayed in the GUI with a red background and red cross to alert the operator to the anomaly (Figure 3.26).

3.1.7.2 Measurement accuracy

The device's accuracy was evaluated with the sensor tape mounted on a ø200 mm circular base and set to 0° axial tilt. Figure 3.31(a) shows the results of ten repeated measurements plotted through AutoCAD. Figure 3.31(b) is the average of ten measurements plotted in blue. Compared with a ø200 mm circle by the AutoCAD software, the maximum measurement error is 2.12 mm. Therefore, the accuracy of the device is approximately 99%.

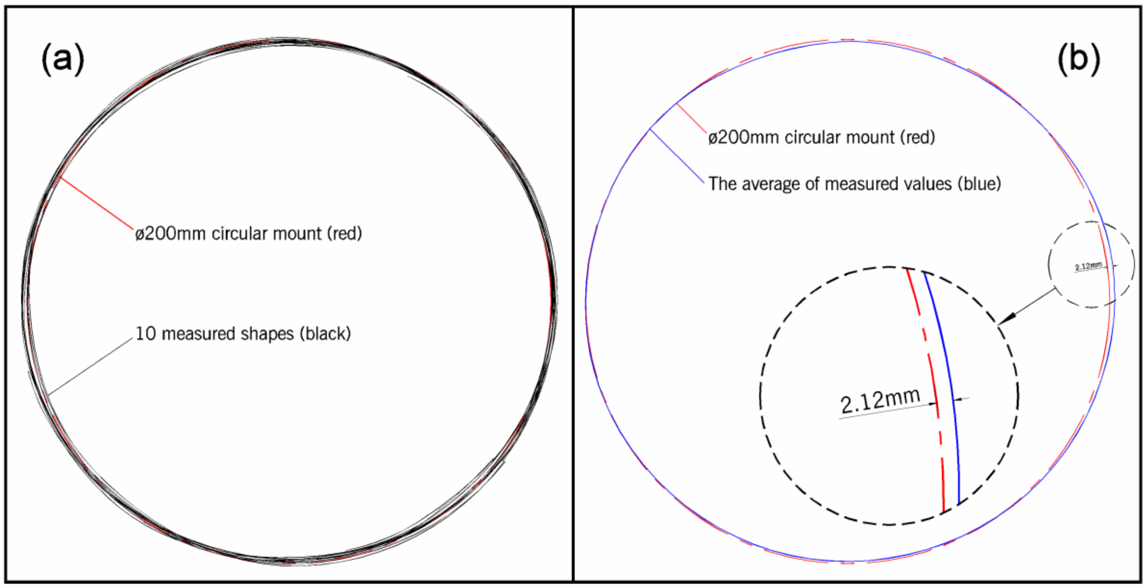

Figure 3.31. Comparison of measured curvatures (Hong et al., 2022). (a) Shapes of ten measurements; (b) Presentation of measurement errors.

3.1.7.3 Reliability

Experiments were conducted to investigate the reliability of the device. Fifteen volunteers without spinal injury, deformity, or pathology were recruited at the university, and their age was (28.6 ± 3.0 years). All volunteers could maintain a standing position with their arms extended horizontally for 5 minutes. This study was reviewed and approved by the departmental research committee of the institutional review board of the Hong Kong Polytechnic University. The reference number for ethical approval is HSEARS0020201223001. All volunteers were notified of the experimental procedures and signed the informed consent document. This experiment was carried out in the human movement laboratory of the Hong Kong Polytechnic University. Experiments include the measurement of spinal curvature in the prone position using a motion capture system and spine curvature measurement using the curvature measurement tape. The reliability of the proposed spine curvature measurement device can be understood by comparing the results of the two methods. A motion capture system with eight cameras (Vicon Nexus, Oxford Metrics Limited, Oxford, United Kingdom) was adopted to obtain the marker coordinates on the volunteer's back. A thin foam mat was located on the ground and near the center of the capture area. The width direction of the mat was parallel to the x-axis of the Vicon system. For head support, a prone pillow (PP83200073, Treasure company, Nangchang city, China) (Figure 3.32) was used and placed above the foam mat.

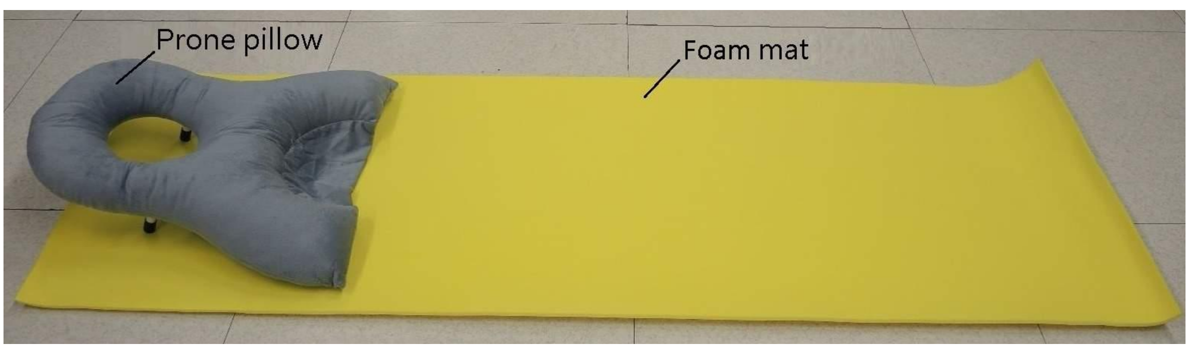

Figure 3.32. The foam mat and prone pillow.

The volunteer was shirtless or wearing tights. The swimming cap with buckle holder (Figure 3.9) was used to secure the start of the curvature measurement tape. The volunteer was lying on the foam mat in a prone position, using the prone pillow for head support and limbs aligned to the body. The curvature measurement tape was placed along the centerline of the volunteer’s back, starting from the occipital protuberance, along the spine, till or over the median sacral crest (Figure

3.33(a)). Wait till a stable prone position of the volunteer; the operator records and saves the data of the curvature measurement tape on the computer through the GUI. The curvature measurement tape was removed, followed by the placement of thirty reflective markers for the motion capture system along the volunteer's back with the same starting and ending points as the curvature measurement tape (Figure 3.33(b)). When the volunteer was in a stable prone position, the operator recorded the coordinates of all marked points through the motion capture system.

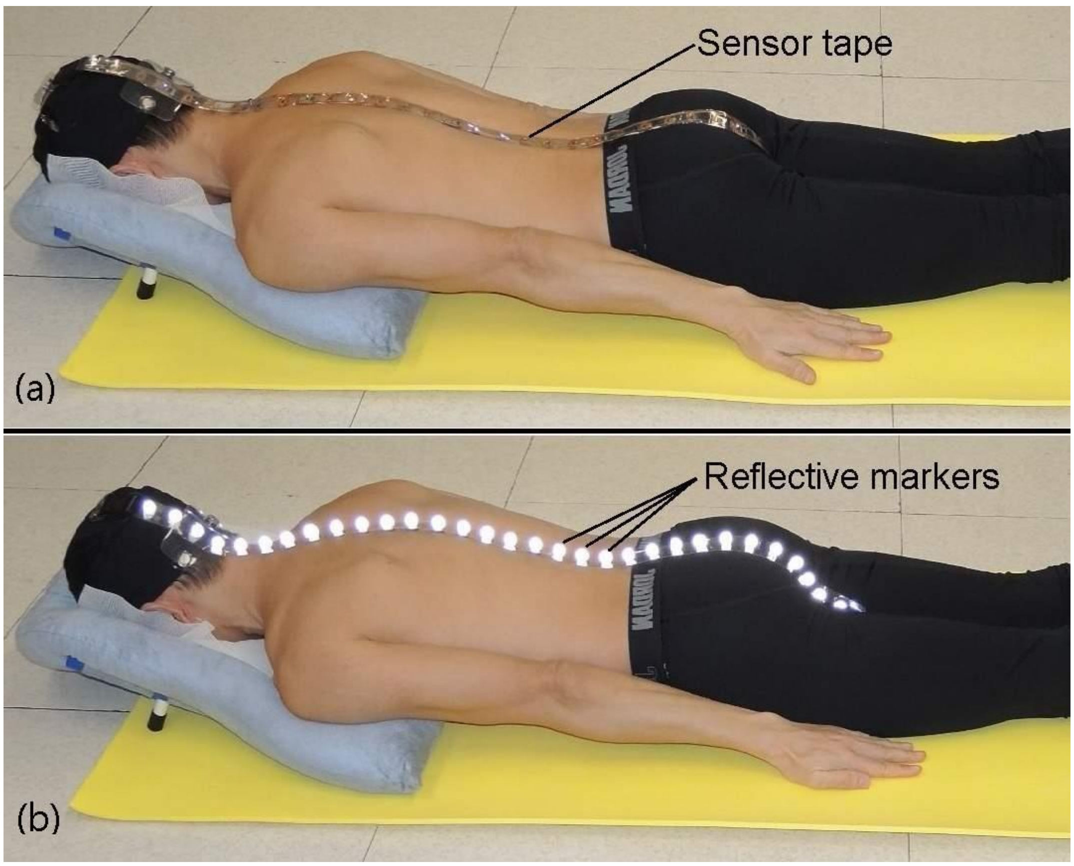

Figure 3.33. Experiments in the prone position (Hong et al., 2022). (a) The experiment of back curvature measurement by the sensor tape; (b) Placement of reflective markers for the motion capture.

Based on the measured curvature, a regression line was constructed between the occipital eminence and the median sacral crest, named body inclination (BI). The regression line represents the inclination of the head and torso. Other regression lines were created to measure the neutral curvatures of the spine. The joint of the regression lines in the cervical region creates the cervical lordosis angle (CLA), the thoracic region creates the thoracic kyphosis (TKA), and the joint of the regression lines in the thoracic and lumbar region creates the lumbar lordosis angle (LLA) (Figure 3.34).

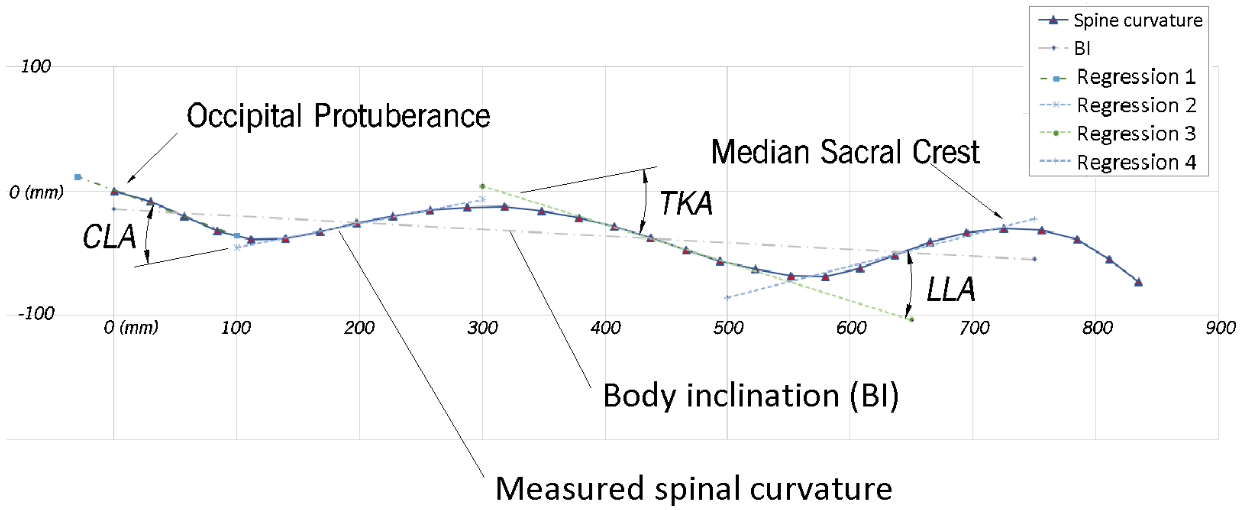

Figure 3.34. Illustration of spine parameters for device validation.

The marker coordinates captured by the motion capture system were the center of ball markers Figure 3.35, which were 14 mm in diameter and had a 7 mm offset from the marker root. For consistent comparisons between the Vicon system and the curvature measurement device, the marker roots' position was calculated instead of the coordinates of ball marker centers. Both the motion capture system and the sensor tape system use the same calculation method to obtain spine parameters, including CLA, TKA, LLA, and BI.Figure 3.35. The graphical user interface of the Vicon Nexus 2.11.

Table 3.2 shows the LLA, TKA, CLA, and BI values. The CLA: device = 32.65 ± 8.21°, Vicon = 32.08 ± 8.10°; The TKA: device = 19.90 ± 7.64°, Vicon = 19.83 ± 7.13°; The LLA: device = 23.60 ± 6.39°, Vicon = 23.70 ± 7.04°. The BI: device = 3.33 ± 10.68°, Vicon = 3.51 ± 11.10°. The parameters' results were comparable between the sensor tape data and recordings from the Vicon system. Strong correlations were found by correlation analysis between LLA, TKA, CLA, and BI (LLA: r = 0.96, TKA: r = 0.99, CLA: r = 0.97, BI: r = 0.98).

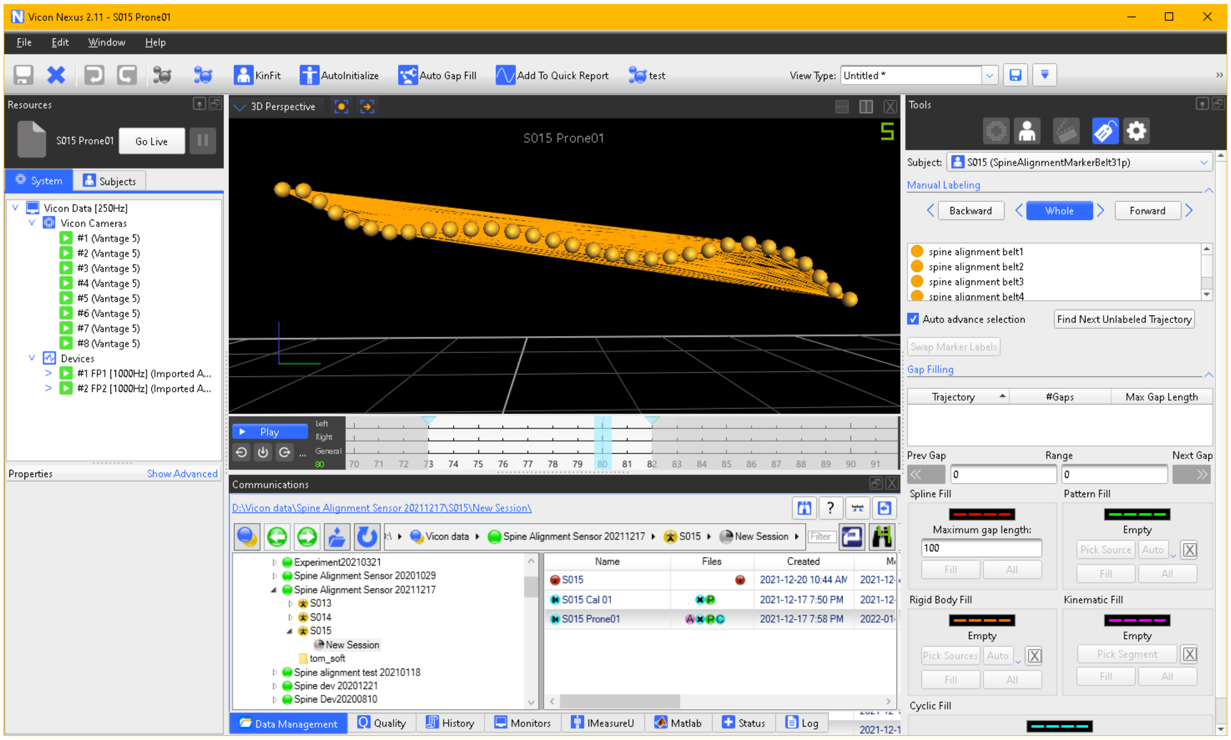

Figure 3.35. The graphical user interface of the Vicon Nexus 2.11.

Table 3.2. Comparison of data measured by the curvature measurement device and the Vicon system (Hong et al., 2022).

	Cervical lordosis		Thoracic kyphosis		Lumbar lordosis		Body inclination	
	Sensor tape	Motion capture	Sensor tape	Motion capture	Sensor tape	Motion capture	Sensor tape	Motion capture
Mean	32.65°	32.08°	19.90°	19.83°	23.60°	23.70°	-3.21°	-3.11°
Standard deviation	8.21°	8.10°	7.64°	7.13°	6.39°	7.04°	1.98°	1.94°
Minimum	21.88°	22.89°	5.69°	6.43°	12.70°	11.15°	-7.15°	-6.49°
Maximum	51.58°	51.03°	30.73°	30.24°	34.64°	35.86°	0.37°	0.41°
correlation	0.97		0.99		0.96		0.98	

Figure 3.36 shows the Bland-Altman plot results of the CLA (a), TKA (b), LLA (c), and BI (d) for the data recorded by the curvature measurement strip and the motion capture system, respectively. The differences in the data were normal distribution (Shapiro-Wilks $p > 0.05$); both curves show 95% confidence intervals, and the diagrams of the Bland-Altman plot were satisfied.

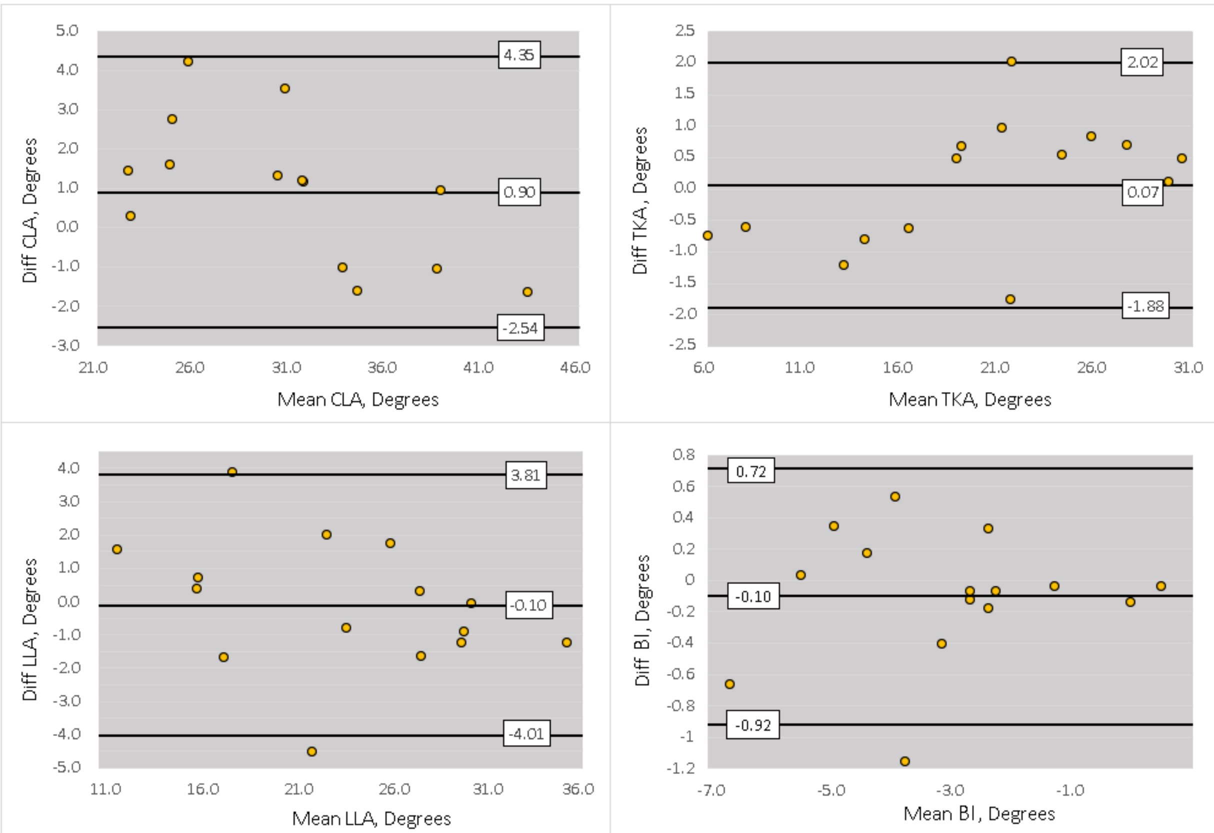

Figure 3.36. Graphically presented each volunteer's mean and difference in curvature measurement device and motion capture system (Hong et al., 2022). (a) The angle of cervical lordosis; (b) The angle of thoracic kyphosis; (c) The angle of lumbar lordosis; (d) Body inclination.

3.1.7.4 Repeatability

The repeatability test was performed by repeating measurements of the supine position with the curvature measurement device and an impression of the back. The laboratory was placed with a mattress in normal stiffness (C123B, Sinomax Limited, Guangdong, China) and a cervical pillow (CH–Pillow–TDI, Benelife Limited, Guangzhou, China). The cervical pillow was placed on the centerline of the mattress. A flexible leak-proof plastic sheet covers the sleeping support system to avoid leaks. Four layers of plaster bandages (P-20066, 3M Company Limited, St. Paul, USA) were placed above the plastic film (Figure 3.37(a)). The volunteer was lying in a supine position, the cervical pillow supported his head, and his legs were stretched and relaxed, with arms paralleled with legs in the sagittal plane. Wait until the cure of plaster bandages to complete the impression of the volunteer's back geometry. Remove the plaster bandage and place the curvature measurement tape on the sleeping support system. Fifteen repeated measurements of the volunteer's spinal curvature using the curvature measurement tape. The data collection procedure was conducted with the volunteer lying relaxed in a supine position. The shape of the plaster bandage (Figure 3.37(b)) was captured by a 3D scanner (HandySCAN-700, Creaform Limited, Quebec, Canada), and the obtained parameters were compared with the results from the curvature measurement tape.

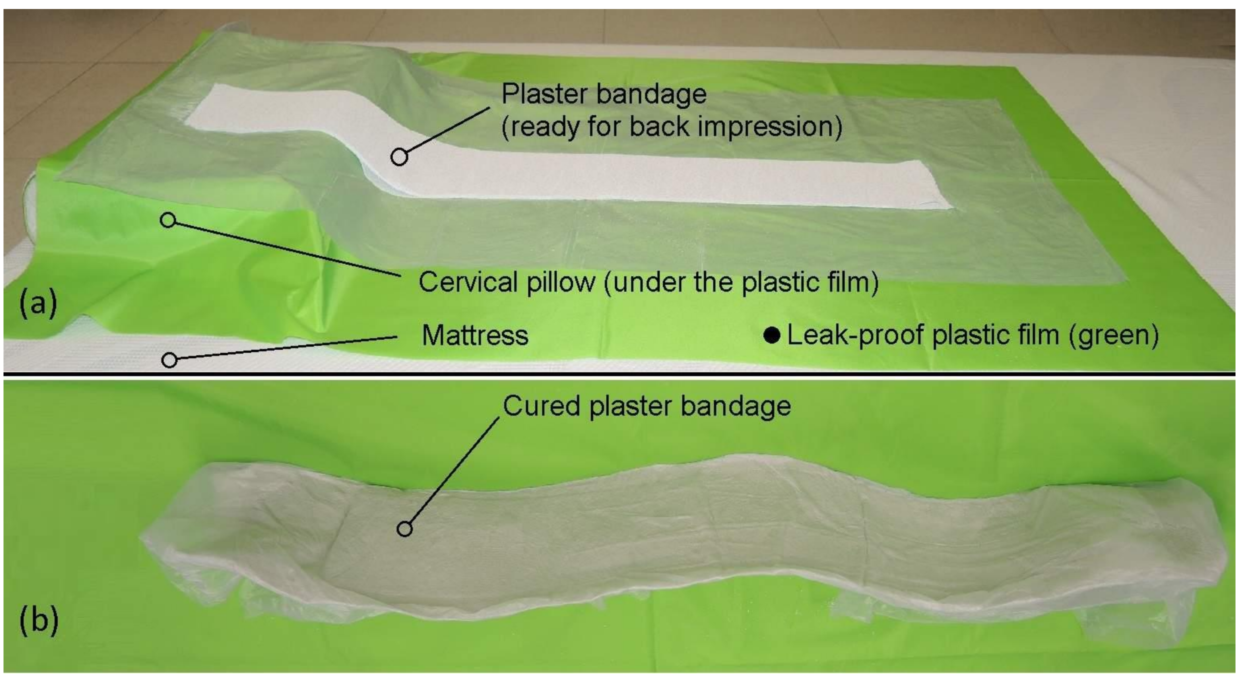

Figure 3.37. Experiment design (Hong et al., 2022). (a) The setup for back impression; (b) The cured plaster bandage.

The repeatability study was conducted with repeated measurements of the spine parameters in the supine position. The volunteers' backs were cast with plaster bandages, the cured plaster bandage was captured with the 3D scanner, and the spine parameters were compared using AutoCAD software. Spine parameters of back impressions were: LLA = 15.17°, TKA = 33.15°, CLA = 36.04°) and angles measured by the curvature measurement tape were: LLA = 15.64 ± 1.12°, TKA = 32.48 ± 0.98°, CLA: 37.63 ± 2.24°) show a high degree of similarity. Figure 3.38 shows that the correlation analysis exhibited a significant linear relationship between the plaster impression and the device measurement. ($r = 0.98$). A Pearson's correlation coefficient of 0.7 to 1.0 represented a strong positive linear relationship through a firm and linear rule (Ratner, 2009).

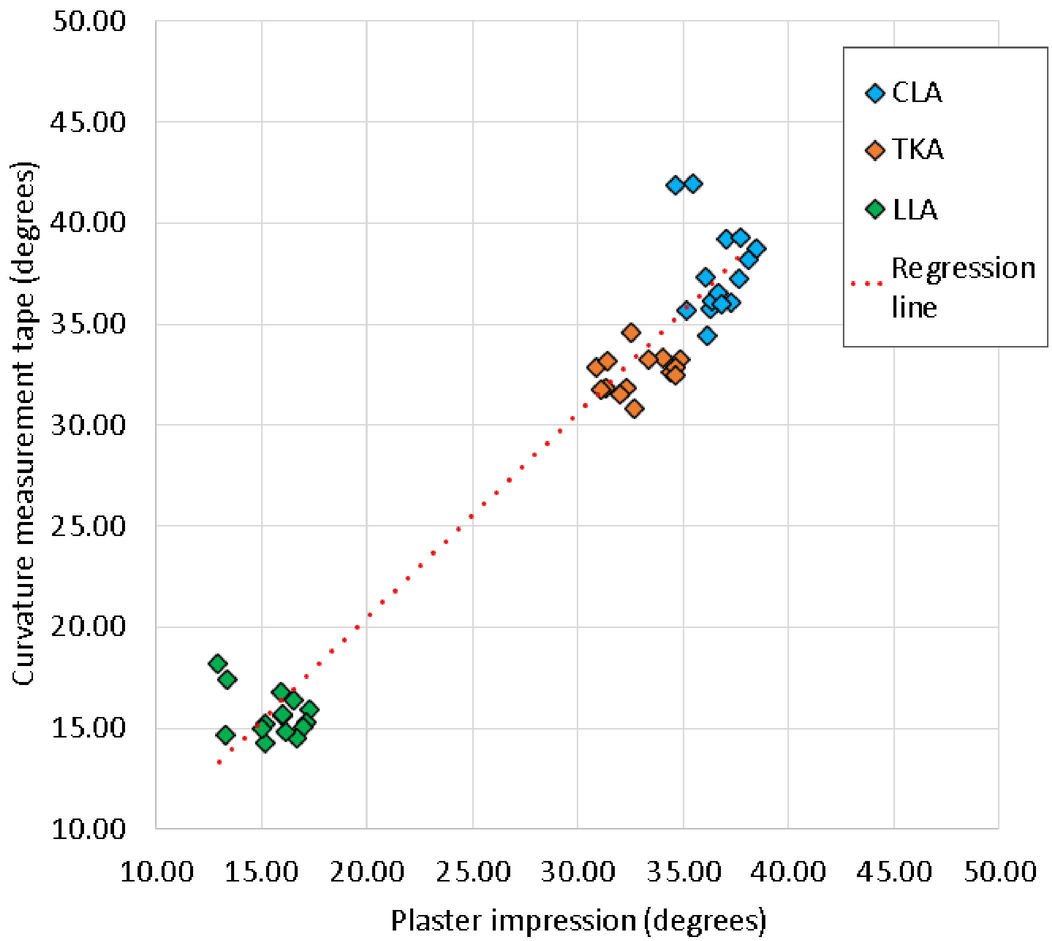

Figure 3.38. Jitter plot results for correlation analysis.

3.2 Experimental design

Previous studies have suggested that mattress stiffness affects spinal curvature, but the curvature in the supine position has less been quantified and described. Moreover, mattress support research was generally concentrated in the C7 to L5 vertebrae, excluding the craniocervical region. Therefore, experiments were conducted to quantitatively measure and depict the whole spinal curvature of lying supine on mattresses of different stiffness to understand the relationship between the mattress stiffness and spinal curvature.

3.2.1 Volunteers

Sixteen volunteers participated in this experiment through the university platform. All volunteers had no history of spinal injury, deformity, or pathology. All volunteers were able to remain standing with their arms extended horizontally for more than 5 minutes. Volunteers' height, weight, age, and BMI were 1.703 ± 0.078 meters, 64.8 ± 13.6 kilograms, 29.4 ± 5.1 years old, and 22.2 ± 3.4. This research was reviewed and approved by the departmental research committee of the Hong Kong Polytechnic University. The tracking number for the ethical approval is HSEARS0020201223001. The experimental procedures and signed informed consent forms were delivered to all volunteers.

3.2.2 Materials

A mattress manufacturer supplied three polymer foam mattresses (C122A / C123B / C105H, Sinomax, Shenzhen, China) of different stiffnesses. The manufacturer considers them representatives of a hard mattress (HM), a medium mattress (MM), and a soft mattress (SM). The 25% compression indentation load deflection (ILD) for mattress materials was HM: 120 lbs, MM:

42 lbs, and SM: 20 lbs. These three mattresses have the exact dimensions of 1900 × 1200 × 200 mm. A common shape cervical pillow (TDI-0553511, Infinitus Company Limited, Guangzhou, China) was used in this research to create a familiar sleep environment. The appearance and dimensions of the pillow and mattress are displayed in Figure 3.39.

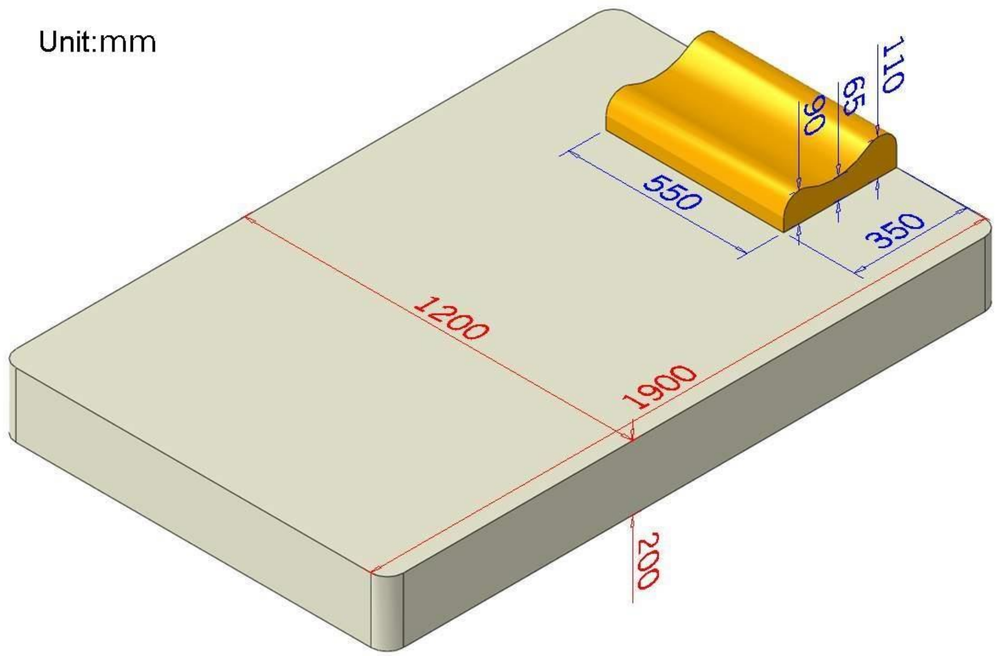

Figure 3.39. The appearance and size of the mattress and pillow.

3.2.3 Equipment

Existing techniques are challenging to measure the spine morphology in the supine position in an effective way. Therefore, this study developed the curvature measurement tape to measure the covered curvature. This experiment adopted this self-developed curvature measurement tape to obtain the spinal curvature in the supine position. This device has been validated in Section 3.1.7, and we believe it can effectively measure spinal curvature in the supine position. The measurement length of the sensor tape is 870 mm, which is long enough to measure the whole spine of a human body. This device integrates 30 small and thin MEMS accelerometers to measure

29 lines or arcs. The improved algorithm converts the sensor data to circular arcs or lines, connecting them into a curvature. The measurement data can be quantified and analyzed by CAD software. This FPC-based sensor tape is thin and flexible, with limited interference with sleeping positions. When measuring a ø200 mm circle, the dimensional accuracy is approximately 99% (Hong et al., 2022).

3.2.4 Experimental procedures

Human experiments were conducted to quantitatively measure the spinal curvature using the curvature measurement tape to compare the spinal curvature under mattresses with different stiffnesses. Figure 3.40 shows that the three mattresses were placed parallel on the laboratory floor, and the cervical pillow was placed on one of the mattresses.

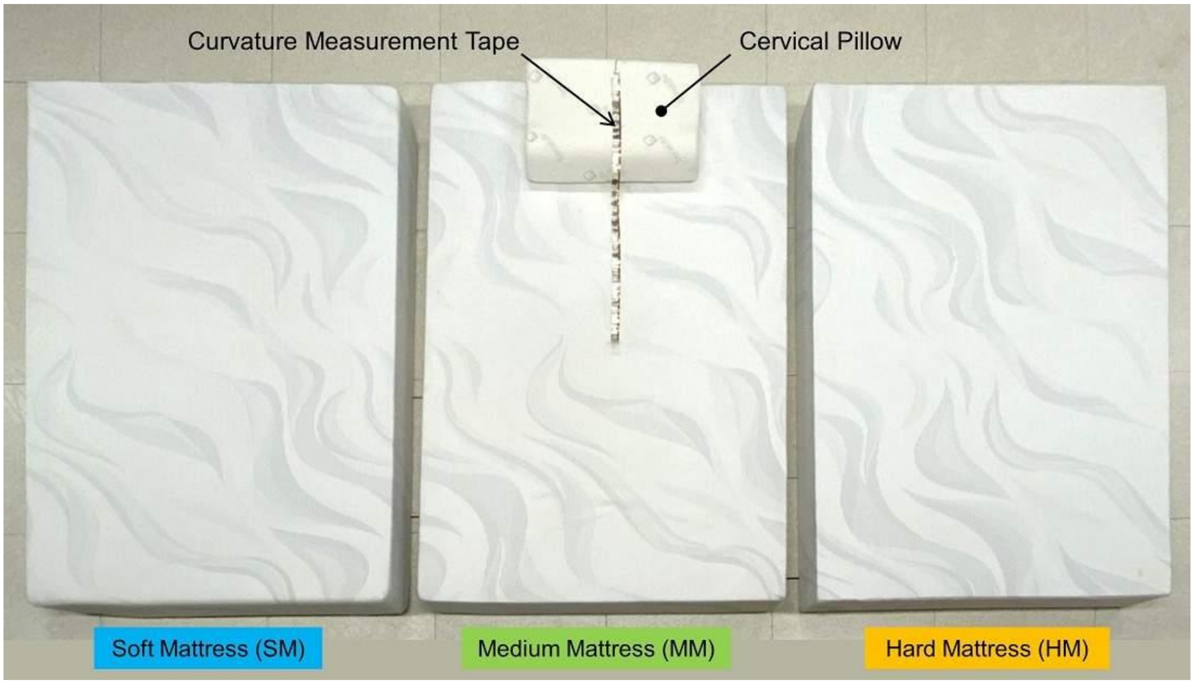

Figure 3.40. The placement of mattresses for the experiments, with the pillow and curvature measurement device on the middle mattress (Hong et al., 2022).

The curvature measurement tape was located on the centerline of one of the mattresses and pillow to measure spinal curvature (Figure 3.41(a)), and Figure 3.41(b) shows the GUI with a measured curvature. Considering that insufficient deformation of the hard mattress may result in a gap between the lumbar lordosis and the top of the mattress, a soft foam was placed below the sensor tape to secure that the sensor tape was in contact with the volunteer's back. Volunteers wore tights or were topless and laid on the sleeping support system in a supine position. Their limbs were aligned to the body. After the volunteers' postures were stabilized, their spine curvatures were obtained through the curvature measurement tape, and the quantified data was stored on a computer. Data collection procedures were repeated on three mattresses based on the randomized crossover trial. The software package represents the spinal curvature by connecting 29 arcs or lines, each with three points (X_{start}, Y_{start}, X_{mid}, Y_{mid}, X_{end}, and Y_{end}) representing a part of the spinal curvature. The data was loaded into CAD software for analysis in the post-processing stage.

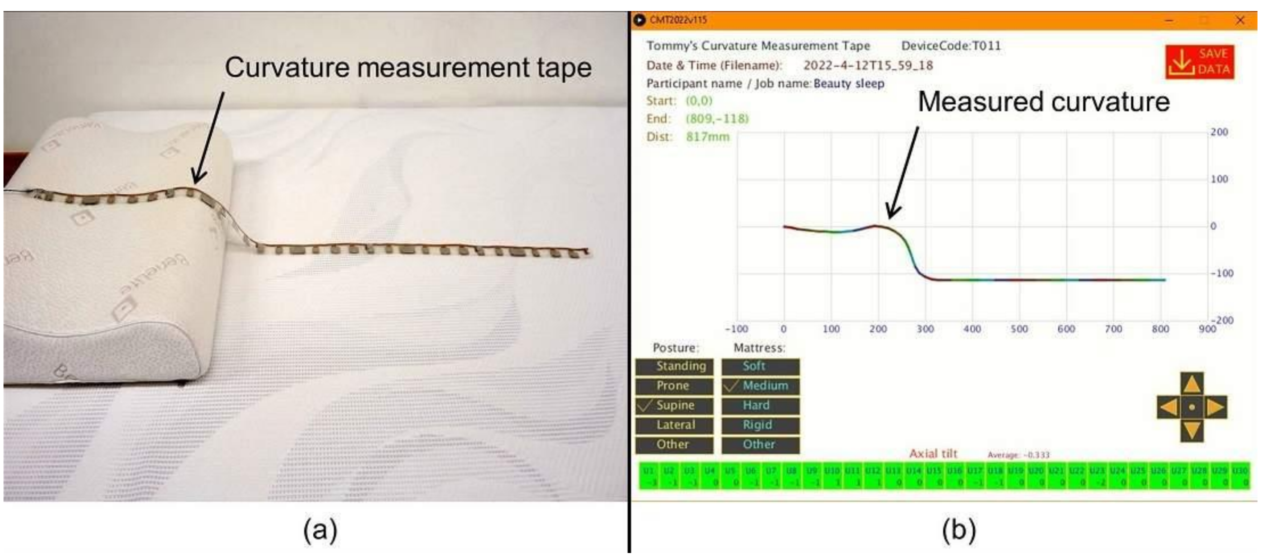

Figure 3.41. Close-up of the experimental setup (Hong et al., 2022). (a) The placement of the sensor tape; (b) The customized graphical user interface.

3.2.5 Spine parameters

Spine parameters were defined in terms of the displacement and deformation of the spine alignment in the sagittal plane. When lying down, the body may have different inclinations based on the stiffness of the mattress (Haex, 2004). Therefore, based on the measured curvature of the spine, as shown in Figure 3.42, a line was linked to the tangent point of the thoracic kyphosis and the sacral kyphosis, which represents the torso inclination (TI). The distance from the rear head to TI was described as head distance (HD), the distance from cervical lordosis to TI was described as cervical lordosis distance (CLD), and the distance from lumbar lordosis to TI was described as lumbar lordosis distance (LLD).

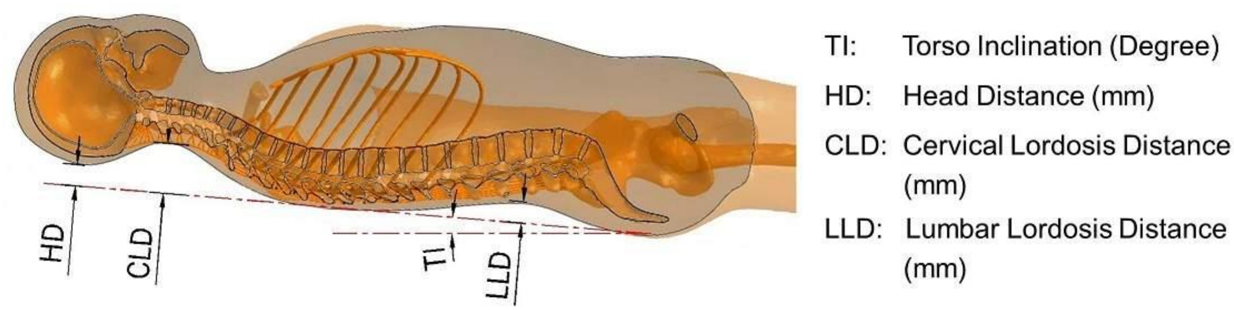

Figure 3.42. Illustration of spinal parameters (Hong et al., 2022).

3.3 Computational simulation

Several human finite element (FE) models were developed and applied for biomechanical analysis, including forces and deformations of the internal structure of the human body. FE models with cervical ligaments (Barker & Cronin, 2020; John et al., 2019; Nikkhoo et al., 2019; Zafarparandeh et al., 2014) and lumbar spine (Bojairami et al., 2020; Zhang et al., 2021) were developed to simulate quasi-static loads. These models were targeted to understand the spine's internal changes under external loads.

Recently, FE models that integrate sleeping support systems and the human model were developed for sleep analysis. These models involved a two-dimensional FE model (Yoshida et al., 2012) that analyzes soft tissue loading to evaluate the impact of mattresses on sleep comfort. Another set of FE models of the human body contour (Lee et al., 2017) was created, with the geometry obtained based on a 3D scanner. The study reported the ability of a FE model to predict the pressure distribution between the body and the bed in the supine position. However, the absence of internal structures such as bones and ligaments may dispute the reliability of the simulation. Overall, the FE models developed in these studies usually with a high degree of simplification. It must be acknowledged that the human body involves complex structures, especially the musculoskeletal system, which includes bones, ligaments, tendons, muscles, and other tissues and organs. The spine contributes stiffness and mobility to the body, and the ribcage and pelvis create higher trunk stiffness (Haex, 2004). Finite element models with more detailed anatomy taking into account the geometry of the intervertebral disc can provide additional evidence for an objective representation of mattress comfort (Wong et al., 2019). However, the previous FE models have highly simplified the human body structure, which may affect the accuracy of the simulation.

This study developed a FE model with more detailed internal structures, including vertebrae, intervertebral discs, and spinal ligaments, to reveal the impact of different sleeping support systems on the internal structure of the human body. The procedures of computational simulation mainly involved the creation of the human body model, construction of sleeping support systems, model assembly, mesh convergence, setup of the boundary and loading conditions, model validation, and computational simulation.

3.3.1 Construction of the human model

The human model was constructed based on a male volunteer, his body was subjected to MRI scans, and the MRI files were 3D reconstructed, assembled, and meshed in preparation for computational simulation.

3.3.1.1 Volunteer information

The volunteer of this study was an adult male without any spinal disease. He was 37 years old, 176 cm, and 74 kg. Figure 3.43 illustrates the human model's construction processes, including medical image acquisition, geometric reconstruction, creation of ligaments, and FE simulation mesh generation.

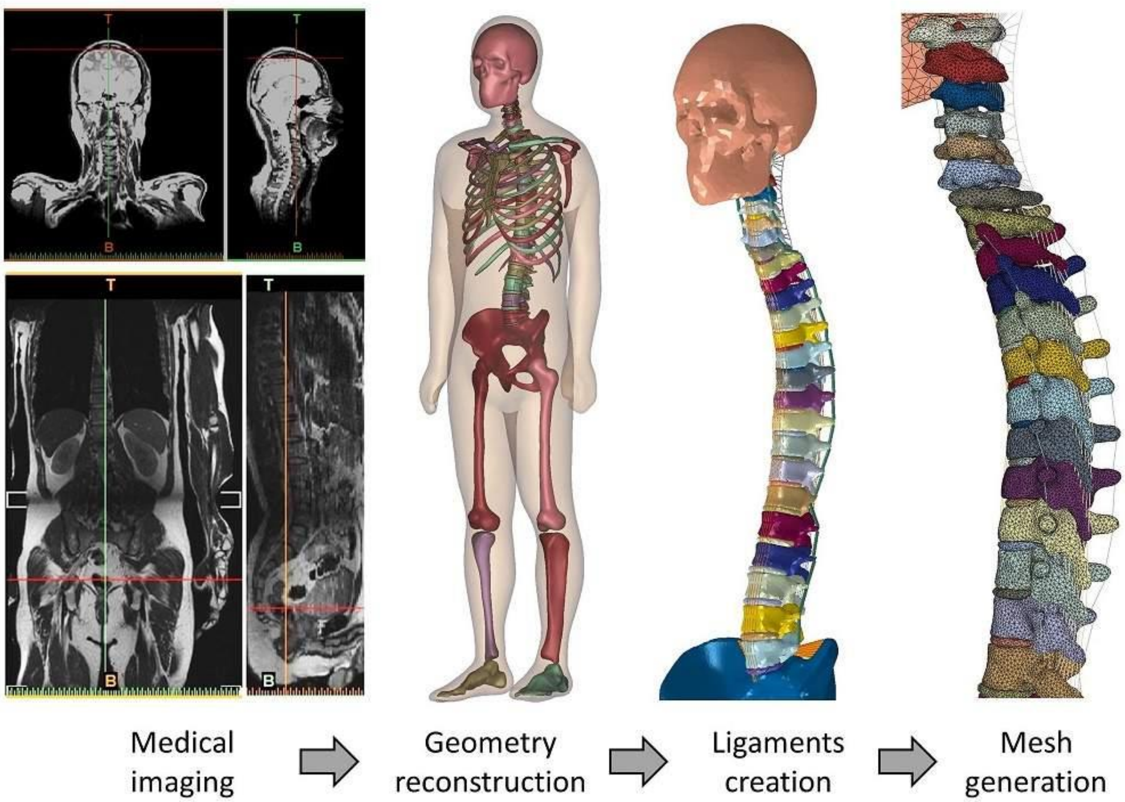

Figure 3.43. Illustration of the human model creation process from medical imaging to mesh creation (Hong et al., 2022).

3.3.1.2 Geometry reconstruction

The volunteer's body contours and internal structures were obtained by an MRI (Philips Achieva-3.0T, Philips Healthcare, MA, USA) medical imaging machine. The scanned files were saved with digital imaging and communications in medicine (DICOM) format. As shown in Figure 3.43, the files were loaded and processed by 3D medical image engineering software Mimics (Mimics V19, Materialize, Leuven, Belgium) for geometry reconstruction (Figure 3.44). The structures of the body contour, skull, vertebrae, rib cage, shoulder blades, clavicles, pelvis, femurs, shanks, and feet were reconstructed.

The reconstructed stereolithography (STL) files were loaded into 3-matics software (version 19, Materialise, Leuven, Belgium) for parts post-processing. All 3D parts were remeshed and smoothed. Figure 3.44(a) shows that an intervertebral disc was created based on vertebrae subtraction to match the endplate geometries. A local smoothing process was applied to remove the sharp edges, and the smoothed part is shown in Figure 3.45(b). Since MRI scans have limited resolution, some anatomy books (Drake et al., 2020; Gilroy et al., 2020; Vital & Cawley, 2020) were also used as references for the modeling process.

The solid parts included the bulk soft tissue throughout the body, 34 pieces of bones, 24 pieces of intervertebral discs, the rib cage, and the brain tissue inside the skull. Intervertebral discs are located between two nearby vertebrae. They were created by filling the space between the two vertebrae through the Boolean subtraction.

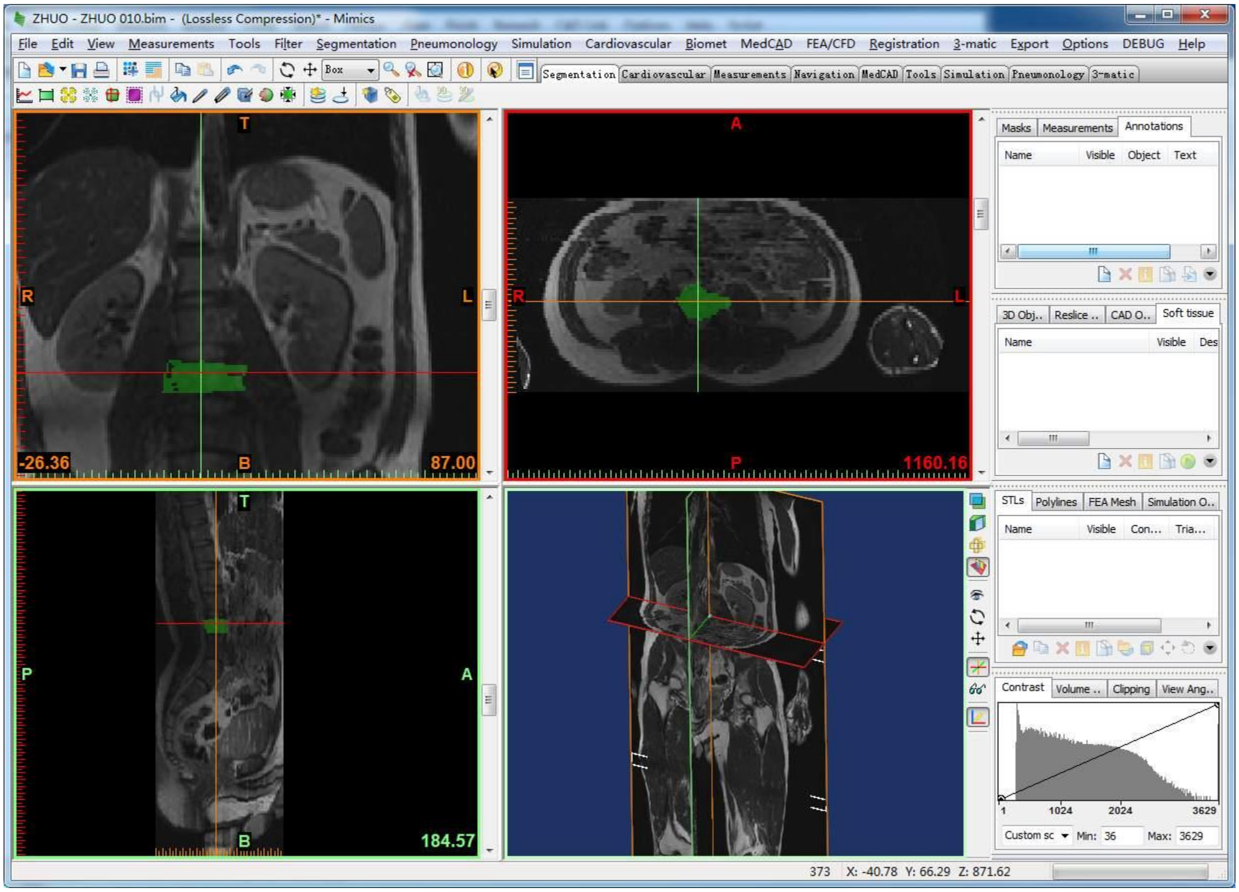

Figure 3.44. Screen capture of Mimics interface.

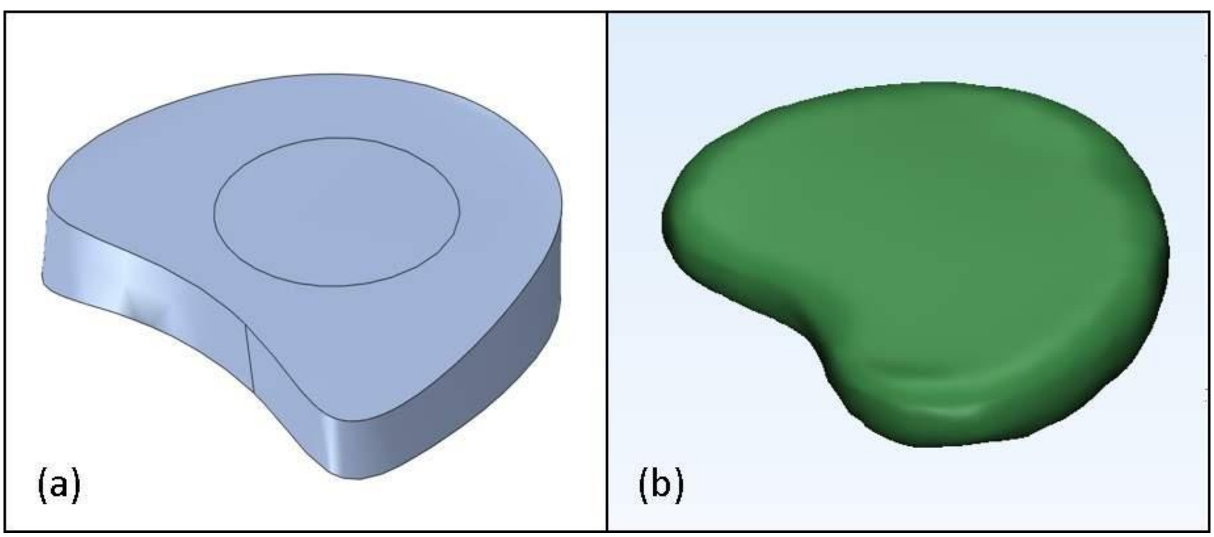

Figure 3.45. An intervertebral disc during processing. (a) Intervertebral disc created based on boolean subtraction of parts; (b) local smoothing of an intervertebral disc.

3.3.1.3 Ligaments creation

Ligaments play an essential role in stabilizing the spine (Izzo et al., 2013; Sharma et al., 1995). Major spinal ligaments were constructed based on anatomy atlases (Drake et al., 2020; Gilroy et al., 2020; Vital & Cawley, 2020). This model involved multiple ligaments, including the anterior longitudinal ligament, ligamentum flavum, interspinous ligament, transverse ligament, posterior longitudinal ligament, and facet capsular ligament (Figure 3.46).

The model configuration significantly impacts the calculation accuracy of the FE model. Therefore, the careful creation of ligaments is beneficial to the accuracy of computational simulations. The cross-sectional area of each ligament group for different spinal regions was obtained from the literature. This study constructed multiple parallel or near-parallel trusses to represent a membrane-like ligament. The number of truss elements used for each ligament is listed in Table 3.3. The truss diameter was calculated based on the cross-sectional area of the ligament and the number of trusses representing the ligament.

When the ligament is under tension, such as the anterior longitudinal ligament in the posture of spine extension, the ligament limits the displacement between the vertebrae. Conversely, when the ligament is under compression, such as the anterior longitudinal ligament in the flexion of the spine, the ligament does not function biomechanically.

In the initial phase, ligaments relax, and they function to limit the movement of bones under tensile loads.

Table 3.3. Cross-section area of spinal ligaments and the truss creation parameters.

		Cross-section area of ligament (mm^2)	References	Number of truss elements	Truss diameter (mm)
Cervical region	Anterior longitudinal ligament	11.1	(Nikkhoo et al., 2019)	5	1.7
	Capsular ligament	42.2		12	2.1
	Flava ligament	46		5	3.4
	Interspinous ligament	42.2		7	2.8
	Intertransverse ligament	13		2	2.9
	Posterior longitudinal ligament	11.3		5	1.7
Thoracic region	Anterior longitudinal ligament	33.1	(Balasubramanian et al., 2022; Chazal et al., 1985)	5	2.9
	Capsular ligament	28.7		12	1.7
	Flava ligament	28.6		5	2.7
	Interspinous ligament	20.9		7	1.9
	Intertransverse ligament	21		2	3.7
	Posterior longitudinal ligament	18		5	2.1
Lumbar region	Anterior longitudinal ligament	32.4	(Balasubramanian et al., 2022; Pintar et al., 1992)	5	2.9
	Capsular ligament	42.2		12	2.1
	Flava ligament	84.2		5	4.6
	Interspinous ligament	35.1		7	2.5
	Intertransverse ligament	25.2		2	4.0
	Posterior longitudinal ligament	5.2		5	1.2

3.3.1.4 Material properties

This FE model involves various materials, including soft tissue, bone, intervertebral discs, ribs, and ligaments. All materials were defined as linear elastic materials. The parts' mechanical properties were acquired through literature and listed in Table 3.4.

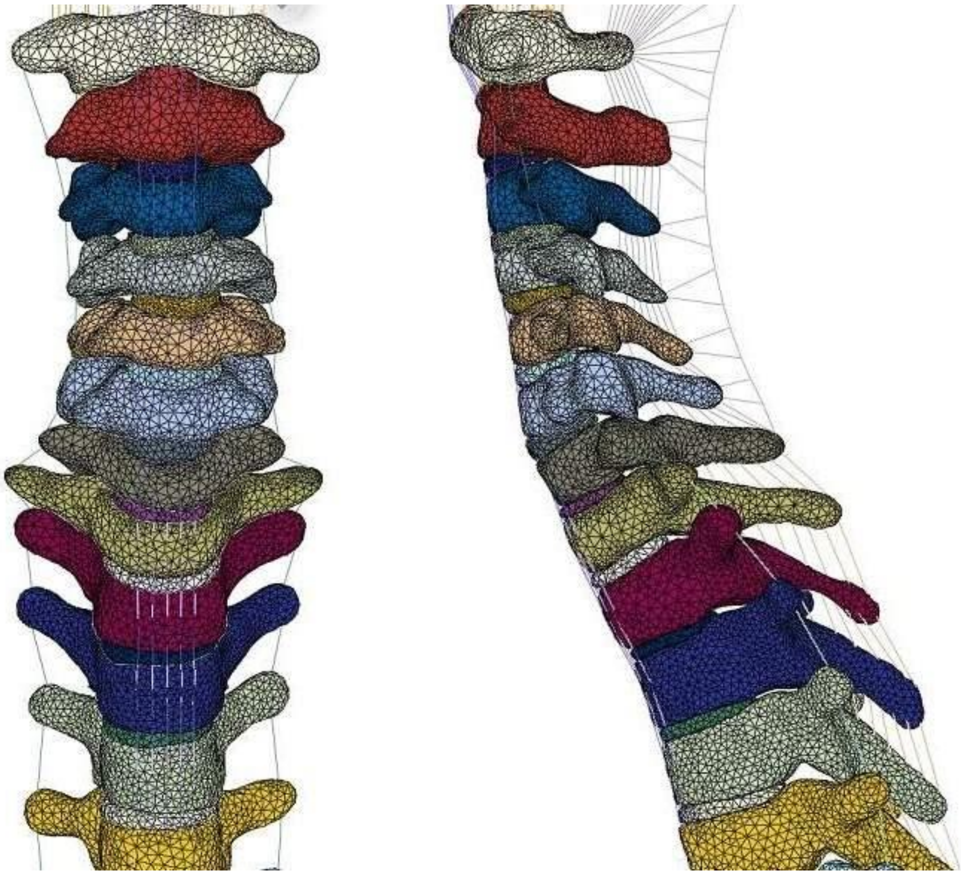

Figure 3.46. Part of spinal ligaments involved in the FE model.

3.3.2 Sleeping support system

The sleep support system was constructed in a different way than the human model. The material properties were obtained through material tests, and the geometry of the sleeping support systems was obtained through measurement and then reconstructed through CAD software.

Table 3.4. Properties of materials adopted for the computational simulation (Hong et al., 2022).

Parts	Property of materials	References
Rigid bones	E = 12.0 GPa / ν = 0.30	(Chi et al., 2015)
Rib cage	E = 4.9 GPa / ν = 0.30	(Agnew et al., 2013)
Encapsulated soft tissue	E = 15.0 KPa / ν = 0.49	(Lizee et al., 1998)
Ligaments		
Anterior longitudinal	E = 11.9 MPa / ν = 0.39	(Jones & Wilcox, 2008; Kumaresan et al., 1999; Nikkhoo et al., 2019)
Capsular	E = 7.7 MPa / ν = 0.39	
Flava	E = 2.4 MPa / ν = 0.39	
Interspinous	E = 3.4 MPa / ν = 0.39	
Intertransverse	E = 10.0 MPa / ν = 0.40	
Posterior longitudinal	E = 12.5 MPa / ν = 0.39	
Foam material		
Soft mattress	Figure 3.48 / ν = 0.01	
Medium mattress		
Hard mattress		
Pillow		
The ground	*Rigid*	

3.3.2.1 Material test

Polymer foams were fabricated from solid materials through a foaming process. Since foam materials have low density and take up a lot of space for transportation and storage, manufacturers usually perform the foaming process to improve space utilization. Therefore, most foam materials for mattresses are non-standard. A machine for the plastic tensile test (Instron-5569, Instron Company Limited, MA, USA) was adopted to obtain the foam materials' stress-strain properties (Figure 3.47) for computational simulation.

Figure 3.47. The material test machine and a specimen being tested.

The test results are shown in Figure 3.48. The testing specimens were cut to 14 cm in diameter and 20 cm in height. Poisson's ratios were obtained by measuring the material diameter during the material testing and are listed in Table 3.2.

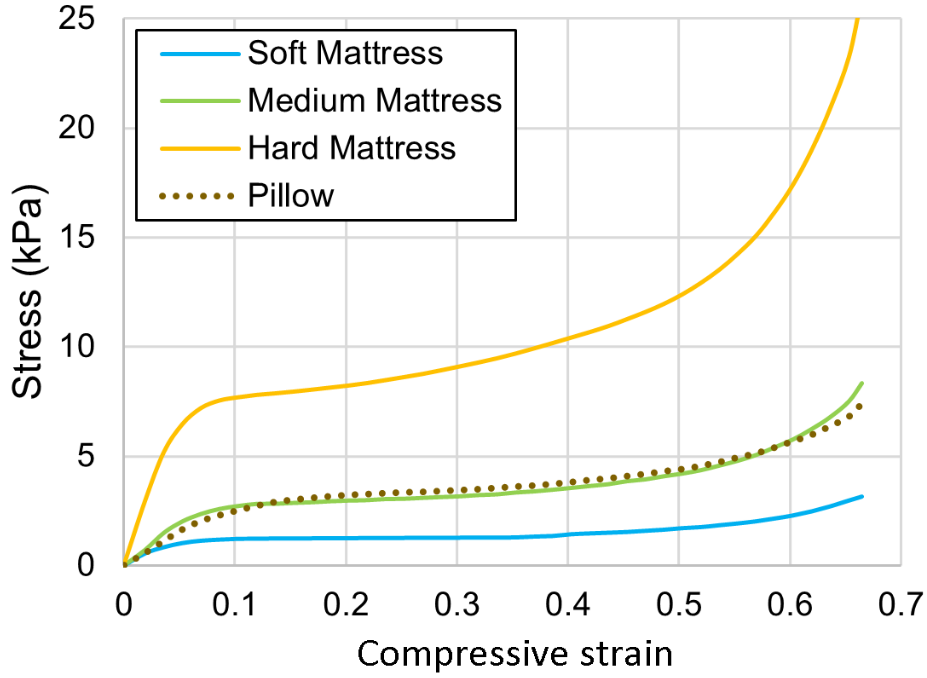

Figure 3.48. Plot of compressive stress-strain curves from material tests.

3.3.2.2 Computational model of sleeping support systems

The computational model of sleeping support systems was reconstructed by CAD software (AutoCAD R13, Autodesk, California, USA) based on the mattresses and the pillow used in the experiments. The appearance and dimensions of the mattress and pillow are shown in Figure 3.39.

3.3.3 Meshing parts

Mesh creation is an integral part of computational simulation. Proper mesh type and size are critical for an efficient simulation. This study used Abaqus 6.14 (Simulia, Dassault Systèmes Limited, France) to mesh the FE model. The solid parts involved the skull, brain, 24 pieces of vertebrae, 24 pieces of intervertebral discs, scapula, sacrum, pelvis, femur, lower leg, and feet. These parts meshed with linear tetrahedral elements (C3D4). A total of 986 trusses were created as ligaments and attached to the bone structure; all ligaments meshed with two-node truss elements (T3D2). The sleeping support system consists of a pillow and a mattress, and meshed with hexahedral elements (C3D8) and placed on a rigid, nondeformable ground plate.

If the mesh is too coarse, the calculation accuracy may be reduced. If the mesh is too fine, it may significantly consume computing power and cause excessive calculation time. Literature suggests that cervical discs are smaller in volume than other discs (Waxenbaum et al., 2017), and previous studies have indicated that the lower part of the cervical spine is the region of most degenerative cervical myelopathy (Nouri et al., 2015). Therefore, the mesh convergence process was conducted under an axial loading applied to the C4-C5 vertebrae and the intervertebral disc between the two vertebrae. Figure 3.49 shows the configuration of the mesh convergence test. The vertebrae C5 was fixed, and a compressive load was applied on the top of vertebrae C4. Concerning the weight of the head in an upright position (Hansraj, 2014), the force applied to the vertebra C4 was set to 50N.

Referring to other studies of computational simulation (Peng et al., 2021; Wong et al., 2018), the initial value of the mesh size for the mesh convergence test was set to 5mm, and the mesh size was refined at an interval of 10%. The peak value of Von Mises stress at intervertebral disc C4-C5 was compared during the mesh refinement procedure. In the end, the mesh size of the vertebrae and intervertebral discs was determined to be 3.0 mm since the deviation of the new calculation result was less than 5% compared with the previous one, which was considered the appropriate mesh size (Chen et al., 2019).

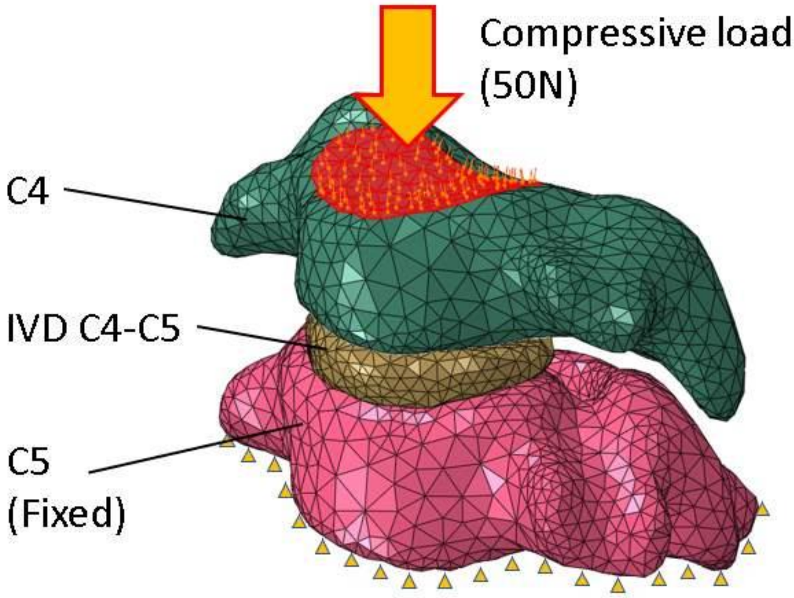

Figure 3.49. The loading and boundary condition for the mesh convergence test.

3.3.4 Boundary and loading conditions

Boundary conditions were created to constrain the model. If the model lacks constraints, an extreme case would be an endless fall of the whole model. This study created a non-deformable rigid plate as the ground to support the sleeping support system (Figure 3.50). The ground plate was fully constrained from movement or rotation. The mattress on the ground has degrees of freedom in all aspects and can be freely deformed. The cervical pillow was placed on top of the mattress, and the contact area had a friction coefficient of 0.65. The human model was located above the pillow and the mattress with zero clearance.

When gravity is applied, the human body will sink, and the sleeping support system will bear the weight of the human body, both of which may be deformed. The relatively fine and complete spine structure helps to make the deformation of the human model closer to the actual situation.

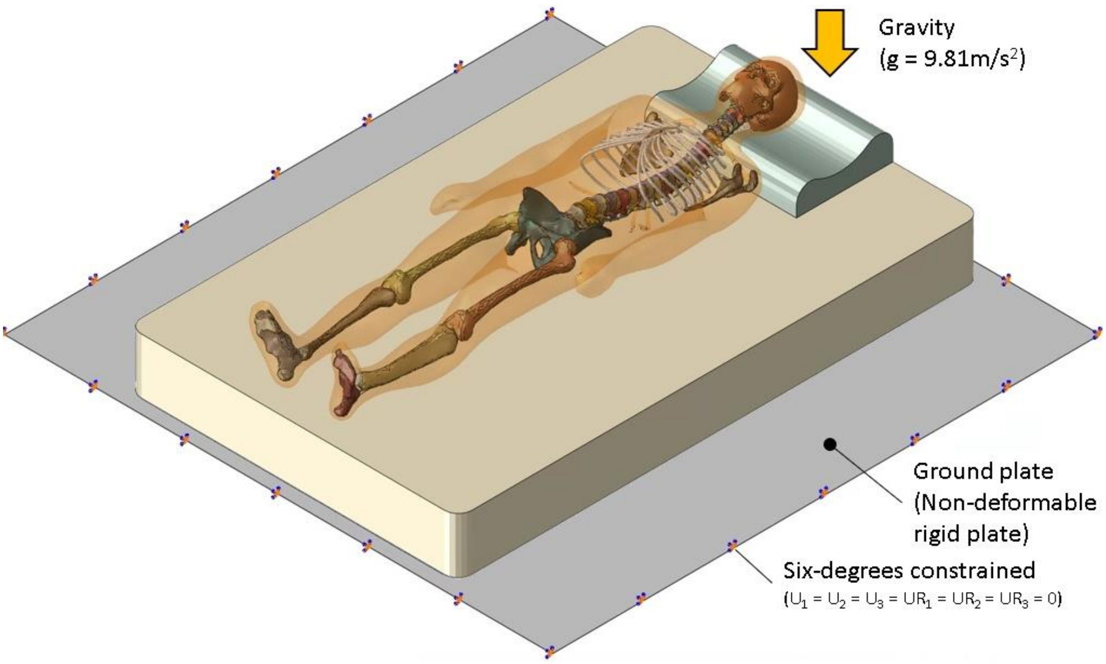

Figure 3.50. The configuration of boundary and loading conditions for the finite element analysis.

Loads were applied to the FE model through the setup of loading conditions. There are various types of loading that can be created in the FE. The loads can be applied to points, surfaces, edges, nodes, and elements. As shown in Figure 3.50, a uniform gravity (g = 9.81) downward to the ground plate was created, and the loading was applied to the whole model. The ground plate was locked, supporting the sleeping support. Under gravity loading, the sleeping support system and the human model above were both deformed.

3.3.5 Interaction between components

Interactions were created to connect the components between the human model, the sleeping support system, and the interaction between the two.

From C2 to the sacrum, there are 24 vertebrae and intervertebral discs. Vertebra endplates and intervertebral disc surfaces were connected in "Tie" contacts. A large number of ligaments were also connected to the corresponding locations of the vertebrae and bone surfaces in tie constraints. Due to the vertebrae's high mechanical strength properties, the deformation of the vertebral column is generally achieved by the deformation of intervertebral discs.

Bones interact with the bulk soft tissues through "Tie" contacts. The joints that connect the bones were contacted in a "frictionless" tangential behavior to allow the movement of the limbs when subjected to gravity.

Contact behavior is another critical factor affecting the accuracy of computational simulation. Improper settings can cause intrusions between components and result in inaccuracies. Based on the test data, the coefficient of friction between the mattress and the pillow was set to 0.65. Displacement of the mattress bottom in the *z*-direction was restricted, and a friction coefficient of 0.5 was applied above the ground plate, which supports the sleeping support system and the human model. The friction coefficient between the human model and the sleeping system was set to 0.4 (Lee et al., 2017; Zhang & Mak, 1999).

The musculoskeletal system would deform when loading gravity onto the human model, and contact may happen between components. The sleeping support system supports the human body in multiple regions, such as the head, neck, back, buttocks, and legs. In the supine position, gravity deforms the soft tissues and sleeping support system; the bones are hard enough that only slight deformation occurs. However, the bones can be rotated along the joints to change the limb positions in response to gravity. Changes in the shape of the vertebral column cause stress and deformation of the intervertebral discs. Spinal ligaments constrain and limit the motion of the vertebrae.

3.3.6 Model validation

As described in Section 3.2, the human experiments were conducted and measured the spinal curvatures while lying on different stiffness of mattresses. Sixteen volunteers were supine on three mattresses of different stiffness, with their heads supported by the same cervical pillow. The experimental data was adopted to validate the FE model.

The FE model was validated through the comparison of the spine parameters between the experimental measurements and the computational calculations. Spine parameters were extracted by CAD software, including the HD, CLD, and LLD. Measurement of lying supine on the soft mattress: HD = 85.8 ± 21.5 mm, CLD = 96.6 ± 18.3 mm, LLD = 22.9 ± 6.5 mm; while model calculation: HD = 71.8 mm, CLD = 94.6 mm, LLD = 22.8 mm. Measurement of lying supine on the medium mattress: HD = 55.3 ± 8.9 mm, CLD = 69.9 ± 6.8 mm, LLD = 22.2 ± 4.8 mm; while the computational result: HD = 51.8 mm, CLD = 82.4 mm, LLD = 22.3 mm. Measurement of lying supine on the hard mattress: HD = 60.0 ± 11.0 mm, CLD = 70.2 ± 6.3 mm, LLD = 11.6 ± 5.2 mm; while the FE prediction: HD = 49.5 mm, CLD = 79.0 mm, LLD = 14.3 mm.

Eventually, there are 48 non-zero distance data pairs (n = 48) between experimental measurements and FE predictions. Data were analyzed by SPSS 21 (IBM, New York, NY, United States). As shown in Figure 3.51, the correlation analysis indicated a clear linear relationship between experimental measurements and computational predictions ($r = 0.88$; $p < 0.001$). Since Pearson's correlation coefficient is greater than 0.7, this can infer a strong positive linear relationship through a firm and linear rule (Ratner, 2009).

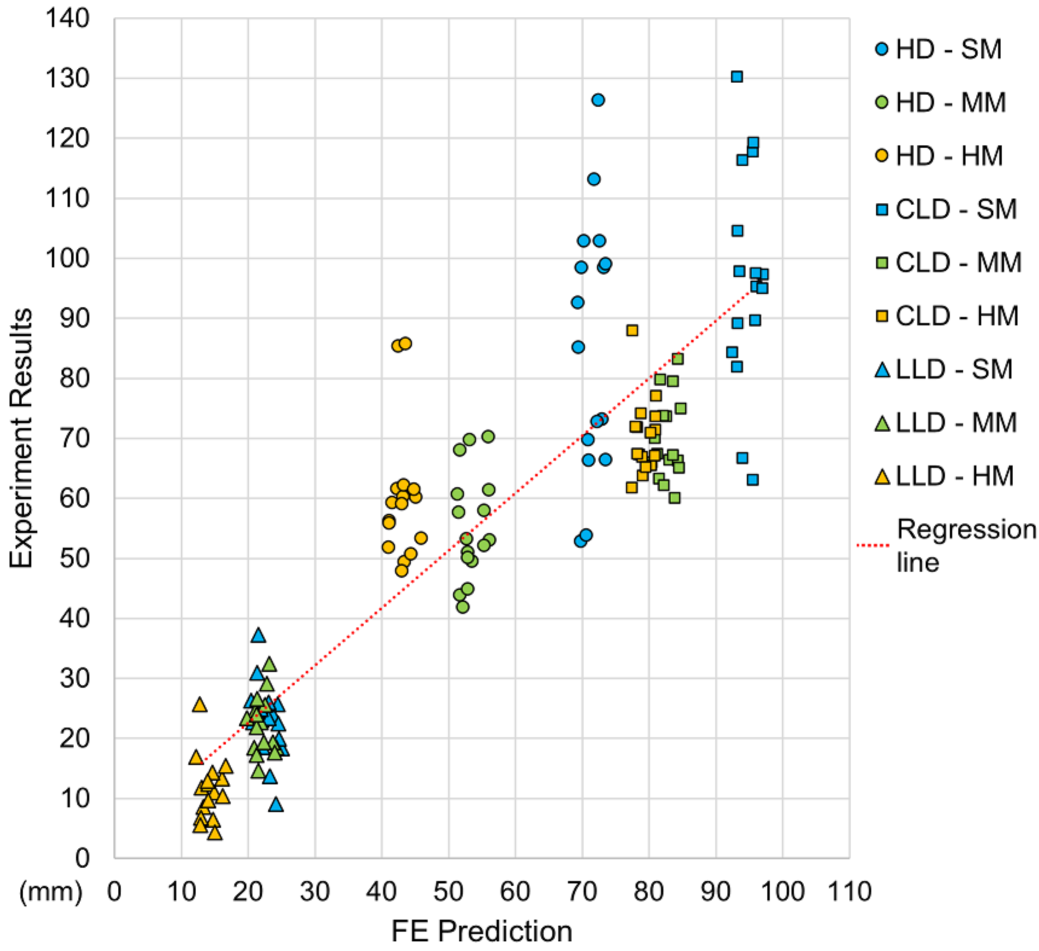

Figure 3.51. Jitter plot for correlation analysis between computational predictions and experimental measurements for model validation (Hong et al., 2022).

Chapter 4 Results

This study consists of three parts, including the development of the curvature measurement tape to measure the covered curvature for research purposes, human experiments on the influence of mattress stiffness on spinal curvature, and the implementation of the FE method to understand changes and loads on the human body model. Since the development and validation of the curvature measuring tape were reported in Section 3.1, this chapter will present the measurement results of human experiments and the prediction results of the FE method.

4.1 Experimental results

Experiments were conducted at the biomechanics laboratory on the university campus. Sixteen volunteers were lying supine on three mattresses of various stiffness, named hard, medium, and soft, with indentation load deflections of 120, 42, and 20 lbs. The volunteer's head was supported using a cervical pillow. Figure 4.1 shows side views of lying on mattresses with different stiffnesses; visually, the trunk sinks deeper into the soft mattress, but there was no noticeable difference in the head height between the three mattresses. However, the spinal curve between the sleeping support system and the human body cannot be measured quantitatively by visual inspection.

Table 4.1. Measurement results of human experiments.

	Soft mattress	Medium mattress	Hard Mattress
TI (°)	6.86 ± 4.85	3.64 ± 1.09	1.56 ± 0.63
HD (mm)	85.8 ± 21.5	55.3 ± 8.9	60.0 ± 11.0
CLD (mm)	96.6 ± 18.3	69.9 ± 6.8	70.2 ± 6.3
LLD (mm)	22.9 ± 6.5	22.2 ± 4.8	11.6 ± 5.2

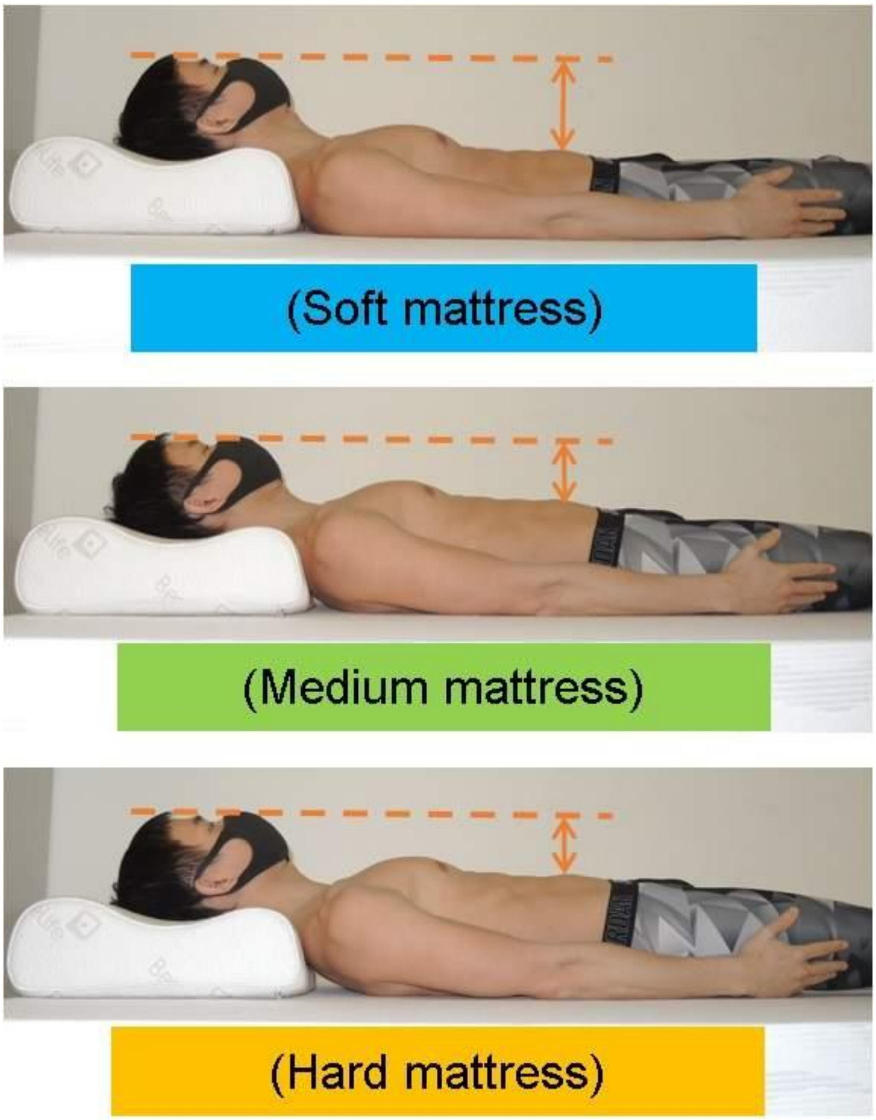

Figure 4.1. Side views of lying supine on different stiffness sleeping support systems.

The curvature measurement tape measured the spinal curvature, and the spine parameters were extracted by CAD software and shown in Table 4.1.

Figure 4.2 shows the box plot of the experiment results, with the TI, HD, CLD, and LLD presented separately. In a comparison of TI between the three mattresses, the soft mattress environment measured the highest average value of TI as 6.86 ± 4.85°, a moderate TI value was obtained in the medium mattress environment as 3.64 ± 1.09°, and the smallest TI value was exhibited in the hard mattress environment as 1.56 ± 0.63°. Significant differences in TI values were found, the soft versus medium mattress, $p < 0.05$, the soft versus hard mattress, $p < 0.001$, and the medium versus hard mattress, $p < 0.001$.

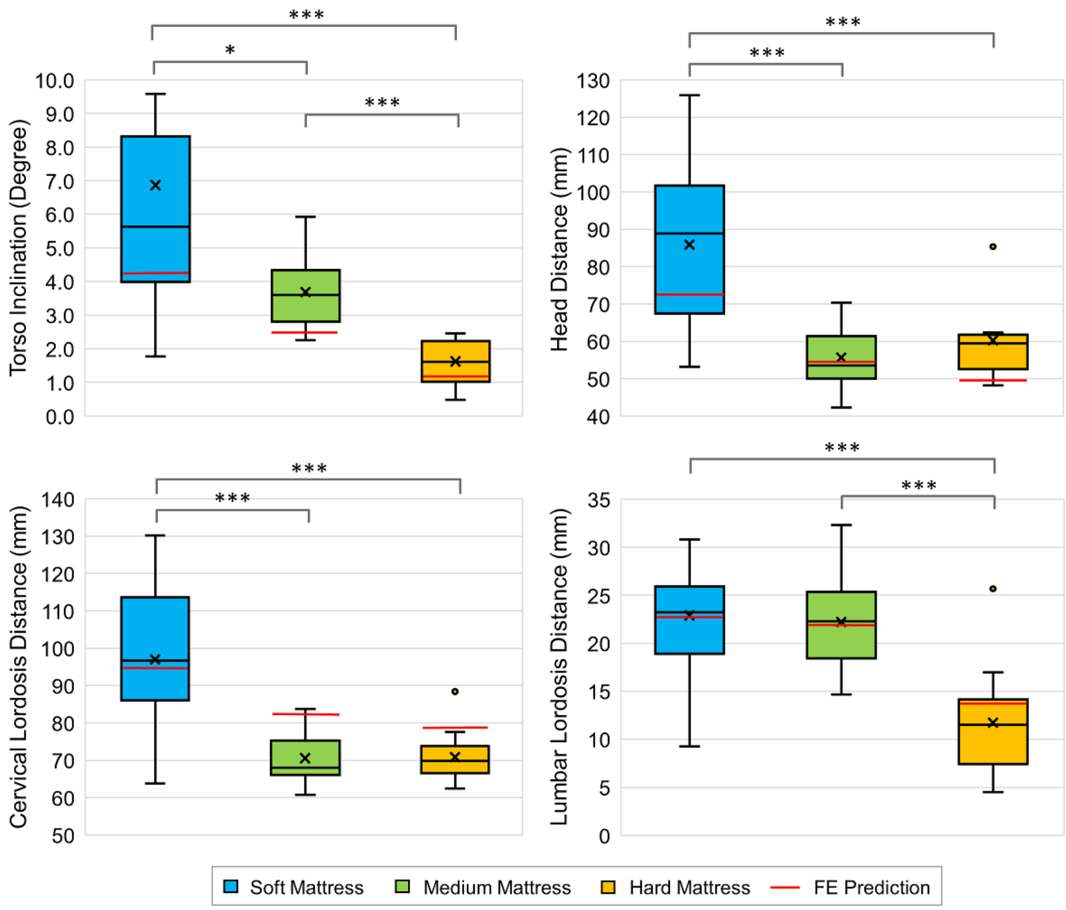

Figure 4.2. Box plot of experimental results and computational predictions of spine parameters; * represents $p \leq 0.05$, *** represents $p \leq 0.001$, and ° represents an outlier (Hong et al., 2022).

HD represents the closest distance of the head to the TI. A lower HD value means the head is lower while lying. In the soft mattress environment, the highest average value of HD was measured at 85.8 ± 21.5 mm, the HD value in the medium mattress environment was 55.3 ± 8.9 mm, and it was 60.0 ± 11.0 mm in the hard mattress environment. There were significant differences in HD values between the soft mattress and the other two mattresses, the soft versus medium mattress, $p < 0.001$, the soft versus hard mattress, $p < 0.001$, and there was no significant difference between the medium and hard mattress, $p > 0.05$.

Measurements of CLD appear to have a similar pattern to HD. The greatest CLD was measured in the soft mattress environment as 96.6 ± 18.3 mm, the same parameter measured in the medium mattress environment was 69.9 ± 6.8 mm, and it was 70.2 ± 6.3 mm in the hard mattress environment. There were significant differences in CLD values between the soft mattress and the other two mattresses, the soft versus medium mattress, $p < 0.001$, the soft versus hard mattress, $p < 0.001$, and no significant difference found between the medium and hard mattress, $p > 0.05$.

The LLD values measured based on three mattresses appear to have a unique pattern. The measurement in the soft mattress environment was the largest, at 22.9 ± 6.5 mm. The same parameter measured in the medium mattress environment was 22.2 ± 4.8 mm, very close to the value of the soft mattress. The LLD measured in the hard mattress environment was 11.6 ± 5.2 mm. There was no significant difference in LLD between the soft and medium mattresses, $p > 0.05$; however, there was a significant difference between the soft and hard mattresses, $p < 0.001$, and there was a significant difference between the medium and hard mattresses, $p < 0.001$.

Overall, this study quantitatively measured the spinal curvature of all volunteers using curvature measurement tape. Figure 4.3 shows one set of the measured spinal curvatures. The curvature measurement device measured the spinal curvatures. The AutoCAD software reconstructed the obtained data with sensor coordinates and performed the parametric calculations.

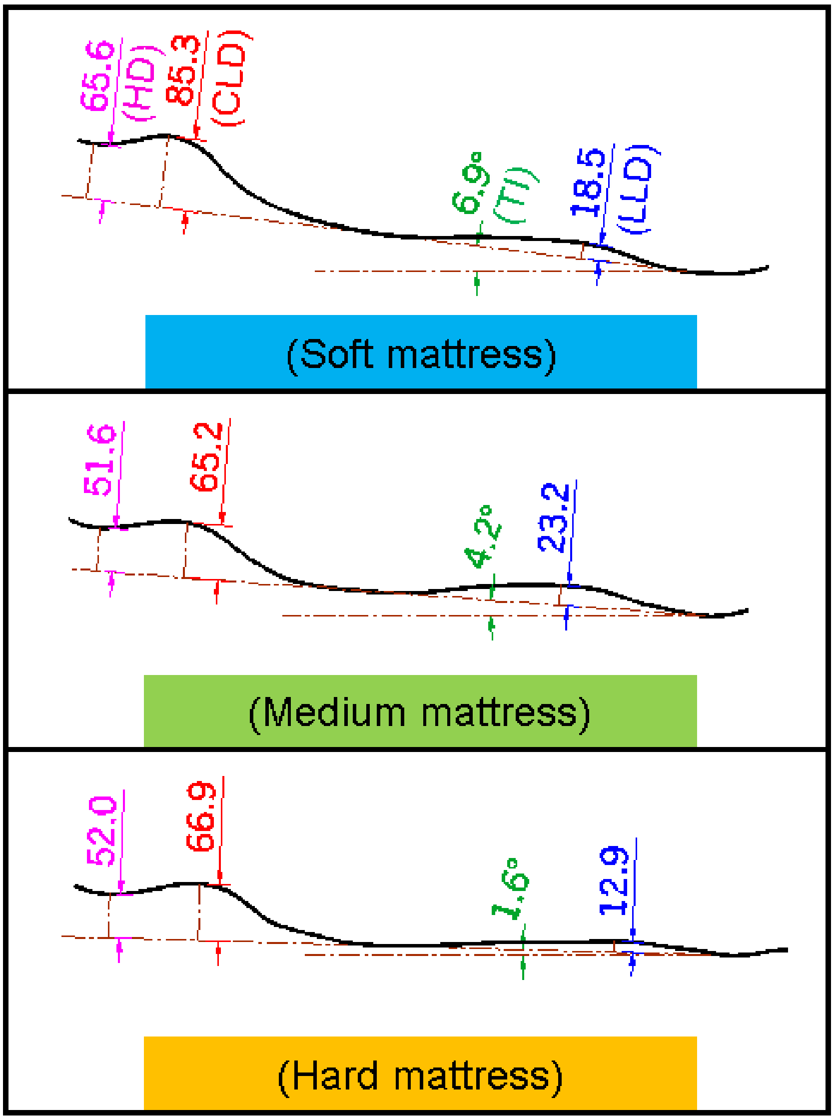

Figure 4.3. The measured spinal curvatures by the curvature measurement tape.

4.2 Computational predictions

The FE method is widely used in biomechanical analysis. Biomechanical information can be predicted using computational models, whether the concern is on the surface or deep within the human body. Various data were obtained from computational simulations, including spinal curvatures for model validation, contact pressure for sleep comfort assessment, and intervertebral disc loading for sleep health evaluation.

Based on computational simulations, the loading distribution and the highest loading of the intervertebral discs in the supine position have been estimated, which is very challenging to be measured by in vivo measurements.

4.2.1 Predicted spinal curvature

Although the back was contacted with and covered by the sleeping support system, the spinal curvature can be visualized by a cross-sectional view in the sagittal plane. The spine parameters were extracted by CAD software and shown in Figure 4.4.

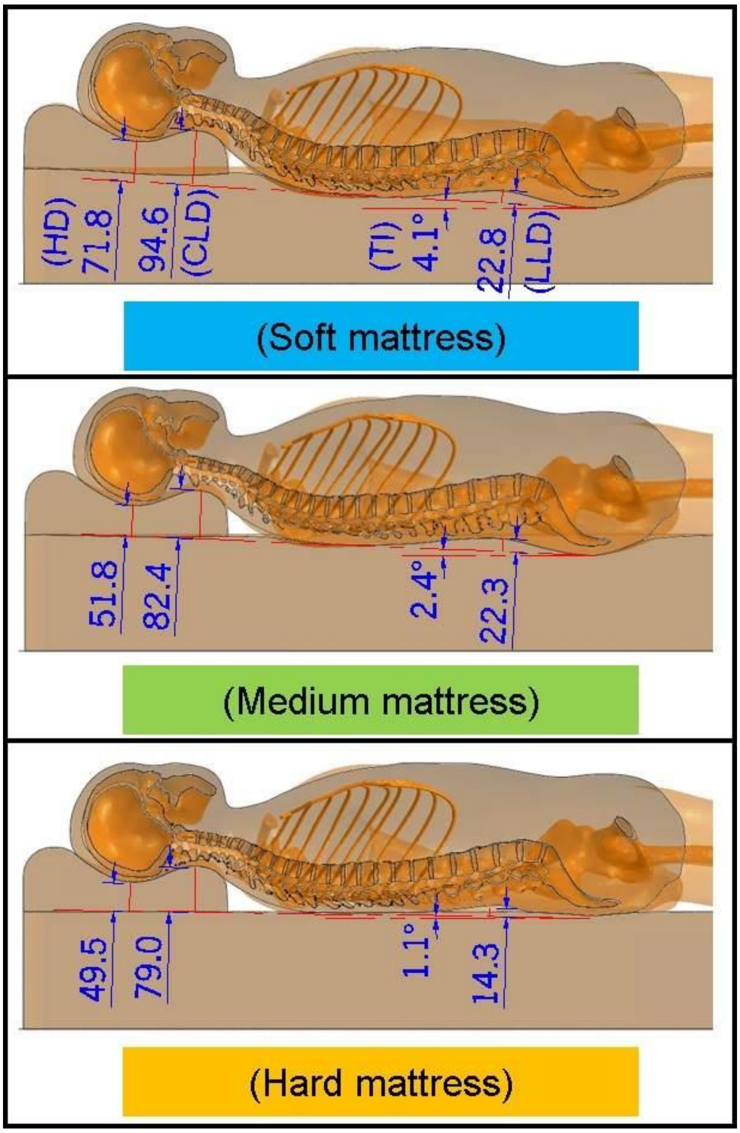

Figure 4.4. Spine parameters which predicted by the finite element model (Hong et al., 2022).

Measurements of spine parameters such as TI, HD, CLD, and LLD were performed using CAD software based on the sectional computer graphics predicted by FE simulation. These data were used for model validation (Section 3.3.5) and are also shown in Figure 4.2.

4.2.2 Predicted contact pressure

Contact pressure measurement systems were designed using flexible and slim sheet sensors to minimize interference in sleeping support (Chen et al., 2014; Lee et al., 2015). Anyway, the sensor sheet may still disperse the concentrated loading and cause an underestimate of the peak pressure (Wong et al., 2019). The FE method also has the ability to obtain the contact pressure without the interference of the sensor sheet. This method of predicting the contact pressure through computer calculations is widely used. The computer-predicted contact pressure between the sleeping support systems and the human model is shown in Figure 4.5.

In most cases, the soft mattress environment appears to have the smallest value of peak contact pressures (cervical = 9.7 kPa, occiput = 7.5 kPa, scapula = 4.5 kPa, hip = 5.9 kPa, calve = 3.3 kPa, heel = 6.9 kPa). Most areas of the medium mattress environment predicted higher peak pressure than the same region in soft mattress (cervical = 7.7 kPa, occiput = 7.7 kPa, scapula = 7.2 kPa, hip = 8.9 kPa, calves = 5.3 kPa, heels = 10.1 kPa). Predicted peak contact pressure for lying supine on the hard mattress is usually significantly higher than the same region in the soft and medium mattress environments (cervical = 5.2 kPa, occiput = 8.9 kPa, scapula = 24.3 kPa, hip = 28.6 kPa, calve = 7.4 kPa, heel = 17.9 kPa). The only exception in the data above is the peak contact pressure of the cervical region, with the highest predicted values for the soft mattress environment and the lowest for the hard mattress environment.

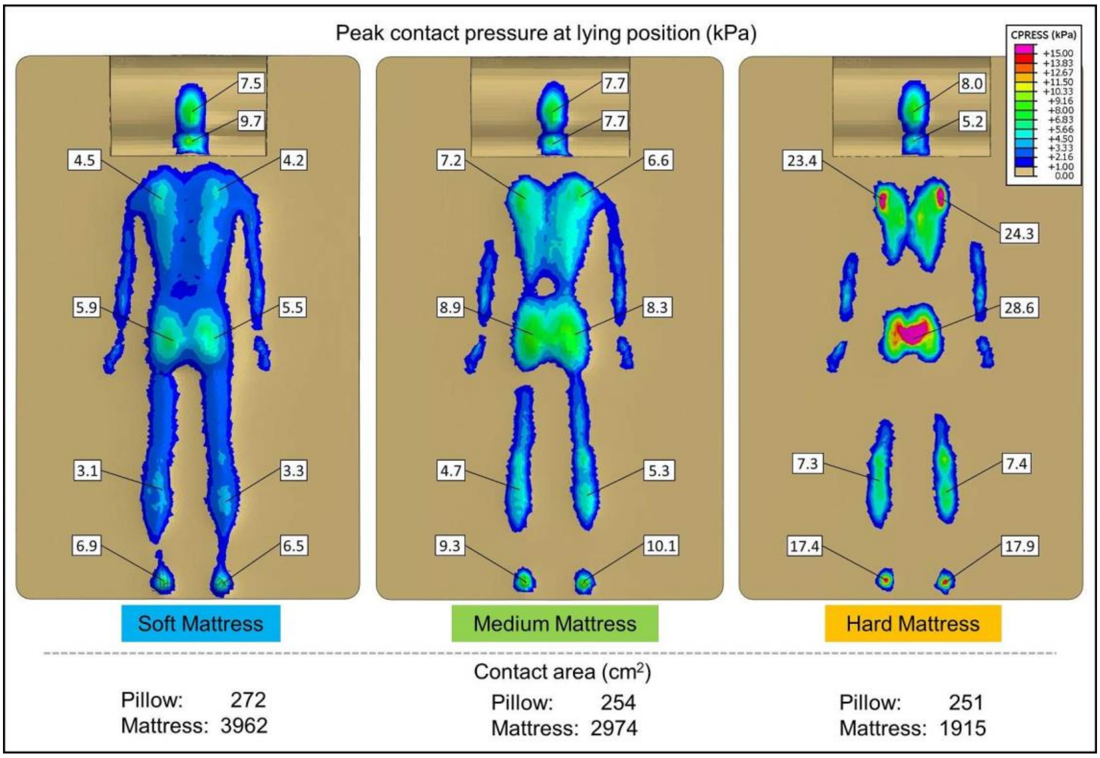

Figure 4.5. Computed pressure distribution and body contact area by FE method (Hong et al., 2022).

The computational simulations also predicted the contact area of the human body with the sleeping support system. Soft mattress environment: pillow = 272 cm^2, mattress = 3962 cm^2; medium mattress environment: pillow = 254 cm^2, mattress = 2974 cm^2; hard mattress environment: pillow = 251 cm^2, mattress = 1915 cm^2. The contact area measurement was counted on the area with a pressure greater than 1.0 kPa.

4.2.3 Peak loading of intervertebral discs

One of the advantages of FE analysis is that it can observe the internal structures of the human body. In this study, all vertebrae and intervertebral discs were modeled. All the intervertebral disc's Von Mises stress values were extracted in the field output as computational results. FE analyses predicted the loading of each intervertebral disc of the human model lying supine on the three sleep support systems, and the peak value is listed in Table 4.2.

Table 4.2. Computational prediction of intervertebral disc peak loading (kPa).

Intervertebral disc	Soft mattress	Medium mattress	Hard mattress
C2—C3	167	97	60
C3—C4	249	131	81
C4—C5	184	87	114
C5—C6	316	212	186
C6—C7	143	46	36
C7—T1	173	41	28
T1—T2	109	24	14
T2—T3	84	28	27
T3—T4	63	48	40
T4—T5	41	43	51
T5—T6	30	73	97
T6—T7	29	74	109
T7—T8	24	67	92
T8—T9	20	63	85
T9—T10	27	59	84
T10—T11	46	68	78
T11—T12	51	65	87
T12—L1	93	117	119
L1—L2	50	55	83
L2—L3	92	67	81
L3—L4	56	45	53
L4—L5	66	64	78
L5—Sacrum	40	84	103

Supine placement of the FE model on sleeping support systems of different stiffness resulted in significant differences in peak intervertebral disc loading. When lying on the soft mattress, high peak loading of the cervical and upper thoracic discs was observed, while low peak loading of the lower thoracic and lumbar discs appeared. In the medium mattress environment, the peak loading of the cervical and upper thoracic disc was lower than that of the soft mattress. It was similar to that of the hard mattress environment. The peak loading of the lower thoracic and lumbar intervertebral discs in the hard mattress environment was slightly higher than that of the soft and medium mattresses. The loading distribution of intervertebral discs is presented in Figure 4.6(a), and the peak loading of each disc is shown in Figure 4.6(b).

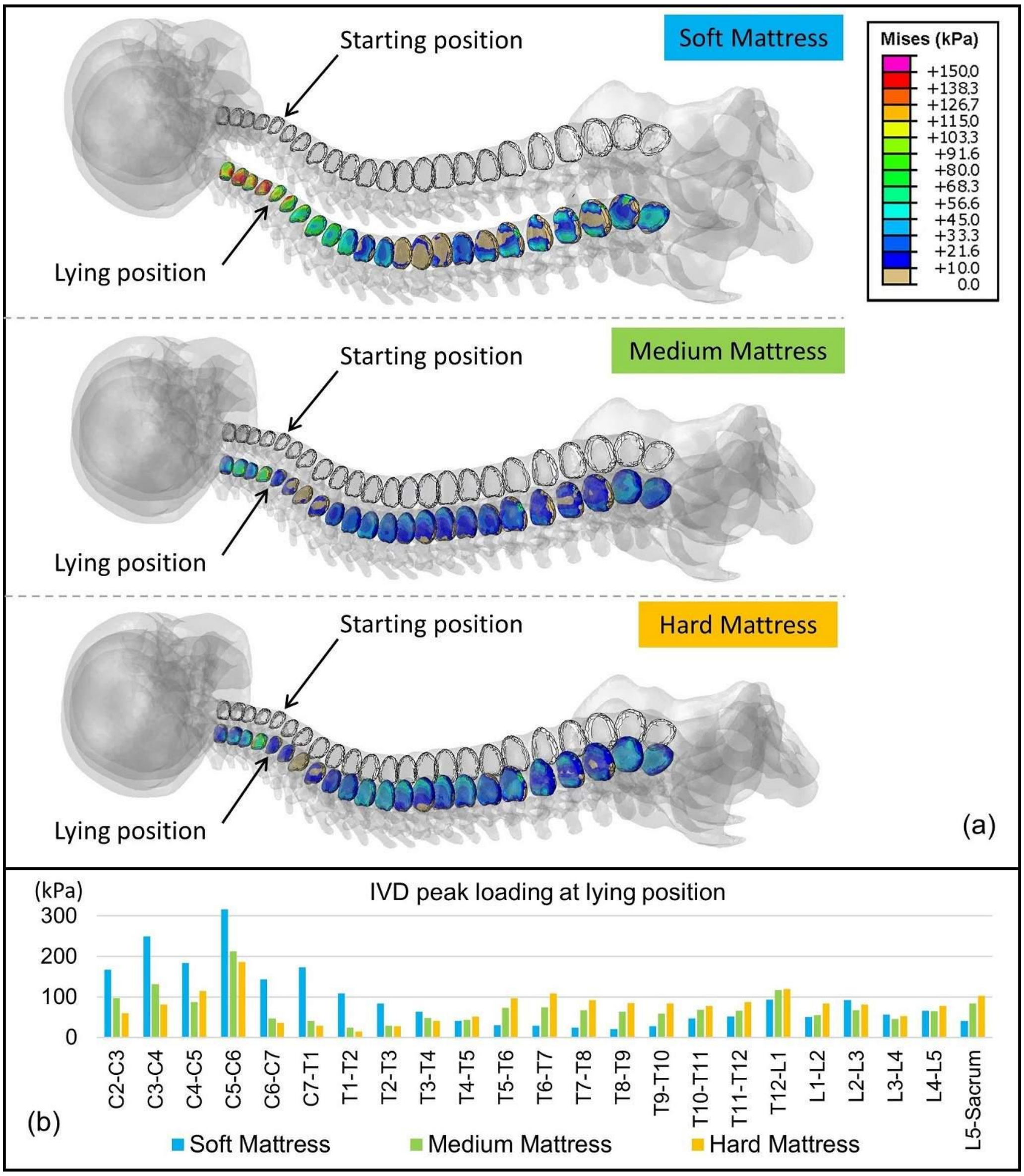

Figure 4.6. Presentation of intervertebral disc loading (Hong et al., 2022). (a) Diagram of intervertebral discs loading distribution; (b) Peak value of loading on the intervertebral discs in the lying position.

4.2.4 Insufficient upper back support

This study used a B-shaped cervical pillow. In a side view, the edges of the pillow were higher than the concaved middle zone. The pillow edges were designed at different heights, as shown in Figure 3.39. Users can choose either a lower edge or a higher edge to support the neck according to their preference. The distance between the higher edge and the pillow bottom was 110 mm, between the middle zone and the pillow bottom was 65 mm, and between the lower edge and the bottom of the pillow was 90 mm. The pillow profile was designed to provide mechanical support to the neck to maintain the neutral lordosis of the cervical spine. In this study, the lower edge was used to support the neck. However, the upper back appears suspended, it can be observed in Figure 4.1, and a perspective drawing of the FE model is shown in Figure 4.7.

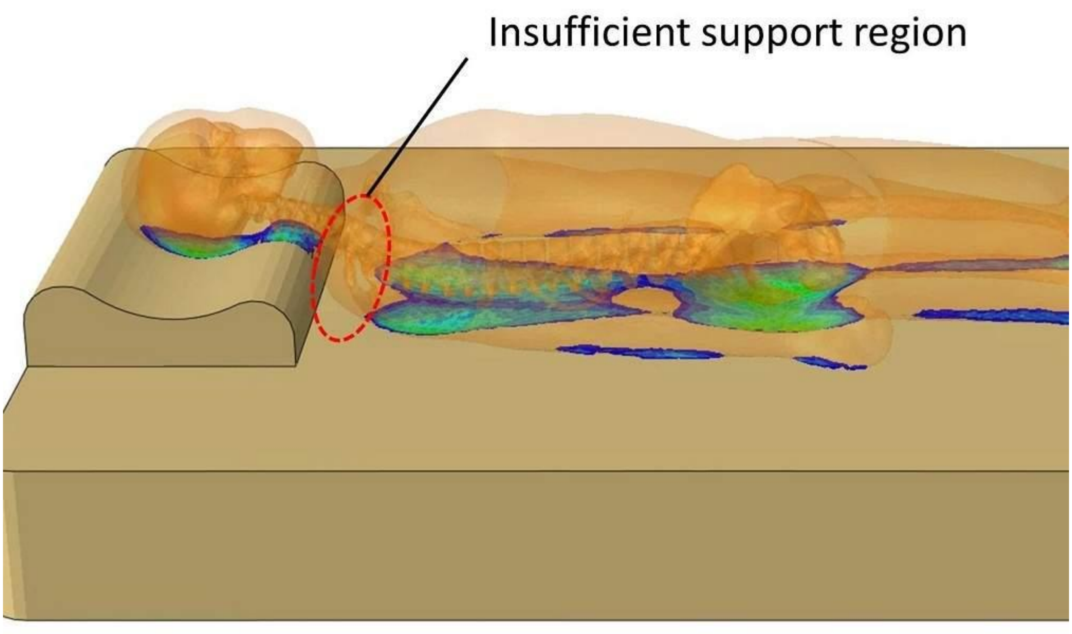

Figure 4.7. Illustration of insufficient support region (Hong et al., 2022).

The low edge of the cervical pillow was 90 mm in height (Figure 4.7). The considerable height of the cervical pillow is suddenly established on the surface of the mattress. Such sleeping support may not be the most suitable for the curvature of the human back.

Future development may vary the shape or material of pillows and mattresses to develop sleeping support systems that support the human body more evenly.

Chapter 5 Discussion

This study developed novel devices for external measurement of spinal curvature and internal prediction of intervertebral disc loading. Experiments were carried out with three mattresses of different stiffness, and spinal curvature was measured and compared.

The curvature measurement tape was constructed based on a tape of integrated inertial sensors. Sensors were assembled on the flexible circuit using surface mount technology to achieve low thickness and high flexibility. A new algorithm was developed during the device improvement phase to improve measurement accuracy. A new GUI was programmed to provide a real-time curvature display of the curvature measurement device. The concept of axial tilt was introduced, the tilt angle can be displayed on the GUI in real-time, and any abnormally tilted sensor will have a red cross warning on the GUI. Equipment testing was performed to evaluate equipment accuracy and understand the acceptable range of axial tilt. The device has been tested and validated and is believed to be able to obtain spinal curvature in the supine position.

A cervical pillow and three mattresses of varying stiffness were used for human experiments. The mattresses were hard, medium, and soft, with indentation load deflections of 120, 42, and 20 lbs. The volunteers were lying supine, and the curvature measurement tape was applied to obtain their spinal curvatures. Spine parameters were extracted by CAD software and compared. The experiment found that when lying supine on a soft mattress, the volunteers' head distance was raised by 30.5 ± 15.9 mm, and the cervical lordosis distance was raised by 26.7 ± 14.9 mm compared with the medium mattress. The head and cervical lordosis distances while lying supine on the hard mattress were similar to those of the medium mattress, but the lumbar lordosis distance was reduced by 10.6 ± 6.8 mm.

The FE method was adopted for the biomechanical analysis. Model validation was performed by comparing the measured spine curves with the predicted values of the FE model. As stated in the previous paragraph, the distance between the head and the cervical lordosis was increased when lying supine on the soft mattress. The FE model shows that when lying on the soft mattress, the peak disc loading was increased by 49% compared to the medium mattress environment. The lumbar lordosis distance was reduced when lying on the hard mattress. However, no significant rise in the peak loading of intervertebral discs was observed. The FE method also predicted the contact pressure between the human back and the sleeping support system. It was found that the contact pressure of the hard mattress scenario was significantly higher, which may lead to discomfort and an increased risk of health problems for the user.

5.1 Curvature measurement tape

5.1.1 Significance of the device

Spine alignment plays an essential role in sleep health, and spine misalignment can lead to neck pain (Blanpied et al., 2017; Genebra et al., 2017) or lower back pain (Chohan et al., 2019; Lam et al., 2022). The spinal curvature in the supine position can provide important biomechanical information (Haex, 2004) for assessing and improving sleeping health. However, the existing spinal measurement methods cannot effectively measure the spine alignment in the supine position. Although medical imaging methods such as MRI, CT, or X-ray scans can obtain the spine alignment in the supine position, limitations include limited scanning size and expensive. Pinpunched mattresses (Haex et al., 2020) have been used to measure spinal curvature in the supine position, but they are expensive, have low resolution, and have low accuracy. The curvature measurement method developed in this study can address the limitations and effectively measure spine alignment in the supine position.

This study proposes a new method based on existing research, which divides the whole curvature into multiple arcs. The sensor tape is 1.8 mm thick with highly flexible, and the measurement accuracy is high. In contrast, other studies have used too thick sensors, typically 10 mm in thickness (Stollenwerk et al., 2018). Measurements between the sleeping support system and the back of the human body need to minimize interference with posture (Haex, 2004). Too thick sensors significantly affect the measurement accuracy in the supine position; Hence, previous methods are not applicable.

Furthermore, this study proposes to monitor the axial tilt of the sensor tape, and the acceptable threshold was set to ± 30°. The axial tilt value of the sensor tape can be displayed on the GUI in real-time and alerts the operator when an abnormality occurs. This function can be used to understand whether the sensor tape is twisted, effectively preventing the sensor tape from twisting during the experiment.

Device validation has shown that the curvature measurement tape is accurate and reliable for measuring the spinal curvature in the supine position. Overall, this study provides a valuable device for future studies on spine alignment in the supine position.

When measuring spinal curvature in a standing or sitting position, it is recommended to place the sensor tape on the participant's back. For example, to evaluate the impact of carrying a backpack, sitting on a chair, or riding a bicycle.

In the supine position, the Sensor tape can be placed over the mattress and pillow for more effective spinal curvature measurement. Without the attachment of sensors to the participant's body, it will comfort the experience and reduce interference with the sleeping posture.

5.1.2 Comparison with literature

This flexible and thin curvature measurement device can measure the spinal curvature in the supine position with limited disruption to sleeping positions. The significant increases in the sensor quantity and novel algorithms tend to detect curvature more precisely. Here, the new device was compared with previous studies to understand the device's performance and applicability.

A commonly used method for measuring the spine curve is using a flexible ruler. The volunteer stood in a relaxed position with the back exposed. As shown in Figure 5.1(a), the flexible ruler was moulded into the midline profile of the spine, and then it was carefully removed and traced to a piece of paper. Finally, the spinal curvature was drawn carefully with the shape of the flexible ruler (Ajit Singh et al., 2018). However, this requires a skilled technician to manually adjust the flexible ruler with the back of the spine to replicate the spinal curvature. This method is not applicable for the measurement in the supine position because the back is covered.

In contrast, this study's curvature measurement tape with built-in 30 sensors can replace the traditional flexible tape. The spinal curvature can be quickly measured by placing the sensor tape on the volunteer's back.

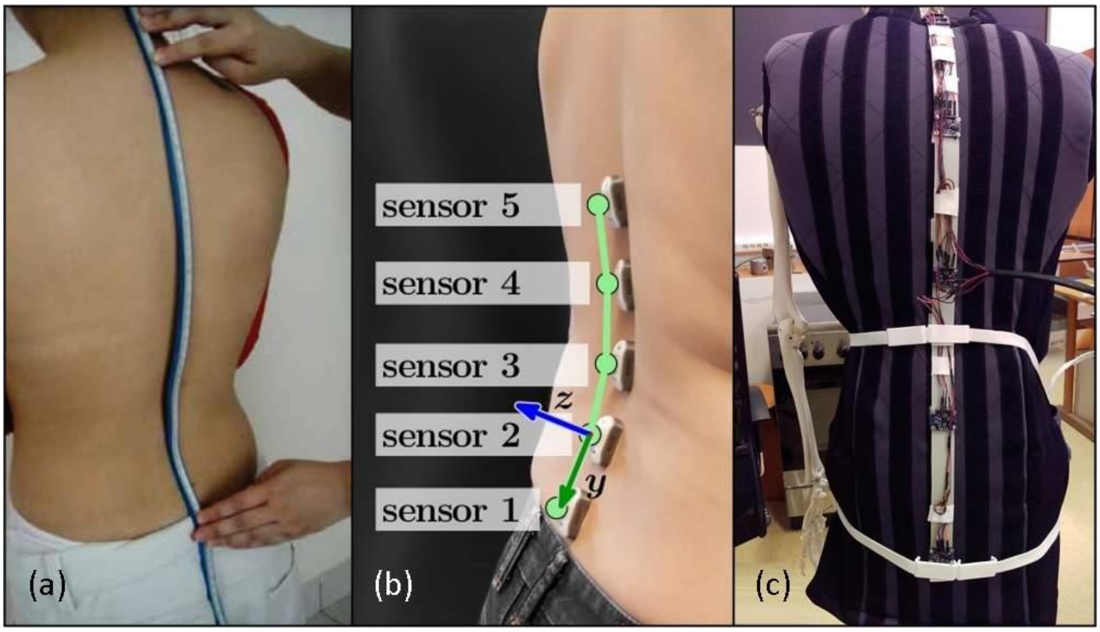

Figure 5.1. Measurement of spinal curvature by other studies. (a) Measurements of the degree of thoracic and lumbar lordosis using a flexible ruler (Ajit Singh et al., 2018); (b) Side view of sensor placement on the back (Ajit Singh et al., 2018); (c) Wearable spine monitoring with flexible straps (Voinea et al., 2017).

Previous research employed wearable devices to capture the alignment of the lumbar spine. Five IMUs were used in the study. The dimensions of each sensor were 33 mm × 16 mm × 10 mm (Stollenwerk et al., 2019). Double-sided tape attached all sensors to the volunteer's lumbar spine (Figure 5.1(b)). The system was developed for postural training to treat low back pain. The device demonstrates the ability to measure spine alignment using inertial units. However, the device's thickness makes it unsuitable for spinal measurements in the supine position. The sensor tape proposed in this study is only 1.8 mm thick, which can address this problem.

Another research has developed a wearable strap-like spine monitoring system. Five inertial sensors were installed at an equal distance on the flexible strap (Voinea et al., 2017). The shape of the curvature was reconstructed through a mathematical model. However, no human experiments were performed for the study. They plotted curves in a paper for error assessment and reported that the cumulative error could be low as 2.5 mm or 5% from the mathematical model.

On the other hand, their research did not simplify the circuit. As can be seen from Figure 5.1(c), multiple wires connected the sensor units. It will be a big challenge in the case of connecting a large number of sensors.

Therefore, various concepts and improvements were proposed in this study, such as the adoption of more sensors to reduce the measurement error to 1% (measuring a circle with a diameter of 200mm), the development of a concise and flexible circuit to lower the thickness of the sensor tape and provide high flexibility. Furthermore, this study introduced the concept of the management of axial tilt. These improvements bring clear benefits for spinal curvature measurement in the supine position.

5.1.3 Comparison with the preliminary version

The improved sensor tape has the same length and number of sensors as the preliminary version, but the improved version of sensor tape own a reduced thickness and increased flexibility. The thickness comparison of the two versions is shown in Figure 5.2. There are apparent differences in thickness, flexibility, and weight between the two. The preliminary version is constructed of 30 3D-printed plastic shells, and its' weight is over 300 grams. The improved sensor tape weighs only 33 grams, which creates a significantly differs when worn on the body.

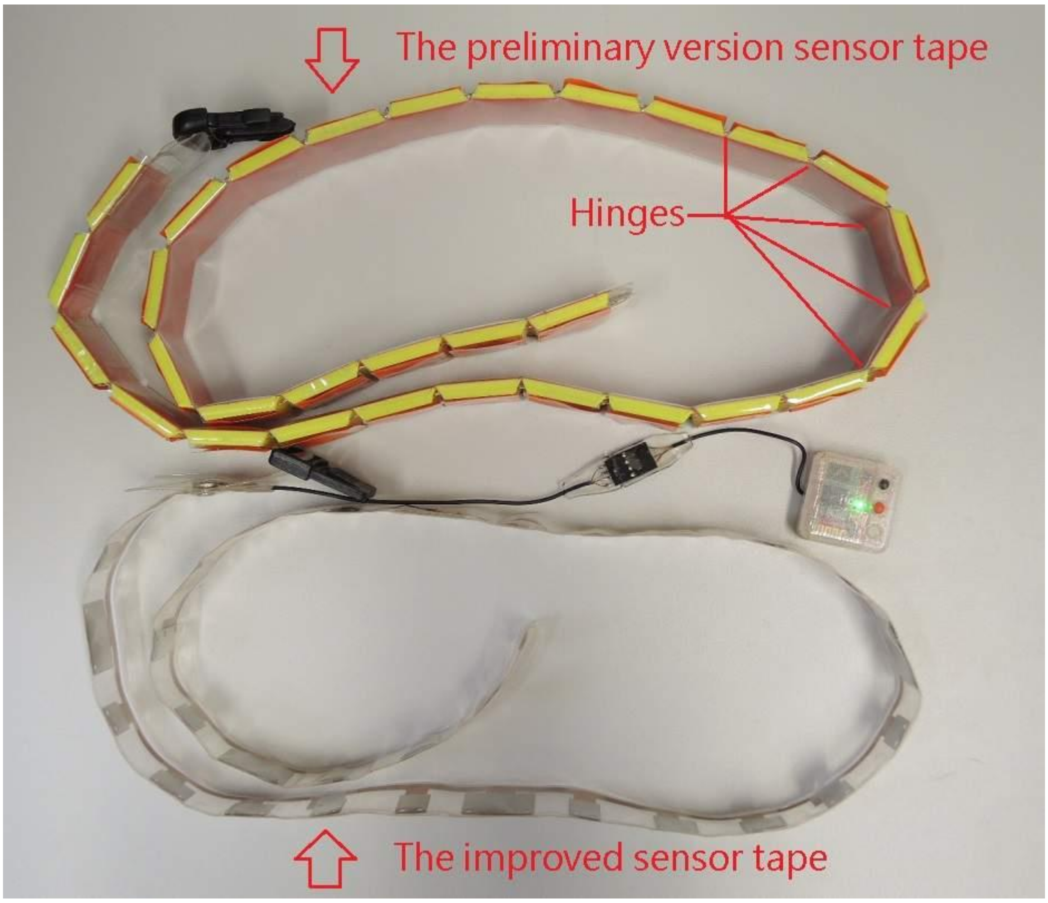

Figure 5.2. A comparison of two versions of sensor tape.

Since the initial version of the sensor tape used existing sensor modules, the size of an ADXL345 circuit board is 20 × 15× 3.3 mm, and the size of a TCA9548A circuit board is 31× 22× 2.6 mm. To develop a thin and flexible sensor tape, the size of the circuit boards is a big challenge. Based on the size of circuit boards, board holders were made by 3D printing. A pliable tape was used to link up board holders to form the sensor tape. The connecting hinges of the adjacent sensor units can be rotated, and it is the only place where the preliminary version of sensor tape can deform. The thickness of the sensor tape is 6 mm.

Since each sensor unit is rigid and non-deformable, it cannot be deformed according to the arc when measuring a curved surface. Figure 5.3 shows that gaps were created and caused measurement errors. As discussed in Section 3.1.5.4, when measuring a ø200 mm circle, the theoretical error is 1.12mm. More significant measurement errors occur when measuring smaller curvatures.

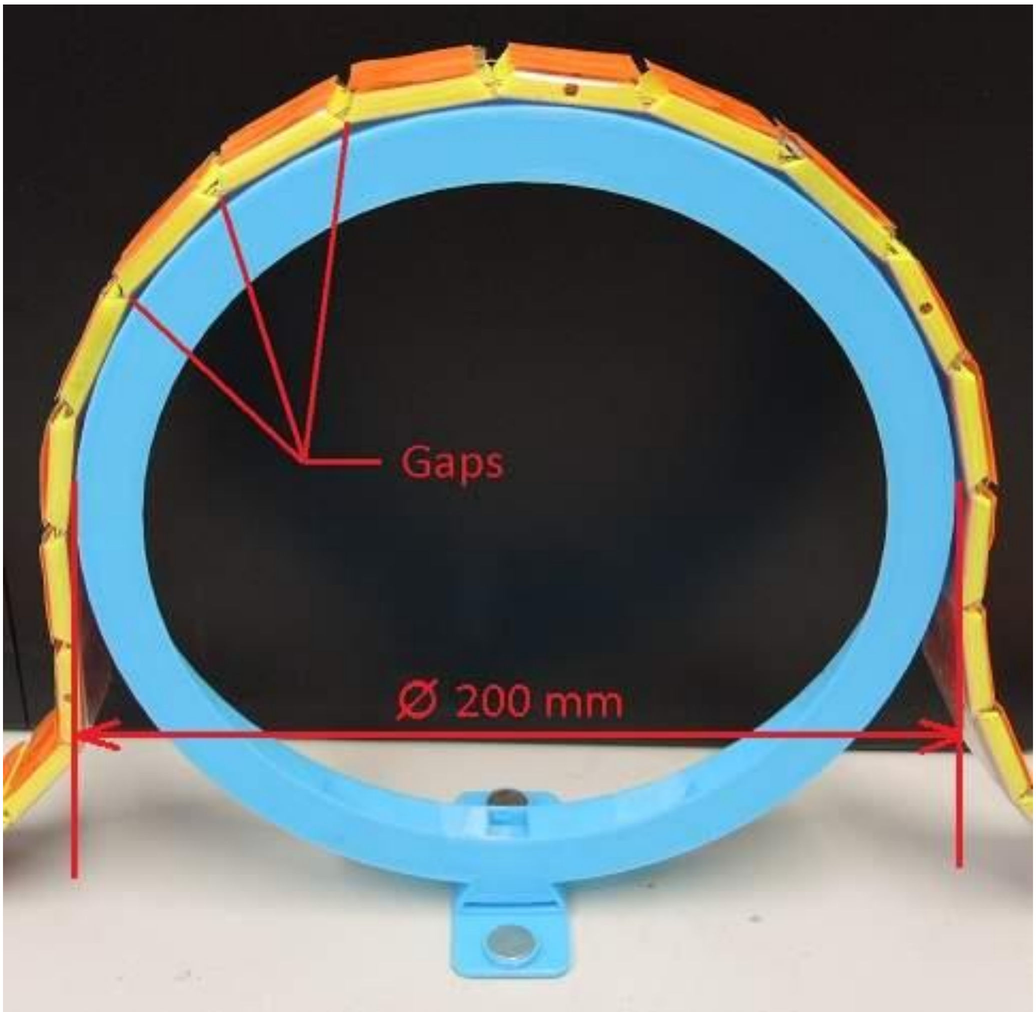

Figure 5.3. Gaps between the sensor tape and the measurement surface.

As shown in Figure 5.4(a), while using the preliminary version of sensor tape to measure a ø100 mm circle, the theoretical error is 2.24mm. The improved version of the curvature measurement tape can fit the measured object well with zero theoretical error since the sensor tape can deform according to the surface being measured (Figure 5.4(b)).

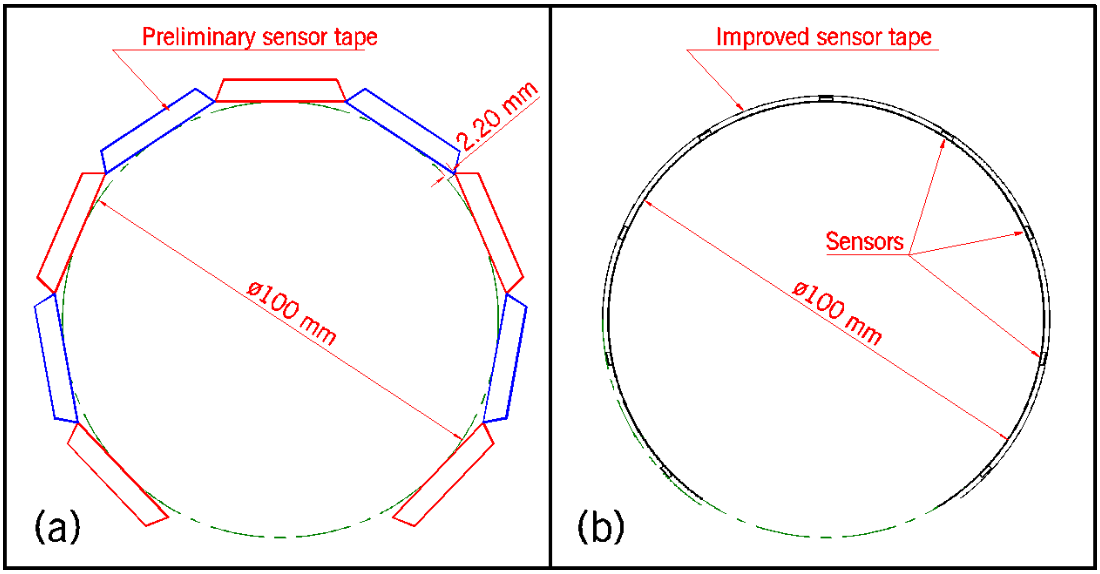

Figure 5.4. The sensor shape when measuring a ø100 mm circle. (a) The use of the preliminary version of sensor tape; (b) The use of the improved sensor tape.

The device shown in Fig. 3.8 & 3.7 is the preliminary version of the device. There are limitations, such as the sensor tape is still thick, about 5 mm in thickness; the sensor units were fabricated by rigid 3D-printed parts, and a single hinge connected the nearby sensor units to provide rotation of the sensor tape. An improved version of the sensor tape was developed and shown in Fig. 3.26. The improved version of the sensor tape adopted flexible printed circuits, achieving a high degree of flexibility with a reduced thickness. The 3-axis ADXL345 accelerometer can sense the pitch and roll. The pitch values were used for sensing the curvature, and the roll value of the individual sensor was used for twist control of the sensor tape.

Overall, the improved version of the curvature measurement tape is thinner and softer, the algorithm has been improved, and the monitoring of axial tilt has been innovatively developed, which beneficiate to the measurement of the spinal curvature in the supine position.

5.1.4 Cost and production feasibility

This study presents a new method for curvature measurement using highly customized components in hardware to lower device thickness, enhance flexibility, and enable real-time curvature display. The previous chapters described and discussed the device development process, including hardware development and programming. The precision and accuracy of the device have been evaluated, showing high measurement accuracy while the axial tilt between -30° to 30°.

Besides being used for spine measurements, the device can also measure other curvatures, especially masked surfaces, because measuring covered curvatures is incredibly challenging. The sensor tape contains 30 ADXL345 accelerometers. According to official information, each sensor costs $3.30. Other parts inside the device include the microcontroller, I^2C switches, resistors, capacitors and other electronic components. The device can cost less than $200 for components and assembly.

By comparison, each MRI scan already costs more than $200. Moreover, this device can be repeated use. Except for MRI scans, few methods can obtain the spinal curvature in the supine position. The system that pins pierced the mattress can measure spinal curvature in the supine position. However, customizing the bed with pins drilled from the top to the bottom of the sleeping support system is costly and suffers from low resolution and accuracy. Therefore, the device has obvious advantages in price and efficiency.

The circuit diagram of an individual segment of the sensor tape has been designed and described in Section 3.1.6. A few samples have been fabricated according to the specification of mass production (Figure 5.5).

Figure 5.5. Fabricated sensor segments.

Each device includes five sensor segments and a control box. The control box was designed and developed. The customized printed circuit board has been produced, and the electronic parts were assembled by SMT (Figure 5.6).

A 4-core wire connects the sensor tape and the control box. To avoid damage caused by the accidental stretch and facilitate maintenance, a 4-core connector was designed in the middle of the wire.

The controller housing used in this study was made with 3D printing. For small order quantities, it is possible to consider the production of controller housings with the same technology. In mass production, the controller housing can be produced by injection molding. Overall, this study has a high possibility of productization.

Figure 5.6. The printed circuit board of the control box.

5.1.5 Measurement length and resolution

This study presented a design for connecting multiple I^2C sensors through a concise electronic circuit. Every sensor segment contained a TCA9548A I^2C switch. Since an I^2C switch can provide eight different I^2C addresses, based on it, up to 8 sensor units can be connected in parallel without changing the circuit design. A long sensor tape was fabricated that contains eight sensor units. This long sensor has been tested and works properly.

This study found that downstream pairs of I^2C switches can be linked to devices with various I^2C addresses. Since one ADXL345 sensor can be defined with two different I2C addresses, eight downstream pairs of TCA9548A can connect sixteen ADXL345 accelerometers. In a design of eight I^2C switches connected in parallel, the circuit can connect 128 ADXL345 accelerometers. If the distance between adjacent sensors is kept at 30 mm, the device length reaches 381 cm while using the existing measurement resolution.

Reducing the distance between the sensor units will enhance the measurement resolution. The dimension of an ADXL345 is 5.0 × 3.0 × 1.0 mm; based on it, the distance of adjacent sensors can be reduced to 10mm. A higher-resolution sensor tape will help to obtain more details of the measurement surface. There are some smaller inertial measurement units on the market. For example, the size of an LSM303AGR (STMicroelectronics, Geneva, Switzerland) is 2.0 × 2.0 × 1.0 mm. A small sensor helps reduce sensor distance and enhance the measurement resolution.

Using chip-on-board (COB) technology is another way to fabricate the sensor tape to be slimmer and narrower. The dimension of an accelerometer chip is about 2.0 × 2.0 mm (Wang et al., 2020). If using COB technology to mount the sensor chips and I^2C switch on the FPC substrate directly (Figure 5.7), the sensor tape can be thinner, narrower, and higher resolution.

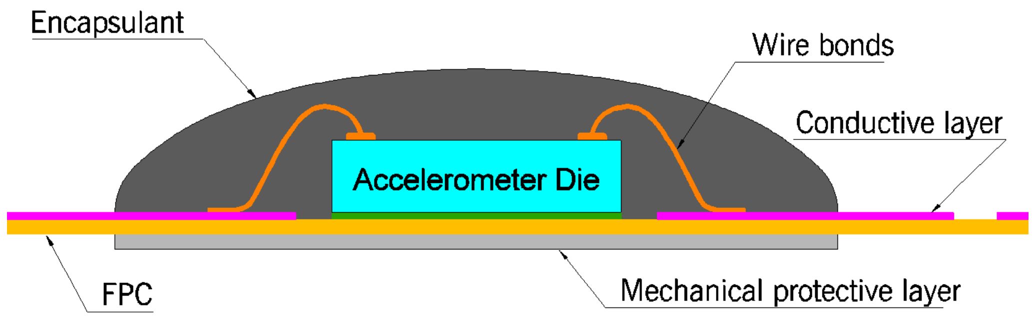

Figure 5.7. Illustration of a chip-on-board mounting to reduce the size of the sensor tape.

5.1.6 Measurement of compressed pillow height

As described in Section 2.2.3, compressed pillow height provides useful biomechanical information but remains challenging to measure. Since the skull and the mattress covered the pillow surfaces, the compressed pillow height is hard to measure. The curvature measurement tape developed in this study can measure covered curvatures, which can be used to measure the pillow height. The curvature measurement tape was placed in a circle along the centerline of the pillow. Therefore, the shape of the longitudinal section of the pillow can be measured in real-time (Figure 5.8).

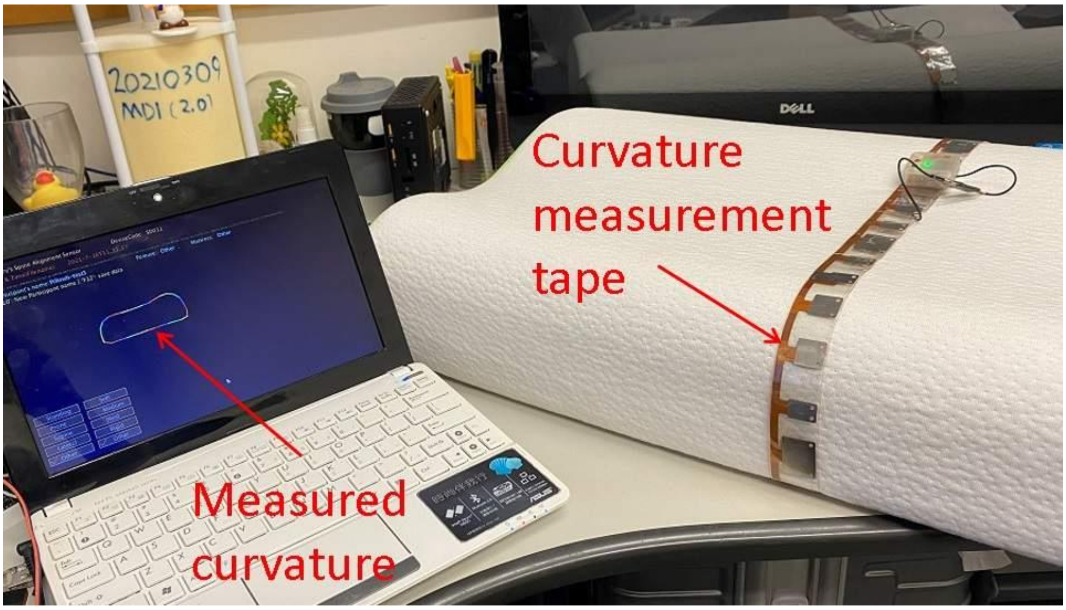

Figure 5.8. The placement of curvature measurement tape for pillow height measurement.

The experiment compared two cervical pillows of the same shape (Figure 3.39) but with different stiffness (pillow A: ILD = 40 lbs, pillow B: ILD = 28 lbs). Sixteen volunteers were lying on their backs and sides using the middle mattress.

In the lying position, the volunteer lay on the medium mattress with the cervical pillow for head support and their limbs aligned with the body. Data collection was performed after the sleeping position was stable. The sectional curvature of the compressed pillow was collected through the curvature measurement tape.

Preliminary results are shown in Figure 5.9. Although the outer dimensions are the same, the compressed height of the soft pillow was approximately 10 mm less than that of the hard pillow.

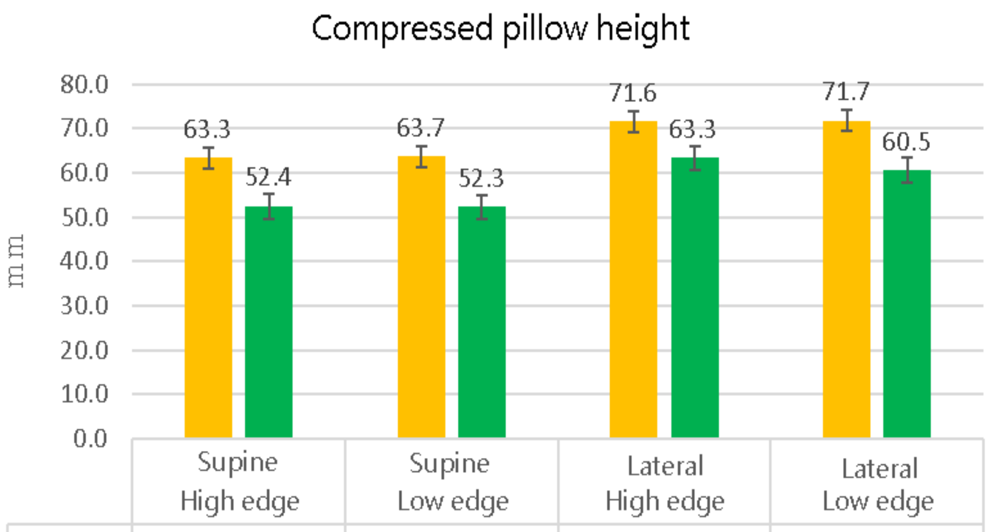

	Supine High edge	Supine Low edge	Lateral High edge	Lateral Low edge
Pillow A	63.3 ±6.02	63.7 ±5.72	71.6 ±6.02	71.7 ±5.98
Pillow B	52.4 ±5.81	52.3 ±5.20	63.3 ±6.47	60.5 ±4.56

Figure 5.9. Compressed pillow height of pillow A and pillow B.

5.1.7 Measurement of spinal curvature in other aspects

In addition to measuring spinal curvature in the supine position, the curvature measurement tape can be used to obtain spinal curvature in standing or sitting positions. In some cases, it is necessary to assess the obscured back to obtain biomechanical information. For example, the impact of backpacks on the spinal curvature or how different seats change the curvature of the spine. Future studies can use the curvature measurement tape to obtain spine curvature for these scenarios.

5.1.8 Dynamic response

Compared with motion analysis systems such as the Vicon system, The developed sensor tape is compact, portable, fast-setup, cost-effective, and able to be used in a covered environment. Since the curvature measurement tape is designed for sleeping analysis, which requires static data collection. Therefore, the device run in low frequency and low power consumption mode. The sample rate of the developed device is five frames per second. However, motion analysis requires the ability to capture dynamic data. ADXL345 accelerometer can run in a high sampling mode of 3200 Hz (Holovatyy et al., 2017), and the TCA9548A I^2C switch runs up to 400,000 Hz clock frequency. Therefore, the curvature measurement tape has the potential for dynamic data collection.

5.1.9 Three-dimensional measurement

Since MEMS accelerometers sense gravity at static status, a 3-axis accelerometer can obtain its pitch and roll but cannot measure the yaw. In recent years, 6-axis sensors combining accelerometers and magnetometers in a single package have been developed (Figure 5.10(a)). For example, an FXOS8700CQ (NXP USA Inc, Austin, USA) sensor.

The 3-axis magnetometer can sense yaw, a combination of the 3-axis accelerometer and the 3-axis magnetometer can sense its orientation in 3-dimensional space. The sensors were placed inside a thin, flexible tube with a fixed distance between two nearby sensors. Two nearby sensors formed an angle due to the deformation of the tube. The three-dimensional angle detected by two nearby sensors will derive a plane that the arc can be established based on the sensor data (Figure 5.10(b)). The connection of multiple 2D arcs can create a 3D curvature.

Benefiting from the rapid development of chip technology, the chip size of this sensor is 3 × 3 × 1 mm. Such a compact size facilitates the development of a slim sensor tube.

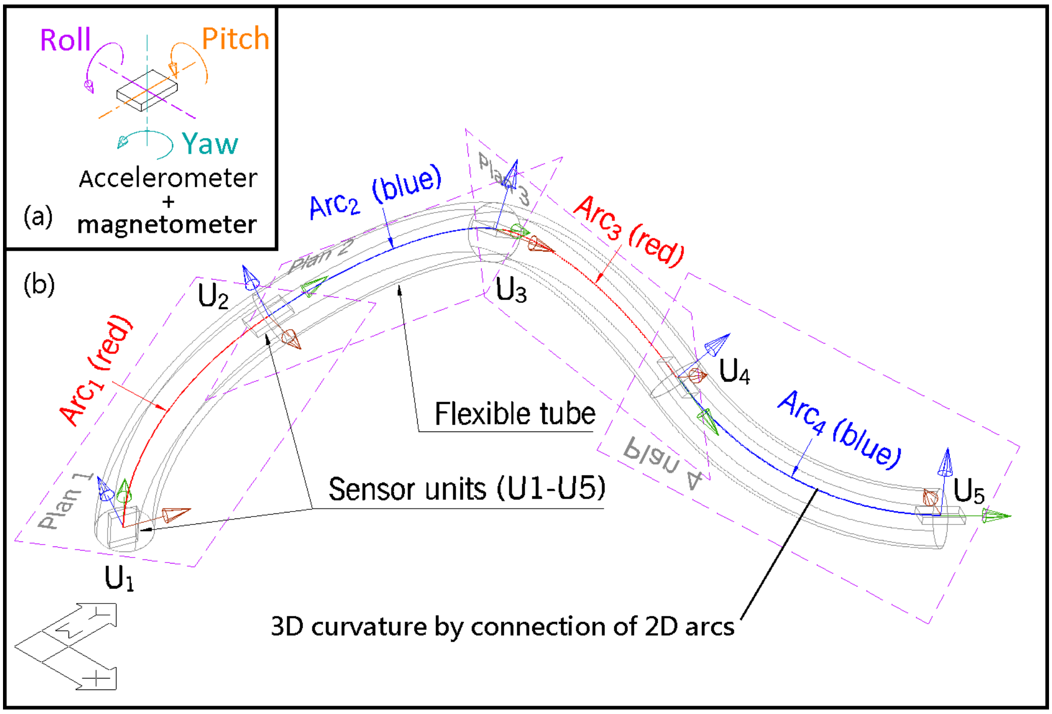

Figure 5.10. (a) The pitch, roll, and yaw detection of a 6-axis sensor; (b) Three-dimensional curvature measurement design concept (Hong et al., 2022).

The 3D curvature measurement function may have a variety of application scenarios, such as measuring scoliosis, measurement of spine alignment in three-dimensional during a lying position, or being integrated into an endoscope to measure the shape of a robotic arm in real-time.

5.2 Experiments

5.2.1 Changes in the craniocervical region

Experiments were performed while lying supine on three mattresses of different firmness, with the head supported by a cervical pillow. The curvature measurement device was adopted to obtain the spinal curvatures. When lying on the soft mattress, the trunk sinks deeper into the soft mattress, causing an increase in the head and cervical lordosis height, thus resulting in a high loading on the cervical discs.

Although the experiment involved the same pillow, the pillow appeared more supportive when placed on the soft mattress. The weight of the craniocervical results in a loading applied to the top of the pillow; the loading then spreads through the foam material. The loading exhibits a larger force area and lower pressure at the bottom of the pillow (Figure 5.11). The dispersed, weaker loading leads to a minor deformation of the craniocervical region on the mattress. From the material test (Figure 3.48), there were similar mechanical properties between the cervical pillow and the medium mattress, while the soft mattress was much weaker. In this case, the stiffer pillow act as a hard plate to spread the weight of the head and neck. From the FE calculation, the contact area of the head and neck region was about 272 cm^2, and the area of the occipital base was $55 \times 35 = 1925$ cm^2. Due to the increased support area and reduced pressure, the mattress under the pillow deforms less than in other regions.

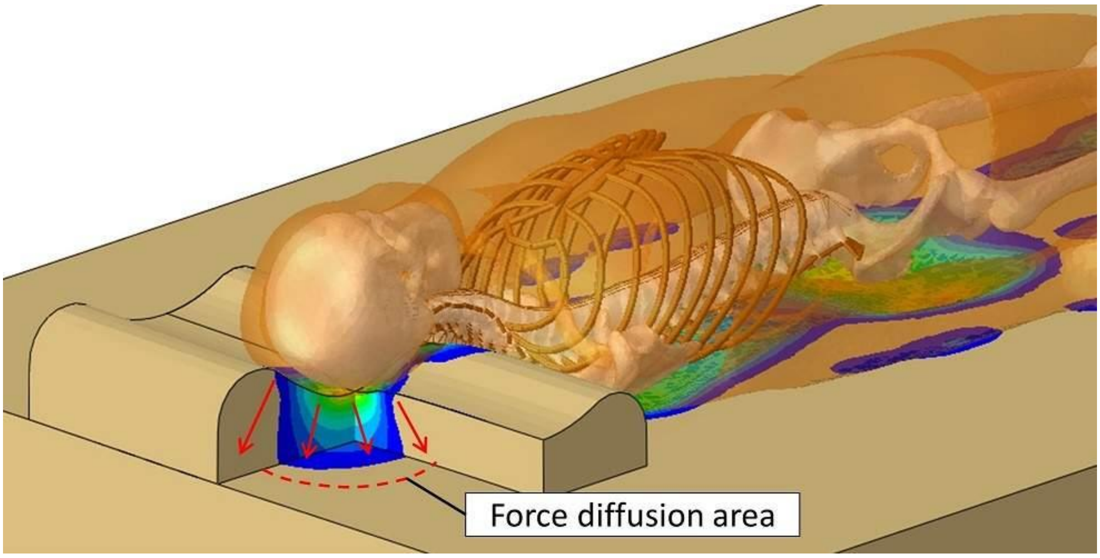

Figure 5.11. Spread of the load inside the pillow (Hong et al., 2022).

5.2.2 Changes in the lumbar region

Since the hard mattress deformed too little, the lower back was suspended while lying supine on it. As a result, gravity pulls the abdomen down, resulting in flattened lumbar lordosis. The lumbar lordosis distance was reduced by 10.6 mm compared to the medium mattress environment. The FE analysis showed that the loadings on the lumbar intervertebral disc did not increase significantly. It can be considered that a hard mattress has no significant impact on the health of the lumbar spine.

However, the FE results show that the contact pressure of the body to the hard mattress was higher than on other mattresses, especially in the upper back and hip regions. While lying supine on the hard mattress, peak pressures of the torso were 3-4 times higher than lying on the medium mattress. High contact pressure can cause discomfort and even skin ulcers (Schubert & Heraud, 1994). Hence, mattresses that are too hard are considered unsuitable.

5.3 Finite element model

Finite element analysis provided some prediction data that were challenging to obtain by experimental measurements, including the cross-sectional view of the human body, the loading on the intervertebral disc, and the contact pressure between the human back and the sleep support system. These computational results help to understand the causes of the changes.

5.3.1 Soft tissue deformation

The computational method predicted the contact pressure between the back of the FE model and the sleeping support system. The results showed that the contact pressure was generally high when lying supine on the hard mattress, especially in the upper back and hip regions. Conversely, lower contact pressure was usually found if supine on the soft mattress. The only exception was the cervical region, where the peak pressure measured on the soft mattress environment was obviously higher than that of the other two sleeping support systems. According to the findings in Section

4.1.1, the craniocervical region was elevated higher in the soft mattress environment. It leads to a high contact pressure between the craniocervical region and the pillow. Therefore, measuring the contact pressure of the craniocervical region makes it possible to realize whether the relevant area was excessively elevated.

The contact area is another output of the FE analysis. There is a marked difference in the contact area of the human model lying supine on the soft, medium, and hard mattresses. A mattress that is too soft makes the human body sink deeply, which may bring about heat dissipation and ventilation problems. Although the contact pressure is low, it may not be comfortable. Previous research has shown that sleep quality was improved when using a sleeping system with a moderate pressure distribution (Chen et al., 2014). Therefore, the medium mattress can be considered more suitable for use.

5.3.2 Limitations of the finite element model

The human body involves complex structures in which bones, muscles, tendons, ligaments, fascia, and skin have major biomechanical impacts. To improve the accuracy of the computational simulations, the FE human model developed in this study involves the skull, 24 pieces of vertebrae, 24 pieces of intervertebral discs, major ligaments surrounding the spine, and a bulk soft tissue representing the whole body. However, it does not take into account the muscles and assumes that all muscles were relaxed in the supine position. It is undeniable that some involuntary muscles contribute to the stabilization of the spine and body in the supine position. Further research should be conducted to develop computational models that involve muscle tissue to achieve a higher degree of computational accuracy.

Tetrahedral and hexahedral elements are most commonly used in FE methods. When dealing with complex anatomical structures, generating hexahedral meshes is time-consuming due to the geometric complexity introduced by branching and embedded structures. Tetrahedral meshing is the preferred method for FE analysis as it is easier to automate (Zafarparandeh et al., 2014). Each linear tetrahedral element (C3D4) has only four nodes, requires less computer cost, and is widely used (Hu et al., 2017; Jiang et al., 2021; Zhang et al., 2021). In comparison, ten-node quadratic tetrahedral elements (C3D10) have the advantage of deformation. However, previous studies have found that models meshed with quadratic tetrahedral elements required expensive computation power and raised the calculation time by around three (Tadepalli et al., 2011). This study adopted linear tetrahedral elements to ensure the computability of this complex model. With the enhancement of computing power, future research should try meshing with quadratic tetrahedral elements to improve mesh convergence.

This study obtained the pressure distribution of intervertebral discs by computational estimation. The computer-predicted results can be used as references for evaluating sleeping support systems. However, in vivo validation of computer-predicted disc loads requires the installation of pressure transducers in every intervertebral disc of the volunteer, which is controversial in ethics review.

A previous study in vivo measured the L4-L5 intervertebral disc loading in a prone position with eight healthy participants, and the measured result was 90 ± 27 kPa (Sato et al., 1999). The results predicted by the computational simulations show agreements with the in vivo measurements.

5.4 Future development

A sound sleep support system provides a comfortable sleeping environment and benefits musculoskeletal health. A sleep position sensor is proposed here, which can be used for sleep measurement in different postures and provides experimental data for product improvement.

5.4.1 Sleep position sensor

In this study, the curvature measurement tape was developed to reveal the deformation of the spine in the sagittal plane. However, as stated in Section 2.2.4, the spine's deformation occurs not only by the stretching and compression of the intervertebral discs but also by twisting the intervertebral disc endplates. Rotating the spine results in twisting intervertebral discs in the transverse plane. It occurred in the rotation of the head, chest, and hip.

The sleep position sensor contains three wearable sensors to measure the relative angle between the head, chest, and pelvis. Figure 5.12 shows the three inertial sensors connected with flexible wires. These three sensor units were named head, chest, and pelvis sensor; the pelvis sensor was the largest one since it was integrated with the control box.

There is an elongated hole on both sides of each sensor unit, which is designed for the sensor unit's fixture on the human body's surface. The medical plaster can easily pass through these two elongated holes and attach the corresponding sensor unit on the chin, chest, and lower abdomen.

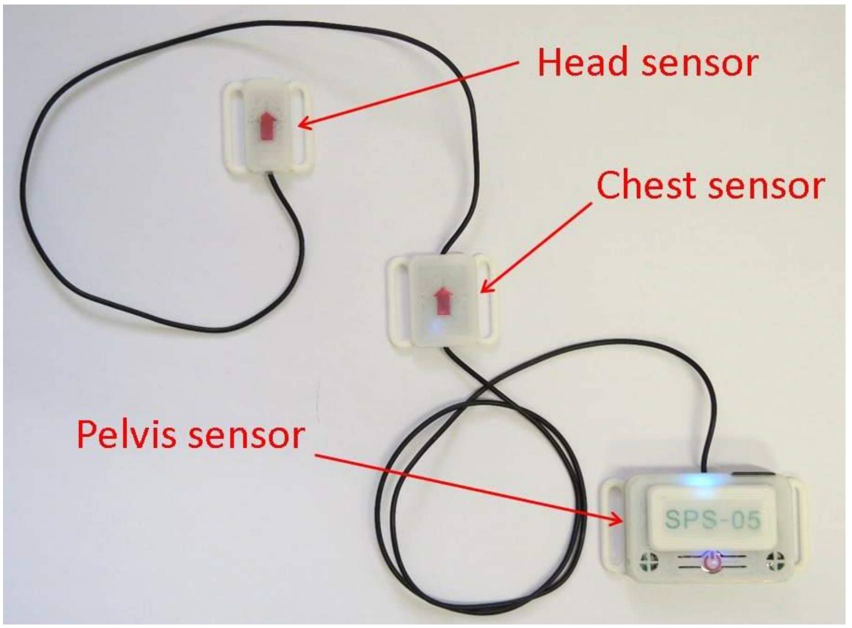

Figure 5.12. Three sensors of the sleep position device.

The circuit board of the control box was designed and fabricated in a compact size; as shown in Figure 5.13, the outer dimension of the PCB is 24.8 ×39.9 mm.

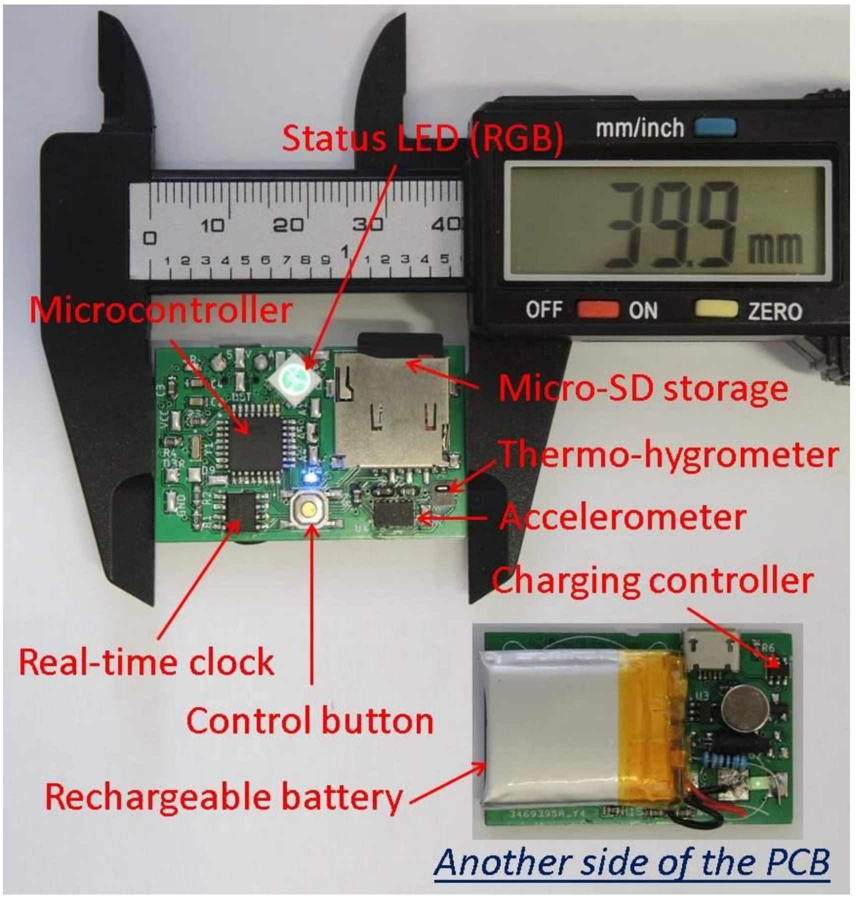

Figure 5.13. Illustration of the PCB used in the sleep position device.

The head sensor only contains a MEMS accelerometer, and the sensor size can be relatively compact. Considering the device may be used for sleep analysis and sleep posture detection throughout the night, the head sensor was designed to be attached to the chin position of the subject's mandible (Figure 5.14) to minimize sleep disturbances. The mandible is connected to the skull by the Temporomandibular joint, which is considered a rigid body when the mouth is closed.

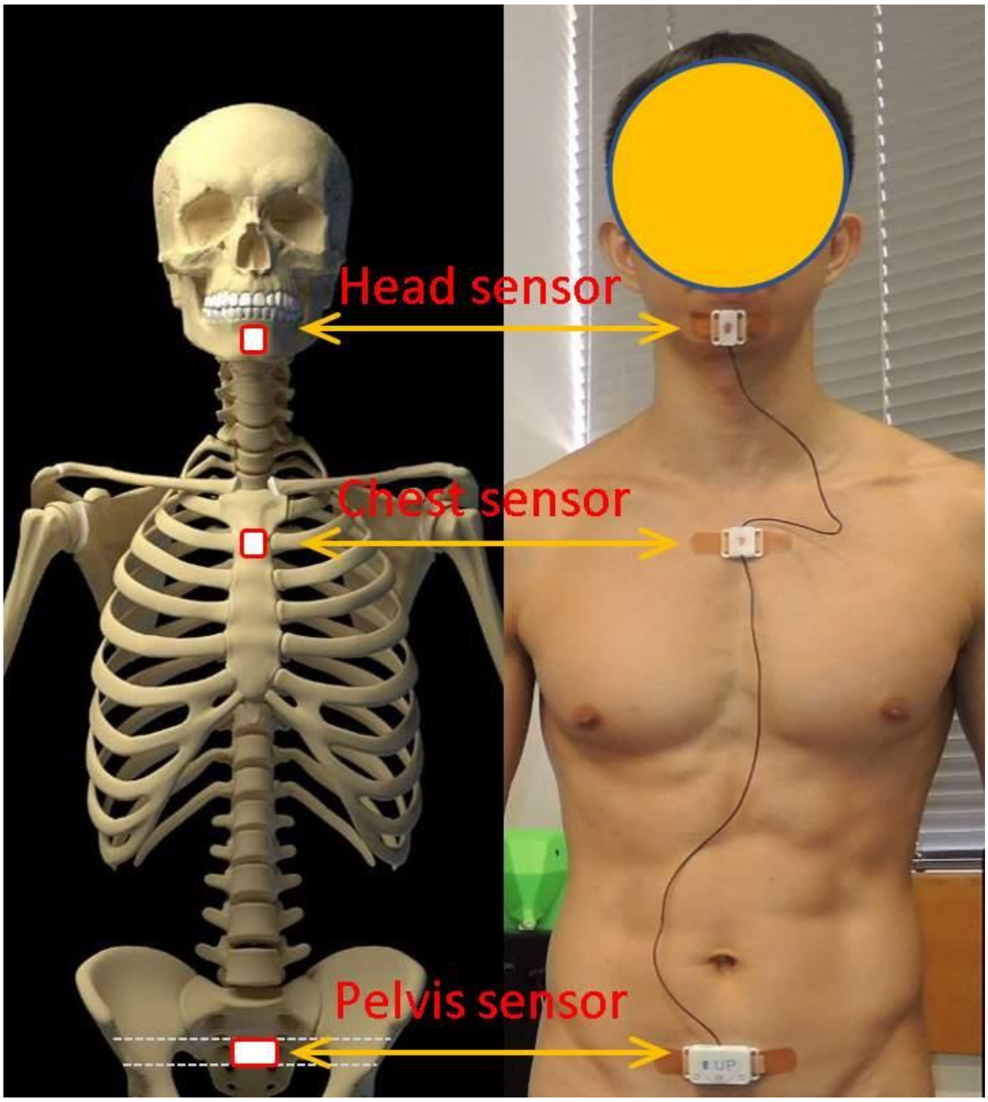

Figure 5.14. Sensor locations of the sleep position device.

The chest sensor was designed to be attached to the manubrium. An MPU6050 (TDK, Munich, Germany) inertial sensor was used for the chest sensor to avoid the same I^2C address in the system since two ADXL345 were used and occupied all available I^2C addresses. Using the MPU6050 has an extra benefit as this sensor has a built-in thermometer. The body temperature of the volunteer's chest can be measured and recorded. Body temperature can be a valuable reference when used for sleep analysis throughout the night.

The pelvis sensor was integrated with the control box. It was designed to be attached below the belly button or fixed on the pants. The inertia sensor used was an ADXL345. The control box contains a microcontroller, Bluetooth module, real-time clock, thermo-hygrometer, memory card holder, charge controller, and a rechargeable Lithium battery. The sensor's data can be transmitted via Bluetooth and viewed in real-time on the computer. The data can also be recorded on a Micro-SD memory card for subsequent processing.

5.4.1.1 Graphical user interface

A graphical user interface was developed using the Processing program (Figure 5.15). Several 3D objects were created, mainly involving a head, chest, and pelvis model. These models can be rotated in real-time by the program based on data received from the sensors of the sleep position device.

Since each volunteer has unique physical characteristics, the location of the sensors may differ from previous attachments. Therefore, a sensor attachment calibration procedure was developed. Figure 5.16 shows that all sensor axes were set to parallel the anatomical plane when performing the calibration procedure. The sensor's *x*, *y*, and *z* axes parallel the volunteer's coronal, transverse, and sagittal planes.

The graphical user interface design includes the function of recording experimental information. The saved information includes the volunteer's name, lying position, sleeping support system, and experiment duration (Figure 5.15). Among them, the body posture of the volunteer was automatically recognized by the program based on the inclination and orientation of the chest sensor. Data can be saved in text format through the software package, allowing subsequent analysis by other software.

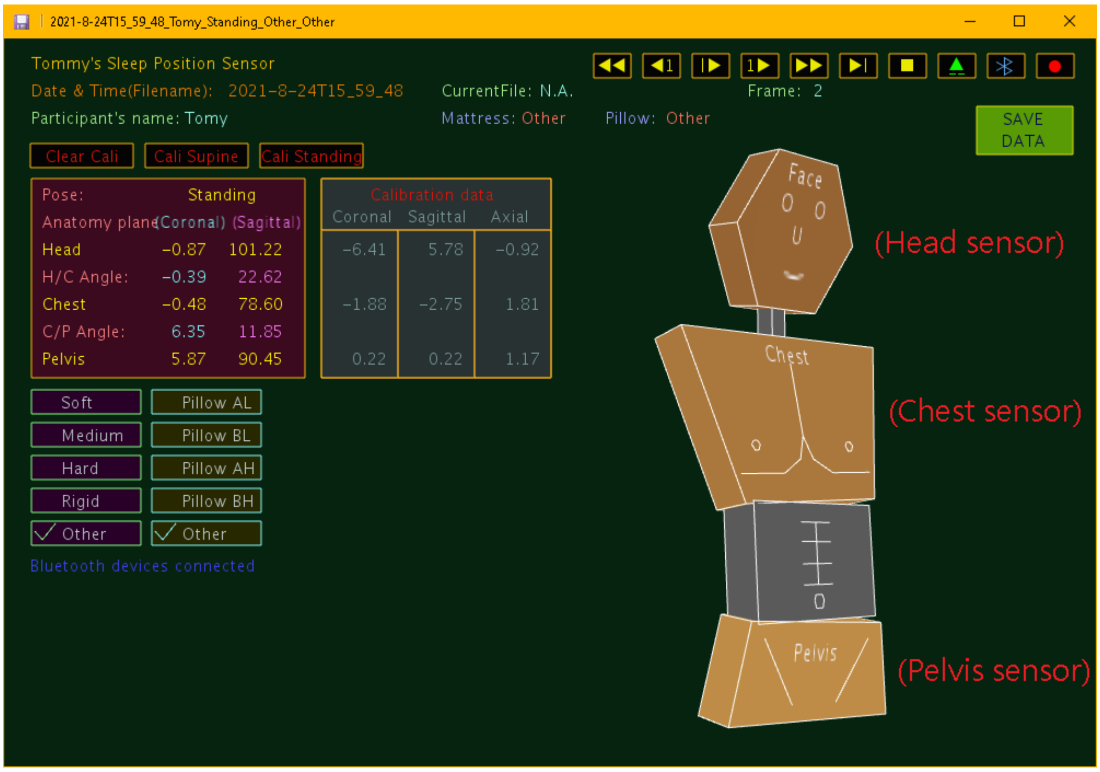

Figure 5.15. The graphical user interface of the sleep position device.

The sleep position sensor can be attached to the human body to record sleep positions throughout the night, and the data interval is 10 seconds. The upper right corner of the GUI is the operation of data playback.

While the recorded data is copied from the Micro-SD card to the computer, the software package reads and plays the recorded data. It can continuously replay the sleep postures of the whole night or show the frames one by one to facilitate subsequent research.

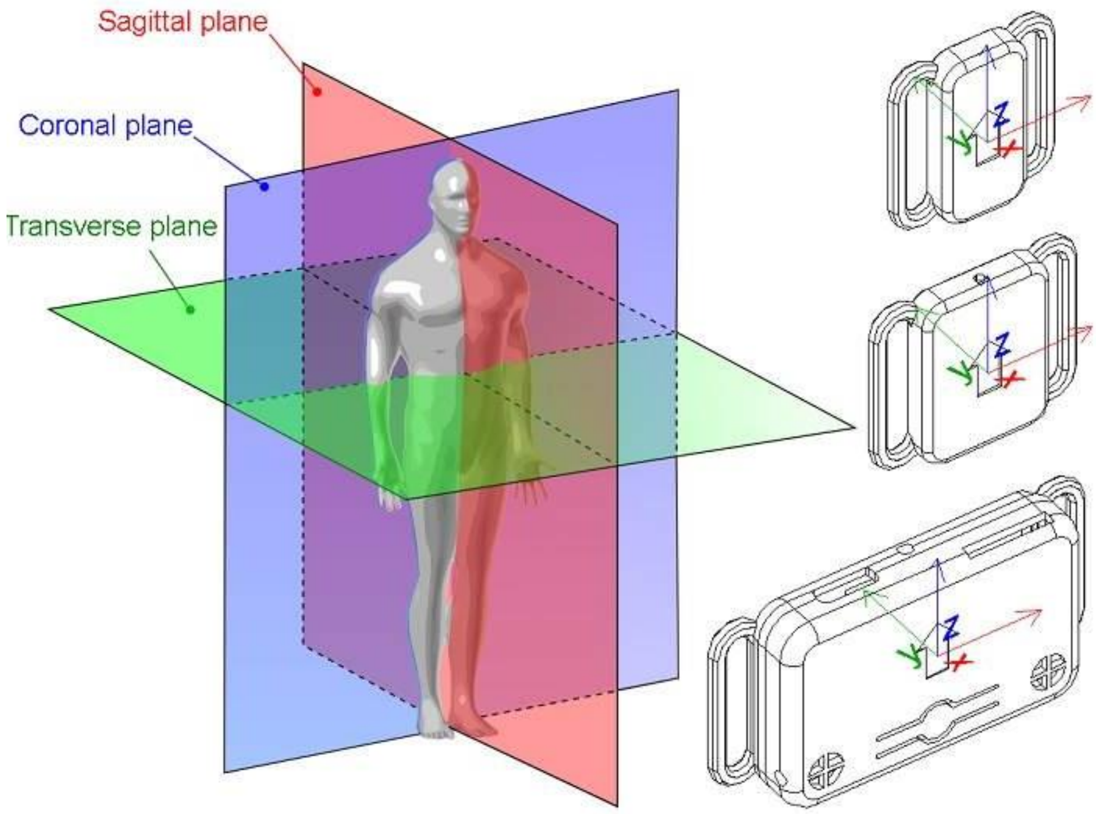

Figure 5.16. Illustration of the calibration for sensors attachment biases (the left side of the figure from Wikipedia (Zuccarello, 2012)).

After calibration, the angular changes of the three body segments of the head, chest, and pelvis can be measured during the change of postures. Based on the characteristics of the three-axis accelerometer to measure the inclination angle, the angle of the body in different anatomical planes can be calculated under different body postures. When standing, the inclination of the sagittal and coronal planes can be measured.; when lying supine, the inclination of the sagittal plane (Figure 5.17(a)) and the transverse plane (Figure 5.17(c)) can be measured; when lying lateral, the inclination of the coronal plane (Figure 5.17(b)) and the transverse plane can be measured.

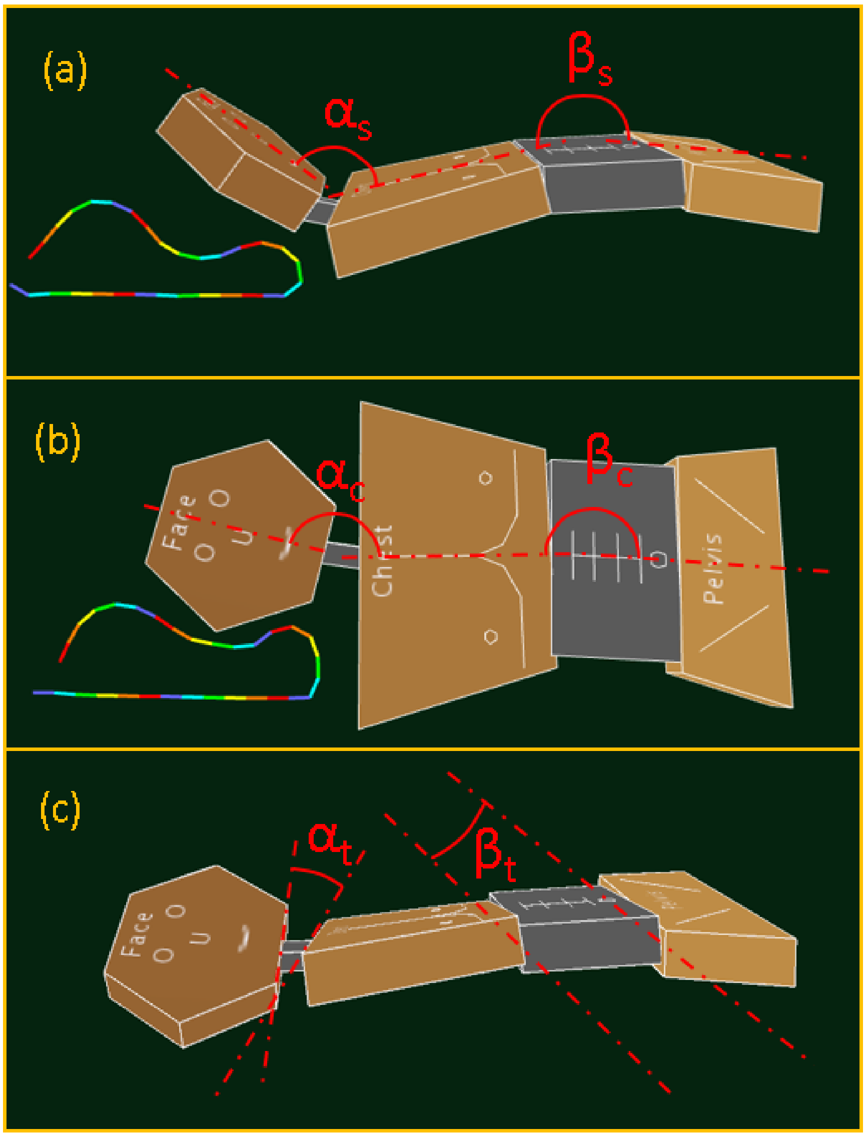

Figure 5.17. Illustration of different measurements under various body postures. (a) measurements in the sagittal plane; (b) in the corona plane; (c) in the transverse plane.

5.4.1.2 Application

The sleep position device was designed for two uses. First, this device can be used to evaluate sleeping support systems. In the experiment, sleeping support systems can be investigated and compared. The data collection was conducted based on controlled sleeping positions, such as supine, lateral, and prone. Section 5.4.1.2 presents the ability of this device to collect data in different anatomy planes. For example, in a lateral lying experiment, the angle between the head and chest (α_c) and the angle between the chest and pelvis (β_c) in the coronal plane were measured (Figure 5.17).

According to past research, an optimal sleeping support system should keep the spine in a straight line if look from the coronal plane. Therefore, the preferred values for both α_c and β_c should be 180°.

Another use of the sleep posture device is the overnight measurement of sleep posture. The volunteer wore the device throughout the night, and the device saved data to the Micro-SD memory card at a few seconds intervals. The volunteer was sleeping in unrestricted sleeping positions. The recorded data includes the inclinations of the head, chest, and pelvic sensors, the chest sensor's temperature, and the pelvic sensor's temperature and humidity. The measured data can be used to understand the volunteer's sleep habits and for sleep health assessment.

A pilot trial was carried out with the prototype of the sleep position sensor. A volunteer wears this device to record the sleep position overnight. As shown in Figure 5.18, the resulting graph sounds like that described in the literature (Koninck et al., 1992). The volunteer's sleeping position changed dozens of times during the night. It can be found that the volunteer's head was rotated during the supine position, which appeared on the timeline of the resulting graph 00:50-01:40, 03:10-03:35, and 06:50-07:10. The yellow line and the blue line indicate that the volunteer was lying flat. Still, his head (pink line) was rotated at a certain angle. This phenomenon is worthy of further study.

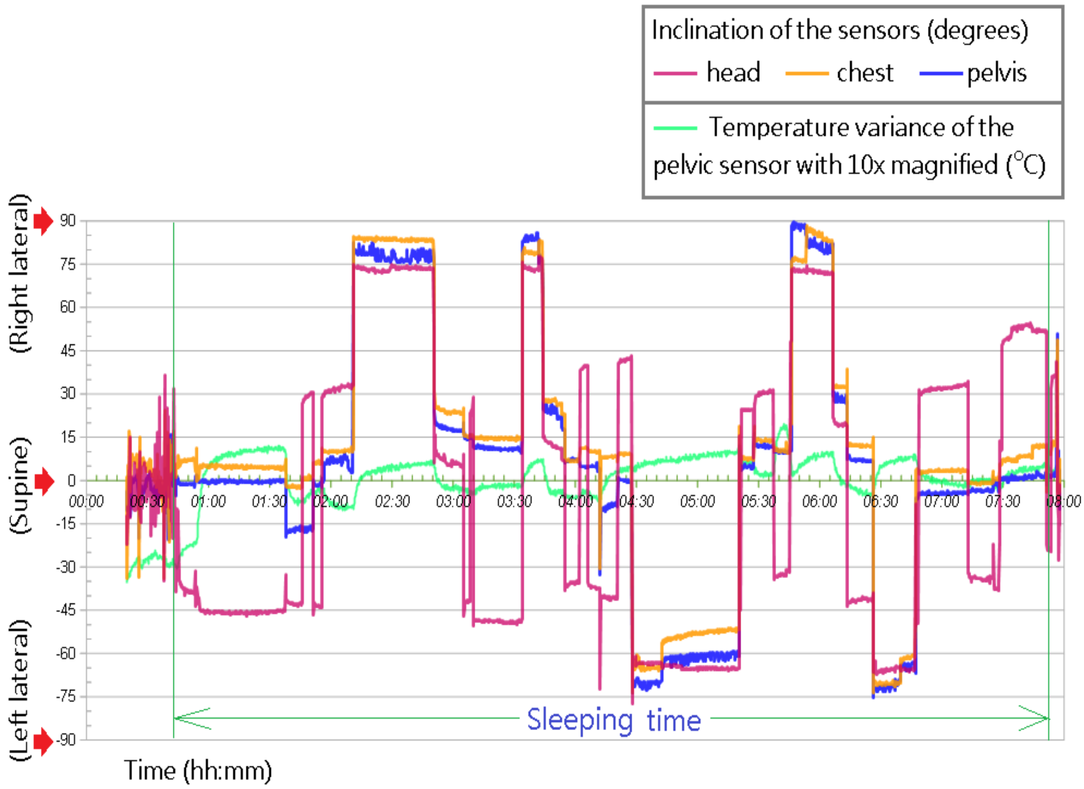

Figure 5.18 Result graph of a pilot run of the sleep position device.

The device records data from each sensor at 10-second intervals and stores it on the Micro-SD memory card. The pelvis sensor has the function of recording temperature and humidity. The temperature variance was presented in the result graph. This study found an interesting phenomenon: increased body temperature usually results in a change in sleep posture.

Overall, preliminary tests demonstrated the uniqueness and functionality of the device. The advantages of this device include small size, ease of use, low cost, measurement of a variety of data, and overnight recording. However, device validation is required before subsequent experiments can be performed.

5.4.2 Experiments

This study focused on comparing mattresses of various stiffnesses. However, the material's stiffness is not the only issue that influences the performance of the sleeping support system. There are multiple types of mattresses on the market; the common ones are spring, foam, fiber, and air-bag mattresses. The structure of a spring mattress can be an innerspring or pocket spring mattress; materials used for foam mattresses can be divided into memory foam, latex foam, polyester, etc. Additionally, many mattress structures incorporate various materials in different areas or layers.

Pillows can be made from various materials—for example, foam, polyester, cotton, latex, and feather. Different materials impact sleep quality and duration (Radwan et al., 2020). Except for the type of material, the pillow shape is another critical element of pillow design as it provides a level of craniocervical support and the overall comfort of the user. Future research can evaluate sleeping support systems with different types, shapes, materials, and brands.

Although females and males are different in physiques, a previous study showed that gender and pillow height had no significant interaction with craniocervical pressure (Ren et al., 2016). Besides, seldom have gender-specific beddings been launched on the market. Therefore, this study did not consider gender. Overall, this study was based on adults, the findings and suggestions may not be suitable for kids. Nevertheless, the impact of sleeping support systems on kids is worth investigating since they are going through a rapid growth period, and sleeping support systems may influence their growth.

5.4.3 Design improvement

5.4.3.1 Choose a pillow of the proper height

This study found that mattress stiffness significantly impacts head and cervical support. When lying supine on the soft mattress, the trunk sinks more than the craniocervical area. As a result, the head and neck were raised.

Predicted by FE analysis, the elevation of the craniocervical region increases intervertebral disc loading. It may increase the risk of neck pain. Although the stiffness of the mattress is a personal preference, it is necessary to consider the impact of spine alignment when choosing a sleeping support system. Also, there is room for improvement in product design. For example, the stiffness or ILD value of the pillow and mattresses can be labeled, and the consumer can choose a similar stiffness of pillow and mattress. The pillow core inside the pillow cover can be composed of multiple layers. The user can adjust the pillow's height according to the curvature measurement tape data to reasonably support the head and neck.

5.4.3.2 Development of a pillow with upper back support

As stated in Section 4.2.4, the study found the B-shaped cervical pillow, which shown in Figure 5.19(a), may not provide sufficient support for the upper back. A new design of cervical pillow was proposed to improve the upper back support.

As shown in Figure 5.19(b), the width of the new pillow has been increased, with an extension of 50 mm in the pillow's cross-sectional width to support the upper back of the human body. The expected increase in support area is shown in Figure 5.19(c).

However, this design should be verified experimentally. People usually change their sleeping positions during the night, and the most common sleeping positions include supine and lateral. The effect of the new design on lateral position also needs to be evaluated and verified by experiments.

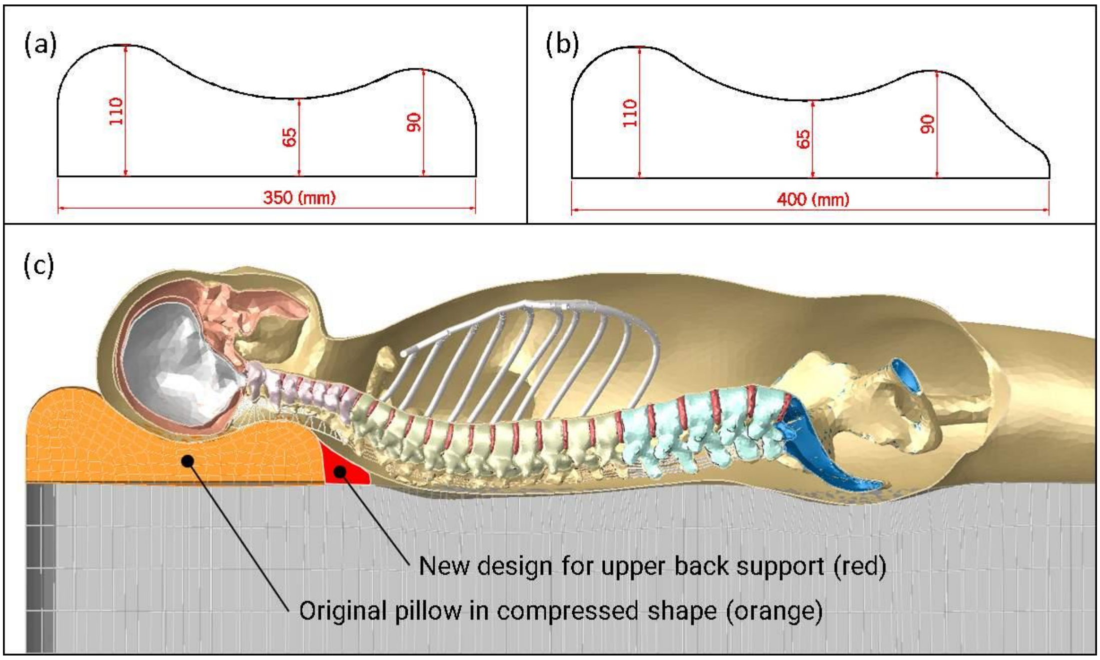

Figure 5.19. Proposal for the new pillow design. (a) Cross-sectional view of the original pillow; (b) Cross-sectional view of the new pillow design; (c) Illustration of the expected support area..

5.4.4 Body support and cervical disc loading

The sleep support system influences the spinal curvature when lying supine, in which the support of the head, neck, back, and hips play a major role. The spinal curvature influences intervertebral disc loading. High loading is detrimental to disc rehydration and causes degeneration and neck pain (Adams & Roughley, 2006; Peng & DePalma, 2018).

Keeping the cervical lordosis in a proper shape should help relieve the stress of the discs and promote sleep health. However, the over-supported cervical region can result in a forward head posture, causing spinal misalignment and risk of neck pain.

5.4.4.1 Head support

Pillow height, material, and mattress firmness influence the head height. However, there is an atlanto-occipital joint between the skull and the cervical spine. As shown in Figure 5. 20, the atlanto-occipital joint contributes to a certain degree of head rotation in the sagittal plane (Bogduk & Mercer, 2000). Higher head support results in head flexion and vice versa. To a certain degree, the head rotates along the atlanto-occipital joint, and the supporting force of the bed is not transmitted to the neck. Therefore, the head height does not significantly alter the spinal curvature and intervertebral disc loading to a certain extent.

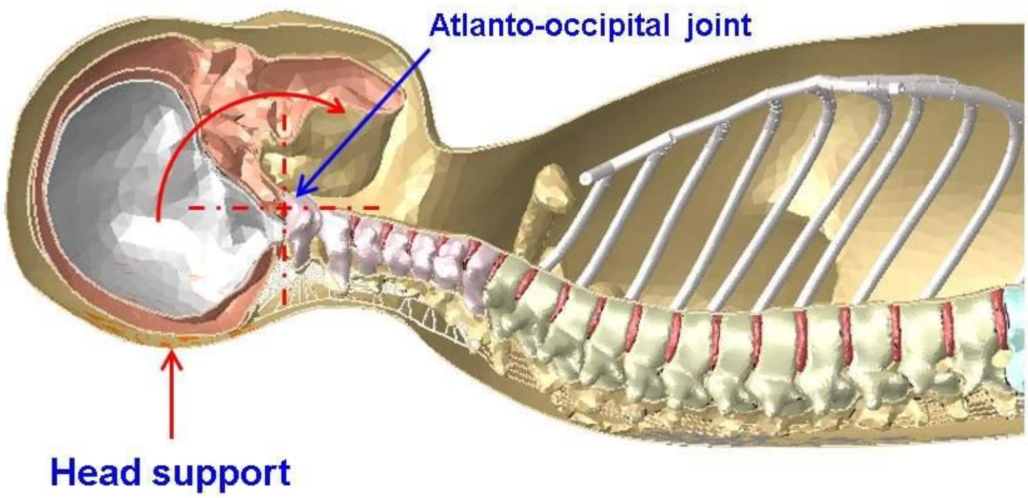

Figure 5. 20. Head rotation based on the strength of head support.

5.4.4.2 Cervical support

Cervical pillows are claimed to provide support for the neck to relax the associated muscles. Some studies have argued that a cervical pillow relieves neck pain and improves sleep quality (Radwan et al., 2020). This study found that mattress stiffness also impacts cervical support. A simulation of excessive cervical support is shown in Figure 5. 21. From the C2 to the sacrum, the vertebrae are mechanically connected in three positions in the transverse plane, including the pair of posterior facet joints and the intervertebral disc (Adams & Dolan, 2005). Excessive cervical support results in flexion of the neck in the supine position. The cervical region is being raised, and the tissues on the front side of the neck are compressed. As the primary structure for biomechanical support, cervical discs undergo compressive and shear stresses. Therefore, the strength of the cervical support must be strictly controlled to avoid damage to the intervertebral disc due to excessive support. The curvature measurement tape may be an effective tool for assessing cervical support; the cervical pillow should not alter the cervical curvature too much. Another assessment method could be to place pressure sensors above the pillow to measure the contact pressure of the cervical region. Excessive cervical support should be associated with high contact pressure. However, the association between these two factors need to be further investigated.

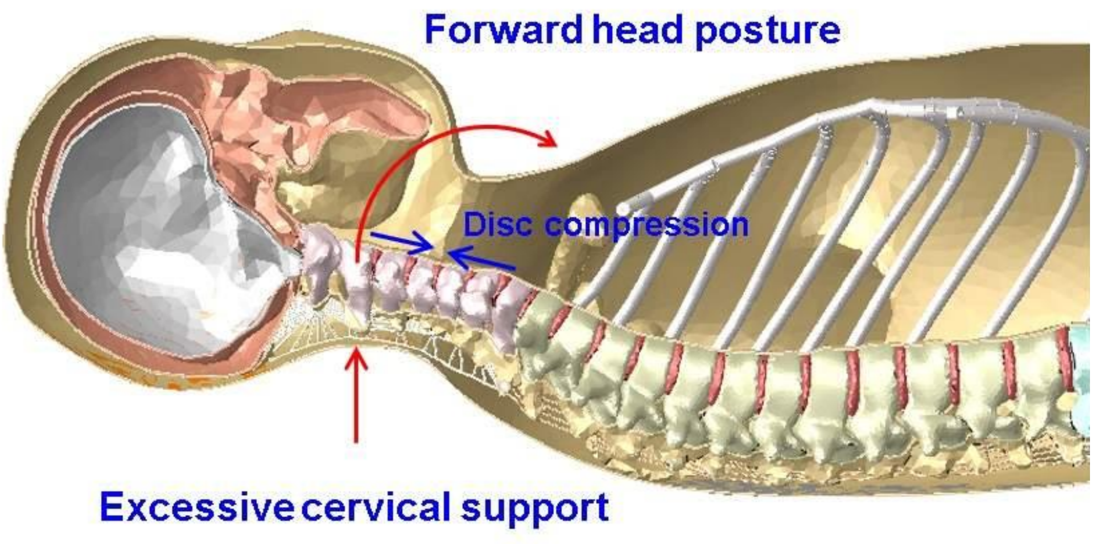

Figure 5. 21. Excessive cervical support and its consequences.

5.4.4.3 Upper back support

The human back has a large area in the coronal plane and is significant to bear the body weight in the supine position. This study found that the sleep support systems used in the experiments provided insufficient support for the upper back. If upper back support can be established, the pressure generated by the weight of the torso and arms in the supine position can be distributed, reducing peak back pressure and improving sleep comfort. Moreover, cervical discs may benefit from proper upper back support. As shown in Figure 5. 22, in the supine position, the neck is suspended due to the upper back supporting, resulting in a cervical extension. Neck extension releases the loading on the intervertebral discs and facilitates disc rehydration. Therefore, the proper upper back support can benefit the cervical spine and disperse the contact pressure on the back.

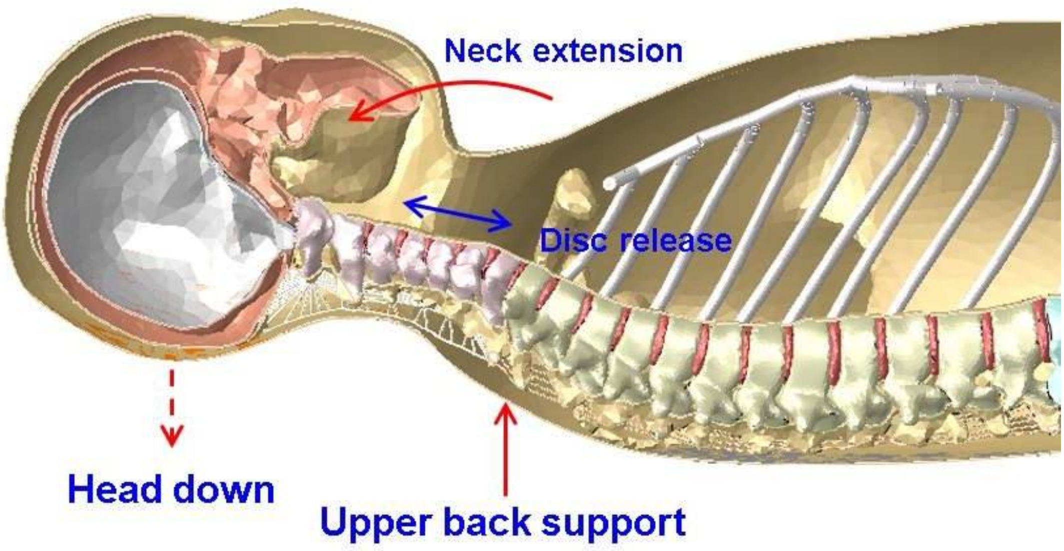

Figure 5. 22. Upper back support and its consequences.

Chapter 6 Conclusion

This study focuses on spine biomechanics, including external measurement of spinal curvatures and prediction of internal loads. Novel devices were developed to address the gaps in existing research, including a curvature measurement tape that can measure the covered back in the supine position and a human FE model to predict biomechanical information.

The curvature measurement tape consists of a sensor tape with integrated accelerometers, a control box, algorithms, and a graphical user interface (Figure 6.1). The sensor tape is thin and flexible, with a maximum thickness of 1.8mm. The measurement accuracy is approximately 99% when measuring a ø200 circle (Hong et al., 2022).

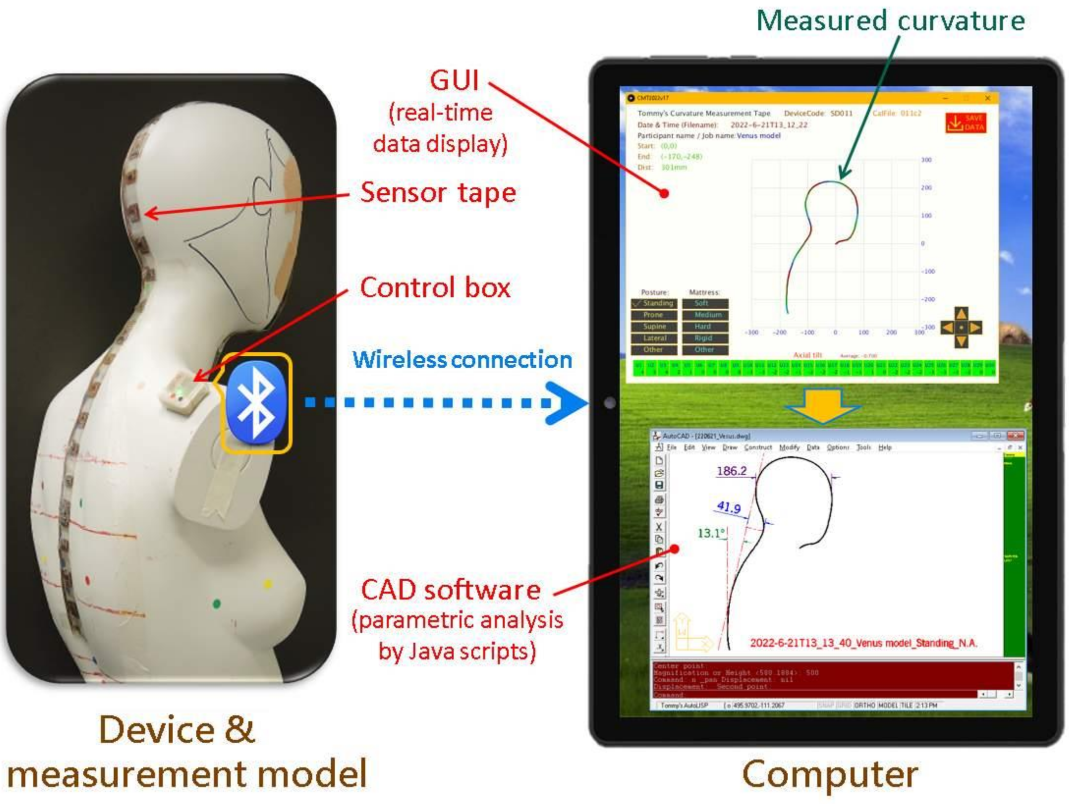

Figure 6.1. The curvature measurement tape and the computer interface.

Experiments were conducted with volunteers lying supine on three mattresses with different stiffness and using a cervical pillow. The curvature measurement device was adopted to obtain the spinal curvature quantitatively, and spine parameters were extracted from the measured spine curvatures through CAD software.

A graphical summary of the experiment results is shown in Figure 6.2. The torso sinks significantly into the soft mattress, while the height of the head is similar in all three experimental scenarios.

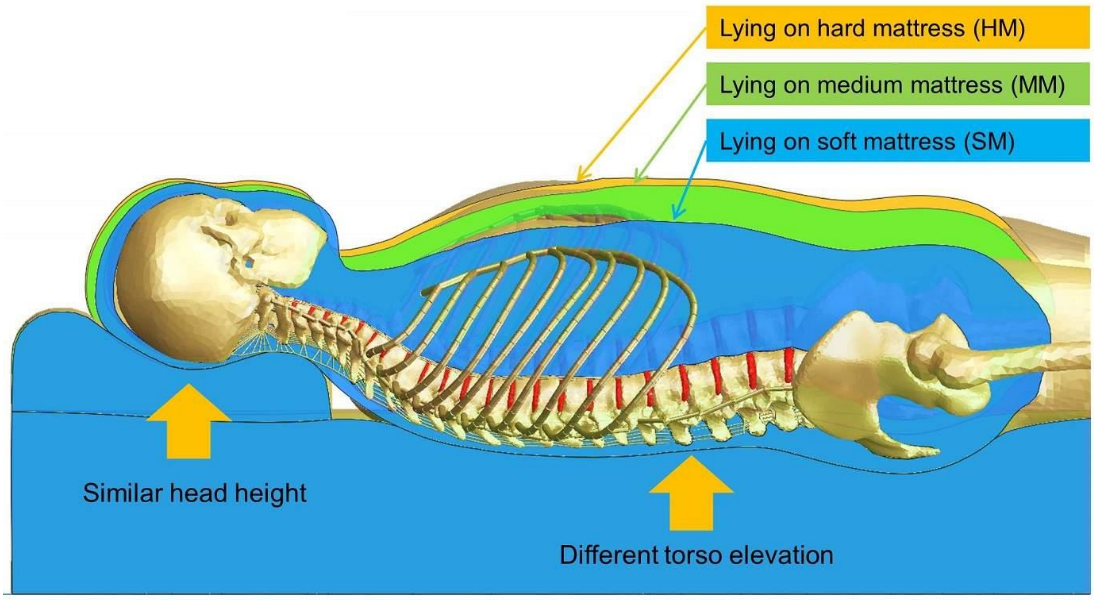

Figure 6. 2. A graphical summary of the experimental results.

The quantitative results showed that when using a soft mattress, cervical lordosis height was raised by 26.7 ± 14.9 mm, head height was raised by 30.5 ± 15.9 mm, and no significant change in lumbar lordosis if compared with the medium mattress. Finite element simulations predicted that the rise in cervical lordosis height resulted in a 49% increase in cervical disc peak loading.

Compared with the medium mattress, the cervical lordosis distance did not change much when lying supine on the hard mattress, and the lumbar lordosis decreased by 10.6 ± 6.8 mm. The reduction in lumbar lordosis distance results in a slight rise in lumbar disc peak loading, but a slight increase is unlikely to cause health problems. However, the significantly increased contact pressure of the human body with the hard mattress can lead to discomfort and skin ulcer.

Overall, this study understands changes in spine alignment induced by the sleeping support system and reveals internal stress through computational simulations. The research proposes possible room for product improvement and makes suggestions. The findings will help develop better sleeping support systems and improve sleep health.

References

Adams M. A., & Dolan, P. (2005). Spine biomechanics. *Journal of Biomechanics, 38*(10), 1972-1983. doi:10.1016/j.jbiomech.2005.03.028

Adams M. A., & Roughley P. J. (2006). What is intervertebral disc degeneration, and what causes it? *Spine, 31*, 11.

Agnew A. M., Moorhouse K., Kang Y.-S., Donnelly B. R., Pfefferle K., Manning A. X., . Bolte J. H. (2013). The response of pediatric ribs to quasi-static loading: mechanical properties and microstructure. *Annals of Biomedical Engineering, 41*(12), 2501-2514. doi:10.1007/s10439-013-0875-6

Ajit Singh D. K., Lim A. Y., Harithasan D., Ab Rahman N. N. A., Mohamed Sharif N. et al. (2018). Gender differences in spinal morphological attributes among young adults: a preliminary study. *Jurnal Sains Kesihatan Malaysia, 16*(02), 119-124. doi:10.17576/jskm-2018-1602-15

Bakker E. W., Verhagen A. P., Can Trijffel E., Lucas C., & Koes B. W. (2009). Spinal mechanical load as a risk factor for low back pain: a systematic review of prospective cohort studies. *Spine, 34*(8), E281-E293. doi:10.1097/BRS.0b013e318195b257

Ban E., Zhang S., Zarei V., Barocas V. H., Winkelstein B. A., & Picu C. R. (2017). Collagen organization in facet capsular ligaments varies with spinal region and with ligament deformation. *Journal of Biomechanical Engineering, 139*(7). doi:10.1115/1.4036019

Barker J. B., & Cronin D. (2020). Multi-level validation of a male neck finite element model with active musculature. *Journal of Biomechanical Engineering , 143*(1), 143. doi:10.1115/1.4047866

Barreto T., & Svec J. H. (2019). Chronic neck pain: nonpharmacologic treatment. *American family physician, 100*(3), 180-182. Retrieved from https://www.ncbi.nlm.nih.gov/pubmed/31361100

Barrett E., Lenehan B., O'Sullivan K., Lewis J., & McCreesh K. (2018). Validation of the manual inclinometer and flexicurve for the measurement of thoracic kyphosis. *Physiother Theory Pract, 34*(4), 301-308. doi:10.1080/09593985.2017.1394411

Barrett E., McCreesh K., & Lewis J. (2013). Intrarater and interrater reliability of the flexicurve index, flexicurve angle, and manual inclinometer for the measurement of thoracic kyphosis. *Rehabil Res Pract, 2013*, 475870. doi:10.1155/2013/475870

Barrett E., McCreesh K., & Lewis J. (2014). Reliability and validity of non-radiographic methods of thoracic kyphosis measurement: a systematic review. *Manuel Therapy, 19*(1), 10-17. doi:10.1016/j.math.2013.09.003

Barrey C., & Darnis A. (2015). Current strategies for the restoration of adequate lordosis during lumbar fusion. *World Journal of Orthopedics, 6*(1), 117-126. doi:10.5312/wjo.v6.i1.117

Battié M. C., Videman T., Kaprio J., Gibbons L. E., Gill K., Manninen H. Peltonen L. (2009). The Twin spine study: contributions to a changing view of disc degeneration. *The Spine Journal, 9*(1), 47-59. doi:10.1016/j.spinee.2008.11.011

Bermel E. A., Barocas V. H., & Ellingson A. M. (2018). The role of the facet capsular ligament in providing spinal stability. *Computer Methods in Biomechanics Biomedical Engineering, 21*(13), 712-721. doi:10.1080/10255842.2018.1514392

Blackley D. C. (2012). *Polymer latices: science and technology volume 3: applications of latices*: Springer Science & Business Media.

Blanpied P. R., Gross A. R., Elliott J. M., Devaney L. L., Clewley D., Walton, et al,. (2017). Neck nain: revision 2017. *Journal of Orthopaedic and Sports Physical Therapy, 47*(7), A1-A83. doi:10.2519/jospt.2017.0302

Bogduk N. (2008). Evidence-informed management of chronic low back pain with facet injections and radiofrequency neurotomy. *The Spine Journal, 8*(1), 56-64. doi:10.1016/j.spinee.2007.10.010

Bogduk N. (2012). Degenerative joint disease of the spine. *Radiologic Clinics of North America, 50*(4), 613-628. doi:10.1016/j.rcl.2012.04.012

Bogduk N., & Mercer S. (2000). Biomechanics of the cervical spine. I: Normal kinematics. *Clinical Biomechanics, 15*(9), 633-648.

Brink R. C., Colo D., Schlosser T. P. C., Vincken K. L., Van Stralen M., Hui S., et al. (2017). Upright, prone, and supine spinal morphology and alignment in adolescent idiopathic scoliosis. *Scoliosis Spinal Disord, 12*, 6. doi:10.1186/s13013-017-0111-5

Bucke J., Spencer S., Fawcett L., Sonvico L., Rushton A., & Heneghan N. R. (2017). Validity of the digital inclinometer and iphone when measuring thoracic spine rotation. *Journal of Athletic Training, 52*(9), 820-825. doi:10.4085/1062-6050-52.6.05

Buckle P., & Fernandes A. (1998). Mattress evaluation—assessment of contact pressure, comfort and discomfort. *Applied Ergonomics, 29*(1), 35-39. doi:10.1016/s0003-6870(97)00023-9

Busching F., Kulau U., Gietzelt M., & Wolf L. (2012). Comparison and validation of capacitive accelerometers for health care applications. *Comput Methods Programs Biomed, 106*(2), 79-88. doi:10.1016/j.cmpb.2011.10.009

Chaudhry F. F., Danieletto M., Golden E., Scelza J., Botwin G., Shervey M., et al. (2020). Sleep in the natural environment: a pilot study. *Sensors (Basel), 20*(5). doi:10.3390/s20051378

CHEN H.-B., YANG K. H., & WANG Z.-G. (2009). Biomechanics of whiplash injury. *Chinese Journal of Traumato, 12*(305), 10. doi:10.3760/cma.j.issn.1008-1275.2009.05.011

Chen T. L., Wong D. W., Wang Y., Lin J., & Zhang M. (2019). Foot arch deformation and plantar fascia loading during running with rearfoot strike and forefoot strike: A dynamic finite element analysis. *Journal of Biomechanics, 83*, 260-272. doi:10.1016/j.jbiomech.2018.12.007

Chen Z., Li Y., Liu R., Gao D., Chen Q., Hu Z., & Guo J. (2014). Effects of interface pressure distribution on human sleep quality. *PLoS One, 9*(6), e99969. doi:10.1371/journal.pone.0099969

Chi H., Talischi C., Lopez-Pamies O., & H. Paulino G. (2015). Polygonal finite elements for finite elasticity. *International Journal for Numerical Methods in Engineering, 101*(4), 305-328. doi:10.1002/nme.4802

Chohan A., Ramli K., Cook A., May K., Selfe J., & Richards J. (2019). “Spinal alignment” cushion in the management of low back pain – a randomized controlled study. *Prm+, 2*(2), 35.

Cirillo Totera, J. I., Fleiderman Valenzuela, J. G., Garrido Arancibia, J. A., Pantoja Contreras, S. T., Beaulieu Lalanne, L., & Alvarez-Lemos, F. L. (2021). Sagittal balance: from theory to clinical practice. *EFORT Open Reviews, 6*(12), 1193-1202. doi:10.1302/2058-5241.6.210062

Coenen P., Gouttebarge V., Van der Burght A. S., Van Dieën J. H., Frings-Dresen M. H., Van der Beek, et al. (2014). The effect of lifting during work on low back pain: a health impact assessment based on a meta-analysis. *Occupational and Environmental Medicine, 71*(12), 871-877. doi:10.1136/oemed-2014-102346

Coenen P., Kingma I., Boot C. R., Bongers P. M., & Van Dieën J. H. (2014). Cumulative mechanical low-back load at work is a determinant of low-back pain. *Occupational and Environmental Medicine, 71*(5), 332-337. doi:10.1136/oemed-2013-101862

Cohen S. P., & Hooten W. M. (2017). Advances in the diagnosis and management of neck pain. *BMJ, 358*, j3221. doi:10.1136/bmj.j3221

Comer C., & Conaghan P. G. (2009). Tackling persistent low back pain in primary care. *The Practitioner, 253*(1721), 32-35. Retrieved from https://www.ncbi.nlm.nih.gov/pubmed/19873857

D'Amico M., Kinel E., & Roncoletta P. (2017). Normative 3D opto-electronic stereo-photogrammetric posture and spine morphology data in young healthy adult population. *PLoS One, 12*(6), e0179619. doi:10.1371/journal.pone.0179619

Damasceno G. M., Ferreira A. S., Nogueira L. A. C., Reis F. J. J., Andrade I. C. S., & Meziat-Filho N. (2018). Text neck and neck pain in 18-21-year-old young adults. *European Spine Journal, 27*(6), 1249-1254. doi:10.1007/s00586-017-5444-5

De Zoete R. M., Armfield N. R., McAuley J. H., Chen K., & Sterling M. (2021). Comparative effectiveness of physical exercise interventions for chronic non-specific neck pain: a systematic review with network meta-analysis of 40 randomised controlled trials. *British Journal of Sports Medicine, 55*(13), 730-742. doi:10.1136/bjsports-2020-102664

Diebo B. G., Varghese J. J., Lafage R., Schwab F. J., & Lafage V. (2015). Sagittal alignment of the spine: What do you need to know? *Clin Neurol Neurosurg, 139*, 295-301. doi:10.1016/j.clineuro.2015.10.024

Dierendonck D. v., & Nijenhuis J. T. (2007). Flotation restricted environmental stimulation therapy (REST) as a stress-management tool: A meta-analysis. *Psychology & Health, 20*(3), 405-412. doi:10.1080/08870440412331337093

Drake R., Vogl A. W., Mitchell A. W., Tibbitts R., & Richardson P. (2020). *Gray's Atlas of Anatomy E-Book*: Elsevier Health Sciences. 21-24

El Bojairami I., El-Monajjed K., & Driscoll M. (2020). Development and validation of a timely and representative finite element human spine model for biomechanical simulations. *Scientific Reports, 10*(1), 21519. doi:10.1038/s41598-020-77469-1

Fatoye F., Gebrye T., & Odeyemi I. (2019). Real-world incidence and prevalence of low back pain using routinely collected data. *Rheumatology International, 39*(4), 619-626. doi:10.1007/s00296-019-04273-0

Fazli F., Farahmand B., Azadinia F., & Amiri A. (2018). A preliminary study: The effect of ergonomic latex pillow on pain and disability in patients with cervical spondylosis. *Medical Journal of the Islamic Republic of Iran, 32*, 81. doi:10.14196/mjiri.32.81

Fess P., James D., Myers J., Murphy J., Rooney M., Taylor J., & Torii L. (2015). *Effect of mattresses and pillow designs on promoting sleep quality, spinal alignment and pain reduction in adults: Systematic reviews of controlled trials.* (Doctoral dissertation). Utica College,

Fortin C., Feldman D. E., Cheriet F., & Labelle H. (2011). Clinical methods for quantifying body segment posture: a literature review. *Disability and Rehabilitation, 33*(5), 367-383. doi:10.3109/09638288.2010.492066

Frange C., & Coelho F. M. S. (2022). *Sleep Medicine and Physical Therapy: A Comprehensive Guide for Practitioners*: Springer. 173-174. doi:10.1007/978-3-030-44447-1

Fung Y. C. (1993). Biomechanics: mechanical properties of living tissues. *Springer Science & Business Media.*

Furlanetto T. S., Sedrez J. A., Candotti C. T., & Loss J. F. (2016). Photogrammetry as a tool for the postural evaluation of the spine: A systematic review. *World Journal of Orthopedics, 7*(2), 136-148. doi:10.5312/wjo.v7.i2.136

Genebra C., Maciel N. M., Bento T. P. F., Simeao S., & Vitta A. (2017). Prevalence and factors associated with neck pain: a population-based study. *Brazilian Journal of Physical Therapy, 21*(4), 274-280. doi:10.1016/j.bjpt.2017.05.005

Giamberardino M. A., Affaitati G., Fabrizio A., & Costantini R. (2011). Myofascial pain syndromes and their evaluation. *Best Practice & Research Clinical Rheumatology, 25*(2), 185-198. doi:10.1016/j.berh.2011.01.002

Gilroy A. M., MacPherson B. R., Wikenheiser J. C., Schuenke M., Schulte E., & Schumacher U. (2020). *Atlas of Anatomy* (4th Edition ed.): Thieme Stuttgart. 24-25. doi:10.1097/PRS.0000000000008001

Gracovetsky S., & Farfan H. F. (1986). The optimum spine. *Spine, 11*(6), 543. doi:10.1097/00007632-198607000-00006

Gray H. (1973). *Anatomy of the human body* (29th American ed., edited by Charles Mayo Goss. With new drawings by Don M. Alvarado.. ed.). Philadelphia: Philadelphia : Lea & Febiger.

Guzman J., Hurwitz E. L., Carroll L. J., Haldeman S., Cote P., Carragee E. J., et al. (2009). A new conceptual model of neck pain: linking onset, course, and care: the bone and joint decade 2000-2010 task force on neck pain and its associated disorders. *Journal of Manipulative & Physiological Therapeutics, 32*(2 Suppl), S17-28. doi:10.1016/j.jmpt.2008.11.007

Haex B. (2004). *Back and Bed: Ergonomic Aspects of Sleeping*. Boca Raton, FL, USA: CRC Press. 47-48.

Haex B., Vander Sloten, J., & Van Audekercke, R. (2020). Required stiffness distribution in a mattress for an optimal curvature of the human spine during bedrest. *Computer Methods in Biomechanics & Biomedical Engineering–2* (pp. 413-420): CRC Press.

Hannink E., Shannon T., Barker K. L., & Dawes H. (2020). The reliability and reproducibility of sagittal spinal curvature measurement using the

Microsoft Kinect V2. *Journal of Back and Musculoskeletal Rehabilitation , 33*(2), 295-301. doi:10.3233/BMR-191554

Hasegawa K., Okamoto M., Hatsushikano S., Caseiro G., & Watanabe K. (2018). Difference in whole spinal alignment between supine and standing positions in patients with adult spinal deformity using a new comparison method with slot-scanning three-dimensional X-ray imager and computed tomography through digital reconstructed radiography. *BMC Musculoskelet Disord, 19*(1), 437. doi:10.1186/s12891-018-2355-5

Hinman M. R. (2004). Comparison of thoracic kyphosis and postural stiffness in younger and older women. *Spine J, 4*(4), 413-417. doi:10.1016/j.spinee.2004.01.002

Hong T. T.-H., Wang Y., Tan Q., Zhang G., Wong D. W.-C., & Zhang, M. (2022). Measurement of covered curvature based on a tape of integrated accelerometers. *Measurement, 193*, 110959. doi:10.1016/j.measurement.2022.110959

Hong T. T.-H., Wang Y., Wong D. W.-C., Zhang G., Tan Q., Chen T. L.-W., & Zhang M. (2022). The influence of mattress stiffness on spinal curvature and intervertebral disc stress—an experimental and computational study. *Biology, 11*(7). doi:10.3390/biology11071030

Hu P., Wu T., Wang H. z., Qi X. z., Yao J., Cheng X. d., et al. (2017). Influence of different boundary conditions in finite element analysis on pelvic biomechanical load transmission. *Orthopaedic Surgery, 9*(1), 115-122. doi:10.1111/os.12315

Hurwitz E. L., Randhawa K., Yu H., Cote P., & Haldeman S. (2018). The global spine care initiative: a summary of the global burden of low back and neck pain studies. *European Spine Journal , 27*(6), 796-801. doi:10.1007/s00586-017-5432-9

Ivancic P. C., Coe M. P., Ndu A. B., Tominaga Y., Carlson E. J., Rubin W., et al. (2007). Dynamic mechanical properties of intact human cervical spine ligaments. *Spine Journal, 7*(6), 659-665. doi:10.1016/j.spinee.2006.10.014

Izzo R., Guarnieri G., Guglielmi G., & Muto M. (2013). Biomechanics of the spine. Part I: spinal stability. *European Journal of Radiology , 82*(1), 118-126. doi:10.1016/j.ejrad.2012.07.024

James S. L., Abate D., Abate K. H., Abay S. M., Abbafati C., Abbasi N., et al. (2018). Global, regional, and national incidence, prevalence, and years lived with disability for 354 diseases and injuries for 195 countries and territories, 1990–2017: a systematic analysis for the global burden of disease study 2017. *The Lancet, 392*(10159), 1789-1858. doi:10.1016/s0140-6736(18)32279-7

Jeng P., & Wang L.-C. (2017). Stream data analysis of body sensors for sleep posture monitoring: an automatic labelling approach. *IEEE Access*. doi:10.1109/WOCC.2017.7928969

Jeng P. Y., Wang L. C., Hu C. J., & Wu D. (2021). A wrist sensor sleep posture monitoring system: an automatic labeling approach. *Sensors (Basel), 21*(1). doi:10.3390/s21010258

Jeon M. Y., Jeong H., Lee S., Choi W., Park J. H., Tak S. J., et al. (2014). Improving the quality of sleep with an optimal pillow: a randomized, comparative study. *The Tohoku Journal of Experimental Medicine, 233*(3), 183-188. doi:10.1620/tjem.233.183

Jiang D., Zhan S., Wang L., Shi L. L., Ling M., Hu H., & Jia W. (2021). Biomechanical comparison of five cannulated screw fixation strategies for young vertical femoral neck fractures. *Journal of Orthopaedic Research®, 39*(8), 1669-1680. doi:10.1002/jor.24881

John J. D., Saravana Kumar G., & Yoganandan N. (2019). Cervical spine morphology and ligament property variations: A finite element study of their influence on sagittal bending characteristics. *Journal of Biomechanics , 85*, 18-26. doi:10.1016/j.jbiomech.2018.12.044

Jones A. C., & Wilcox R. K. (2008). Finite element analysis of the spine: towards a framework of verification, validation and sensitivity analysis. *Medical Engineering & Physics, 30*(10), 1287-1304. doi:10.1016/j.medengphy.2008.09.006

Kim H. C., Jun H. S., Kim J. H., Ahn J. H., Chang I. B., Song J. H., & Oh J. K. (2015). The effect of different pillow heights on the parameters of cervicothoracic spine segments. *Korean Journal of Spine, 12*(3), 135-138. doi:10.14245/kjs.2015.12.3.135

Kim J. H., Won B. H., Sim W. S., & Jang K. S. (2016). Biomechanical effectiveness and anthropometric design aspects of 3-dimensional contoured pillow. *Journal of the Ergonomics Society of Korea, 35*(6), 503-517. doi:10.5143/jesk.2016.35.6.503

Kim M. S. (2015). Influence of neck pain on cervical movement in the sagittal plane during smartphone use. *Journal of Physical Therapy Science, 27*(1), 15. doi:10.1589/jpts.27.15

Koninck J. D., Lorrain D., & Gagnon P. (1992). Sleep positions and position shifts in five age groups: an ontogenetic picture. *Sleep, 15*(2), 7. doi:10.1093/sleep/15.2.143

Kumaresan S., Yoganandan N., & Pintar F. A. (1999). Finite element analysis of the cervical spine: a material property sensitivity study. *Clinical Biomechanics, 14*(1), 41-53. doi:10.1016/s0268-0033(98)00036-9

Lam W.-K., Chen B., Liu R.-T., Cheung J. C.-W., & Wong D. W.-C. (2022). Spine Posture, mobility, and stability of top mobile esports athletes: a case series. *Biology, 11*(5), 737. doi:10.3390/biology11050737

Lan L., Tsuzuki K., Liu Y. F., & Lian Z. W. (2017). Thermal environment and sleep quality: A review. *Energy and Buildings, 149*, 101-113. doi:10.1016/j.enbuild.2017.05.043

Le Huec J. C., Thompson W., Mohsinaly Y., Barrey C., & Faundez A. (2019). Sagittal balance of the spine. *European Spine Journal , 28*(9), 1889-1905. doi:10.1007/s00586-019-06083-1

Lee T. T.-Y., Cheung J. C.-W., Law S.-Y., To M. K. T., Cheung J. P. Y., & Zheng Y.-P. (2019). Analysis of sagittal profile of spine using 3D ultrasound imaging: a phantom study and preliminary subject test. *Computer Methods in Biomechanics and Biomedical Engineering: Imaging & Visualization, 8*(3), 232-244. doi:10.1080/21681163.2019.1566025

Lee W.-D., Lee J.-U., Park J., & Kim J. (2015). Analysis of the body pressure-related sensory changes in the static supine position for healthy science research: a randomized controlled pilot trial. *Toxicology and Environmental Health Sciences, 7*(3), 211-216. doi:10.1007/s13530-015-0240-2

Lee W., Won B. H., & Cho S. W. (2017). Finite element modelling for predicting the contact pressure between a foam mattress and the human body in a supine position. *Comput Methods Biomech Biomed Engin, 20*(1), 104-117. doi:10.1080/10255842.2016.1203421

Lee Y.-C., Lee C.-Y., & Wang M.-J. (2020). Better combination of thickness and hardness of mattress topper for supine sleeping posture: A physiological measurements evaluation. *International Journal of Industrial Ergonomics, 78*, 102979. doi:10.1016/j.ergon.2020.102979

Leilnahari K., Fatouraee N., Khodalotfi M., Sadeghein M. A., & Kashani Y. A. (2011). Spine alignment in men during lateral sleep position: experimental study and modelling. *Biomedical Engineering Online, 10*, 1-11. doi:10.1186/1475-925X-10-103

Liu J. J., Xu W., Huang M.-C., Alshurafa N., Sarrafzadeh M., Raut N., & Yadegar B. (2014). Sleep posture analysis using a dense pressure sensitive bedsheet. *Pervasive and Mobile Computing, 10*, 34-50. doi:10.1016/j.pmcj.2013.10.008

Liu S. F., Lee Y. L., & Liang J. C. (2011). Shape design of an optimal comfortable pillow based on the analytic hierarchy process method. *Journal of Chiropractic Medicine, 10*(4), 229-239. doi:10.1016/j.jcm.2011.04.002

Lizee E., Robin S., Song E., Bertholon N., Le Coz J.-Y., Besnault B., & Lavaste F. (1998). Development of a 3D finite element model of the human body. *SAE Transactions*, 2760-2782.

Mahmoud N. F., Hassan K. A., Abdelmajeed S. F., Moustafa I. M., & Silva A. G. (2019). The relationship between forward head posture and neck pain: a systematic review and meta-analysis. *Current Reviews in Musculoskeletal Medicine , 12*(4), 562-577. doi:10.1007/s12178-019-09594-y

McGillion S. (2022). Anatomy of the spine. *Spinal Surgeon.* Retrieved from www.wessexspinalsurgeon.co.uk/spinal-anatomy/

Nadeau M., McLachlin S. D., Bailey S. I., Gurr K. R., Dunning C. E., & Bailey C. S. (2012). A biomechanical assessment of soft-tissue damage in the cervical spine following a unilateral facet injury. *The Journal of Bone and Joint Surgery, 94*(21), e156. doi:10.2106/JBJS.K.00694

Nikkhoo M., Cheng C. H., Wang J. L., Khoz Z., El-Rich M., Hebela N., et al. (2019). Development and validation of a geometrically personalized finite element model of the lower ligamentous cervical spine for clinical applications. *Computers in Biology and Medicine , 109*, 22-32. doi:10.1016/j.compbiomed.2019.04.010

Nouri A., Tetreault L., Singh A., Karadimas S. K., & Fehlings M. G. (2015). Degenerative cervical myelopathy: epidemiology, genetics, and pathogenesis. *Spine, 40*(12), E675-693. doi:10.1097/BRS.0000000000000913

Östh J., Mendoza-Vazquez M., Sato F., Svensson M. Y., Linder A., & Brolin K. (2017). A female head–neck model for rear impact simulations. *Journal of Biomechanics, 51*, 49-56. doi:10.1016/j.jbiomech.2016.11.066

Panzer M. B., Fice J. B., & Cronin D. S. (2011). Cervical spine response in frontal crash. *Medical Engineering & Physics, 33*(9), 1147-1159. doi:10.1016/j.medengphy.2011.05.004

Partanen J. V., Ojala T. A., & Arokoski J. P. (2010). Myofascial syndrome and pain: A neurophysiological approach. *Pathophysiology, 17*(1), 19-28. doi:10.1016/j.pathophys.2009.05.001

Peng B., & DePalma M. J. (2018). Cervical disc degeneration and neck pain. *Journal of Pain Research , 11*, 2853-2857. doi:10.2147/JPR.S180018

Peng B., Yang L., Li Y., Liu T., & Liu Y. (2021). Cervical proprioception impairment in neck pain-pathophysiology, clinical evaluation, and management: A narrative review. *Pain and Therapy, 10*(1), 143-164. doi:10.1007/s40122-020-00230-z

Perolat R., Kastler A., Nicot B., Pellat J. M., Tahon F., Attye A., et al. (2018). Facet joint syndrome: from diagnosis to interventional management. *Insights Imaging, 9*(5), 773-789. doi:10.1007/s13244-018-0638-x

Persson L. (2009). Neck pain and pillows – A blinded study of the effect of pillows on non-specific neck pain, headache and sleep. *Advances in Physiotherapy, 8*(3), 122-127. doi:10.1080/14038190600780239

Pivotto L. R., Navarro I., & Candotti C. T. (2021). Radiography and photogrammetry-based methods of assessing cervical spine posture in the sagittal plane: A systematic review with meta-analysis. *Gait & Posture, 84*, 357-367. doi:10.1016/j.gaitpost.2020.12.033

Price J., Rushton A., Tyros I., Tyros V., & Heneghan N. R. (2020). Effectiveness and optimal dosage of exercise training for chronic non-specific neck pain: A systematic review with a narrative synthesis. *PLoS One, 15*(6), e0234511. doi:10.1371/journal.pone.0234511

Quinn K. P., Lee K. E., Ahaghotu C. C., & Winkelstein B. A. (2007). Structural changes in the cervical facet capsular ligament: potential contributions to pain following subfailure loading. *Stapp Car Crash Conference , 51*, 169. doi:10.4271/2007-22-0008

Radwan A., Ashton N., Gates T., Kilmer A., & VanFleet M. (2020). Effect of different pillow designs on promoting sleep comfort, quality, & spinal alignment: a systematic review. *European Journal of Integrative Medicine*. doi:10.1016/j.eujim.2020.101269

Radwan A., Fess P., James D., Murphy J., Myers J., Rooney M., et al. (2015). Effect of different mattress designs on promoting sleep quality, pain reduction, and spinal alignment in adults with or without back pain; systematic review of controlled trials. *Sleep Health, 1*(4), 257-267. doi:10.1016/j.sleh.2015.08.001

Ran Q., Zhou K., Yang Y.-L., Kang J., Zhu L., Tang Y., & Feng J. (2020). High-precision human body acquisition via multi-view binocular stereopsis. *Computers & Graphics, 87*, 43-61. doi:10.1016/j.cag.2020.01.003

Rasoulinejad P., McLachlin S. D., Bailey S. I., Gurr K. R., Bailey C. S., & Dunning C. E. (2012). The importance of the posterior osteoligamentous complex to subaxial cervical spine stability in relation to a unilateral facet injury. *Spine Journal, 12*(7), 590-595. doi:10.1016/j.spinee.2012.07.003

Ratner B. (2009). The correlation coefficient: Its values range between+ 1/− 1, or do they? *Journal of Targeting, Measurement and Analysis for Marketing, 17*(2), 139-142. doi:10.1057/jt.2009.5

Remondino F. (2004). 3-D reconstruction of static human body shape from image sequence. *Computer Vision and Image Understanding, 93*(1), 65-85. doi:10.1016/j.cviu.2003.08.006

Ren S., Wong D. W., Yang H., Zhou Y., Lin J., & Zhang M. (2016). Effect of pillow height on the biomechanics of the head-neck complex:

investigation of the cranio-cervical pressure and cervical spine alignment. *PeerJ, 4*, e2397. doi:10.7717/peerj.2397

Schubert V., & Heraud J. (1994). The effects of pressure and shear on skin microcirculation in elderly stroke patients lying in supine or semi-recumbent positions. *Age and Ageing, 23*(5), 405-410. doi:10.1093/ageing/23.5.405

Seidi F., Rajabi R., Ebrahimi I., Alizadeh M. H., & Minoonejad H. (2014). The efficiency of corrective exercise interventions on thoracic hyper-kyphosis angle. *Journal of Back and Musculoskeletal Rehabilitation , 27*(1), 7-16. doi:10.3233/BMR-130411

Seidler A., Bergmann A., Jäger M., Ellegast R., Ditchen D., Elsner G., et al. (2009). Cumulative occupational lumbar load and lumbar disc disease–results of a German multi-center case-control study (EPILIFT). *BMC Musculoskeletal Disorders, 10*(1), 1-13. doi:10.1186/1471-2474-10-48

Sharma M., Langrana N. A., & Rodriguez J. (1995). Role of ligaments and facets in lumbar spinal stability. *Spine, 20*(8), 887-900. doi:10.1097/00007632-199504150-00003

Sheeran L., Sparkes V., Busse M., & Van Deursen R. (2010). Preliminary study: reliability of the spinal wheel. A novel device to measure spinal postures applied to sitting and standing. *European Spine Journal , 19*(6), 995-1003. doi:10.1007/s00586-009-1241-0

Shields N., Capper J., Polak T., & Taylor N. (2006). Are cervical pillows effective in reducing neck pain? in *Database of Abstracts of Reviews of Effects (DARE): Quality-assessed Reviews [Internet]*: Centre for Reviews and Dissemination (UK).

Sironi R., Standoli C. E., Perego P., & Andreoni G. (2019). Digital human modelling and ergonomic design of sleeping systems. In *DHM and Posturography* (pp. 385-396).

Stausberg J., Lehmann N., Kröger K., Maier I., Schneider H., Niebel W., et al. (2010). Increasing pressure ulcer rates and changes in delivery of care: a retrospective analysis at a university clinic. *Journal of Clinical Nursing, 19*(11-12), 1504-1509. doi:10.1111/j.1365-2702.2010.03231.x

Steilen D., Hauser R., Woldin B., & Sawyer S. (2014). Chronic neck pain: making the connection between capsular ligament laxity and cervical instability. *The Open Orthopaedics Journal, 8*, 326. doi:10.2174/1874325001408010326

Stollenwerk K., Muller J., Hinkenjann A., & Kruger B. (2019). Analyzing spinal shape changes during posture training using a wearable device. *Sensors (Basel), 19*(16). doi:10.3390/s19163625

Stollenwerk K., Müllers J., Müller J., Hinkenjann A., & Krüger B. (2018). Evaluating an accelerometer-based system for spine shape monitoring. In *Computational Science and Its Applications – ICCSA 2018* (pp. 740-756).

Su L., & Xu M. (2017). Sleep comfort analysis using a part-based mixture model with nighttime infrared video. *Neurocomputing, 259*, 66-75. doi:10.1016/j.neucom.2016.08.128

Tadepalli S. C., Erdemir A., & Cavanagh P. R. (2011). Comparison of hexahedral and tetrahedral elements in finite element analysis of the foot and footwear. *Journal of Biomechanics, 44*(12), 2337-2343. doi:10.1016/j.jbiomech.2011.05.006

Theirl M., & Collentro J. (2020). The best sleep positions for neck and back pain. *Q4PT.* Retrieved from www.q4pt.com/new-blog/sleep-positions-for-back-and-neck-pain

Twomey L., & Taylor J. (1983). Sagittal movements of the human lumbar vertebral column: a quantitative study of the role of the posterior vertebral elements. *Archives of Physical Medicine And Rehabilitation,* *64*(7), 322-325. Retrieved from https://www.ncbi.nlm.nih.gov/pubmed/6860110

Urits I., Burshtein A., Sharma M., Testa L., Gold P. A., Orhurhu V., et al. (2019). Low back pain, a comprehensive review: pathophysiology, diagnosis, and treatment. *Current Pain and Headache Reports, 23*(3), 23. doi:10.1007/s11916-019-0757-1

Vergroesen P. P., Kingma I., Emanuel K. S., Hoogendoorn R. J., Welting T. J., Van Royen B. J., et al. (2015). Mechanics and biology in intervertebral disc degeneration: a vicious circle. *Osteoarthritis Cartilage, 23*(7), 1057-1070. doi:10.1016/j.joca.2015.03.028

Verhaert V., Druyts H., Van Deun D., Exadaktylos V., Verbraecken J., Vandekerckhove M., et al. (2012). Estimating spine shape in lateral sleep positions using silhouette-derived body shape models. *International Journal of Industrial Ergonomics, 42*(5), 489-498. doi:10.1016/j.ergon.2012.08.002

Verhaert V., Haex B., De Wilde T., Berckmans D., Verbraecken J., de Valck E., et al. (2011). Ergonomics in bed design: the effect of spinal alignment on sleep parameters. *Ergonomics, 54*(2), 169-178. doi:10.1080/00140139.2010.538725

Vital J. M., & Cawley D. T. (2020). *Spinal Anatomy: Modern Concepts*: Springer International Publishing.

Voinea G.-D., Butnariu S., & Mogan G. (2017). Measurement and geometric modelling of human spine posture for medical rehabilitation purposes using a wearable monitoring system based on inertial sensors. *Sensors (Basel), 17*(1), 3. doi:10.3390/s17010003

Walsh N. P., Halson S. L., Sargent C., Roach G. D., Nedelec M., Gupta, L., et al. (2020). Sleep and the athlete: narrative review and 2021 expert consensus recommendations. *British Journal of Sports Medicine*. doi:10.1136/bjsports-2020-102025

Wang Y., Zhao X., & Wen D. (2020). Fabrication and characteristics of a three-axis accelerometer with double l-shaped beams. *Sensors (Basel), 20*(6). doi:10.3390/s20061780

Watson D. (2017). Introduction to ATmega328. *The Engineering Projects.* Retrieved from www.theengineeringprojects.com/2017/08/introduction-to-atmega328.html

Wong D. W. C., Chen T. L. W., Wang Y., Lin J., & Zhang M. (2019). Sleeping mattress determinants and evaluation: a biomechanical review and critique. *PeerJ, 7*, e6364. doi:10.7717/peerj.6364

Wong W. Y., & Wong M. S. (2008). Detecting spinal posture change in sitting positions with tri-axial accelerometers. *Gait & Posture, 27*(1), 168-171. doi:10.1016/j.gaitpost.2007.03.001

Yanagisawa S., Sato N., Shimizu M., Saito K., Yamamoto A., & Takagishi K. (2015). Relation among the knee, sagittal spinal alignment, and the spinal range of motion: Investigation in local medical check-ups using the SpinalMouse. *Asia-Pacific Journal of Sports Medicine, Arthroscopy, Rehabilitation and Technology , 2*(2), 68-71. doi:10.1016/j.asmart.2015.01.002

Yoganandan N., Kumaresan S., Voo L., & Pintar F. A. (1996). Finite element applications in human cervical spine modelling. *Spine, 21*(15), 1824-1834. doi:10.1097/00007632-199608010-00022

Yoon H., Hwang S., Jung D., Choi S., Joo K., Choi J., et al. (2015). Estimation of sleep posture using a patch-type accelerometer based device. *IEEE*, 4942-4945. doi:10.1109/EMBC.2015.7319500

Yoshida H., Kamijo M., & Shimizu Y. (2010). Finite element analysis to investigate sleeping comfort of mattress. *International Conference of Kansei Engineering and Emotion Research* (KEER2010) (pp. 277-284).

Yoshida H., Kamijo M., & Shimizu Y. (2012). A study to investigate the sleeping comfort of mattress using finite element method. *Kansei Engineering International Journal, 11*(3), 155-162. doi:10.5057/kei.11.155

Zafarparandeh I., Erbulut D. U., Lazoglu I., & Ozer A. F. (2014). Development of a finite element model of the human cervical spine. *Turkish Neurosurgery, 24*(3), 312-318. doi:10.5137/1019-5149.JTN.8486-13.0

Zafarparandeh I., & Lazoglu I. (2012). Application of the finite element method in spinal implant design and manufacture. *The Design and Manufacture of Medical Devices*, 153-183. doi:10.1016/B978-1-907568-72-5.50004-2

Zhang N., Cao B., & Zhu Y. (2018). Indoor environment and sleep quality: A research based on online survey and field study. *Building and Environment, 137*, 198-207. doi:10.1016/j.buildenv.2018.04.007

Zhang Q., Chon T., Zhang Y., Baker J. S., & Gu Y. (2021). Finite element analysis of the lumbar spine in adolescent idiopathic scoliosis subjected to different loads. *Computers in Biology and Medicine, 136*, 104745. doi:10.1016/j.compbiomed.2021.104745

Zhang Q. H., Teo E. C., Ng H. W., & Lee V. S. (2006). Finite element analysis of moment-rotation relationships for human cervical spine. *Journal of Biomechanics, 39*(1), 189-193. doi:10.1016/j.jbiomech.2004.10.029

Zhong S., Shen L., Zhou L., & Guan Z. (2014). Predict human body indentation lying on a spring mattress using a neural network approach. *Proceedings of the Institution of Mechanical Engineers, Part H: Journal of Engineering in Medicine, 228*(8), 787-799. doi:10.1177/0954411914547552

Zhou G. Q., Li D. S., Zhou P., Jiang W. W., & Zheng Y. P. (2020). Automating spine curvature measurement in volumetric ultrasound via adaptive phase features. *Ultrasound in Medicine & Biology , 46*(3), 828-841. doi:10.1016/j.ultrasmedbio.2019.11.012

Zuccarello N. (2012). Human anatomy planes. *Wikimedia Commons.* Retrieved from commons.wikimedia.org/wiki/File:Human_anatomy_planes.svg